MICHIGAN STATE UNIVERSITY LIBRARIES
3 1293 01016 4543

pt. 1

This is to certify that the

dissertation entitled

STUDIES ON THE REACTIVITY OF LANTHANIDES, ACTINIDES, AND HIGHLY OXOPHILIC TRANSITION METALS IN REACTIVE MOLTEN ALKALI METAL/POLYCHALCOGENIDE SALTS AT INTERMEDIATE TEMPERATURES (250-600 °C)

presented by

Anthony C. Sutorik

has been accepted towards fulfillment
of the requirements for

Ph.D. degree in Chemistry

Major professor

Date 11/14/94

MSU is an Affirmative Action/Equal Opportunity Institution

O-12771

LIBRARY
Michigan State
University

PLACE IN RETURN BOX to remove this checkout from your record.
TO AVOID FINES return on or before date due.

DATE DUE	DATE DUE	DATE DUE

MSU is An Affirmative Action/Equal Opportunity Institution
c:\circ\datedue.pm3-p.1

STUDIES ON THE REACTIVITY OF LANTHANIDES, ACTINIDES, AND HIGHLY OXOPHILIC TRANSITION METALS IN REACTIVE MOLTEN ALKALI METAL/POLYCHALCOGENIDE SALTS AT INTERMEDIATE TEMPERATURES (250-600 °C)

By

Anthony C. Sutorik

A DISSERTATION

Submitted to
Michigan State University
in partial fulfillment of the requirements
for the degree of

DOCTOR OF PHILOSOPHY

Department of Chemistry

1994

ABSTRACT

STUDIES ON THE REACTIVITY OF LANTHANIDES, ACTINIDES, AND HIGHLY OXOPHILIC TRANSITION METALS IN REACTIVE MOLTEN ALKALI METAL/POLYCHALCOGENIDE SALTS AT INTERMEDIATE TEMPERATURES (250-600 °C)

By

Anthony C. Sutorik

Although the chemistry of many metals with polychalcogenide ligands [$(Q_x)^{2-}$, Q=S, Se, Te; n=2-6] have been extensively studied using solution chemistry techniques, this is not the case for the whole periodic table. Specifically, cations of the lanthanides, actinides, and early transition metals are all very hard acids and so are very oxophilic. As such any chalcogenide ligand would be easily displaced by smaller and harder oxygen-containing species. In order to study the polychalcogenide chemistry of these metal in polar solvents, rigorous precautions must be taken to exclude any possible source of oxygen from the system so as to not poison the reaction.

Molten alkali metal/polychalcogenide salts (A_2Q_x) have melting points in a temperature region (250-600 °C) which is hotter than that which is used in conventional solution chemistry but cooler than the classical realm of solid state synthesis. By using these salts as reactive fluxes, the

chemistry between metals and polychalcogenides can be explored directly, without the need for some solvent medium, and the unique temperature region accessible with these fluxes has lead to the discovery of many new and metastable metal/chalcogenide compounds. Given these characteristics of the molten A_2Q_x fluxes, a systematic investigation was undertaken to explore the reactivity of lanthanides, actinides, and early transition metals in this unique chemical medium.

Many new phases have resulted. In systems where a single metal is allowed to react in a molten A_2Q_x flux, the new ternary phases K_4USe_8, $KCeSe_4$, $KTbSe_4$, $RbCeTe_4$, $NaLaS_3$, and $NaCeS_3$ have been isolated and characterized. Increasing the complexity of these reactions by including a second metal, in this case copper, has resulted in several new quaternary phases: $KCuCe_2S_6$, $KCuLa_2S_6$, $CsCuCe_2S_6$, $KCuCe_2Se_6$, $K_2Cu_2CeS_4$, $CsCuCeS_3$, $KCuUSe_3$, and $K_6Cu_{12}U_2S_{15}$. Lastly the utility of these polychalcogenide fluxes for the synthesis of new metal oxychalcogenides was explored. These experiments resulted in the discovery of $Ba_6Ti_5S_{15}O$, $K_2CuCe_2Se_6OH$, $Cs_4(UO_2)S_6$, $Na_4(UO_2)S_6 \cdot Na_2S_3$, and $Na_4Cu_2(UO_2)S_4$. The structural diversity in all of these compounds has ranged from discrete anions through three-dimensional lattices, and several of them have exhibited interesting physical properties as well. The synthetic work performed here has laid the groundwork for further exploration of these and related systems.

DEDICATION

To Myself

ACKNOWLEDGMENTS

The hardest part of this thesis is on this page. The brief words of thanks that I now express actually represent a much greater wealth of emotions.

Mercouri G. Kanatzidis has served as my research advisor, and his talent and intellect are reflected in both the sheer volume and high quality of the work presented here. The challenges he presented, the support he offered, the faith he held, and the vision he shared are all gratefully acknowledged.

Graduate school has afforded me the opportunity to be associated with many of the finest people I am every likely to meet, and I am fortunate enough to have met them here, where the excitement of discovery and the intensity of hard work result in the deep intimacy of shared experiences. To all the friends I've made at this time in my life, I have become a better person for knowing each of you, and I will carry my memories of you with pride, happiness, and deep affection.

My young son Isaac was born during these years, and when he reads this in future times, I want him to know how my frustration and stress was always relieved by his screaming my name followed by a big running hug at the end of a day. I am blessed to receive his love and joy, and I'm very proud of him.

Through it all, I have had at my side, my beautiful wife, Shelly. Every joy I felt, I felt with her. Every pain I felt, I felt with her. I have burdened her considerably over the last few years, but she has continued to love and support me, and so at this point in my life I feel resurrected in very facet of my being because of her. I love you, Shelly.

TABLE OF CONTENTS

Page

LIST OF TABLES.....xii
LIST OF FIGURES.....xviii

CHAPTER 1: The Case for Studying Metal Reactivity in Molten Alkali Metal /Polychalcogenide Salts at Intermediate Temperatures (250-600 °C).....1

I. Introduction.....2

II. The Nature of the Polychalcogenide Flux.....8

A. Physio-chemical Characteristics.....8

B. Reactivity.....13

CHAPTER 2: Ternary reactions of Lanthanides and Actinides in Molten Alkali Metal/Polychalcogenide Fluxes at Intermediate Temperature (250-600 °C).....25

A. Introduction.....26

B. Expeimental.....35

1. Synthesis.....35

Reagents.....35

Potassium Selenide, K_2Se.....36

Sodium Sulfide, Na_2S.....36

Rubidium Telluride, Rb_2Te.....36

Tetrapotasium Uranium Octaselenide, K_4USe_8 37
Potassium Cerium Tetraselenide, $KCeSe_4$ 41
Potassium Terbium Tetraselenide, $KTbSe_4$ 44
Potassium Terbium Tetraselenide, $RbCeTe_4$ 46
Sodium Cerium Trisulfide, $NaCeS_3$ 48
Sodium Lanthanum Trisulfide, $NaLaS_3$ 52
2. Physical Measurements.....55
C. Results and Discussion.....60
1. K_4USe_8.....60
Structure.....60
Magnetic Properties.....66
Spectroscopy.....68
1. $ALnQ_4$ (A=K; Ln=Ce, Tb; Q=Se or
A=Rb; Ln=Ce; Q=Te).....69
Structure.....69
Magnetic Properties.....78
Spectroscopy.....81
1. $NaLnS_3$ (Ln=La, Ce).....83
Structure.....83
Magnetic Properties.....93
Spectroscopy.....95
D. Conclusions.....97

CHAPTER 3: New Quaternary Compounds Resulting from the Reaction of Copper and f-block Metals in Molten Polychalcogenide Salts at Intermediate Temperatures.....105
A. Introduction.....106

B. Expeimental.....109
1. Synthesis.....109
Reagents.....109
Potassium selenide, K_2Se.....109
Potassium sulfide, K_2S.....109
Cesium sulfide, Cs_2S.....110
Potassium copper dicerium hexasulfide, $KCuCe_2S_6$..110
Potassium copper dilanthanum hexasulfide, $KCuLa_2S_6$.....115
Cesium copper dicerium hexasulfide, $CsCuCe_2S_6$.....118
Potassium copper dicerium hexaselenide, $KCuCe_2S_6$ 121
Dipotassium dicopper cerium tetrasulfide, $K_2Cu_2CeS_4$ 124
Cesium copper cerium trisulfide, $CsCuCeS_3$ 127
Potassium copper uranium triselenide, $KCuUSe_3$.....131
Hexapotassium dococacopper diuranium pentadecasulfide, $K_6Cu_{12}U_2S_{15}$.....135
2. Physical Measurements.....138

C. Results and Discussion..... 143
1. $ACuLn_2Q_6$.....143
Structure.....143
Magnetic Susceptibility Studties.....158
Spectroscopic Data.....163
2. $K_2Cu_2CeS_4$.....168
Structure.....168

Magnetic Susceptibility Studties.....175
Charge-Transport Measurements..... 177
Spectroscopy.....181
3. $ACuMQ_3$.(A=Cs, M=Ce, Q=S; or A=K, M=U, Q=Se)....182
Structure.....182
Magnetic Susceptibility 190
Spectroscopy.....195
Charge-Transport Measurements.....196
3. $K_6Cu_{12}U_2S_{15}$.....202
Structure.....202

CHAPTER 4: New Metal/Oxychalcogenide Compounds Resulting from Reactions in Molten Polychalcogenide Salts: A Measure of Kinetic Control in the Fight Against Thermodynamically Stable Binary Oxides.....226
Part I: Introduction.....227

Part II: $Ba_6Ti_5S_{15}O$: A New Metal/Oxysulfide Resulting from the Inclusion of BaO into the $BaTiS_3$ Structure Type.....232
A. Introduction.....232
B. Experimental.....233
1. Synthesis..... 233
Reagents.....233
Hexabarium pentatitanium oxydocapentasulfide $Ba_6Ti_5S_{15}O$ 233
2. Physical Measurements..... 238
C. Results and Discussion.....241

Structure.....241
Spectroscopic Data.....249
D. Conclusions.....251
PART III: $K_2CuCe_2Se_6O(H?)$: A Kinetically Sensitive Derivative of the $ACuM_2Q_6$ (M=Lanthanide, Q=Chalcogenide) Structure Type with the Possible Presence of a Hydroxide for Charge Neutrality.....254
A. Introduction.....254
B. Experimental.....254
1. Synthesis..... 254
Reagents.....254
Potassium Selenide, K_2Se.....255
Dipotassium copper dicerium hydroxyhexaselenide, $K_2CuCe_2Se_6OH$ 233
2. Physical Measurements..... 259
C. Results and Discussion.....263
Structure.....263
Magnetic Susceptibility.....269
Spectroscopy.....272
D. Conclusions and Summary.....275
Part VI: $Cs_4(UO_2)S_6$, $Na_4(UO_2)S_6 \cdot Na_2S_3$, and $Na_4Cu_2(UO_2)S_4$: The *in situ* Formation and Subsequent Reaction of Uranyl Cations in Molten Alkali Metal/ Polychalcogenide Salts.....277
A. Introduction.....277
B. Experimental.....278
1. Synthesis.....278

Reagents.....278
Cesium sulfide, Cs_2S.....278
Sodium sulfide. Na_2S.....278
Tetracesium tris(disulfido)bis-oxo uranate, $Cs(UO_2)S_6$ 278
Tetrasodium tris(disulfido)bis-oxo uranate disodium trisulfide, $Na_4(UO_2)(S_2)_3 \cdot Na_2S_3$ 282
Tetrasodium tetrasulfidobisoxo dicopper uranate, $Na_4Cu_2(UO_2)S_4$ 282
2. Physical Measurements.....286
C. Results and Discussion.....289
1. $Cs(UO_2)S_6$ and $Na_4(UO_2)(S_2)_3 \cdot Na_2S_3$ 289
Structure.....289
Spectroscopy.....300
2.$Na_4Cu_2(UO_2)S_4$.....302
Structure.....302
Spectroscopy.....309
D. Conculsions.....310

LIST OF TABLES

Page

Table 1.1: Melting Points (°C) for Known Alkali Metal/ Polychalcogenide Salts....11

Table 1.2: Examples of Metal (M)/Polychalcogenide (Q_x^{2-}) Coordination Complexes....15

Table 2.1 Calculated and Observed X-ray Powder Diffraction Pattern for K_4USe_8 (Cu radiation)....38

Table 2.2 Calculated and Observed X-ray Powder Diffraction .Pattern for $KCeSe_4$ (Cu radiation)....42

Table 2.3 Calculated and Observed X-ray Powder Diffraction Pattern for $KTbSe_4$ (Cu radiation)....45

Table 2.4 Calculated and Observed X-ray Powder Diffraction Pattern for $RbCeTe_4$ (Cu radiation)....47

Table 2.5 Calculated and Observed X-ray Powder Diffraction .Pattern for $NaCeS_3$ (Cu radiation)....50

Table 2.6 Calculated and Observed X-ray Powder Diffraction Pattern for $NaLaS_3$ (Cu radiation)....53

Table 2.7: Crystallographic Data for K_4USe_8, $KCeSe_4$, $KTbSe_4$, $RbCeTe_4$, $NaCeS_3$, and $NaLaS_3$....58

Table 2.8 Selected Bond Distances (Å) and Angles (°) for K_4USe_8 with Standard Deviations in Parentheses....63

Table 2.9 Fractional Atomic Coordinates and B_{eq}^a values for K_4USe_8 with Estimated Standard Deviations in Parentheses....64

Table 2.10 Selected Bond Distances (Å) and Angles (°) for KCeSe4 with Standard Deviations in Parentheses.....73
Table 2.11 Selected Bond Distances (Å) and Angles (°) for KTbSe4 with Standard Deviations in Parentheses.....73
Table 2.12 Fractional Atomic Coordinates and B_{eq}^{a} values for KCeSe4 with Estimated Standard Deviations in Parentheses.....74
Table 2.13 Fractional Atomic Coordinates and B_{eq}^{a} values for KTbSe4 with Estimated Standard Deviations in Parentheses.....74
Table 2.14 Selected Bond Distances (Å) and Angles (°) for RbCeTe4 with Standard Deviations in Parentheses.....75
Table 2.15 Fractional Atomic Coordinates and B_{eq}^{a} values for RbCeTe4 with Estimated Standard Deviations in Parentheses.....75
Table 2.16 Fractional Atomic Coordinates and B_{eq}^{a} values for NaLaS3 with Estimated Standard Deviations in Parentheses.....87
Table 2.17 Fractional Atomic Coordinates and B_{eq}^{a} values for NaCeS3 with Estimated Standard Deviations in Parentheses.....87
Table 2.18 Selected Bond Distances (Å) and Angles (°) for NaLaS3 with Standard Deviations in Parentheses.....88
Table 2.19 Selected Bond Distances (Å) and Angles (°) for NaCeS3 with Standard Deviations in Parentheses.....88
Table 3.1 Calculated and Observed X-ray Powder Diffraction Pattern for $KCuCe_2S_6$ (Cu radiation).....112

Table 3.2 Calculated X-ray Powder Diffraction Pattern for $KCuCe_2S_6$ and Observed X-ray Powder Diffraction Pattern for $KCuLa_2S_6$ (Cu radiation).....116

Table 3.3 Calculated and Observed X-ray Powder Diffraction Pattern for $CsCuCe_2S_6$ (Cu radiation).....119

Table 3.4 Calculated and Observed X-ray Powder Diffraction Pattern for $KCuCe_2Se_6$ (Cu radiation).....122

Table 3.5 Calculated and Observed X-ray Powder Diffraction Pattern for $K_2Cu_2CeS_4$ (Cu radiation).....125

Table 3.6 Calculated and Observed X-ray Powder Diffraction Pattern for $CsCuCeS_3$ (Cu radiation).....129

Table 3.7 Calculated and Observed X-ray Powder Diffraction Pattern for $KCuUSe_3$ (Cu radiation).....132

Table 3.8 Calculated and Observed X-ray Powder Diffraction Pattern for $K_6Cu_{12}U_2S_{15}$ (Cu radiation)....136

Table 3.9: Crystallographic Data for $KCuCe_2S_6$, $CsCuCe_2S_6$, $KCuCe_2Se_6$, $K_2Cu_2CeS_4$, $CsCuCeS_3$, $KCuUSe_3$, and $K_6Cu_{12}U_2S_{15}$.....140

Table 3.10: Fractional Atomic Coordinates and B_{eq}^a values for $KCuCe_2S_6$ with Estimated Standard Deviations in Parentheses.....147

Table 3.11: Selected Bond Distances (Å) and Angles (°) for $KCuCe_2S_6$ with Estimated Standard Deviations in Parentheses.....148

Table 3.12: Fractional Atomic Coordinates and B_{eq}^a values for $CsCuCe_2S_6$ with Estimated Standard Deviations in Parentheses.....152

Table 3.13: Fractional Atomic Coordinates and B_{eq}^{a} values for $KCuCe_2Se_6$ with Estimated Standard Deviations in Parentheses.....153
Table 3.14: Selected Bond Distances and Angles for $CsCuCe_2S_6$ and $KCuCe_2Se_6$ with Estimated Standard Deviations in Parentheses.....154
Table 3.15 Peaks from the Far-IR spectra of $KCuCe_2S_6$, $KCuLa_2S_6$, $CsCuCe_2S_6$, and $KCuCe_2Se_6$.....167
Table 3.16: Fractional Atomic Coordinates and B_{eq} values for $K_2Cu_2CeS_4$ with Estimated Standard Deviations in Parentheses.....171
Table 3.17: Selected Bond Distances (Å) and Angles (°) for $K_2Cu_2CeS_4$ with Estimated Standard Deviations in Parentheses.....172
Table 3.18: Selected Bond Distances and Angles for $CsCuCeS_3$ and $KCuUSe_3$ with Estimated Standard Deviations in Parentheses.....186
Table 3.19: Fractional Atomic Coordinates and B_{eq}^{a} values for $CsCuCeS_3$ with Estimated Standard Deviations in Parentheses.....187
Table 3.20: Fractional Atomic Coordinates and B_{eq}^{a} values for $KCuUSe_3$ with Estimated Standard Deviations in Parentheses.....188
Table 3.21: Fractional Atomic Coordinates and B_{eq}^{a} values for $K_6Cu_{12}U_2S_{15}$ with Estimated Standard Deviations in Parentheses.....205

Table 3.13: Fractional Atomic Coordinates and B_{eq}^{a} values for $KCuCe_2Se_6$ with Estimated Standard Deviations in Parentheses.....153
Table 3.14: Selected Bond Distances and Angles for $CsCuCe_2S_6$ and $KCuCe_2Se_6$ with Estimated Standard Deviations in Parentheses.....154
Table 3.15 Peaks from the Far-IR spectra of $KCuCe_2S_6$, $KCuLa_2S_6$, $CsCuCe_2S_6$, and $KCuCe_2Se_6$.....167
Table 3.16: Fractional Atomic Coordinates and B_{eq} values for $K_2Cu_2CeS_4$ with Estimated Standard Deviations in Parentheses.....171
Table 3.17: Selected Bond Distances (Å) and Angles (°) for $K_2Cu_2CeS_4$ with Estimated Standard Deviations in Parentheses.....172
Table 3.18: Selected Bond Distances and Angles for $CsCuCeS_3$ and $KCuUSe_3$ with Estimated Standard Deviations in Parentheses.....186
Table 3.19: Fractional Atomic Coordinates and B_{eq}^{a} values for $CsCuCeS_3$ with Estimated Standard Deviations in Parentheses.....187
Table 3.20: Fractional Atomic Coordinates and B_{eq}^{a} values for $KCuUSe_3$ with Estimated Standard Deviations in Parentheses.....188
Table 3.21: Fractional Atomic Coordinates and B_{eq}^{a} values for $K_6Cu_{12}U_2S_{15}$ with Estimated Standard Deviations in Parentheses.....205

Table 3.22: Selected Bond Distances (Å) and Angles (°) for $K_6Cu_{12}U_2S_{15}$ with Estimated Standard Deviations in Parentheses 206
Table 4.2.1: Calculated and Observed X-ray Powder Diffraction Patterns for $Ba_6Ti_5S_{15}O$ (Cu Radiation).....236
Table 4.2.2: Fractional Atomic Coordinates and B_{eq}^a values for $B_6Ti_5S_{15}O$ with Estimated Standard Deviations in Parentheses 237
Table 4.2.3: Selected Bond Distances (Å) and Angles (°) for $Ba_6Ti_5S_{15}O$.....247
Table 4.3.1: Calculated and Observed X-ray Powder Diffraction Pattern for $K_2CuCe_2S_6OH$ (Cu radiation) 256
Table 4.3.2: Crystallographic Data for $K_2CuCe_2Se_6OH$ 261
Table 4.3.3 Fractional Atomic Coordinates and B_{eq}^a values for $K_2CuCe_2Se_6OH$ with Estimated Standard Deviations in Parentheses 262
Table 4.3.4: Selected Bond Distances (Å) and Angles (°) for $K_2CuCe_2Se_6OH$ with Estimated Standard Deviations in Parentheses 268
Table 4.4.1: Calculated and Observed X-ray Powder Diffraction Pattern for $Cs_4(UO_2)S_6$ (Cu radiation).....281
Table 4.4.2: Calculated and Observed X-ray Powder Diffraction Pattern for $Na_4Cu_2(UO_2)S_4$ (Cu radiation).....284
Table 4.4.3: Crystallographic Data for $Cs_4(UO_2)S_6$, $Na_4(UO_2)S_6 \cdot Na_2S_3$, and $Na_4Cu_2(UO_2)S_4$ 288

Table 4.4.4: Selected Bond Distances (Å) and Angles (°) for $Cs_4(UO_2)S_6$ with Estimated Standard Deviations in Parentheses 293

Table 4.4.5 Fractional Atomic Coordinates and B_{eq}^a values for $Cs_4(UO_2)S_6$ with Estimated Standard Deviations in Parentheses 295

Table 4.4.6 Fractional Atomic Coordinates and B_{eq}^a values for $Na_4(UO_2)S_6 \cdot Na_2S_3$ with Estimated Standard Deviations in Parentheses 296

Table 4.4.7: Selected Bond Distances (Å) and Angles (°) for $Na_4(UO_2)S_6 \cdot Na_2S_3$ (Standard Deviations in Parentheses) 297

Table 4.4.8: Selected Bond Distances (Å) and Angles (°) for $Na_4Cu_2(UO_2)S_6$ with Standard Deviations in Parentheses 307

Table 4.4.9 Fractional Atomic Coordinates and B_{eq}^a values for $Na_4Cu_2(UO_2)S_4$ with Estimated Standard Deviations in Parentheses 308

LIST OF FIGURE

Page

Figure 1.1: A hypothetical reaction coordinate plot of (A) a typical high temperature solid state reaction and (B) a reaction with increased diffusion of reactants 4

Figure 2.1: Phase diagram of theK_2S/S system (adapted from ref. 21).....10

Figure 2.1: Fragments of the anionic networks of (a) $K_4Ti_3S_{14}$ [5], (B) $Na_2Ti_2Se_8$ [6], and (C) $K_3Nb_2Se_{11}$ [7](solid circles= metal; empty circles=chalcogneide).....28

Figure 2.2: Schematic representation of the structures of several known binary lanthanide/chalcogenides: (A) LnQ_2 [8], (B) $LnTe_3$ [9], (C) Ln_2Te_5 [10] (Ln=lanthanide, Q=chalcogenide).....30

Figure 2.3: A schematic of the $ALnQ_2$ structure type.....32

Figure 2.4: A Schematic representation of the AgLnSe2 structure type (Ln=lanthanide).....34

Figure 2.5: (A): Ortep representation of the $[U(Se_2)_4]^{4-}$ anion (B): An ideal triangulated dodecahedron.....62

Figure 2.6: Ortep drawings of the coordination environments of the atoms K(1), (A), and K(2), (B), in the structure of K_4USe_8 65

Figure 2.7: Inverse molar magnetic susceptibility ($1/\chi_M$) plotted against temperature (K) for K_4USe_8 (5000 Gauss) 67

Figure 2.8: The immediate coordination environment of the Ln3+ cations in the ALnQ4 structure type (A=alkali, Ln=lanthanide, Q=Se, Te) 70

Figure 2.9: The view perpendicular to the anionic layers of $ALnQ_4$ 71

Figure 2.10: $ALnQ_4$ as seen parallel to the crystallographic [110] direction 72

Figure 2.11: Inverse molar magnetic susceptibility ($1/\chi_M$) plotted against temperature (2-300 K) for $KCeSe_4$ (300 G). The inset graph shows an expanded view of the region 2-50 K 79

Figure 2.12: Inverse molar magnetic susceptibility ($1/\chi_M$) plotted against temperature (2-300 K) for $KTbSe_4$ (5000 G). (B) shows an expanded view of the region 2-25 K 80

Figure 2.13: The solid state diffuse reflectance spectra of $KCeSe_4$ (solid line) and $KTbSe_4$ (dashed line) plotted as absorption coefficient (a/S) vs. energy (eV) 82

Figure 2.14: Ortep representation of the immediate coordination environment of the Ln^{3+} cations in $NaLnS_3$ (Ln=La, Ce).....84

Figure 2.15: The face-sharing connection between two [LnS_6] trigonal prisms featured in the structure of $NaLnS_3$.....85

Figure 2.16: The extended structure of $NaLnS_3$ as seen parallel to the c-axis (circles with nonshaded octants: Na; open circles: Ln; circles with shaded octants: S).....86

Figure 2.17: Schematic drawing of the immediate coordination environment of a Ce atom in the structure of CeS_2.....90

Figure 2.18: A schematic showing the monosulfide environments about the lanthanide cations in the structures of (A) CeS_2 and (B) $NaLnS_3$.(solid circles: metal; open circle: sulfide; semisolid circle: two eclipsed sulfides).....91

Figure 2.19: Schematic drawings of the (A) CeS^2 and (B) $NaLnS^3$ structures where the edge sharing rhombi represent bilayers of Ln^{3+} and S^{2-}; the solid lines, sheets of $(S_2)^{2-}$; and the open circles, Na^+ cations.....92

Figure 2.20: Inverse molar magnetic susceptibility ($1/\chi_M$) plotted against temperature (2-300 K) for $NaCeS_3$ (2000 G). (B) shows an expanded view of the region 2-25 K.....94

Figure 2.21: The solid state diffuse reflectance spectra of $NaCeS_3$ (solid line) and $NaLaS_3$ (dashed line) plotted as absorption coefficient (α/S) vs. energy (eV).....96

Figure 3.1 The extended structure of $KCuCe_2S_6$ as seen down the [101] direction both without (A) and with (B) the compound's Cu+ cations (Circles with nonshaded octants: K; large open circles: Cu; small open circles: Ce; circles with shaded octants: S).....145

Figure 3.2 A fragment of the anionic structure of $KCuCe_2S_6$ highlighting the coordination environment of the compounds Cu and Ce atoms.....146

Figure 3.3 The extended structure of the orthorhombic form of $ACuCe_2Q_6$ as seen down the a-axis (Circles with nonshaded octants: A; large open circles: Cu; small open circles: Ce; circles with shaded octants: Q).....150

Figure 3.4 A fragment of the anionic structure of $ACuCe_2Q_6$ (A=Cs, Q=S; A=K, Q=Se) highlighting the coordination environment of the compounds Cu and Ce atoms.....151

Figure 3.5 (A) The extended structure of the $NaLnS_3$ structure type. (B) The extended structure of the $ACuLn_2Q_6$ structure type (Circles with nonshaded octants: A; large open circles: Cu; small open circles: Ce; circles with shaded octants: Q).....157

Figure 3.6: Inverse molar magnetic susceptibility ($1/\chi_M$) plotted against temperature (2-300 K) for $KCuCe_2S_6$ (2000 G). The inset graph shows an expanded view of the region 2-25 K.....159

Figure 3.7: Inverse molar magnetic susceptibility ($1/\chi_M$) plotted against temperature (2-300 K) for $CsCuCe_2S_6$ (2000 G). (B) shows an expanded view of the region 2-25 K.....161

Figure 3.8: Inverse molar magnetic susceptibility ($1/\chi_M$) plotted against temperature (2-300 K) for $KCuCe_2Se_6$ (2000 G). (B) shows an expanded view of the region 2-25 K.....162

Figure 3.9: The solid state diffuse reflectance spectra of $KCuCe_2S_6$ (—), $CsCuCe_2S_6$ (- - -), and $KCuLa_2S_6$ (---) plotted as absorption coefficient (α/S) vs. energy (eV).....164

Figure 3.10: The solid state diffuse reflectance spectra of $KCuCe_2Se_6$ plotted as absorption coefficient (α/S) vs. energy (eV).....165

Figure 3.11: The view of a single anionic layer of $K_2Cu_2CeS_4$ (Large open circles: Cu; small open circles: Ce; circles with shaded octants: S).....169

Figure 3.12: The extended structure of $K_2Cu_2CeS_4$ as seen down the b-axis, parallel to the anionic layers

(Circles with nonshaded octants: K; large open circles: Cu; small open circles: Ce; circles with shaded octants: S)..... 170

Figure 3.13: Inverse molar magnetic susceptibility ($1/\chi_M$) plotted against temperature (2-300 K) for $K_2Cu_2CeS_4$ (1000 Gauss). The inset graph shows an expanded view of the region 2-25 K.....176

Figure 3.14: Conductivity (log σ/cm) plotted against temperature (K) for a pressed pellet sample of $K_2Cu_2CeS_4$.....178

Figure 3.15: Thermopower (μV/K) plotted against temperature (K) for a pressed pellet sample of $K_2Cu_2CeS_4$.....179

Figure 3.16: The view perpendicular to a single anionic layer of the $ACuMQ_3$ structure type, where A=Cs, M=Ce, Q=S; or A=K, M=U, Q=Se (Large open circles: Cu; small open circles: M, circles with shaded octants: Q).....184

Figure 3.17: The $ACuMQ_3$ structure type (A=Cs, M=Ce, Q=S; or A=K, M=U, Q=Se) as seen down the a-axis, parallel to the anionic layers (circles with nonshaded octants: A; large open circles: Cu; small open circles: M, circles with shaded octants: Q) 185

Figure 3.18: Inverse molar magnetic susceptibility ($1/\chi_M$) plotted against temperature (2-300 K) for $CsCuCeS_3$

(1000 Gauss). Plot (B) shows an expanded view of the region 2-25 K.....192

Figure 3.19: Inverse molar magnetic susceptibility ($1/\chi_M$) plotted against temperature (2-300 K) for $KCuUSe_3$ (5000 Gauss). The inset graph shows an expanded view of the region 2-50 K.....194

Figure 3.20: Conductivity (log σ/cm) plotted against temperature (K) for a pressed pellet sample of $CsCuCeS_3$ 197

Figure 3.21: Thermopower (μV/K) plotted against temperature (K) for a pressed pellet sample of $CsCuCeS_3$.....198

Figure 3.22: Conductivity (log σ/cm) plotted against temperature (1000/K) for a pressed pellet sample of $KCuUSe_3$ 200

Figure 3.23: Thermopower (μV/K) plotted against temperature (K) for two different single crystals of $KCuUSe_3$ 201

Figure 3.24: The basic structural building block of $K_6Cu_{12}U_2S_{15}$: a $[US_6]$ octahedra edge-sharing with six $[CuS_3]$ trigonal planes.....207

Figure 3.25: A fragment of the one-dimensional columns of $K_6Cu_{12}U_2S_{15}$ which are formed by corner-sharing connections between $[CuS_3]$ trigonal planes on neighboring building blocks.....208

Figure 3.26: A fragment of $K_6Cu_{12}U_2S_{15}$ highlighting an S(2) atom in its function as a bridge between two neighboring columns.....209

Figure 3.27: A stereo view of a fragment of $K_6Cu_{12}U_2S_{15}$, highlighting an S(2) atom in its function as a bridge between two neighboring columns.....210

Figure 3.28: A fragment of the one-dimensional columns of $K_6Cu_{12}U_2S_{15}$ highlighting how the tetrahedra about the S(2) atoms alternate their directions along the column.....211

Figure 3.29: The unit cell of $K_6Cu_{12}U_2S_{15}$, as seen parallel to the a-axis.....212

Figure 3.30: A stereo view of the unit cell of $K_6Cu_{12}U_2S_{15}$, as seen parallel to the a-axis.....213

Figure 3.31: The unit cell of $K_6Cu_{12}U_2S_{15}$, as seen parallel to the [1-10] direction.....214

Figure 3.32: A stereo view of the unit cell of $K_6Cu_{12}U_2S_{15}$, as seen parallel to the [1-10] direction.....215

Figure 3.33: The unit cell of $K_6Cu_{12}U_2S_{15}$, as seen parallel to the [1-11] direction.....216

Figure 3.34: A stereo view of the unit cell of $K_6Cu_{12}U_2S_{15}$, as seen parallel to the [1-11] direction.....217

Figure 4.2.1: The basic repeating unit in the structure of $Ba_6Ti_5S_{15}O$: five face-sharing Ti-centered octahedra.244

Figure 4.2.2: The view perpendicular to a single anionic layer from $Ba_6Ti_5S_{15}O$.....245

Figure 4.2.3: The structure of $Ba_6Ti_5S_{15}O$ as seen parallel to the a-axis.....246

Figure 4.2.4: The solid state diffuse reflectance spectra of $Ba_6Ti_5S_{15}O$ plotted as absorption coefficient (α/S) vs. energy (eV).....250

Figure 4.3.1: A fragment on the structure of $K_2CuCe_2Se_6OH$, highlighting the coordination environment of the metal atoms.....265

Figure 4.3.2: The extended structure of $K_2CuCe_2Se_6OH$ as seen parallel to the b-axis.....266

Figure 4.3.3: The extended structure of $KCuCe_2Se_6$ as seen parallel to the c-axis.....267

Figure 4.3.4: Inverse molar magnetic susceptibility ($1/\chi_M$) plotted against temperature (2-300 K) for $K_2CuCe_2Se_6OH$ (1000 Gauss). Plot (B) shows an expanded view of the region 2-25 K.....270

Figure 4.3.5: The solid state diffuse reflectance spectra of $K_2CuCe_2Se_6OH$ plotted as absorption coefficient (α/S) vs. energy (eV).....273

Figure 4.3.6: Spectra in the mid-IR region of (a) $K_2CuCe_2Se_6OH$ and (b) $KCuCe_2Se_6$ (KBr matrix).....274

Figure 4.4.1: The $[(UO_2)(S_2)_3]^{4-}$ anion.....291

Figure 4.4.2: Two views of the $[(UO_2)(S_2)_3]^{4-}$ anion: (A) parallel and (B) perpendicular to the equatorial plane.....292

Figure 4.4.3: The unit cell of $Cs_4(UO_2)S_6$ as seen parallel to the b-axis 299

Figure 4.4.4: The solid state diffuse reflectance spectra of $Cs_4(UO_2)S_6$ plotted as absorption coefficient (α/S) vs. energy (eV).....301

Figure 4.4.5: The view perpendicular to an anionic layer of $Na_4Cu_2(UO_2)S_4$ 304

Figure 4.4.6: The $[Cu_4S_8]$ cluster present in the structure of $Na_4Cu_2(UO_2)S_4$ 305

Figure 4.4.7: A fragment of the structure of $Na_4Cu_2(UO_2)S_4$ showing the immediate coordination environment around the U atoms.....306

Chapter 1

The Case for Studying Metal Reactivity in Molten Alkali Metal/Polychalcogenide Salts at Intermediate Temperatures (250-600 °C)

I. Introduction

The critical role of solid state chemistry and physics to modern technology is in little doubt. Solid state compounds have been the foundation of the entire electronics industry for many years, and many emerging technologies such as nonlinear optics, superconductivity, high energy density storage batteries, and photovoltaic energy conversion, to name just a few, will hinge on developments in the economical processing of existing solid state materials and the discovery of new materials with new or enhanced properties. In this context, the importance of exploratory solid state synthesis cannot be over emphasized.

Perhaps no other area of chemical synthesis more deserves the title "exploratory" that does solid state synthesis. The majority of synthetic chemists have a measure of predictability in that the molecular units they work with remain relatively intact throughout their reactions, and so their goal is mainly to link one molecule to the next or to perform specific changes on molecular functional groups. The solid state synthesist has almost no predictability in his reactions save for the simplest cases of elemental substitution, and even then can still have his predictions frustrated.

This lack of predictability arises in part from the high reaction temperatures (>600 ^{o}C) used in typical solid state syntheses. Because the starting materials used in such reactions are usually solids themselves, very high temperatures have been necessary in order to cause sufficient diffusion for a reaction to take place. These high temperatures give rise to two important synthetic limitations. First, the reactions almost always proceed to the most thermodynamically stable products; the high energies involved often leave little room for kinetic control. These

thermodynamically stable products are typically the simplest of binary or ternary compounds, and because of their high lattice stability, they become synthetic road blocks which often take a considerable investment of effort to circumvent, if they can be circumvented at all. Second, the high reaction temperatures also dictate that only the simplest chemical building blocks can be used; that is, elements on the atomic level. Attempts to synthesize using molecules of known structure are doomed because the high temperatures used sunder all bonds and reduce the system to atoms rushing to a thermodynamic minimum. Hence, multinary compounds are more difficult to form, the preference lying with the more stable binary and ternary compounds. Being almost totally at the mercy of thermodynamics, the solid state chemist has traditionally relied on experience and intuition, rather than a set of predictable rules.

Are there any ways to increase the odds for new compound formation and against the thermodynamic traps? Consider Fig. 1.1. Plot A shows a conceptual trace of a typical high temperature solid state reaction. Note that the solid reactants encounter a large activation barrier before proceeding to the highly stable end products. The large E_{act} in this case is mainly due to the diffusion requirement of the solid reactants; hence solid state reactions are diffusion limited. If one were to develop methodology that would allow for greater diffusion of reactants, the activation energy barrier would be considerably lowered. Very high temperatures would no longer be needed, and the reaction could proceed at lower temperatures to some other outcome. Such a scenario is shown in Plot B. Note that the relative energies of the products in A and B are totally arbitrary; B could be more stable than A just as easily as it could be metastable with respect to A. Certain systems may go to A, their original

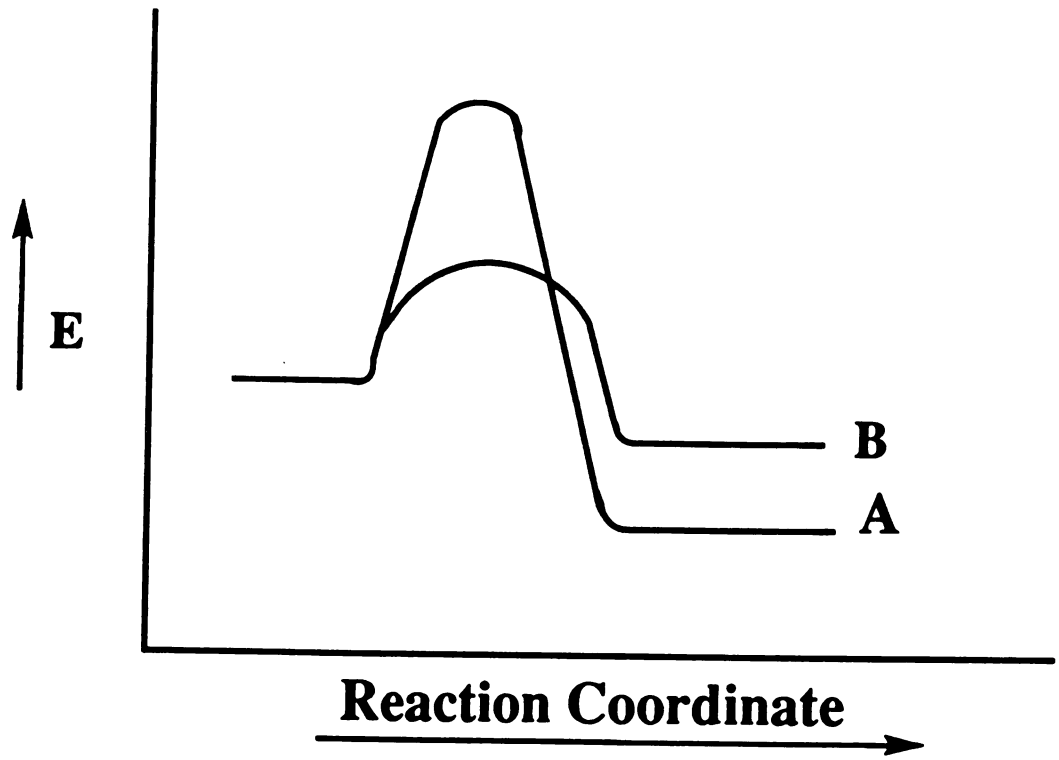

Figure 1.1: A hypothetical reaction coordinate plot of (A) a typical high temperature solid state reaction and (B) a reaction with increased diffusion of reactants

thermodymanic end products, even with reduced activation energy. There is no way to know before hand. *Although thermodynamic influences are not entirely avoided, it is clear that by enhancing the diffusion of the reactants, solid state reactions can be performed at lower temperatures, thereby increasing the likelihood of forming new compounds.* Lower temperatures would also make possible the use of molecular assemblies as building blocks for incorporation into solid state structures.

The amount of diffusion conducive to solid state reactions is not arbitrary. "Infinite diffusion" (from a solid state perspective) could be achieved by simply reacting soluble starting materials in some solvent, but when it comes to extended solids, such solution techniques are prone to produce products in the form of intractable powders. For adequate structural and physical characterization of new phases, single crystals, for use in X-ray diffraction studies, are the requirement. Methodologies for enhanced diffusion at lower temperatures (<600 ^{o}C) must have some mechanism for crystal growth built in or else generate products in a form amenable to other analytical techniques.

Over the past few years, work has been underway on many fronts to move way from the high temperatures of classical solid state synthesis, towards techniques which take advantage of lower reaction temperatures. One technique well known to chemists is chemical vapor deposition (CVD). Here the synthesis of solid state compounds, usually as thin films or other technologically useful forms, proceeds by the intimate gas phase mixing of volatile precursors leading, upon pyrolysis, to deposition of solid state intermetallic materials on various substrates [1]. This technique is intended for the synthesis of known solid state compounds rather than the discovery of new ones. Deposition of thin layers (15-50 Å) of starting materials,

one on top of the other, has been a method used to achieve intimate mixing of reactants by reducing diffusion distances [2, 3]. Although new phases have been successfully synthesized by these techniques, the deposition methods used are amenable only to elemental reactants, while synthesis using molecular species would be limited. The hydro(solvo)thermal technique has proven advantageous in that polyatomic building blocks have been used in the synthesis of solid state frameworks. This method uses solvents heated in closed containers above their boiling point (but below their critical point) as reaction media [4]. Solubility of reactants are increased by virtue of the unusually high temperature and pressure within the container. Diffusion and crystal growth are further enhanced by the inclusion of mineralizers, species which can aid in the solvation and reprecipitation of solid state reactants and products, analogous to the function of the transport agent in chemical vapor transport crystal growth. Solvothermal synthesis has been the method of choice for the synthesis of zeolites [5] and in recent years has broadened in scope to include the formation of new metal phosphates [6], metal selenates and seleites [7], alkoxopolyoxovanadium clusters [8], and metal polychalcogenides [9], to name a few. The question of synthetic outcome from reactions performed in supercritical solvents has begun to be explored only recently although the solvation of normally insoluble materials and subsequent superior diffusion in such a media makes this an especially exciting approach [10]. Performing reactions using molten salts as solvents is also a highly attractive option. Such media have been employed for well over 100 years for high temperature single crystal growth [11]. Although many salts are high melting species, eutectic combinations of binary salts and salts of polyatomic species often have melting points well below the temperatures of classical solid state synthesis,

making possible their use in the exploration of new chemistry at intermediated temperatures. In some cases, such salts act not only as solvents, but also as reactants, providing species which can be incorporated into the final product.

One class of low melting salts that are especially intriguing candidates for solid state synthesis is the alkali-metal polychalcogenides, A_2Q_x (A=alkali metal, Q=chalcogenide). This is because there already exists many metal chalcogenide compounds which have technical importance. Polysulfide ligands have been implied in the hydrodesulfurization of crude oil, where they are thought to be present at the surface of metal sulfide catalysts [12]. Polychalcogenide glasses are important as materials for non-linear optics, IR wave guides, photoconductivity, optical switching, and optical information storage, but the structure/property relationships have not been well determined due to the amorphous nature of the compounds [13]. Well characterized crystalline polychalcogenides could serve as models which would aid in illuminating such structure/property relationships. Solid state compounds with Q-Q bonds undergo reversible redox reactions with Li as shown in Equation 1:

$$2\,Li + (Q\text{-}Q)^{2-} \longrightarrow 2\,Li^{+} + 2\,Q^{2-} \qquad (1)$$

and so have been tested as rechargeable cathodes for high energy density batteries [14]. Also, reactions between metals and alkali metal polychalcogenides provide insights into the corrosion problems associated with Na/S high energy density batteries [15]. Several metal chalcogenides are photoconductive [16a,b], and $CuInSe_2$ in particular has a high radiation tolerance making it a candidate for extended extraterrestrial photovoltaic

applications [16c]. Group 15 chalcogenides of the formula M_2Q_3 (M=As, Sb, Bi; Q=S, Se, Te) have unique applications as thermoelectric cooling materials [17]. From these few examples, there is ample motivation for exploring metal reactivity in molten polychalcogenide salts both as a route to new materials with technologically interesting properties and as a way to answer long standing corrosion problems in the molten salt area.

Over the last several years, the use of molten alkali metal /polychalcogenide salts as a low temperature (200-600 °C) solid state synthesis media has been under investigation in our laboratory. The remainder of this report will be devoted to this technique and the myriad new compounds which ourselves and others have discovered through its use.

II. The Nature of the Polychacogenide Flux

A. Physio-chemical Characteristics

Molten salts of all sorts have been used for over 100 years as high temperature recrystalization media for a variety of binary and some ternary compounds [18]. In the case of alkali metal polychalcogenides, Na_2S_x melts have been used to recrystallize binary and ternary metal sulfides at temperatures greater than 700 °C by Scheel [18] and others [19]. Examples of such recrystallized materials include ZnS, CdS, MnS, PbS, $NaCrS_2$, $KCrS_2$, $NaInS_2$, $KFeS_2$, FeS_2, NiS_2, CoS_2, MoS_2, NbS_2, LaS_{2-x}, Cu_3VS_4, and HgS. The use of other polychalcogenide congeners was speculated on by the investigators but only in the context of crystal growth, rather than new compound synthesis. They did recognize, however, that lower reaction

temperatures could facilitate the formation of such compounds. Such an application was finally first demonstrated in 1987 by Sunshine, Kang, and Ibers [20].

As solvents for intermediate temperature reactions, molten A_2Q_x salts are especially well suited. Figure 1.2 shows a phase diagram for K_2S/S which has been adapted from studies done in connection with sodium/β-alumina/sulfur rechargeable batteries [21]. It can be seen that the melting points of K_2S_x species range between the extremes of K_2S at about 800 °C to K_2S_4 at 145 °C, with the majority of compositions melting at <300 °C. Although few detailed phase diagram studies of the other congeners have been performed, the melting points of many polychalcogenide salts of specific compositions have been determined and are shown in Table 1.1 [22]. Minimum melting points are higher for the heavier chalcogenides, being ca. 250 °C for the polyselenides and 350 °C for the polytellurides. Although low melting, A_2Q_x fluxes remain nonvolatile over a wide temperature range, and so once above the melting point, reaction temperatures can be varied considerably without concern for solvent loss. Polychalcogenide fluxes have the added benefit of being soluble in many common polar solvents. This allows for easy isolation of products after a reaction since excess flux can simply be dissolved away. Naturally, this also requires that any products formed be insoluble. With several solvents to choose from, the most commonly used being water, methanol, or dimethylformamide (DMF), it is usually possible to find at least one which leaves the products intact.

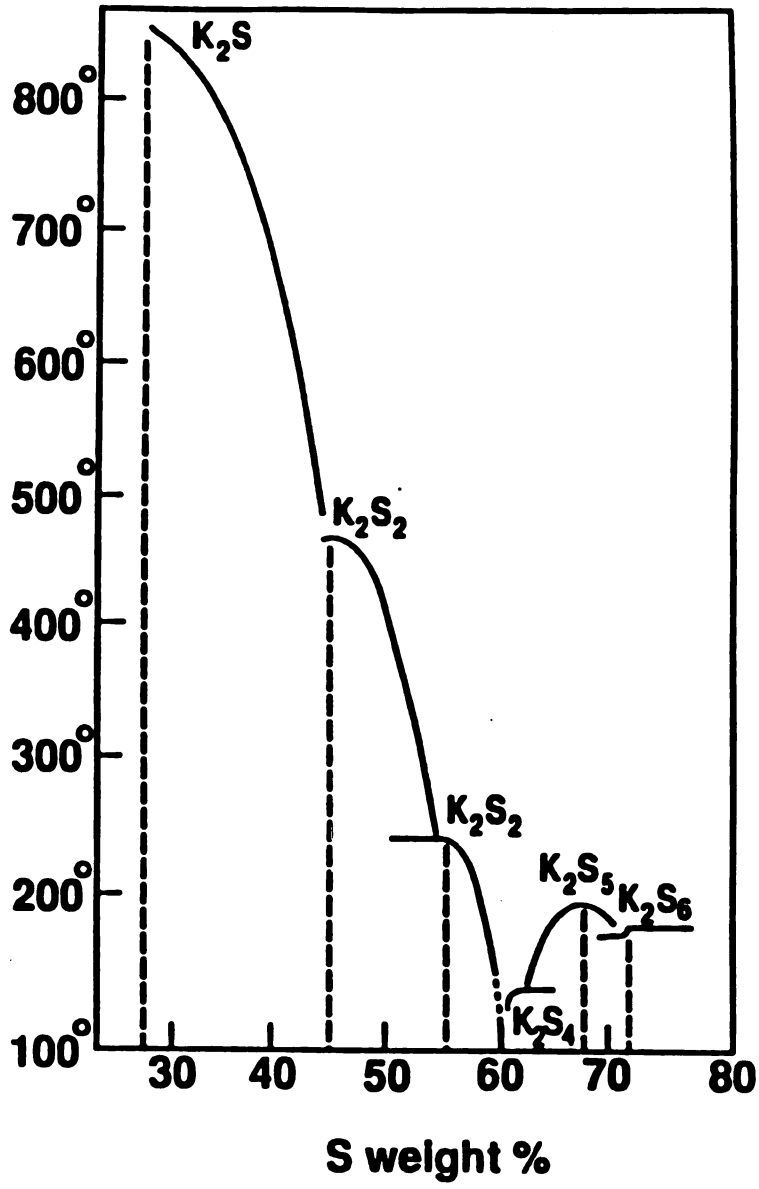

Figure 2.1: Phase diagram of theK_2S/S system (adapted from ref. 21)

Table 1.1: Melting Points (°C) for Known Alkali Metal/ Polychalcogenide Salts [22].

Li_2S 900-975	Li_2S_2 369.5				
Na_2S 1180	Na_2S_2 490	Na_2S_3 228.8	Na_2S_4 275	Na_2S_5 251.8	
Na_2Se >875	Na_2Se_2 495	Na_2Se_3 313	Na_2Se_4 290		Na_2Se_6 258
Na_2Te 953	Na_2Te_2 348				Na_2Te_6 436
K_2S 840	K_2S_2 470	K_2S_3 252	K_2S_4 145	K_2S_5 206	K_2S_6 189
	K_2Se_2 460	K_2Se_3 380	K_2Se_4 205	K_2Se_5 190	
Rb_2S 530	Rb_2S_2 420	Rb_2S_3 213	Rb_2S_4 160	Rb_2S_5 225	Rb_2S_6 201
	Cs_2S_2 460	Cs_2S_3 217	Cs_2S_4 160	Cs_2S_5 210	Cs_2S_6 186

The exact compositional nature of a molten A_2Q_x flux remains unclear. Polychalcogenides form chain fragments of various lengths, and it is known that in solution these $(Q_x)^{2-}$ chains undergo complex self-redox equilibria of the type shown in Equation 2 (23)

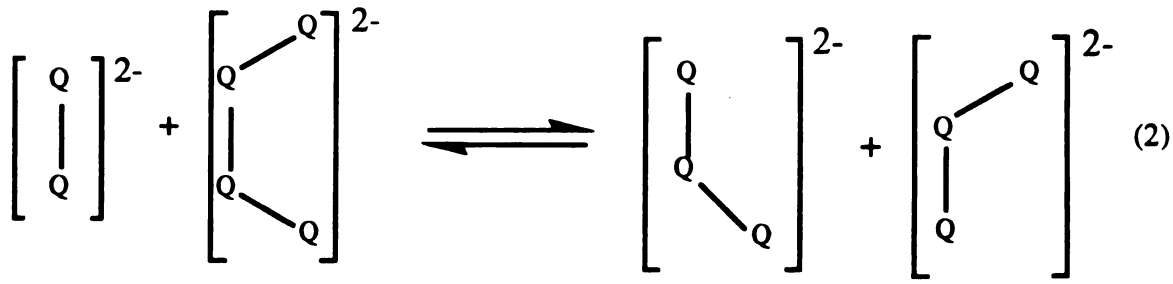

(2)

a situation which is presumably mimicked to some extent in the molten salt state. As a general phenomenon, the larger the $(Q_x)^{2-}$ fragment, the more prone it is to fall apart at higher temperatures, and so at low temperatures (250-400 °C) the self redox equilibria of the flux favors long polychalcogenide chains. Also the inclusion of elemental Q in a reaction mixture dilutes the basicity of the polychalcogenide flux somewhat, helping to promote longer $(Q_x)^{2-}$ chains. Although providing no guarantees, working under conditions which promote the presence of long $(Q_x)^{2-}$ chains has led to the discovery of many new solid state compounds which contain such ligands in extended structures, a feature which until a few years ago had been a rarity for $(Q_x)^{2-}$ species of length greater than two. Of course, new phases are not required to possess long $(Q_x)^{2-}$ chains; many metastable phases containing either partially or exclusively monochalcogenides are also encountered in molten salt synthesis at intermediate temperatures.

B. Reactivity

Using molten A_2Q_x fluxes as reactive solvents is especially intriguing when one considers the bonding diversity of $(Q_x)^{2-}$ ligands and the wide variety of new phases that can be potentially accessed. Simple monochalcogenides already possess a high degree of flexibility in their coordination to metal cations. They can be terminal or bridging and have common coordination numbers between one and eight. Polychalcogenides retain all of the bonding versatility of monochalcogenides and then some. Table 1.2 shows some common binding modes found for $(Q_x)^{2-}$ chains along with an example of each [24]. Most metal coordination to $(Q_x)^{2-}$ ligands occurs at the terminal atoms because of all the members of the chain, they are the most basic, being formally 1- in the same way as the S atom on an organic thiolate. There are several cases where an internal Q atom will also coordinate to a metal center, although this is comparatively rare. Polychalcogenides also have extensive chelation chemistry, and examples have been seen in the solid state from $(Q_2)^{2-}$ all the way to $(Q_6)^{2-}$. Solid state compounds incorporating $(Q_x)^{2-}$ are especially intriguing in that when they function as bridging ligands between two metal centers, large cages or pores can potentially be formed in the solid state. The flexibility of $(Q_x)^{2-}$ chains leads to a variety of conformational possibilities as well. The adaptability of $(Q_x)^{2-}$ ligands means that they can easily accommodate other parameters of solid state compound formation, such as the coordination number and geometry of the metal ion and the size of charge balancing counter cations. Anionic M/Q frameworks form at all levels of dimensionality: 1D chains, 2D layers and 3D lattices. Even discrete anionic clusters have been synthesized.

Table 1.2: Examples of Metal (M)/Polychalcogenide (Q_x^{2-}) Coordination Complexes

TYPE	EXAMPLE	REF.
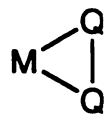	$(PPh_4)_2[W_2Se_4(Se_2)(Se_4)]$	24[a]
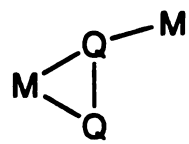	$(\eta^5\text{-}C_5H_5)Fe(CO)_2(Se_2)Cr(CO)_2(\eta^5\text{-}C_5H_5)$	24[b]
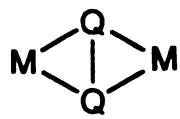	$(\eta^5\text{-}C_5H_5)Cr_2(CO)_4Se_2$	24[c]
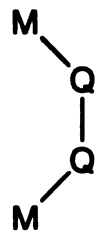	$(\eta^5\text{-}C_5H_4Me)_2V_2Se(Se_2)_2$	24[d]
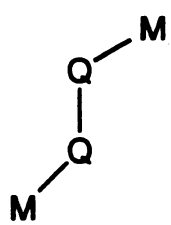	$[(\eta^5\text{-}C_5H_4Me)_2Ti]_2(Se_2)_2$	24[e]

Table 1.2: Examples of Metal (M)/Polychalcogenide (Q_x^{2-}) Coordination Complexes (cont.)

TYPE	EXAMPLE	REF.
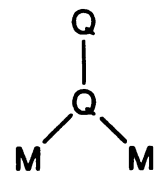	[K-2,2,2-crypt]2[Mo4(Te2)5(Te3)2(en)4]	24f
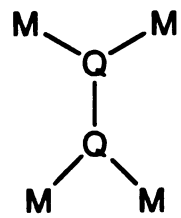	[NBu4]4[Hg4Te12]	24g
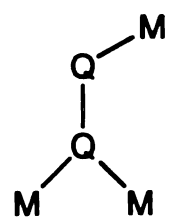	[{(η^5-C5H5)(CO)2Fe}3(Se2)][BF4]	24h
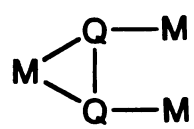	[(CO)5W(m-Te2)][W(CO)5]2	24i
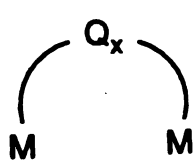	x=3; (PPh4)2[Au2(Se3)(Se2)] x=4; (PPh4)2[Au2(Se2)(Se4)2] x=5; (PPh4)2[In2(Se4)4(Se5)]	24j 24j 24k

Table 2. Examples of Metal (M)/Polychalcogenide (Q_x^{2-}) Coordination Complexes (cont.)

TYPE	EXAMPLE	REF.
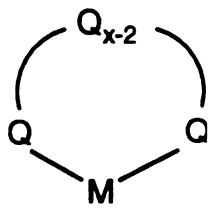	x=3; (PPh4)2[W2Se4(Se3)2] x=4;[(PPh3)2N]2[Au2Se2(Se4)2] x=5; (PPh4)2[Fe2Se2(Se5)2]	24a 24l 24m
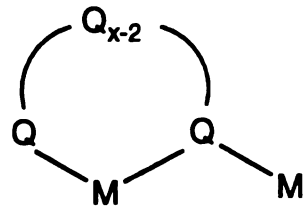	x=4; (PPh4)2[Hg2(Se4)3]	24n
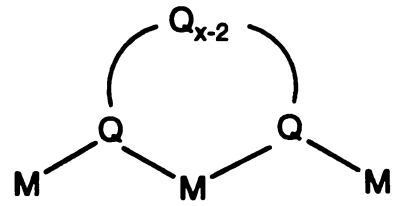	x=4; (Pr4N)2[Ag4(Se4)3]	24o
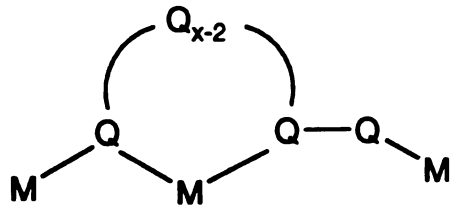	x=5; (Me4N)[Ag(Se5)]	24o

Compounds resulting from molten $(Q_x)^{2-}$ reactions are often metastable, either in forming only in a limited temperature window or in being dependent on the molten A_2Q_x flux for the appropriate reaction conditions. Many times, however, materials first discovered from a molten flux reaction turn out to be highly stable and can be subsequently prepared from high temperature, direct combination reactions of the elements or binary chalcogenides.

Reactions between metals and molten A_2Q_x are performed *in situ*. The powdered reagents (polychalcogenide and metal or metal chalcogeinde) are mixed under inert atmosphere and loaded into reaction vessels of either pyrex or quartz. The tube are evacuated to a pressure appropriate for the temperature used ($< 3x10^{-3}$ mbar for <600 °C; $<1x10^{-4}$ mbar for >600 °C). Once evacuated, the tubes are flame sealed and subjected to the desired heating program in a computer controlled furnace.

The polychalcogenide salt loaded into the reactions can be made in one of two ways, and the method used may have a profound effect on the reaction. First, by reacting stoichiometric amounts of elemental chalcogenide with alkali metal in liquid NH_3 [25], a direct redox reaction takes place and A_2Q_x is formed. Then *in situ* reactions with the metal may be performed. Using this method, each different length of A_2Q_x must be made separately. The second approach is to prepare one length of $(Q_x)^{2-}$ from the above NH_3 reaction and then form different polychalcogeides in situ by combining various ratios of A_2Q_x and Q. Upon heating, these combinations fuse together, forming the polychalcogenide flux via the self redox equilibria previously mentioned. The metal, which has been in situ with the A_2Q_x/Q mixture all along, then proceeds to react with the flux. In situ polychalcogenide formation is convenient for accessing fluxes over a

wide compositional range without making large quantities of various starting materials; however, this method might not be appropriate for certain very reactive metals. Such metals may react with the original starting materials before the polychalcogenide flux has a chance to form. If this premature reaction leads to phases with high thermodynamic stability, the reaction is dead in the water. Under such circumstances, new phases may be more readily accessible if the metal is reacted with already formed polychalcogenide.

Polychalcogenide fluxes are highly reactive towards metals because they are very strong oxidants. This phenomenon arises from the fact that, although the terminal atoms of the $(Q_x)^{2-}$ chains are formally 1-, the internal atoms are all formally zero valent. Metals are drawn into solution by being oxidized by the internal atoms of the $(Q_x)^{2-}$ chains, which, upon being reduced, split into smaller fragments. The solvated metal cations are then coordinated by the basic atoms of the $(Q_x)^{2-}$ ligands, forming some manner of soluble intermediate, which is followed by nucleation into solid crystals. Presumably, the nucleated species are in equilibrium with the soluble intermediates, especially if the flux is present in excess, and hence a solvation/reprecipitation effect (often referred to as the mineralizer effect) occurs. This aids in the growth of high quality single crystals because the flux can redissolve small or poorly formed crystallites and then reprecipitate the species onto larger, well-formed crystals. Because these molten salts are so strongly oxidizing, the phases isolated invariably possess metal cations in the highest oxidation states achieveable for a given chalcogenide's electronegativity. That does put some of the most oxidized metal cations beyond the reach of this method, but that is a function of the natural limits of the elements involved.

The composition of a polychalcogenide flux is one of the most important variables which can be manipulated to affect the outcome of a reaction. Such manipulations lie in altering the basicity of the fluxes leading to different reactivities with the metals. Guiding principles in this are: 1) the alkali metal involved (basicity of the A_2Q_x fluxes increases with increasing cation size), and 2) the ratio of alkali metal to chalcogenide (i.e. the $(Q_x)^{2-}$ chain length). The second point is, in fact, complex and requires further elaboration. Since charge neutrality in the A_2Q_x flux must be preserved, as A is increased and Q kept constant, the system is driven to shorter and shorter $(Q_x)^{2-}$ chains. This increases the amount of terminal basic atoms relative to the internal oxidizing atoms, increasing the overall basicity of the flux. As the internal atoms disappear, the oxidizing power of the flux reduces somewhat as well. Hence, not only is the size of the ligands changed but also a metal which is reactive in a flux of long polychalcogenide chains may be unreactive towards one with shorter chains (although such cases may be driven to reaction with increases in temperature). Varying the composition of the polychalcogenide flux is thus akin to varying the pH in aqueous solutions, and in effect amounts to having a large variety of solvents in which to perform reactions, each one having different reactivity. Changes in flux basicity initiate complex changes in reactivity and solubility which are not fully understood and which vary from metal to metal. At this stage of development in this method, each metal explored must be treated as a new and unique system, and similarities to the reactivity of other metals can only be drawn afterwards.

REFERENCES

1) For a recent review see Steigerwald, M. L., in *Inorganometallic Chemistry*, T.P. Fehlner, Ed., Plenum Press, New York, **1992**, p.333-356.

2) Niu, C., Lieber, C. M., *J. Am. Chem. Soc.*, **1992**, 114, 3570.

3) Novet, T., Johnson, D., *J. Am. Chem. Soc.*, **1991**, 113, 3398.

4) Rabenau, A., *Angew. Chem., Int. Ed. Engl.*, **1985**, 24, 1026.

5) Barrer, R. M., *Hydrothermal Chemistry of Zeolites*, Academic Press, New York, **1982**.

6) Haushalter, R. C., Mundi, L. A., *Chem. Mater.*, **1992**, 4, 31.

7) (a) Morris, R. E., Wikinson, A. P., and Cheetham, A. K., *Inorg. Chem.*, **1992**, 31, 4774. (b) Harrison, W. T. A., Stucky, G. D., Morris, R. E., Cheetham, A. K., *Acta Crystallogr.*, **1992**, C48, 1365,. (c) Morris, R. E., Harrison, W. T. A., Stucky, G. D., Cheetham, A. K., *J. Solid State Chem.*, **1991**, 94, 227. (d) Harrison, W. T. A., Morris, R. E., Cheetham, A. K., *Acta Crystallogr.*, **1992**, C48, 1182. (e) Morris, R. E., Hriljac, J. A., Cheetham, A. K., *Acta Crystallogr.*, **1990**, C46, 2013. (f) Morris, R. E., Cheetham, A. K., *Chem. Mater.*, **1994**, 6, 67. (g) Harrison, W. T. A., Stucky, G. D., Cheetham, A. K., *Eur. J. Solid State Inorg. Chem.*, **1993**, 30, 347.

8) (a) Khan, M. I., Chen, Q., Zubieta, J., Goshorn, D. P., *Inorg. Chem.*, **1992**, 31, 1556. (b) Khan, M. I., Chen, Q., Zubieta, J., *J. Chem. Soc., Chem. Commun.*, **1992**, 305. (c) Khan, M. I., Chen,

Q., Goshorn, D. P., Hope, H., Parkin, S., Zubieta, J., *J. Am. Chem. Soc.*, **1992**, 114, 3341. (d) Khan, M. I., Zubieta, J., *J. Am. Chem. Soc.*, **1992**, 114, 10058. (e) Khan, M. I., Chen, Q., Goshorn, D. P., Zubieta, J., *Inorg. Chem.*, **1993**, 33, 672.

9) (a) Liao, J.-H., Kanatzidis, M. G., *Inorg. Chem.*, **1992**, 31, 431. (b) Kim, K., Kanatzidis, M. G., *J. Am. Chem Soc.*, **1992**, 114, 4878.

10) Wood, P. T., Pennington, W. T., Kolis, J. W., *J. Am. Chem. Soc.*, **1992**, 114, 9233.

11) Elwell, D., Scheel, H. J., *Crystal Growth from High-Temperature Solutions*, Academic Press, New York, **1975**.

12) (a) Chianelli, R. R., Pecoraro, T. A., Halbert, T. R., Pan, W.-H., Stiefel, E. I., *J. Catal.*, **1984**, 86, 226. (b) Pecoraro, T. A., Chianelli, R. R., *J. Catal.*, **1981**, 67, 430. (c) Harris, S., Chianelli, R. R., *J. Catal.*, **1984**, 86, 400.

13) (a) Eckert, H., *Angew. Chem., Int. Ed. Engl.*, **1989**, 28, 1723. (b) Zallen, R., *Physics of Amorphous Solids*, Wiley, New York, **1983**. (c) Strand, D., Adler, D., *Proc. SPIE Int. Soc. Opt Eng.*, **1983**, 420, 200. (d) Yamada, N., Ohno, N., Akahira, N., Nishiuchi, K., Nagata, K., Takeo, M., *Proc. Int. Symp. Opt. Memory 1987; J. Appl. Phys.*, **1987**, 26 (Suppl.26-4), 61.

14) (a) Whittingham, M. S., in *Solid State Ionic Devices July 18-23 1988 Singapore*, B. V. R. Chowdari and S. Radhakrishna, Eds., World Scientific, Singapore, **1988**, p. 55-74. (b) Bowen, W. L., Burnette, L. H., DeMuth, D. L., *J. Electrochem. Soc.*, **1989**, 136, 1614. (c)

Murphy, D. W., Trumbore, F. A., *J. Electrochem. Soc.*, **1976**, 123, 960.

15) (a) Brown, A. P., *J. Electrochem. Soc.*, **1987**, 134, 2506. (b) Sudworth, J. L., Tilley, A. R., in *The Sulfur Electrode, Fused Salts and Solid Electrolytes*, R. P. Tischer, Ed., Academic Press, New York, **1983**, p. 235. (c) Brown, A. P., *J. Electrochem. Soc.*, **1987**, 134, 1921. (d) Liu, M., DeJonghe, L. C., *J. Electrochem. Soc.*, **1988**, 135, 741. (e) Yamin, H., Gorenshtein, A., Penciner, J., Sternberg, Y., Peled, E., *J. Electrochem. Soc.*, **1988**, 135, 1045. (f) Knödler, R., *J. App. Electrochem.*, **1988**, 18, 653. (g) Heusler, K. E., Grzegorzewski, A., Knödler, R., *J. Electrochem. Soc.*, **1993**, 140, 426.

16) (a) Möller, H. J., *Semiconductors for Solar Cell*, Artech House, Boston, **1993**. (b) Zweibel, H. J., *Basic Photovoltaic Principles and Methods*, Van Nostrand Reinhold, New York, **1984**. (c) Armstrong, J. H., Pistole, C. O., Misra, M. S., Kapur, V. K., Basol, B. M., in *Space Photovoltaics Research and Technology 1991*, NASA Conference Publication 3121, NASA, Washington D.C., **1991**, p. 19-1-19-8.

17) (a) Rowe, D. M., Bhandari, C. M., *Modern Thermoelectrics*, Holt, Rinehart, and Winston, London, **1983**, p. 103. (b) Borkowski, K., Pyzyluski, J., *J. Mater. Res. Bull.*, **1987**, 22, 381.

18) Scheel, H. J., *J. Cryst. Growth*, **1974**, 24/25, 669.

19) (a) Sanjines, R., Berger, H., Levy, F., *Mater. Res. Bull.*, **1988**, 23, 549. (b) Garner, R. W., White, W. B., *J. Cryst. Growth*, **1970**, 7, 343.

20) Sunshine, S. A., Kang, D., Ibers, J. A., *J. Am. Chem. Soc.* , **1987**, 109 , 6202.

21) (a) *The Sodium-Sulfur Battery*, J. L. Sudworth and A. R. Tilley, Eds., Chapman and Hall, New York, **1985**. (b) Fischer, W., *Mater Res. Soc Symp Proc.*, **1989**, 135, 541. (c) Powers, R. W., Karas, B. R., *J. Electrochem. Soc.*, **1989**, 136, 2787.

22) (a) Pearson, T. G., Robinson, P. L., *J. Chem. Soc.*, **1931**, 1304. (b) Mathewson, G. H., *J. Am. Chem. Soc.*, **1907**, 29, 867. (c) Klemm, W., Sodomann, H., Langmesser, P., *Z. Anorg. Allg. Chem.*, **1939**, 241, 281. (d) *Gmelin's Handbuch der Anorganischen Chemie*, Verlag Chemie, Weiheim/Brgstr, FRG, **1966**; Soduim, Suppl. Part 3, p. 1202-1205 and references therein.

23) (a) Clark, R. J. H., Cobbold, D. G., *Inorg. Chem.*, **1978**, 17, 3169. (b) Dubois, P., Lelieur, J. P., Lepourte, G., *Inorg. Chem.*, **1988**, 27, 73. (c) Sharp, K. W., Koeheler, W. H., *Inorg. Chem.*, **1977**, 16, 2258. (d) Schultz, L., Koeheler, W. H., *Inorg. Chem.*, **1987**, 26, 1989.

24) (a) Wardle, R. W. M., Bhaduri, S., Chau, C. N., Ibers, J. A., *Inorg. Chem.*, **1988**, 27, 1747. (b) Herrmann, W. A., Rohrmann, J., Herdtweck, E., Hecht, C., Ziegler, M. L., Serhadi, O., *J. Organomet. Chem.*, **1986**, 314, 295. (c) Coh, L. Y., Wei, C., Sinn, E., *J. Chem.*

Soc., Chem. Commun., **1985**, 462. (d) Rueingold, A. L., Bolinger, C. M., Rauchfuss, T. B., *Acta Crystallogr.*, **1986**, 42C, 1878. (e) Giolando, D. M., Papavassiliou, M., Pickardt, J., Rauchfuss, T. B., *Inorg. Chem.*, **1988**, 27, 2596. (f) Eichhorn, B. W., Haushalter, R. C., Cotton, F. A., Wilson, B., *Inorg. Chem.*, **1988**, 27, 4084. (g) Haushalter, R. C., *Angew. Chem. Int. Ed. Engl.*, **1985**, 24, 433. (h) Fritz, P. M., Beck, W., Nagel, U., Polborn, K., Hermann, W. A., Hecht, C., Rohmann, J., *Z. Naturforsch,* **1988**, 43B, 665. (i) Scheidsteger, O., Huttner, G., Dehnicke, K., Pebler, J., *Angew. Chem. Int. Ed. Engl.*, **1985**, 24, 428. (j) Kanatzidis, M. G., Huang, S.-P., *Inorg. Chem.*, **1991**, 30, 3572. (k) Kanatzidis, M. G., Dhingra, S., *Inorg. Chem.*, **1989**, 28, 2024. (l) Kanatzidis, M. G., Huang, S.-P., *Inorg. Chem.*, **1989**, 28, 4667. (m) Strasdeit, H., Krebs, B., Henkel, G., *Inorg. Chim. Acta,* **1984**, 89, L11. (o) Kanatzidis, M. G., Dhingra, S., Unpublished Results. (o) Kanatzidis, M. G., Huang, S.-P., *Angew. Chem. Int. Ed Engl,* **1989**, 28, 1513. (p) Kanatzidis, M. G., Huang, S.-P., *Inorg. Chem.*, **1991**, 30, 1455.

25) Feher, F., in *Handbuch der Praparativen Anorganischen Chemie*, G. Brauer, Ed., Ferdinand Enke, Stuttgart, Germany, **1954**, p.280-281.

Chapter 2

Ternary Reactions of Lanthanides and Actinides in Molten Alkali Metal/Polychalcogenide Fluxes at Intermediate Temperatures (250-600 °C)

A. Introduction.

The chemistry between metal cations and polychalcogenide ligands has been studied extensively over the years using a variety of solution based techniques [1]. This has led to a considerable amount of empirical knowledge concerning the complexes that have resulted, although the solution equilibria which polychalcogenides are prone to have made synthetic predictability difficult. In many systems the reaction of metals in molten polchalcogenide salts has been a valuable addendum to theses studies. Because of the unique reaction characteristics of molten A_2Q_x salts discussed in the first chapter, these media have had value in accessing compounds previously unknown even in systems that had been well studied with conventional solution techniques. The new phases seen in molten salt reactions have also tended to be solid state structures with extended covalent bonding in one or more dimensions through the lattice, a sharp contrast to the discrete ionic complexes commonly resulting from solution[2].

For many elements, however, studying metal/$(Q_x)^{2-}$ chemistry can be exceedingly difficult. Group 4 and 5 transition metals, lanthnides, and actinides can access very high oxidation states and hence become very hard Lewis acids. As such they are especially oxophilic species which, when given a choice, would rather coordinate to oxygen containing (hard base) ligands rather than those with chacogenide (soft base) binding sites. In order to study polychalcogenide chemistry with these elements in solution, great care must be taken to avoid any exposure of the reaction to air or water, and for some elements (specifically the f-block metals) even oxygen-containing solvents must be avoided because they can coordinate

preferentially over the chalcogenide ligands. Although some progress has been made with Group 4 and 5 metals using solution techniques [3,4], it is very limited. In the case of the lanthanides and actinides, such chemistry is nonexistant.

By using molten A_2Q_x fluxes, the opportunity presents itself to study the reaction of highly oxophilic metals with polychalcogenide ligands directly, without the need for any sort of polar solvent medium. Eliminating the solvent hence eliminates many of the common sources of oxygen contamination, reducing the problem largely to one of having a good inert atmosphere glove box for the manipulation of the starting materials. Although some manner of solvent in needed after the molten salt reaction for the removal of excess flux, judicious choice of that solvent can still leave the product intact for analysis.

Some of the earliest investigations into using A_2Q_x fluxes as intermediate temperature media were performed on Group 4 and 5 metals. For example $K_4Ti_3S_{14}$ was synthesized from the reaction of K_2S/Ti/S in a 2/1/6 molar ratio heated at 375 °C for 50 hr.[5]. The compound features Ti^{4+} cations linked by $(S_2)^{2-}$ and S^{2-} ligands into a one-dimensional anionic chain. A second titanium compound was found in $Na_2Ti_2Se_8$ (Na_2Se/Ti/Se = 2/1/10, heated at 345 °C for 100 hr)[6], and this phases also possesses anionic chains made of Ti and a mixture of monoselenide and polyselenide species. Lastly, a compound composed of discrete anionic clusters was found in $K_3Nb_2Se_{11}$ from a 3/1/10 molar ratio of K_2Se/Nb/Se heated at 375 °C for 100 hr.[7] Views of all three anionic frameworks are given in Fig. 2.1. With these examples present, a logical extension is to apply molten A_2Q_x methodology to the even more oxophilic lanthanide and actinide metals.

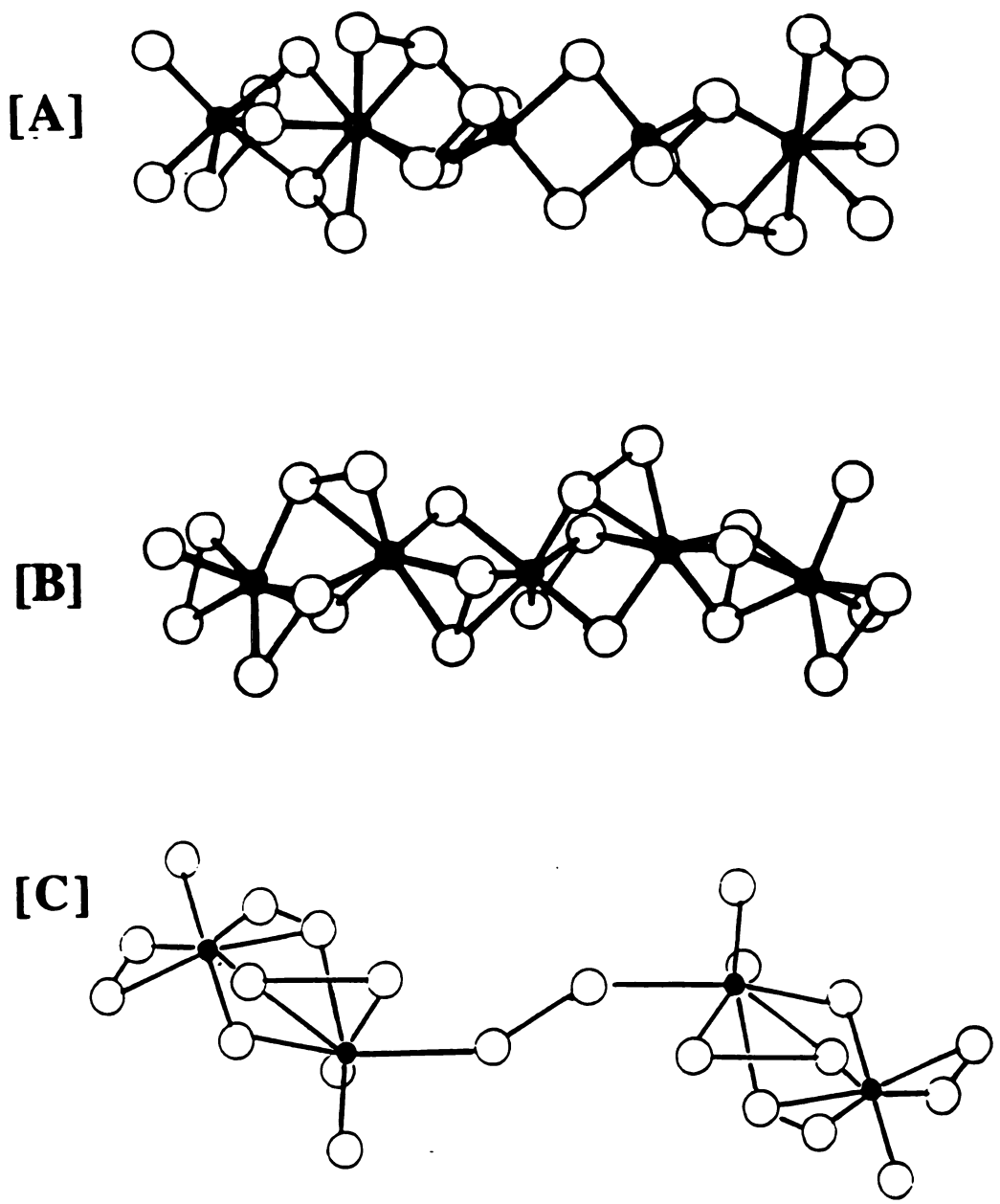

Figure 2.1: Fragments of the anionic networks of (a) $K_4Ti_3S_{14}$ [5], (B) $Na_2Ti_2Se_8$ [6], and (C) $K_3Nb_2Se_{11}$ [7](solid circles= metal; empty circles=chalcogneide).

In solid state lanthanide/polychalcogeinde binary chemistry, the dominant structural theme, shown schematically for several phases in Fig. 2.2, is that of layers of polychalcogenide seperating layers of mixed Ln^{3+}/Q^{2-} composition. The lanthanide cations and Q^{2-} anions in these phases reside in a bilayer which possesses a distorted NaCl motif. Each Ln^{3+} is coordinated to five Q^{2-} arranged in the square pyramidal geometry of an octahedron with one axial position vacant; also the Ln^{3+} is slighty above the square plane of the four basal Q^{2-}, giving the bilayer a corrugated effect. About each Q^{2-} are 5 Ln^{3+}, also forming a quare pyramid, but the corrugations of the layers force the Q^{2-} to reside within that pyramid. Between the bilayers are seperate sheets of coplanar chalcogenide atoms possessing various degrees of Q-Q bonding, depending on the structure type. Many LnQ_2 compounds are known which possess the anti-Fe_2As structure type or distorted variants of it [8]. In these phases the intervening polychalcogenide layer is composed of discrete $(Q_2)^{2-}$ ligands, the actual position of which, relative to the bilayer, varies among the structural modifications (Fig 2.2a). This stoichiometry dominates tor Q=S and Se. For tellurides, another phase occurs, $LnTe_3$.[9] Here the Te layers form an infinite square net with every Te atom bonding to four other Te nearest neighbors, and two of these layers serve to seperate each bilayer (Fig. 2.2b). A third phase, Ln_2Te_5,[10] also possess Te square planar nets, but now the number of nets between the Ln^{3+}/Q^{2-} bilayer alternates between 1 and 2 (Fig. 2.2c). Many other binary Ln/Q phases exist, but all possess exclusively Q^{2-} species.[8]

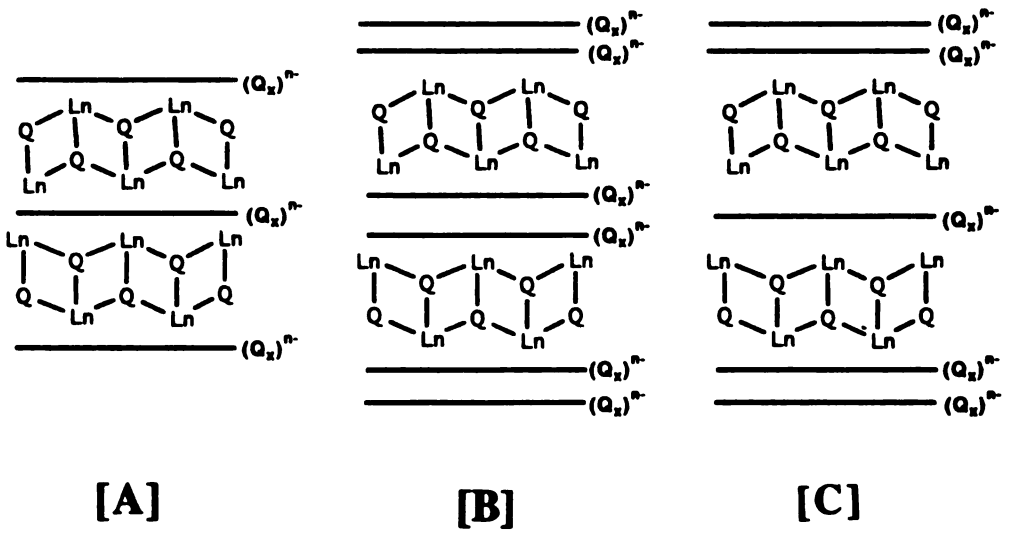

Figure 2.2: Schematic representation of the structures of several known binary lanthanide/chalcogenides: (A) LnQ_2 [8], (B) $LnTe_3$ [9], (C) Ln_2Te_5 [10] (Ln=lanthanide, Q=chalcogenide).

In this work, U has been the only actinide whose reactivity with A_2Q_x fluxes was studied. Several U/Q binaries exist but the only one to have discrete polychalcogenides is UQ_3 (Q=S, Se, Te)[11], which is isostructural to $ZrSe_3$.[12] This structure type, to be discussed at length later, contains $(Q_2)^{2-}$ fragments which, through η^2 coordination, form the short sides of a trigonal prism around the U atoms. Recently, it has been reported that UTe_3 has a β- form which is isostructural to the $LnTe_3$ phases discussed above.[13]

Structural diversity in compounds containing f-block metals and chalcogenides can be increased by the incorporation of other elements into the material, and the number of structurally characterized heterometallic species is considerable.[8] A brief look at known ternary compounds containing monovalent cations is warranted because working with A_2Q_x fluxes naturally leads to the incorporation of A^+ into the resulting lattice. For alkali metals (and Tl^{1+}) only one stoichiometry had been known for many years: $ALnQ_2$.[14] This phase exists in two different structure types depending on the relative sizes of the A^+ and Ln^{3+} cations. Generally, for small alkali metal cations (Li^+ and some Na^+ analogs), the phase is simply a NaCl derivative with the two cations disordered throughout the lattice. As A^+ increases in size, the cations order themselves in the NaCl lattice such that every other layer of cations changes composition between A^+ and Ln^{3+} (Fig. 2.3). The recent characterization of $RbDy_3Se_8$ has added another structure type to the A/Ln/Q family.[15] this phase is a relative of the $LnTe_3$ structure type modified by 1) a layer of Rb^+ inserted between the double layer of polychalcogenides and 2) partial occupancies in the polyselenide sheets, implying a variety of fragment lengths being stablized.

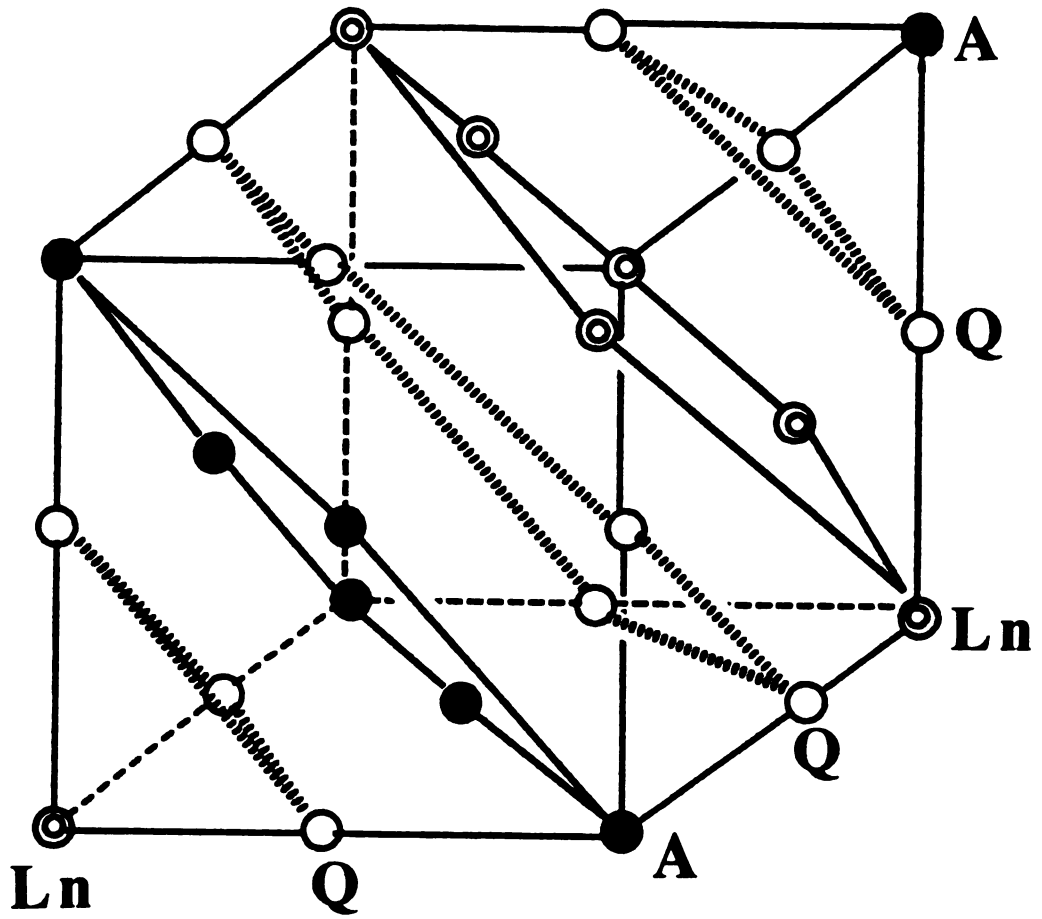

Figure 2.3: A schematic of the $ALnQ_2$ structure type.

Monovalent transition metal cations Cu^+ and Ag^+ have been investigated as well, but much of the work has been limited because of poor crystal growth. Observed phases in Cu^+ containing systems have been $CuCeQ_2$ (Q=S, Se) having the $CuLaS_2$ structure type,[16a] Ce_5CuSe_8 which has the Th_3P_4 structure type,[16b] and two phases of uncharacterized structure, $Ce_4Cu_2S_7$[16c] and Ce_2CuTe_4.[16d] In ternary systems with Ag^+ the $AgLnSe_2$ structure type has been structurally determined for Ln=Er[17] and is known to form for the heavier lanthanides (Dy-Lu), Sc, and Y.[8] A schematic of the structure is shown in Fig. 2.4. The trivalent cations reside in octahedra of Se^{2-} anions. The octahedra link to each other forming infinite double chains which then further connect into a three-dimensional network, resulting in channels running parallel to the chains of octahedra. It is at tetrahedral sites within these channels that the compound's Ag^+ cations reside. The presence of these channels suggests a porosity to the structure, and in fact an appreciable Ag^+ ionic conductivity has been measured for this material.[18]

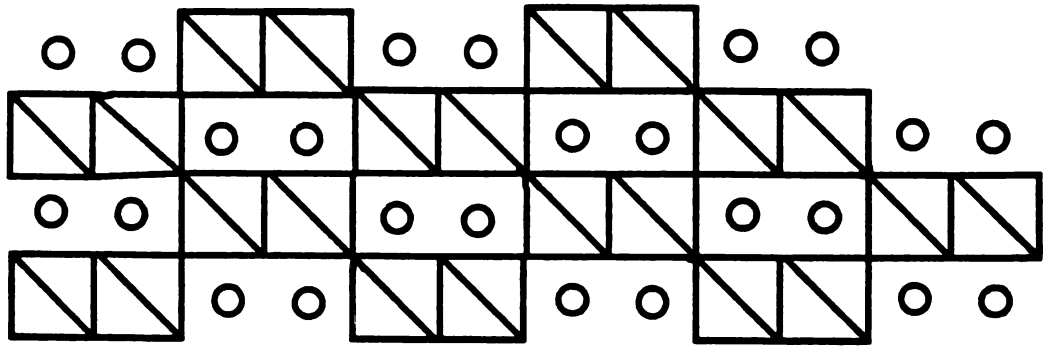

Figure 2.4: A schematic representation of the AgLnSe2 structure type (Ln=lanthanide).

As in binary systems, examples of ternary A/actinide/Q phases are sparce. The unit cell has been reported for KUS_3[19a], but the structure could not be successfully refined. The phases $Cu_2U_6Q_{13}$ is known and features [CuS_3] trigonal planes and [US_8] fragments forming either bicapped trigonal prisms or triangulated dodecahedron [19b,c].

These few compounds discussed have all resulted from classic high temperature (>600 °C) solid state "heat and beat" reactions (except for $RbDy_3Se_8$, grown from a RbCl/LiCl flux at a low "heat and beat" temperature of 680 °C), and so the chemistry between these elements has never been investigated under any but the most extreme synthetic conditions. Molten A_2Q_x fluxes allow for a changing of these conditions for the very first time.

The first stage in the investigation of f-block metal reactivity in A_2Q_x fluxes was to experiment on simple ternary systems. The considerable thermodynamic stability of the known binary and ternary compounds often caused their formation even under the relatively mild synthetic temperatures employed here. Despite this, it was discovered that, with appropriate flux compositions, several new chalcogenides can be accessed by using molten polychalcogenide salts at intermediate temperatures. Preliminary reports on this work have been published previously [20]. In this chapter the synthesis and properties of these new ternary phases will be discussed.

B. Experimental

1. Synthesis

Reagents -- The following reagents were used as obtained: cerium, 40 mesh, Johnson M. Matthey Co., Ward Hill, MA; uranium metal, 60 mesh, Cerac, Milwaukee, WI; lanthanum, 40 mesh, Cerac, Milwaukee, WI;

selenium powder, 100 mesh, Aldrich, Milwaukee, WI; tellurium powder, 200 mesh, Aldrich, Milwaukee, WI; sulfur powder, sublimed, JT Baker Co., Phillipsburg, NJ; rubidium metal, analytical reagent, Johnson Matthey, Ward Hill, MA; potassium metal, analytical reagent, Mallinckrodt Inc., Paris, KY; sodium metal, analytical reagent, Mallinckrodt Inc., Paris, KY; Dimethylformamide, analytical reagent grade, EM Science, Inc., Gibbstown, NJ.

Potassium Sulfide, K_2Se -- The following procedure was modified from that given in the literature.[21] 4.976 g (127.3 mmol) K was sliced in an N_2 filled glove box and combined with 5.024 g (63.6 mmol) Se into a 250 mL round bottom flask. The flask was chilled to -78 °C using a dry ice/acetone bath and approximately 100 mL of NH_3 was condensed, under an N_2 atmosphere, onto the reagents, giving a dark blue solution. The solution was stirred with a magnetic stir bar while the liquid NH_3 was allowed to slowly evaporate off as the reaction warmed to room temperature under a flow of N_2 (approx. 8 hr.). A second portion of NH_3 is usually added and the evaporation repeated to insure complete reaction of the reagents. The resulting light orange product is evacuated on a Schlenk line overnight and then taken into an N_2 filled glove box where it is ground to a fine powder and stored.

Sodium Sulfide, Na_2S -- An amount of 3.156 g (137 mmol) Na was sliced in an N_2 filled glove box and combined with 2.200 g (68.6 mmol) S into a 250 mL round bottom flask. The synthesis proceeded as described above, resulting in a pale yellow powder, stored in an N_2 filled glove box.

Rubidium Telluride, Rb_2Te -- An amount of 5.63 g (65.9 mmol) Rb was transferred to a 250 mL round bottom flask in an N2 filled glove box. After removal from the box, the flask was chilled in a dry ice/acetone bath. Under a flow of N_2, the flask was opened, and a magnetic stir bar and

4.202 g (32.9 mmol) Te was added. .The synthesis proceeded as described above, resulting in a pale grey powder, stored in an N_2 filled glove box.

Tetrapotasium Uranium Octaselenide, K_4USe_8 -- K_4USe_8 has been synthesized from a mixture of 0.126 g (0.80 mmol) K_2Se, 0.095 g (0.40 mmol) U, and 0.257 g (3.25 mmol) Se. These reagents are thoroughly mixed, sealed in an evacuated pyrex ampule, and heated at 300 ^oC for 12 days (cooling 2 ^oC/hr). Afterwards, the tube is opened with a glass cutter, and the entire solid mass is placed in a 250 mL Erlenmeyer flask, which has a side arm attachment to allow for the purging of the flask contents with N_2. Excess polyselenide flux is removed by dissolving it in successive portions of degassed dimethylformamide (DMF). Approximately 50-100 mL of solvent is added to the flask resulting in a green/brown solution as the excess K_2Se_x is dissolved. Nitrogen flow through the flask is maintained during the isolation to prevent oxidation of the solubilized polychalcogenide by ambient O_2 which would cause elemental Se to precipitate. When a portion of solvent becomes saturated (as evidenced by a very dark color to the solution), it is carefully decanted from the remaining solid, and a fresh portion is added. Since K_4USe_8 has proven to be slightly soluble in DMF, washing is continued only until the green/brown color of an Se_x^{2-} solution is replaced by a slowly evolving brown/yellow color, indicating K_4USe_8 as the primary component in solution. The sample is decanted one final time and then dried under vacuum. The remaining material is a black microcrystalline product. Homogeneity was confirmed by comparing the product's powder X-ray diffraction pattern against one calculated using X-ray single crystal data (See Table 2.1). Solubility is slow enough that yields as high as 53% has been achieved (based on uranium).

Table 2.1 Calculated and Observed X-ray Powder diffraction Pattern for K_4USe_8 (Cu radiation)

h k l	d_{calc}/(Å)	d_{obs}/(Å)	I/I_{max} obs (%)
1 1 1	7.34	7.30	20.99
2 2 0	6.63	6.60	45.26
1 3 1	5.17	5.14	50.80
3 1 1	4.703	4.691	25.92
2 4 0	4.425	4.421	2.33
2 0 2	3.927	3.916	4.30
2 2 2	3.669	3.664	20.33
4 4 0	3.314	3.325	16.59
5 1 1	3.187	3.184	11.68
3 5 1	3.133	3.129	26.66
4 2 2	2.959	2.952	100.00
5 3 1	2.919	2.915	12.96
1 7 1	2.754	2.748	20.66
0 6 2	2.707	2.702	4.30
1 3 3	2.668	2.663	9.33
2 6 2	2.585	2.570	27.80
5 5 1	2.539	2.535	26.66
3 7 1	2.512	2.509	35.56
2 8 0	2.466	2.463	40.50

Table 2.1 Calculated and Observed X-ray Powder diffraction Pattern for K_4USe_8 (Cu radiation) (cont.)

h k l	d_{calc}/(Å)	d_{obs}/(Å)	I/I_{max} obs (%)
3 3 3	2.446	2.441	13.76
6 0 2	2.416	2.412	14.30
1 5 3	2.368	2.365	21.66
4 6 2	2.296	2.294	21.66
7 3 1	2.252	2.249	11.44
5 1 3	2.228	2.223	7.84
3 5 3	2.209	2.208	22.35
1 9 1	2.196	2.194	25.18
8 0 0	2.166	2.165	14.03
5 3 3	2.130	2.127	6.30
2 2 4	2.090	2.087	5.42
1 7 3	2.063	2.062	16.00
0 4 4	2.025	2.022	23.39
2 10 0	2.003	2.002	16.59
8 4 0	1.9967	1.9950	21.66
6 6 2	1.9751	1.9731	16.00
2 4 4	1.9719		
6 8 0	1.9213	1.9203	11.44
4 10 0	1 8592	1.8578	11.93

Table 2.1 Calculated and Observed X-ray Powder diffraction Pattern for K_4USe_8 (Cu radiation) (cont.)

h k l	d_{calc}/(Å)	d_{obs}/(Å)	I/I_{max} obs (%)
8 6 0	1.8317	1.8306	7.84
2 10 2	1.8231	1.8219	18.41
1 9 3	1.7948	1.7913	4.60
6 8 2	1.7611	1.7575	2.12
1 1 5	1.7468	1.7438	7.05
10 2 0	1.7090	1.7078	17.18
3 1 5	1.6799	1.6784	5.08
6 10 0	1.6763		
6 4 4	1.6581	1.6491	10.47
5 11 1	1.6186	1.6180	4.92
1 5 5	1.6130	1.6132	4.92
10 0 2	1.6128		
7 7 3	1.5917	1.5907	7.44
2 12 2	1.5719	1.5712	16.29
6 10 2	1.5667	1.5659	18.41
8 8 2	1.5511	1.5510	13.49

Potassium Cerium Tetraselenide, KCeSe4 -- $KCeSe_4$ is synthesized from a reaction of 0.078 g of K_2Se (0.5 mmol), 0.035 g of Ce (0.25 mmol) and 0.158 g Se (2 mmol). These starting materials are thoroughly mixed in a nitrogen atmosphere glove box and loaded into a pyrex tube, which is subsequently evacuated to approximately $2x10^{-3}$ mbar and flame sealed. The mixture is heated at 300 °C for 6 days and cooled at 2 °C/hr to 100 °C followed by cooling to 50 °C in 1 hr. The product is isolated in the manner described for the isolation of K_4USe_8; the excess polyselenide flux is dissolved with several portions of degassed dimethylformamide (DMF) under a nitrogen atmosphere until the solvent remains clear, indicating total polyselenide removal, followed by drying under vacuum. The remaining material is deep blue to black square chunks of $KCeSe_4$. The product is insoluble in DMF and is inert in both air and water for extended periods, although some manner of surface degradation appears to be evident in the magnetic susceptibility studies. Homogeneity is confirmed by comparing the product's powder X-ray diffraction pattern against one calculated using X-ray single crystal data (See Table 2.2). A yield of 61%, based on Ce, is typical.

Table 2.2 Calculated and Observed X-ray Powder diffraction Pattern for $KCeSe_4$ (Cu radiation)

h k l	d_{calc}/(Å)	d_{obs}/(Å)	I/I_{max} obs (%)
0 0 1	8.33	8.33	60.15
1 1 0	4.508		
0 0 2	4.164	4.181	37.24
1 1 1	3.965	3.987	4.35
2 0 0	3.188	3.200	6.35
1 1 2	3.059	3.065	83.43
2 0 1	2.977	2.983	2.73
0 0 3	2.776	2.779	14.28
2 1 1	2.698	2.702	47.47
2 0 2	2.531	2.534	18.76
1 1 3	2.364	2.366	22.69
2 1 2	2.352		
2 2 0	2.254	2.257	5.40
2 2 1	2.176	2.178	4.69
2 0 3	2.094	2.086	100.00
0 0 4	2.082	2.085	47.47
3 1 0	2.016	2.022	23.83
2 1 3	1.9892	1.9950	22.32
2 2 2	1.9824		

Table 2.2 Calculated and Observed X-ray Powder diffraction Pattern for $KCeSe_4$ (Cu radiation) (cont.)

h k l	d_{calc}/(Å)	d_{obs}/(Å)	I/I_{max} obs (%)
3 1 1	1.9597	1.9647	6.75
1 1 4	1.8904	1.8947	3.28
3 1 2	1.8148		
2 2 3	1.7500	1.7480	5.58
2 0 4	1.7433	1.7351	10.17
3 2 1	1.7298		
2 1 4	1.6816	1.6862	13.70
0 0 5	1.6658	1.6698	50.78
3 1 3	1.6314	1.6326	3.28
3 2 2	1.6277		
4 0 0	1.5940		

Potassium Terbite Tetraselenide, KTbSe4 -- $KTbSe_4$ is synthesized from a reaction of 0.039 g (0.25 mmol) of K_2Se, 0.040 g (0.25 mmol) of Tb, and 0.160 g (2 mmol) of Se. These starting materials are thoroughly mixed in a nitrogen atmosphere glove box and loaded into a pyrex tube, which is subsequently evacuated to approximately 2×10^{-3} mbar and flame sealed. The mixture is heated at 350 °C for 5 days and cooled at 2 °C/hr to 100 °C followed by cooling to 50 °C in 1 hr. The product is isolated in the manner described for the isolation of K_4USe_8; the excess polyselenide flux is dissolved with several portions of degassed dimethylformamide (DMF) under a nitrogen atmosphere until the solvent remains clear, indicating total polyselenide removal, followed by drying under vacuum. The remaining material is deep purple to black square chunks of $KTbSe_4$. The product is insoluble in DMF and is inert in both air and water for extended periods. Homogeneity is confirmed by comparing the product's powder X-ray diffraction pattern against one calculated using X-ray single crystal data (see Table 2.3). A yield of 84%, based on Tb, is typical.

Table 2.3 Calculated and Observed X-ray Powder diffraction Pattern for $KTbSe_4$ (Cu radiation)

h k l	d_{calc}/(Å)	d_{obs}/(Å)	I/I_{max} obs (%)
0 0 1	8.23	8.18	100.00
0 0 2	4.114	4.100	15.60
1 1 1	3.896	3.774	0.63
1 1 2	3.012	3.004	4.99
0 0 3	2.742	2.735	9.22
2 1 1	2.648	2.642	0.70
2 0 2	2.490	2.483	0.43
1 1 3	2.331	2.325	1.73
2 1 2	2.313	2.308	0.51
2 0 3	2.061	2.072	0.57
0 0 4	2.057	2.051	18.67
3 1 0	1.9780		
2 1 3	1.9583	1.9535	0.53
2 2 2	1.9478		
1 1 4	1.8650	1.8595	0.40
2 2 3	1.7215		
2 0 4	1.7184	1.7156	0.29
3 2 1	1.6975		
2 1 4	1.6571	1.6545	1.07
0 0 5	1.6454	1.6427	14.25

Rubidium cerium tetratelluride, RbCeTe4 -- $RbCeTe_4$ has been observed and structurally characterized, but attempts to repeat the reaction have, to date, not been successful. Rather, an unknown microcrystalline ternary compound continually appears, and so $RbCeTe_4$ must be a very kinetically sensitive phase.

The original batch of $RbCeTe_4$ resulted from a mixture of 0.149 g (0.50 mmol) of Rb_2Te, 0.035 g (0.25 mmol) of Ce, and 0.255 g (2 mmol) of Te. These starting materials are thoroughly mixed in a nitrogen atmosphere glove box and loaded into a pyrex tube, which is subsequently evacuated to approximately 2×10^{-3} mbar and flame sealed. The mixture is heated at 420 °C for 4 days and cooled to 230 °C in 95 hr followed by cooling to 130 °C in 20 hr and then to 50 °C in 1 hr. The product is isolated in the manner described for the isolation of K_4USe_8; the excess polyselenide flux is dissolved with several portions of degassed dimethylformamide (DMF) under a nitrogen atmosphere until the solvent remains clear, indicating total polyselenide removal, followed by drying under vacuum. The remaining material was black square chunks of $RbCeTe_4$ and black powder, which the powder diffraction pattern showed to be elemental Te. The product is insoluble in DMF and is inert in both air and water for extended periods. The calculated and observed powder X-ray diffraction patterns for $RbCeTe_4$ are given in Table 2.4.

Table 2.4 Calculated and Observed X-ray Powder diffraction Pattern for $RbCeTe_4$ (Cu radiation)

h k l	d_{calc}/(Å)	d_{obs}/(Å)	I/I_{max} obs (%)
0 0 1	9.08	9.27	46.37
0 0 2	4.54	4.59	58.05
1 1 2	3.336	3.363	28.44
0 0 3	3.028	3.052	65.53
2 1 1	2.942	2.964	23.59
2 0 2	2.760	2.780	5.67
1 1 3	2.578	2.594	6.86
2 1 2	2.566		
2 2 1	2.373	2.364	15.62
0 0 4	2.271	2.285	100.00
3 1 0	2.198	2.212	4.39
2 1 3	2.169	2.182	8.16
1 1 4	2.062	2.050	2.78
3 1 2	1.9788	1.9838	4.80
2 1 4	1.8339	1.8435	15.25
0 0 5	1.8168	1.8288	42.56
3 1 3	1.7790	1.7881	2.47
3 2 2	1.7748		
1 1 5	1.7041	1.7099	2.32
4 0 2	1.6232	1.6274	4.80
3 1 4	1.5796	1.5851	4.80
4 2 0	1.5545	1.5483	4.39

Sodium Cerium Trisulfide, $NaCeS_3$ -- $NaCeS_3$ was first observed from an attempted heterometallic reaction of Cu and Ce in a molten Na_2S_x flux. 0.234 g (3.0 mmol) Na_2S, 0.016 g (0.25 mmol) Cu, 0.036 g (0.26 mmol) Ce, and 0.256 g (8.0 mmol) S were thoroughly mixed in a nitrogen atmosphere glove box and loaded into pyrex tubes, which were subsequently evacuated to approximately 2 $x10^{-3}$ mbar and flame sealed. The reaction was heated at 400 °C for 5 days and cooled at 4 °C/hr to 120 °C followed by cooling to 50 °C in 1 hr. The product is isolated by dissolving away the excess polysulfide flux with several portions of degassed dimethylformamide (DMF) as described earlier. Concentrated solutions of $(S_x)^{2-}$ in DMF have a blue color, and so washings are continued until the solvent remains clear, indicating total polysulfide removal. The resulting product was an inhomogenous mixture of red needles and black and orange powder. Semi-quantitative EDS analysis revealed a Na/Ce/S composition of 2/3/8 for the red needles and a Cu/Ce/S ratio of 1/1/1 for the black powder. Single crystal X-ray diffraction studies were subsequently performed on the red needles from this synthesis, leading to the structure of $NaCeS_3$.

Rational synthesis of pure $NaCeS_3$ was achieved from two different ratios of starting materials. Either a mixture of 0.078 g (1.0 mmol) Na_2S, 0.070 g (0.5 mmol) Ce, and 0.096 g (3.0 mmol) S; or 0.040 g (0.5 mmol) Na_2S, 0.070 g (0.5 mmol) Ce, and 0.064 g (2.0 mmol) S can be used. Both have in common that the resulting fluxes (Na_2S_5 and 2 Na_2S_4) are fairly Lewis basic and are present in only a moderate excess to the Ce metal. After being mixed and sealed into pyrex tubes as described earlier, the reactants are heated to 370 °C over 12 hours, held at that temperature for 2 d., and then cooled to 160 °C over 50 hr. followed by quenching to room

temperature. The excess flux is removed using degassed DMF as described above. The resulting brick red powder was confirmed as $NaCeS_3$ by comparing the sample's powder X-ray diffraction pattern with one calculated from the coordinates obtained from the single crystal analysis (See Table 2.5). The material is insoluble in DMF and appears to be stable in dry air. However, $NaCeS_3$ is extremely moisture sensitive; any contact with water turns the entire sample black, which is seen by powder X-ray diffraction to be CeO_2. Even ambient air has sufficient humidity to form a black surface coating of CeO_2 over a short period of time, although the coating seems to be protective of the internal compound as the relative amount of CeO_2 does not increase with longer exposure to the atmosphere.

Table 2.5 Calculated and Observed X-ray Powder diffraction Pattern for $NaCeS_3$ (Cu radiation)

h k l	d_{calc}/(Å)	d_{obs}/(Å)	I/I_{max} obs (%)
0 0 1	9.80	9.90	31.98
1 0 1	4.916	4.941	45.68
1 0 2	3.712	3.728	40.26
1 1 1	3.210	3.216	100.00
0 1 2	3.206		
2 0 0	2.842	2.850	19.48
2 0 1	2.729	2.738	32.77
0 1 3	2.588	2.594	47.56
2 0 2	2.458	2.461	39.39
0 0 4	2.450		
1 1 3	2.355	2.361	48.52
2 1 1	2.294	2.299	62.90
2 0 3	2.144	2.151	23.98
2 1 2	2.126	2.122	37.67
0 2 0	2.119		
0 2 1	2.071	2.068	26.75
1 1 4	1.9874	1.9924	28.94
0 0 5	1.9604	1.9664	16.56
1 2 1	1.9460	1.9467	17.12

Table 2.5 Calculated and Observed X-ray Powder diffraction Pattern for $NaCeS_3$ (Cu radiation) (cont.)

h k l	d_{calc}/(Å)	d_{obs}/(Å)	I/I_{max} obs (%)
2 1 3	1.9132	1.9190	39.39
2 0 4	1.8557	1.8602	42.93
1 0 5	1.8532		
3 0 2	1.7669	1.7692	22.64
3 1 0	1.7294	1.7346	9.21
3 1 1	1.7031	1.7000	23.96
2 2 0	1.6987		
2 2 1	1.6737	1.6744	18.28
3 1 2	1.6309	1.6339	14.39
0 2 4	1.6028	1.6044	13.36
1 0 6	1.5701	1.5748	18.88

Sodium Lanthanum Trisulfide, $NaLaS_3$ -- Either of the following combinations of starting materials may be used to form $NaLaS_3$: 0.060 g (0.77 mmol) Na_2S, 0.105 g (0.75 mmol) La, and 0.096 g (3.0 mmol) S; or 0.117 g (1.5 mmol) Na_2S, 0.105 g (0.75 mmol) La, and 0.144 g (4.5 mmol) S. The former resulted in crystals suitable for single crystal X-ray diffraction studies, while the latter is typically microcrystalline. The starting materials are mixed and sealed into pyrex tubes as described previously. The samples are placed in a computer controlled furnace and heated to 370 °C over 12 hr.. They remain at this temperature for 2 days after which the furnace is cooled to 160 °C over 50 hr. and then allowed to cool naturally to 50 °C. The excess flux is dissolved by washing the sample with degassed DMF as described previously. The isolated product is pale yellow when microcrystalline but orange as the size of the crystals increases. Purity of the sample was confirmed by comparing its X-ray powder diffraction pattern to one calculated from the single crystal diffraction data (See Table 2.6).

$NaLaS_3$ is highly stable in air and common organic solvents and remains intact in H_2O over short periods of time (< 8 hr.). After sufficient contact with water, the phase converts to an amorphous oxide with the scent of H_2S present.

Table 2.6 Calculated and Observed X-ray Powder Diffraction Pattern for $NaLaS_3$ (Cu radiation)

h k l	d_{calc}/(Å)	d_{obs}/(Å)	I/I_{max} obs (%)
0 0 1	9.841	9.78	100.00
1 0 1	4.966	4.935	43.59
0 0 2	4.920		
0 1 1	3.925	3.908	7.55
1 0 2	3.739	3.718	53.08
1 1 1	3.242	3.262	6.84
0 1 2	3.229	3.215	56.57
2 0 0	2.876	2.862	10.85
1 0 3	2.850	2.834	6.76
2 0 1	2.760	2.748	17.57
0 1 3	2.604	2.593	24.14
2 0 2	2.483	2.472	6.17
0 0 4	2.460	2.448	80.99
1 1 3	2.372	2.362	27.58
2 1 1	2.320	2.310	16.62
2 0 3	2.162	2.154	16.26
2 1 2	2.148		
0 2 0	2.140	2.132	9.92
1 1 4	1.9999	1.9904	10.58

Table 2.6 Calculated and Observed X-ray Powder diffraction Pattern for $NaLaS_3$ (Cu radiation) (cont.)

h k l	d_{calc}/(Å)	d_{obs}/(Å)	I/I_{max} obs (%)
1 2 1	1.9653	1.9592	26.77
2 1 3	1.9302	1.9225	9.12
2 0 4	1.8695	1.8638	15.52
1 0 5	1.8622		
1 2 2	1.8573	1.8544	26.25
3 0 2	1.7865	1.7796	8.95
2 1 4	1.7132	1.7120	4.05
		1.7084	3.25
2 2 1	1.6913	1.7021	6.60
0 2 4	1.6146	1.6086	3.84
1 0 6	1.5773	1.5713	20.19

2. Physical Measurements

Powder X-ray Diffraction -- Analyses were performed using a calibrated Rigaku Rotaflex rotating anode powder diffractometer controlled by an IBM computer and operating at 45 kV/ 100 mA, employing Ni-filtered Cu radiation. Samples are ground to a fine powder and mounted by spreading the sample onto a piece of double sided scotch tape affixed to a glass slide. For air sensitive compounds, samples were prepared in an N_2 filled glove box and coated with mineral oil before analysis. Powder patterns were calculated by using the CERIUS ^{TM} molecular modeling program by Molecular Simulations, St. John's Innovation Centre, Cambridge, England.

Infrared Spectroscopy -- Infrared spectra, in the far-IR region (600-50 cm^{-1}), were recorded on a computer controlled Nicolet-740 Fourier Transform infrared spectrophotometer in 4 cm^{-1} resolution. Analyses were performed on finely ground solid samples using CsI as the pressed pellet matrix. For air sensitive compounds, samples were prepared in an N_2 filled glove box and pressed into a pellet immediately upon removal.

Solution UV/Vis Spectroscopy -- Spectra were recorded using a Hitachi U-2000 spectrophotometer. Samples were dissolved and loaded into UV/Vis cells inside an N_2 filled glove box.

Solid State UV/Vis/Near IR Spectroscopy -- Optical diffuse reflectance measurements were performed at room temperature using a Shimadzu UV-3101PC double beam, double monochromator spectrophotometer. The instrument is equipped with integrating sphere and controlled by personal computer. The reflectance versus wavelength

data generated can be used to estimate a material's band gap by converting reflectance to absorption data using the Kubelka-Munk function:[22]

$$\alpha/S=(1-R)^2/2R$$

where R is the sample reflectance at a given wavelength, α, the absorption coefficient, and S , the scattering coefficient. S remains wavelength independent for particles greater than 5 mm in size. Raw data were processed using the Kaleidagraph™ software program. $BaSO_4$ was used as a 100% reflectance standard for all materials. Samples are prepared by grinding them to a fine powder and spreading them on a compacted surface of the powdered standard material, preloaded into a sample holder. The sample is manually pressed onto the sample holder to insure its adhesion to the surface of the standard material. Air sensitive samples were ground in an N_2 filled glove box and loaded into a small PVC bag. The bag was taped shut and upon removal from the box was immediately heat seal. For such samples, an empty bag held against a sample holder containing $BaSO_4$ was used as a standard.

Magnetic Susceptibility -- The magnetic response of the compounds was measured over the range of 2-300 K using a MPMS Quantum Design SQUID magnetometer. Samples were ground to a fine powder to minimize possible anisotropic effects, and loaded into PVC containers. Air sensitive samples were prepared as described above. Corrections for the diamagnetism of the PVC sample containers were made by measuring the magnetic response of the empty container under the same conditions of temperature and field which were measured for the filled container. Core atom diamagnetism was much smaller than the magnitude of the paramagnetism measured and so was ignored. Magnetic susceptibility as a function of field strength (at a constant temperature of 300 K) was first

investigated to determine if the samples experienced saturation of their magnetic signal. For all compounds, magnetization increased linearly with increasing field over the range investigated (100-55,000 Gauss). The subsequent temperature dependent studies were performed at low to moderate field strengths (300-5000 Gauss).

Single Crystal X-ray Diffraction -- Intensity data was collected using a Rigaku AFC6S four-circle automated diffractometer equipped with a graphite crystal monochromator. An ω-2θ scan mode was used. The crystals' stability was monitored with three standard reflections whose intensities were checked every 150 reflections, and unless noted, no crystal decay was detected. An empirical absorption correction based on ψ scans was applied to all data during initial stages of refinement. An empirical DIFABS correction[23] was applied after full isotropic refinement, after which full anisotropic refinement was performed. The structures were solved by direct methods using either MITHRIL[24] (in the case of K_4USe_8) or SHELXS-86 software[25a] (for all other compounds), and full matrix least squares refinement was performed using the TEXSAN software package.[25b] Crystallographic data for the compounds in this section are given in Table 2.7.

Table 2.7: Crystallographic Data for K_4USe_8, $KCeSe_4$, $KTbSe_4$, $RbCeTe_4$, $NaCeS_3$, and $NaLaS_3$

	K_4USe_8	$KCeSe_4$	$KTbSe_4$
a, Å	17.331(4)	6.376(2)	6.255(2)
b, Å	20.584(3)		
c, Å	8.811(3)	8.327(1)	8.227(3)
β, °	90.0	90.0	90.0
V, $Å^3$	3143(1)	338.6(2)	321.9(2)
space group	Fdd2 (#43)	P4/nbm (#125)	P4/nbm (#125)
Z	8	2	2
F.W., g/mol	1026.10	495.06	513.86
d_{calc}, g/cm^3	4.336	4.855	5.301
μ, cm^{-1}	291.703	572.140	340.23
crystal dimensions, mm^3	1.0 x 1.0 x 1.0	0.02 x 0.08 x 0.08	0.04 x 0.42 x 0.46
radiation	Mo K_α	Mo K_α	Mo K_α
2θ max, °	50	60	60
data collection temp., °C	23	23	23
# data collected	797	949	343
# unique data	797	916	325
# $F_o^2 > 3\sigma$	647	302	236
# of variables	60	9	9
R/Rw, % [a]	3.6/4.7	3.9/4.9	6.1/7.4
final Dif. map max. peak, $e^-/Å^3$	3.35	2.0	2.6

[a] $R = \Sigma(|Fo|-|Fc|)/\Sigma|Fo|$ $Rw = \{\Sigma w(|Fo|-|Fc|)^2/\Sigma w|Fo|^2\}^{1/2}$

Table 2.7 Crystallographic Data for K_4USe_8, $KCeSe_4$, $KTbSe_4$, $RbCeTe_4$, $NaCeS_3$, and $NaLaS_3$ (cont.)

	$RbCeTe_4$	$NaCeS_3$	$NaLaS_3$
a, Å	6.952(3)	5.683(1)	5.752(4)
b, Å		4.238(2)	4.2796(6)
c, Å	9.084(4)	9.802(2)	9.841(2)
β, °		90.0	90.0
V, $Å^3$	439.0(6)	236.0(2)	242.2(3)
space group	P4/nbm (#125)	Pmmn (#59)	Pmmn (#59)
Z	2	2	2
F.W., g/mol	735.99	259.29	258.08
d_{calc}, g/cm^3	5.567	3.648	2.538
μ, cm^{-1}	236.07	109.69	99.95
crystal dimensions, mm^3	0.01 x 0.07 x 0.08	0.01 x 0.04 x 0.44	0.02 x 0.26 x 0.40
radiation	Mo K_α	Mo K_α	Mo K_α
2θ max.	55	60	60
data collection temp., °C	20	-75	23
# data collected	623	432	450
# unique data	290	432	450
# $F_o^2>3\sigma$	197	380	411
# of variables	9	19	19
R/Rw, % [a]	3.1/2.4	1.9/2.6	2.6/3.4
final Dif. map max. peak, $e^-/Å^3$	1.69	0.61	1.47

[a] $R= \Sigma(|Fo|-|Fc|)/\Sigma|Fo|$ $Rw=\{\Sigma w(|Fo|-|Fc|)^2/\Sigma w|Fo|^2\}^{1/2}$

C. Results and Discussion

1. K_4USe_8

Structure -- A single $[USe_8]^{4-}$ anion is shown in Figure 2.5a, with selected bond distances and angles in Table 2.8 and fractional atomic coordinates in Table 2.9. The uranium center sits on a crystallographic 2-fold axis, but the entire anion has a triangulated dodecahedral geometry and can hence be assigned a pseudo D_{2d} symmetry. A dodecahedral structure is characterized by the location of coordinating atoms at the corners of two trapezoids which lie orthogonal to each other; in $[USe_8]^{4-}$ the Se-Se bonds form the non-parallel sides of their respective trapezoids. The $[USe_8]^{4-}$ is distorted from an ideal dodecahedron (shown in Fig. 2.5b) in two respects. First, the bases of the Se trapezoids intersect at the U center, leaving the four basal seleniums in a nearly square planar arrangement; in an ideal dodecahedron the trapezoids slice further into each other. Second, the presence of the Se-Se bonds, although slightly elongated (2.38 Å and 2.40 Å), necessitates that the corresponding Se-U-Se angle be smaller than in an ideal dodecahedron (Se(1)-U-Se(2) angle: 49.05°; corresponding dodecahedron angle[26]: 73.69°). Although without precedent in metal-chalcogenide systems, $[USe_8]^{4-}$ is isostructural (but not isoelectronic) with the known peroxo-anions ($[M(O_2)_4]^{n-}$)[27] ($M=Cr^{5+}$, V^{5+}, Nb^{5+}, Ta^{5+}, Mo^{6+}, W^{6+}).

The potassium cations are located in two different sites. The first is coordinated by seven Se atoms in an irregular polyhedron (Fig. 2.6a) (range of K(1)-Se distances: 3.475(7) Å-3.190(7) Å; ave.: 3.357 Å) while the second is in a site coordinated by nine Se atoms, again in an irregular polyhedron (Fig. 2.6b) (range of K(2)-Se distances: 3.694(8) Å-3.253(7) Å; ave.: 3.470 Å). Examples of molecular uranium/chalcogenide

complexes are sparse. A fully characterized homoleptic uranium thiolate has been recently reported.[28] Prior to this, most work has dealt with complexes of uranyl with various sulfur containing ligands,[29] including a complex containing a single η^2-S_2^{2-}.[30,31]

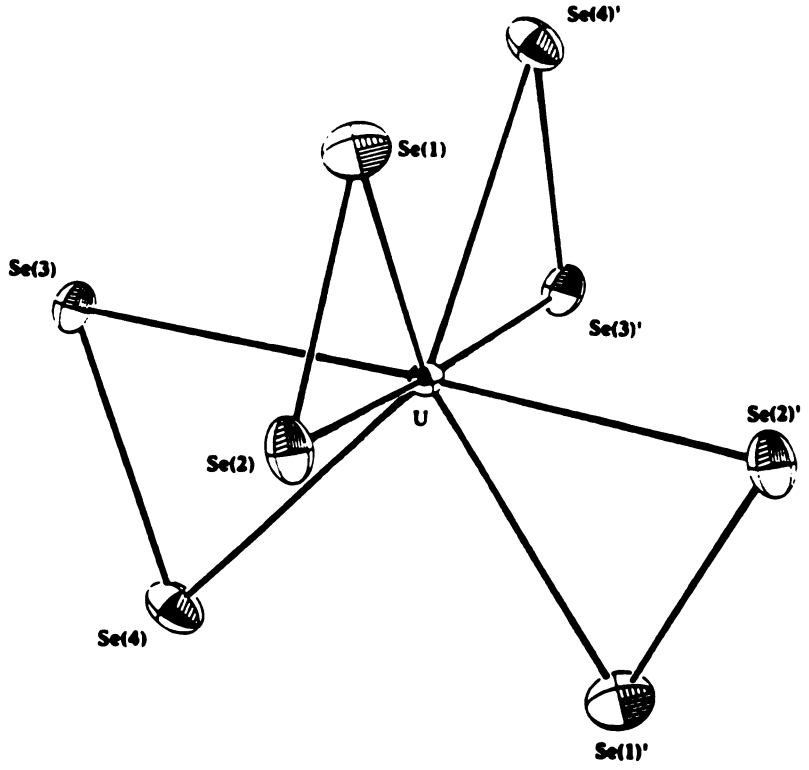

(A)

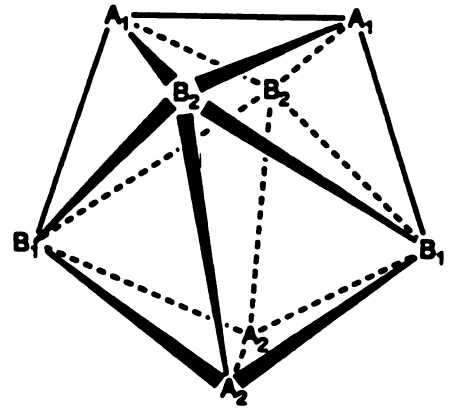

(B)

Figure 2.5: (A): Ortep representation of the $[U(Se_2)_4]^{4-}$ anion

(B): An ideal triangulated dodecahedron

Table 2.8 Selected Bond Distances (Å) and Angles (°) for K_4USe_8 with Standard Deviations in Parentheses.

U-Se(1)	2.840(3)	Se(3)-Se(4)	2.401(4)
U-Se(2)	2.903(3)	Se(1)-K(1)	3.421(7)
U-Se(3)	2.923(3)	Se(1)-K(2)	3.398(7)
U-Se(4)	2.920(3)	Se(2)-K(2)	3.398(7)
Se(1)-Se(2)	2.385(4)	K(1)- K(2)	4.468(9)
Se(1)-U-Se(1)'	127.9(1)	Se(2)-U-Se(4)	94.19(8)
Se(1)-U-Se(2)	49.05(8)	Se(2)-U-Se(4)'	129.00(8)
Se(1)-U-Se(2)'	91.19(9)	Se(3)-U-Se(3)'	86.5(1)
Se(1)-U-Se(3)	90.96(9)	Se(3)-U-Se(4)	48.54(8)
Se(1)-U-Se(3)'	128.48(9)	Se(3)-U-Se(4)'	87.41(9)
Se(1)-U-Se(4)	126.93(9)	Se(4)-U-Se(4)'	121.9(1)
Se(1)-U-Se(4)'	79.95(9)	U-Se(1)-Se(2)	66.8(1)
Se(2)-U-Se(2)'	87.4(1)	U-Se(2)-Se(1)	64.1(1)
Se(2)-U-Se(3)	93.10(8)	U-Se(3)-Se(4)	65.7(1)
Se(2)-U-Se(3)'	177.51(9)	U-Se(4)-Se(3)	65.8(1)

Table 2.9 Fractional Atomic Coordinates and B_{eq}[a] values for K_4USe_8 with Estimated Standard Deviations in Parentheses

atom	x	y	z	B(eq)
U	1	0	0.0217	0.72(5)
Se(1)	1.0379(2)	0.1198(1)	-0.1197(4)	1.9(1)
Se(2)	1.1100(2)	0.0303(1)	-0.2165(4)	1.6(1)
Se(3)	1.1119(2)	0.0244(1)	0.2633(4)	1.7(1)
Se(4)	1.1051(2)	-0.0869(1)	0.1827(4)	1.5(1)
K(1)	0.9981(4)	0.2741(3)	-0.2415(8)	2.3(3)
K(2)	1.2211(4)	0.1662(3)	-0.2042(8)	2.1(3)

[a] B values for anisotropically refined atoms are given in the form of the isotropic equivalent displacement parameters defined as $B_{eq} = (4/3)[a^2B(1,1) + b^2B(2,2) + c^2B(3,3) + ab(\cos\gamma)B(1,2) + ac(\cos\beta)B(1,3) + bc(\cos\alpha)B(2,3)$.

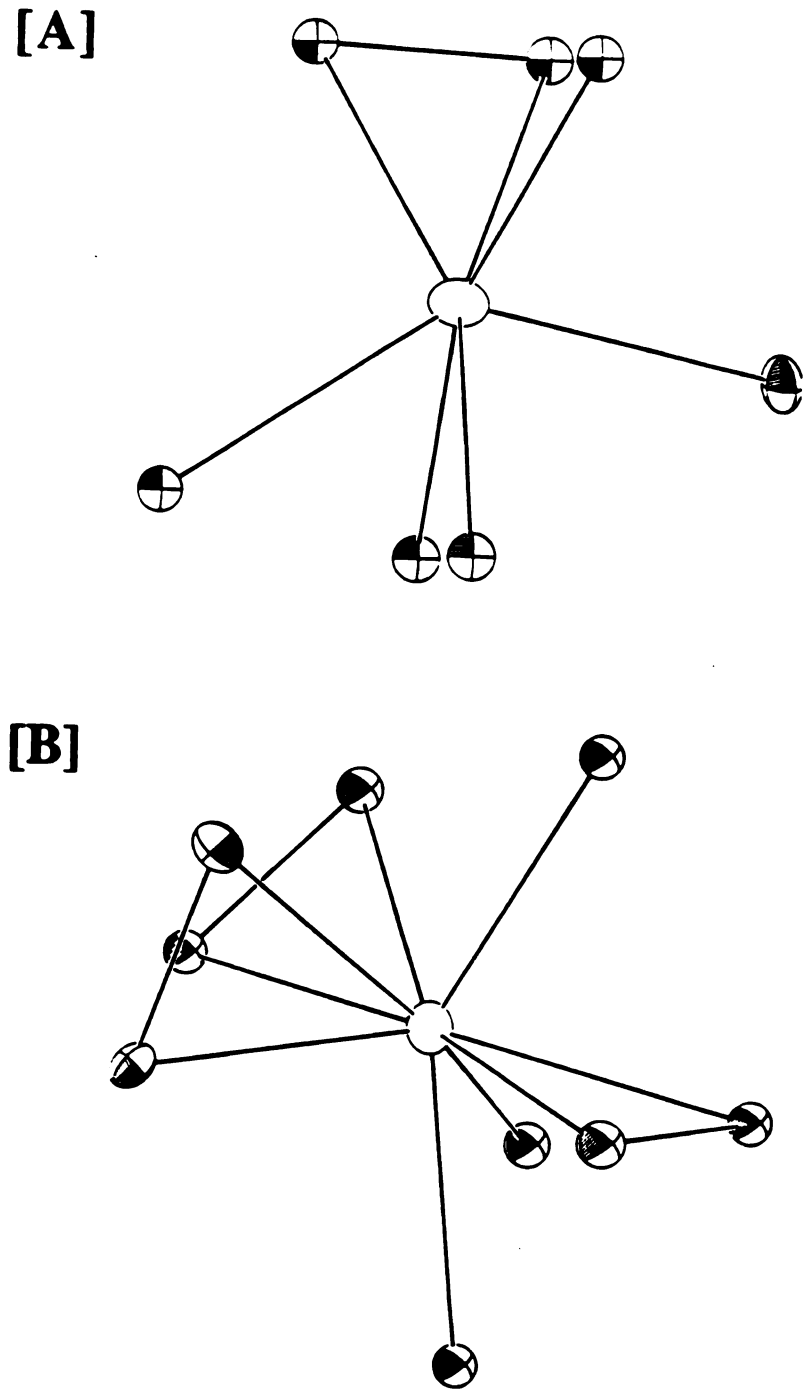

Figure 2.6: Ortep drawings of the coordination environments of the atoms K(1), (A), and K(2), (B), in the structure of K_4USe_8.

Magnetic Properties -- The magnetic susceptibility of K_4USe_8 was measured as a function of temperature (5-250 K) at a constant field of 5000 Gauss. A plot of the data as $1/\chi_M$ vs. T is shown in Figure 2.7. Strong paramagnetic behavior, conforming to Curie-Weiss law, is observed from approximately 120 K on up. Below this region, a transition is observed at approximately 90 K and is then followed by antiferromagnetic ordering which has a critical temperature of 65 K at the midpoint of a broad and shallow transition. The μ_{eff} at 300 K is 3.82 BM, consistent with an f^2 configuration where $L \neq 0$.[32] The exhibited paramagnetic behavior of the compound at high temperatures renders difficult any ^{77}Se NMR study of this compound. Antiferromagnetic transitions of various degrees have been reported for the uranium compounds MU_8Q_{17} (M=Cr, V Co, Fe, Ni) by Noel and Troc,[33] although their data are complicated by the presence of M^{2+}. Neither K^+ nor Se_2^{2-} would contribute to any magnetic phenomenon, so barring any impurity, we are observing behavior based solely on U^{4+}.

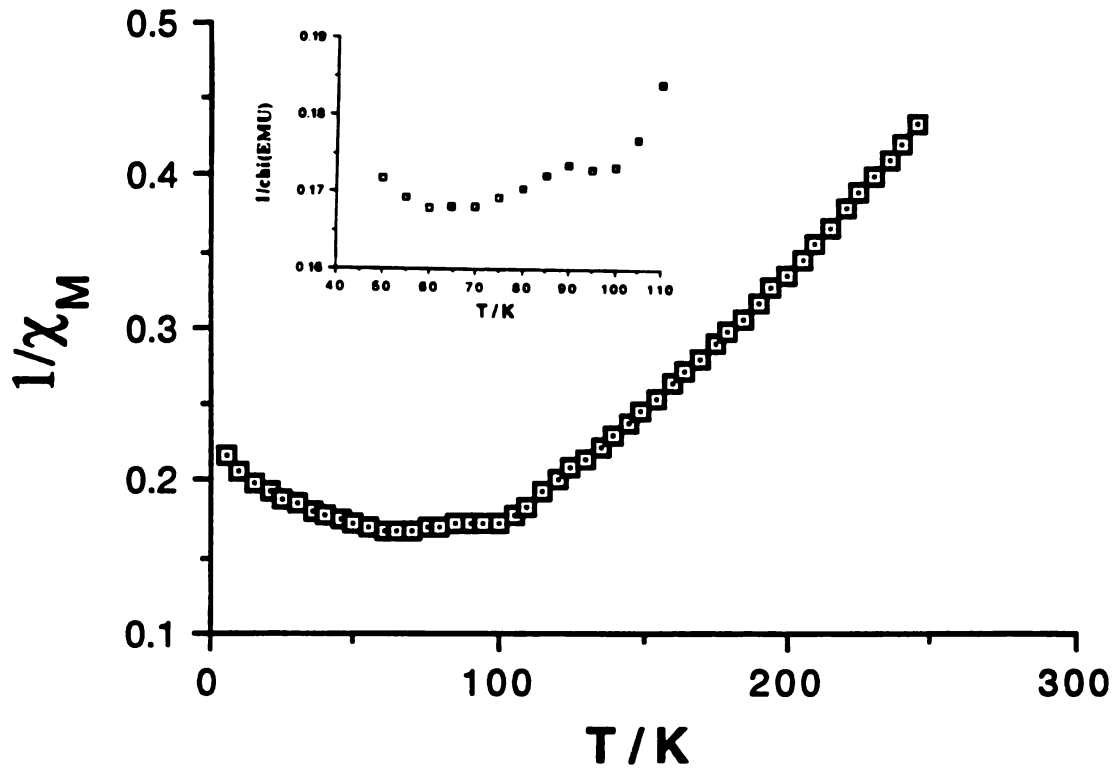

Figure 2.7: Inverse molar magnetic susceptibility ($1/\chi_M$) plotted against temperature (K) for K_4USe_8 (5000 Gauss).

Spectroscopy -- The solid state far-IR spectrum of K_4USe_8 shows three peaks: 261 cm^{-1}, which can be tentatively assigned to Se-Se stretching in the diselenides, 168 cm^{-1} and 153 cm^{-1} which are presumably due to U-Se vibrations.

As mentioned before K_4USe_8 is slowly soluble in DMF, and similar behavior has been found with ethylenediamine. The compound was insoluble in neat acetonitrile, even with the addition of $[Bu_4N]^+$; however, it was successfully dissolved in solutions of either 15C5 or 18C6 crown ethers, or 2,2,2-cryptand in CH_3CN.

In all solvents the solutions of K_4USe_8 gave brown/yellow colors of various hues which were stable, by UV/Vis, out to 3 days. The DMF and CH_3CN/complexant solutions gave similar UV/Vis spectra: one broad plateau at 400-430 nm for DMF and at 390-430 nm for CH_3CN/complexant. After decomposition the solutions revert to brown/green in color, and their UV/Vis spectra show the features of a polyselenide solution (peaks at 440 and 640 nm for DMF, 417 and 560 nm for CH_3CN). Such a decomposition takes place in all solvents tested upon exposure to air, as well as simply upon standing, due to the high oxophilicity of U(IV), making distilled and degassed solvents a requirement. In ethylenediamine solutions of K_4USe_8, UV/Vis shows peaks at 346, 404, 492, and 807 nm, while a polyselenide/ethylenediamine solution shows peaks at 408, 560, and 805 nm. Although clearly not a simple Se_x^{2-} solution, the presence of several peaks in the ethylenediamine solution indicates a significantly stronger solvent interaction with the anion than in either DMF or CH_3CN.

2. $ALnQ_4$ (A=K; Ln=Ce, Tb;Q=Se or A=Rb; Ln=Ce;Q=Te)

Structure -- In the ALnQ4 structure, Ln and Q form two dimensional anionic layers with A^+ in the interlayer gallery. The anionic layers themselves are further partitioned into two layers of $(Q_2)^{2-}$ units sandwiching a layer of Ln^{3+} cations. The Ln^{3+} cations are in a square antiprismatic environment, coordinated to the ends of eight dichalcogenides, four above the Ln plane and four below. A view of this arrangement is shown in Figure 2.8. Selected bond distances and angles are given in Table 2.10 for $KCeSe_4$, Table 2.11 for $KTbSe_4$ (Fractional atomic coordinates are given in Table 2.12 for $KCeSe_4$, Table 2.13 for $KTbSe_4$). It can be seen that the $(Se_2)^{2-}$ units point in a uniform direction within their layer and invert that direction in the layer below. Each $(Se_2)^{2-}$, in turn, bridges four Ln^{3+} cations, each Se bridging in η^2 fashion, and the expanded anionic layer is shown in Figure 2.9. Except for the expected changes in bond distances, the $RbCeTe_4$ analog is almost perfectly isostructural, with the respective bond angles being comparable to those in the selenides. Table 2.14 lists the bond distances and angles of the telluride, and Table 2.15, the fractional atomic coordinates.

A further feature of this structure is that in the direction parallel to (110), channels are formed, bounded on the opposite sides by Ln^{3+} and on the top and bottom by $(Q_2)^{2-}$ (Figure 2.10). Their dimensions are 4.16 Å (Ce to Ce) by 3.61 Å (Se to Se) in $KCeSe_4$, with the analogous dimensions in $KTbSe_4$ being 4.11 Å and 3.64 Å and in $RbCeTe_4$, 4.92 Å and 4.25 Å. Hence they present too small of a volume for intercalation of most species, although Li intercalation may be a possibility via reduction of $(Q_2)^{2-}$ to 2 Q^{2-}.

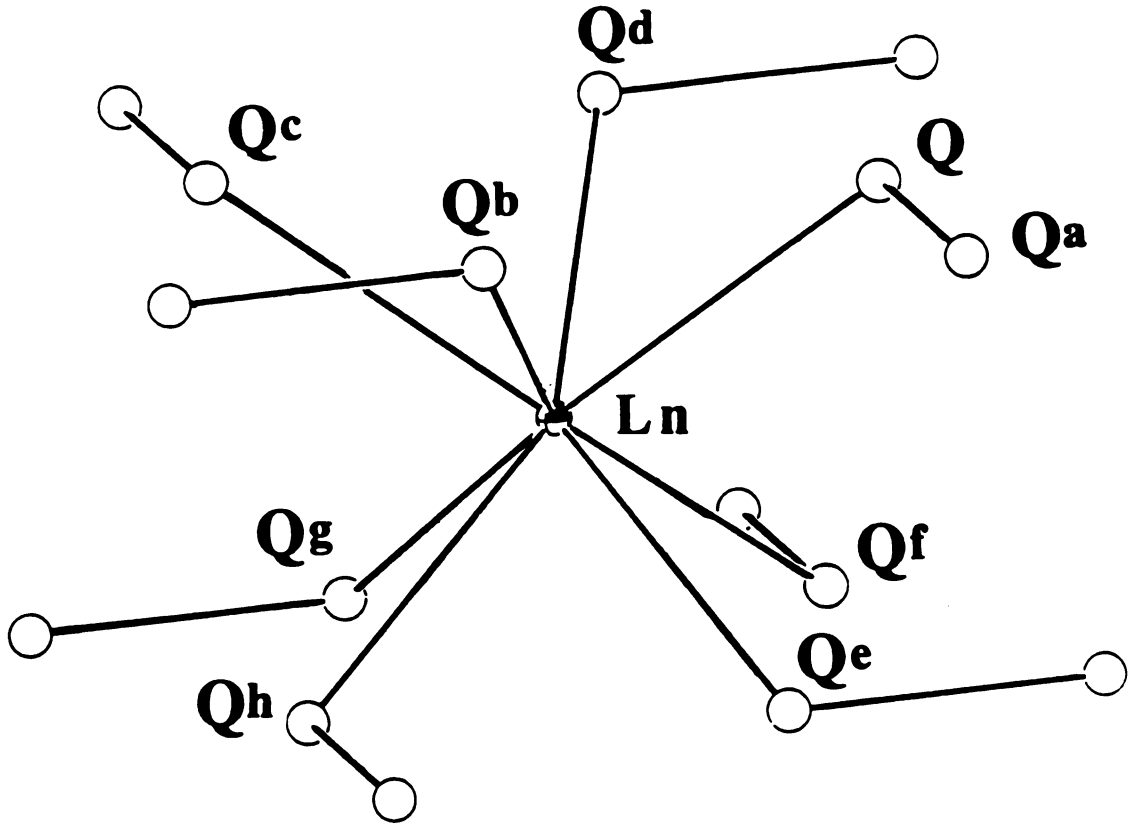

Figure 2.8: The immediate coordination environment of the Ln3+ cations in the ALnQ4 structure type (A=alkali, Ln=lanthanide, Q=Se, Te).

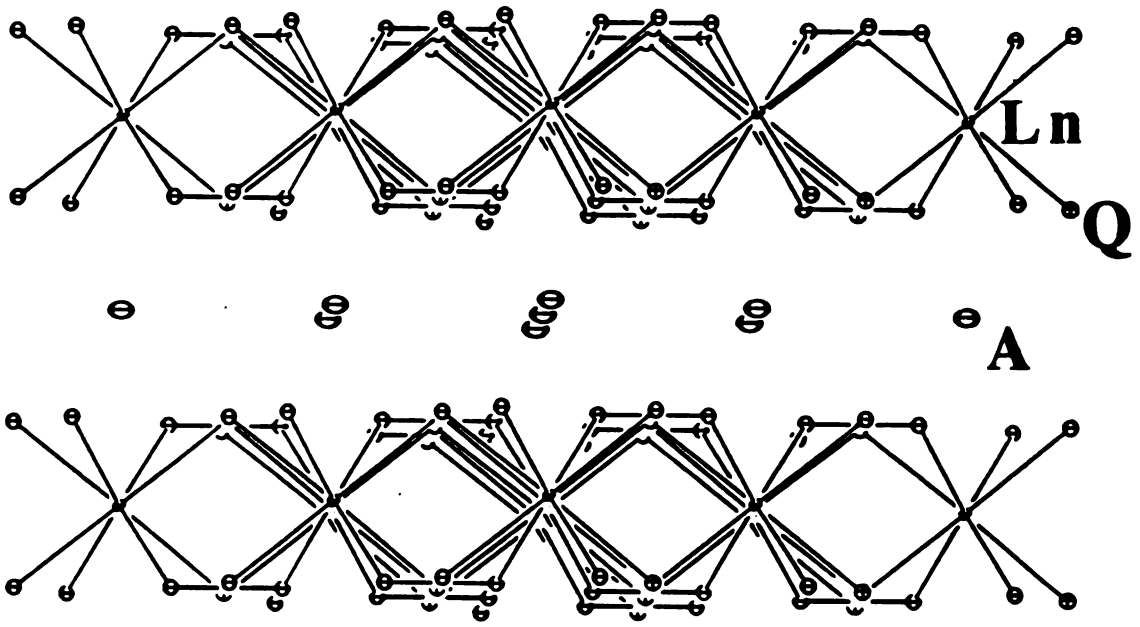

Figure 2.10: $ALnQ_4$ as seen parallel to the crystallographic [110] direction.

Table 2.10 Selected Bond Distances (Å) and Angles (°) for $KCeSe_4$ with Standard Deviations in Parentheses.

Ce-Se	3.075(1)	Se-K	3.434(2)
Ce-K	4.1646(7)	K-K^a	4.509(1)
Se-Se^a	2.385(3)		
Se-Ce-Se^b	69.92(3)	Se-Ce-Se^g	148.17(5)
Se-Ce-Se^c	108.27(7)	Se-Ce-Se^h	139.60(6)
Se-Ce-Se^d	69.92(3)	Ce-Se-Se^a	110.20(3)
Se-Ce-Se^e	80.61(7)	Ce-Se-Ce^a	94.30(5)
Se-Ce-Se^f	85.70(7)	K-Ce-K^a	180.00

Table 2.11 Selected Bond Distances (Å) and Angles (°) for $KTbSe_4$ with Standard Deviations in Parentheses.

Tb-Se	2.980(1)	Se-K	3.414(2)
Tb-K	4.114(1)	K-K^a	4.423(2)
Se-Se^a	2.393(2)		
Se-Tb-Se^b	70.55(4)	Se-Tb-Se^g	147.00(3)
Se-Tb-Se^c	109.51(6)	Se-Tb-Se^h	140.17(4)
Se-Tb-Se^d	70.55(3)	Tb-Se-Se^a	109.92(5)
Se-Tb-Se^e	80.06(6)	Tb-Se-Tb^a	95.85(5)
Se-Tb-Se^f	84.15(6)	K-Tb-K^a	180.00

Table 2.12 Fractional Atomic Coordinates and B_{eq}[a] values for $KCeSe_4$ with Estimated Standard Deviations in Parentheses

atom	x	y	z	B(eq)[a]
Ce	1/4	1/4	0	0.53(5)
Se	-0.1178(2)	0.1178	0.2163(2)	0.81(5)
K	-3/4	1/4	1/2	2.0(2)

Table 2.13 Fractional Atomic Coordinates and B_{eq}[a] values for $KTbSe_4$ with Estimated Standard Deviations in Parentheses

atom	x	y	z	B(eq)[a]
Tb	1/4	1/4	1/2	0.36(4)
Se	0.1147(2)	0.6147	0.7090(2)	0.55(4)
K	1/4	1/4	0	1.4(2)

[a] B values for anisotropically refined atoms are given in the form of the isotropic equivalent displacement parameters defined as $B_{eq} = (4/3)[a^2B(1,1) + b^2B(2,2) + c^2B(3,3) + ab(\cos\gamma)B(1,2) + ac(\cos\beta)B(1,3) + bc(\cos\alpha)B(2,3)$.

Table 2.14 Selected Bond Distances (Å) and Angles (°) for $RbCeTe_4$ with Standard Deviations in Parentheses.

Ce-Te	3.285(1)	Te-Rb	3.765(1)
Ce-Rb	4.542(2)	Rb-Rb[a]	4.916(2)
Te-Te[a]	3.285(1)		
Te-Ce-Te[b]	70.50(2)	Te-Ce-Te[g]	145.23(2)
Te-Ce-Te[c]	109.40(5)	Te-Ce-Te[h]	141.97(2)
Te-Ce-Te[d]	70.50(2)	Ce-Te-Te[a]	109.01(1)
Te-Ce-Te[e]	81.16(4)	Ce-Te-Ce[a]	96.89(4)
Te-Ce-Te[f]	83.1(4)	Rb-Ce-Rb[a]	180.00

Table 2.15 Fractional Atomic Coordinates and B_{eq}[a] values for $RbCeTe_4$ with Estimated Standard Deviations in Parentheses

atom	x	y	z	B(eq)[a]
Ce	1/4	1/4	1/2	0.59(4)
Te	0.6123(9)	0.1055(9)	0.2911(1)	0.78(4)
Rb	1/4	1/4	0	1.81(8)

[a] B values for anisotropically refined atoms are given in the form of the isotropic equivalent displacement parameters defined as $B_{eq} = (4/3)[a^2B(1,1) + b^2B(2,2) + c^2B(3,3) + ab(\cos\gamma)B(1,2) + ac(\cos\beta)B(1,3) + bc(\cos\alpha)B(2,3)$.

The A^+ cations of the structure are colinear with the Ln^{3+}, being displaced from the Ln^{3+} by only half the length of the c-axis. Except for their distances from the $(Q_2)^{2-}$ layers, Ln^{3+} and A^+ have the same coordination environment. This gives the $ALnQ_4$ phases a similarity to the known $ALnQ_2$ compounds which possess the α-$NaFeO_2$ structure type. In these $ALnQ_2$ phases, A^+ and Ln^{3+} also share the same coordination environment (octahedral in this case) and, like $ALnQ_4$, are segmented such that every alternate cation layer is exclusively A^+ or Ln^{3+}.

The change in structural dimensions when comparing the two $KLnSe_4$ analogs is consistent with the ionic radius of Tb^{3+} being smaller than that of Ce^{3+}. The cell volume of the Tb analog is the smaller of the two (321.9(2) $Å^3$ vs. 338.6(2) $Å^3$ for $KCeSe_4$), and the Ln-Se distances exhibit the expected changes as well (Tb-Se: 2.980(1) Å; Ce-Se: 3.075(1) Å). Both Ln-Se distances are consistent with the average values for the respective eight-coordinate Ln^{3+} which have been tabulated by Poix[34]. The changing bond lengths also make their presence felt on the respective Se-Se bonds. In $KTbSe_4$ the slightly stronger Tb-Se interaction results in a slightly longer Se-Se bond (2.393 Å). The bond angles respond somewhat to the change in Ln-Se distances as well; in general the Se-Ln-Se angles between Se atoms in the same plane are increased in the Tb analog while the "trans-plane" angles are slightly smaller from those in $KCeSe_4$.

The repeating unit shown in Fig. 2.8 is the same unit which is found in two closely related three dimensional structure types: $CuAl_2$ and $NbTe_4$. The former is seen in several compounds of the formula TX_2 (T=transition metal, X=Sb, Ge, Sn, or Pb)[35] and is simply the fusing of the anionic layers of $ALnQ_4$, through face-sharing at the square antiprisms, into a three dimensional structure. Indeed, since A and Ln share coordination

environments, $ALnQ_4$ can be considered as a derivative of the $CuAl_2$ structure type where the two cations alternate in the Cu positions along the c-axis. The $NbTe_4$ structure[36] is also closely related to that of $CuAl_2$; the Nb cations reside in half of the Cu positions and are ordered such that every other plane of metal positions is vacant, forming a porous structure. $NbTe_4$ has $(Te_2)^{2-}$ units, analogous to the $(Q_2)^{2-}$ units in $ALnQ_4$.

The known chemical similarities between all members of the lanthanide group would tend to indicate that other elements from that group could also be accommodated in the $ALnQ_4$ structure type. Such possibilities were, in fact, investigated. When Ln=La and Q=Se, reactions analogous to those described resulted only in $LaSe_2$. Phases with powder X-ray diffraction patterns similar to $ALnQ_4$ were isolated from reactions where A=K, Ln=Nd or Eu, and Q=Se, but these were consistently contaminated with large amounts of amorphous binary powder. Apparently, the chemical behavior of the various lanthanides is sufficiently different that direct substitution of one element for another, under these synthetic conditions, is not always possible.

Magnetic Properties -- The magnetic susceptibility of $KCeSe_4$ was measured from 2-300 K at 300 Gauss, and a plot of $1/\chi_M$ vs. T is shown in Figure 2.11. The material appears to be paramagnetic although several anomalies in the data are present. At temperatures below 100 K, the curve is seen to deviate negatively from a straight line extrapolated from the higher temperature data. Such deviation has been reported for several Ce^{3+} compounds and has been attributed to crystal field splitting of the cation's $^2F_{5/2}$ ground state.[37] At temperatures above 100 K, Curie-Weiss law is not strictly adhered to, and a slight curvature remains in the data. In this temperature range an average μ_{eff} of 2.3± 0.2 BM has been calculated. This value is in accordance with the usual range for Ce^{3+} compounds (2.3-2.5 BM) and is close to that of the free ion (2.54 BM) due to the shielding effect the outer electron cloud has on the embedded f-orbitals.[38] It was found that the measurements on $KCeSe_4$ must be done on freshly isolated sample, as a probable phase change in aged samples gives artificially high values for the μ_{eff}. This phase change probably occurs to a small extent on the sample surface because the bulk of the sample remains intact by X-ray powder diffraction.

The temperature dependent magnetic susceptibility of $KTbSe_4$ proved to be of nearly ideal Curie-Weiss behavior with only a slight deviation from linearity beginning below 50 K (Figure 2.12). Above this temperature, a μ_{eff} of 9.25±0.04 BM was estimated by applying a straight line curve fit to the data from several trials. The calculated μ_{eff} of a Tb^{3+} cation (based on the $^7F_6$ ground state) is 9.72 BM with typically observed experimental values being 9.5-9.8 BM.[38] Also the small value of θ (ca. -6 K) indicates that the cation is much less prone to crystal field effects in this environment than is Ce^{3+}.[39]

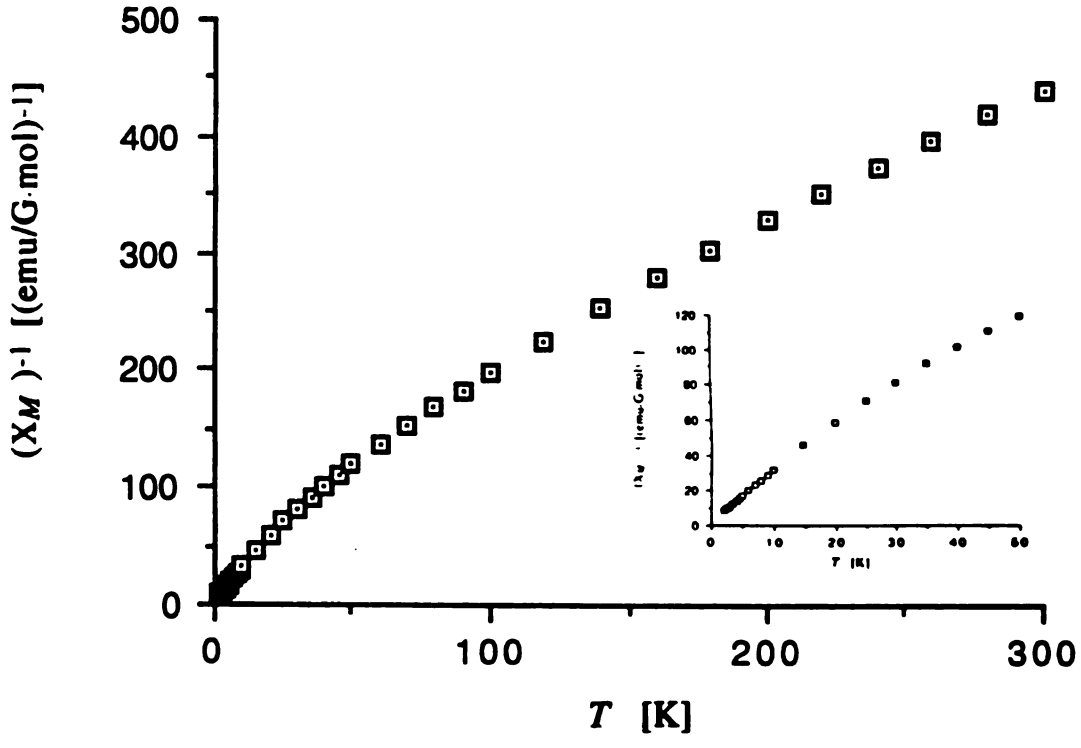

Figure 2.11: Inverse molar magnetic susceptibility ($1/\chi_M$) plotted against temperature (2-300 K) for $KCeSe_4$ (300 G). The inset graph shows an expanded view of the region 2-50 K.

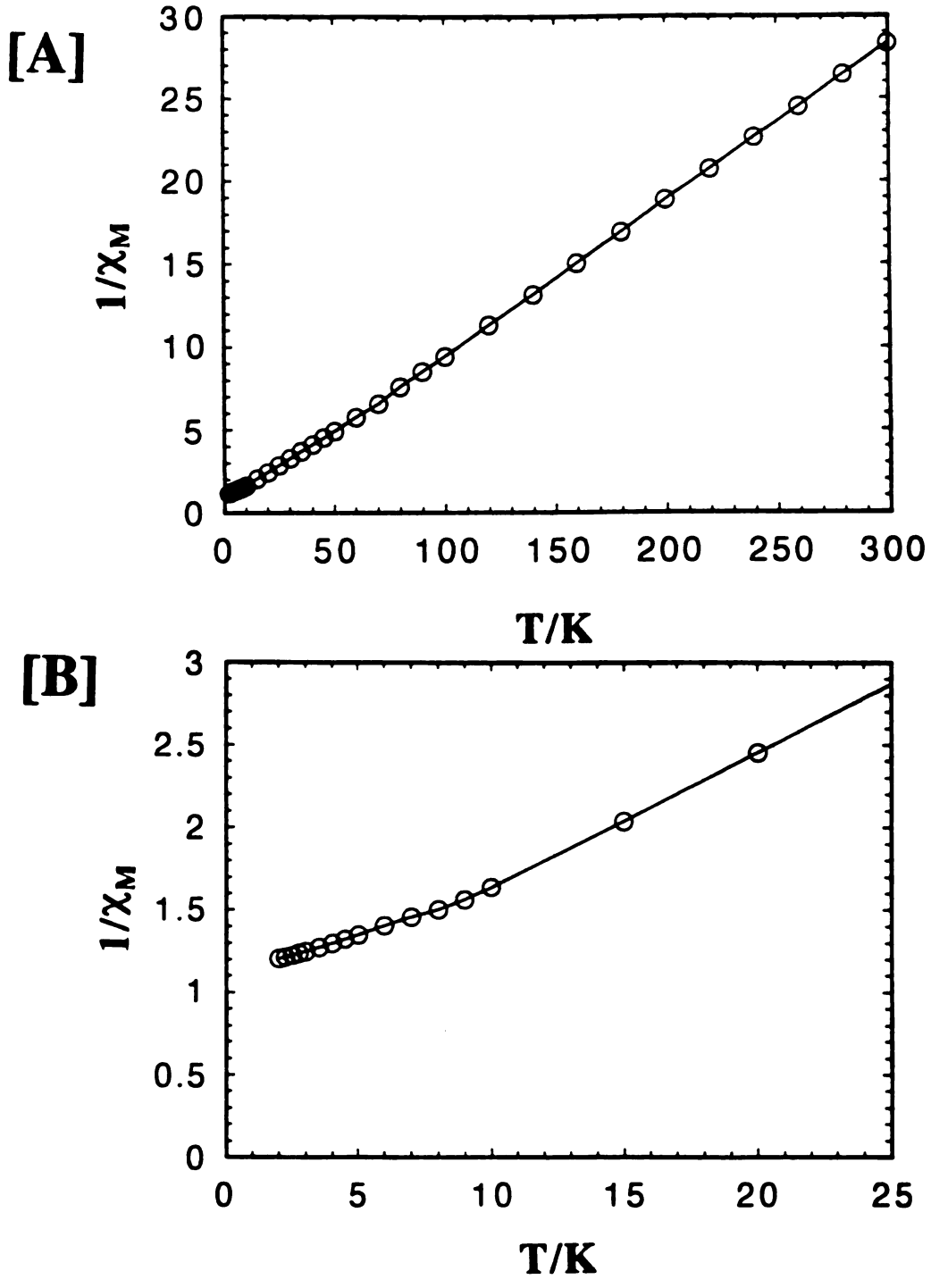

Figure 2.12: Inverse molar magnetic susceptibility ($1/\chi_M$) plotted against temperature (2-300 K) for $KTbSe_4$ (5000 G). (B) shows an expanded view of the region 2-25 K.

Spectroscopy -- A solid state far-IR of $KCeSe_4$ shows no peaks, the only feature being a broad absorbance beginning at 250 cm^{-1}. The presence of this sort of feature is common in metallic materials, and so a four-probe conductivity measurement on a pressed pellet was performed at 300 K. A value of 5.1 $x10^{-6}$ S/cm was found, however, indicating a semiconducting material.

The solid state far-IR of $KTbSe_4$ was somewhat more informative. A strong peak is clearly present at 151 cm^{-1}, which because of its low energy can be safely assigned as a Tb-Se vibration. Two broad peaks are evident at 370 and 515 cm^{-1} with a weak peak at 436 and shoulders on the 370 peak at 325, 268, 227, and 201 cm^{-1}. Although tending to have a broad absorbance similar to that of $KCeSe_4$, the weak shoulders are all in a region where one would expect either Se-Se vibration energy (325 and 268 cm^{-1}) or slightly higher energy modes from the Tb-Se bonds (227 and 201 cm^{-1}).

The solid state diffuse reflectance spectra of both compounds are shown in Figure 2.13. The sharp changes in α/S vs. energy (eV) in the spectra of these materials correspond to estimates of the their band gaps at 1.54 eV for $KCeSe_4$ and 1.65 eV for $KTbSe_4$. This helps to confirm that both are valence precise semi-conductors. Simply on the basis of color one would expect the respective band gaps as $KCeSe_4$ is a dark blue material while $KTbSe_4$ is dark purple. Although extrapolation of the absorption edges gives slightly different band gaps for the two compounds, within experimental error, they are nearly identical.

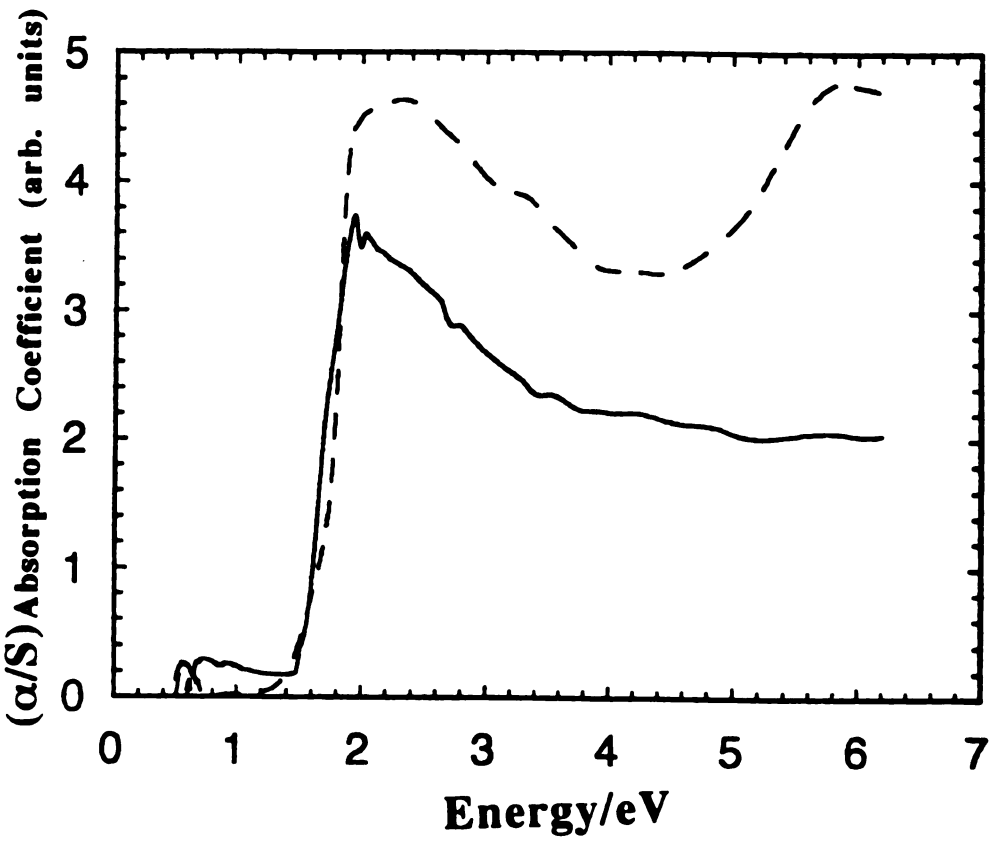

Figure 2.13: The solid state diffuse reflectance spectra of $KCeSe_4$ (solid line) and $KTbSe_4$ (dashed line) plotted as absorption coefficient (a/S) vs. energy (eV).

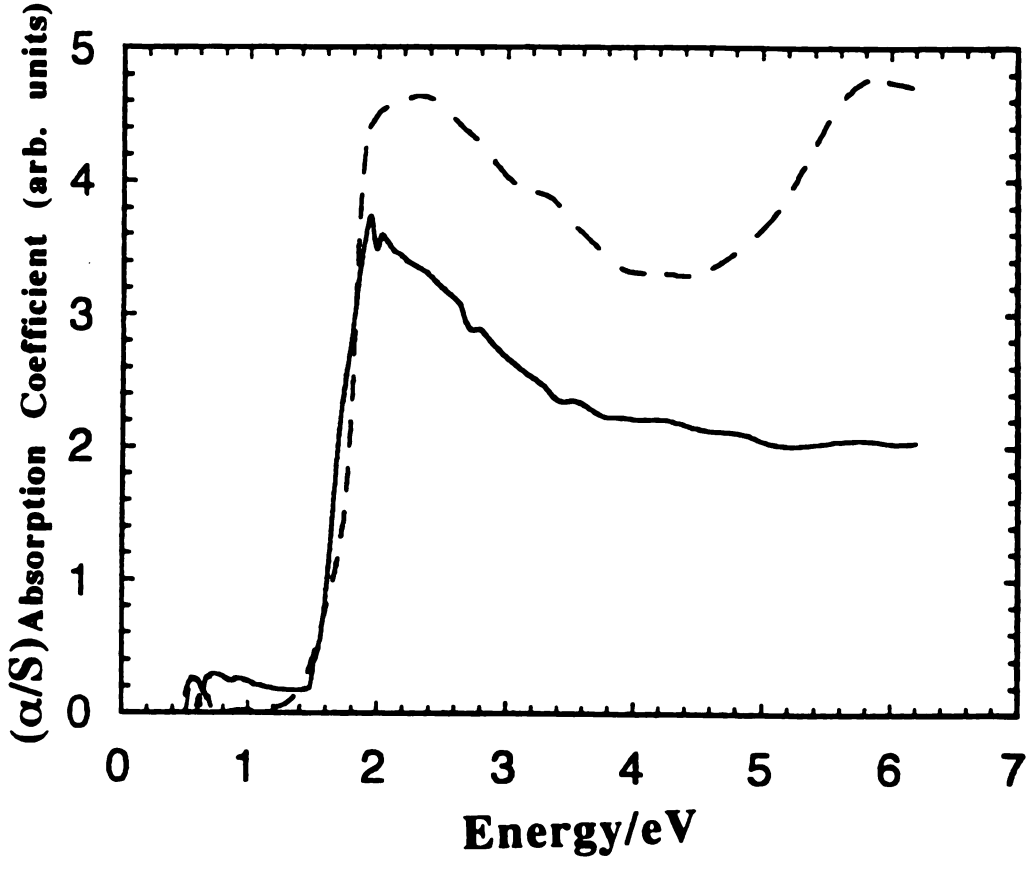

Figure 2.13: The solid state diffuse reflectance spectra of $KCeSe_4$ (solid line) and $KTbSe_4$ (dashed line) plotted as absorption coefficient (a/S) vs. energy (eV).

3. $NaLnS_3$ (Ln=La, Ce)

Structure -- As in the structure of $KLnSe_4$, $NaLnS_3$ possesses anionic Ln/Q layers charge balanced with A^+ in the interlayer gallery. The Ln^{3+} ions in $NaLnS_3$ are again 8-coordinate but now reside in bicapped trigonal prisms of S atoms made of two $(S_2)^{2-}$ units forming the short sides of the prism and four S^{2-} ions at the apex and capping positions (Figure 2.14). The coordination sphere about the Ln^{3+} is nearly identical for either La or Ce, except for the slightly larger bond distances in the La analog due to the cation's slightly larger size. The fractional coordinates for the two phases are given in Table 2.16 for Ln=La and 2.17 for Ln=Ce.

The trigonal prisms of $NaLnS_3$ stack in one dimension by sharing triangular faces (Figure 2.15), forming chains parallel to the c-axis. Layers are formed when neighboring chains share monosulfides; this is done such that the monosulfides of the trigonal prisms in one chain are the capping monosulfides of the neighboring chains (Figure 2.16). This results in the $(LnS_3)_n^{n-}$ portion of the structure being analogous to the known phase, $ZrSe_3$; however, $ZrSe_3$ exhibits elongated Zr-Se bonds between the chains (Zr-Se = 2.72-2.74 Å within the chain, Zr-Se = 2.87 Å between the chains).[12] The larger coordination spheres of the Ln cations easily accommodate the eight sulfur atoms, and in fact, the capping bonds are no longer than any of the other Ln-S bonds present (see Tables 2.18 and 2.19).

The Ce-S distances for $NaCeS_3$ range from 2.838(1) Å to 3.010(1) Å and are comparable with those in previously reported compounds (2.878 Å in $KCeS_2$[14g], 2.88-3.26 Å in CeS_2[40]). The disulfide bond of 2.105(3) Å is also reasonable. In $NaLaS_3$, the corresponding range is from 2.869(1) Å to 3.039 Å, and the disulfide bond is nearly identical at 2.107(3) Å.

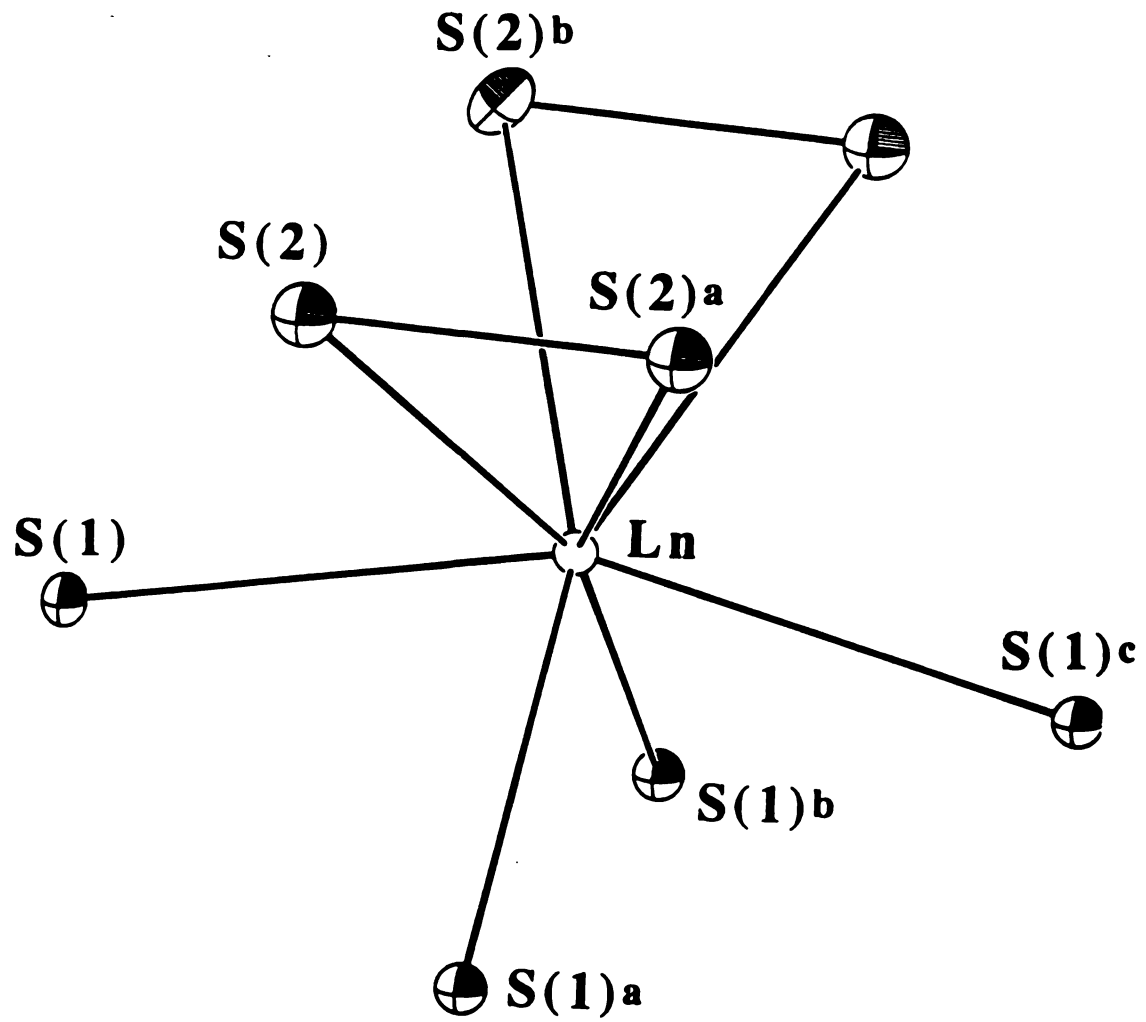

Figure 2.14: ORTEP representation of the immediate coordination environment of the Ln^{3+} cations in $NaLnS_3$ (Ln=La, Ce).

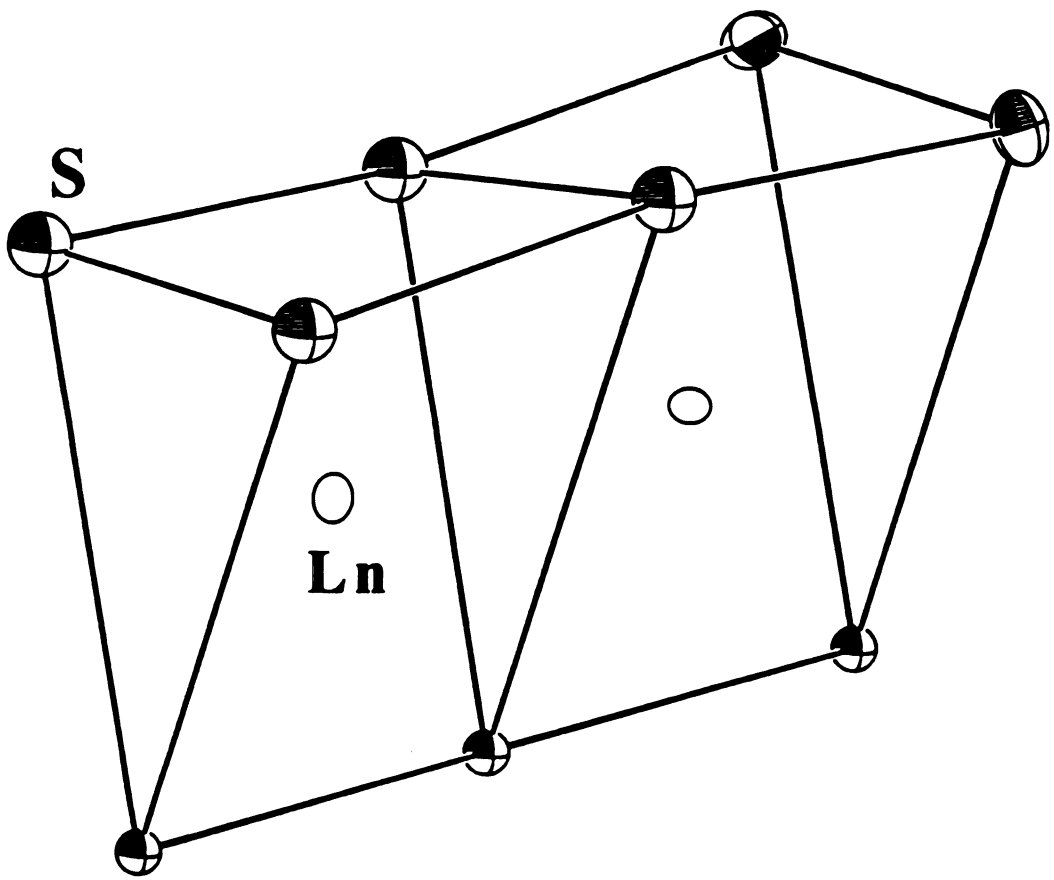

Figure 2.15: The face-sharing connection between two [LnS_6] trigonal prisms featured in the structure of $NaLnS_3$.

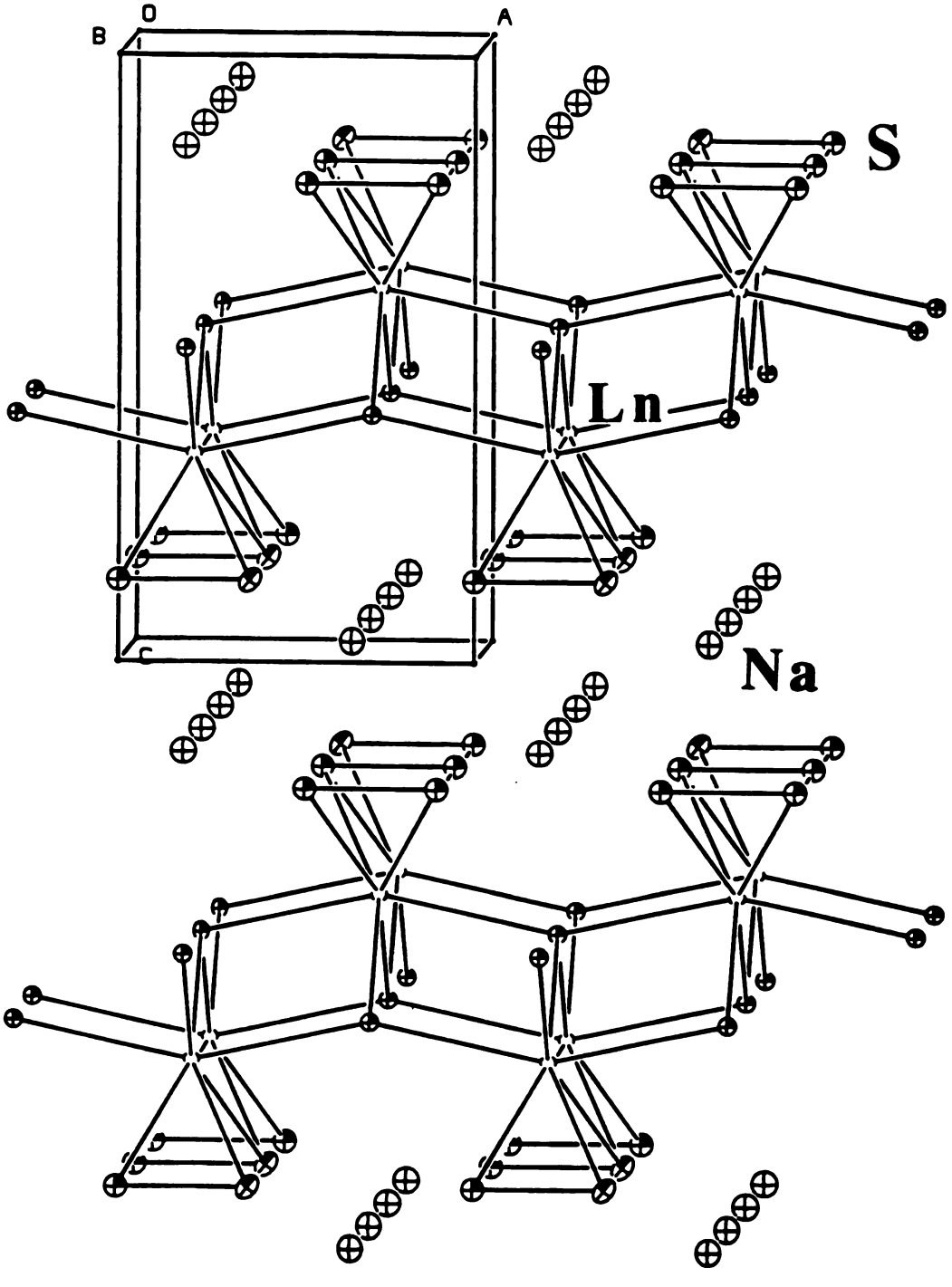

Figure 2.16: The extended structure of $NaLnS_3$ as seen parallel to the c-axis (circles with nonshaded octants: Na; open circles: Ln; circles with shaded octants: S).

Table 2.16 Fractional Atomic Coordinates and B_{eq}[a] values for $NaLaS_3$ with Estimated Standard Deviations in Parentheses

atom	x	y	z	B(eq)[a]
La	1/4	1/4	0.12835(3)	0.83(2)
S(1)	-1/4	1/4	0.0658(2)	0.94(5)
S(2)	0.4332(2)	-1/4	0.3198(1)	1.56(5)
Na	3/4	1/4	0.3963(4)	2.1(1)

Table 2.17 Fractional Atomic Coordinates and B_{eq}[a] values for $NaCeS_3$ with Estimated Standard Deviations in Parentheses

atom	x	y	z	B(eq)[a]
Ce	3/4	1/4	0.37187(4)	0.49(2)
S(1)	1/4	1/4	0.4355(2)	0.63(6)
S(2)	0.5648(2)	-1/4	0.1821(1)	1.02(4)
Na	1/4	-3/4	0.1015(3)	1.3(1)

[a] B values for anisotropically refined atoms are given in the form of the isotropic equivalent displacement parameters defined as $B_{eq} = (4/3)[a^2B(1,1) + b^2B(2,2) + c^2B(3,3) + ab(\cos\gamma)B(1,2) + ac(\cos\beta)B(1,3) + bc(\cos\alpha)B(2,3)$.

Table 2.18 Selected Bond Distances (Å) and Angles (°) for $NaLaS_3$ with Standard Deviations in Parentheses.

La-S(1)	2.941(2)	S(2)-S(2)'	2.107(3)
La-S(1)'	2.869(1)	Na-S(2)	2.910(1)
La-S(2)	3.039(1)		
S(1)-La-S(1)^a	81.99(2)	S(1)^a-La-S(2)	83.55(3)
S(1)-La-S(1)^c	155.86(7)	S(1)^a-La-S(2)^b	159.71(3)
S(1)^a-La-S(1)^b	96.47(6)	S(2)-La-S(2)^a	40.57(5)
S(1)-La-S(2)	77.91(4)	S(2)-La-S(2)^b	89.50(5)
S(1)-La-S(2)^a	117.94(3)	S(2)^a-La-S(2)^b	103.40(5)

Table 2.19 Selected Bond Distances (Å) and Angles (°) for $NaCeS_3$ with Standard Deviations in Parentheses.

Ce-S(1)	2.9091(7)	S(2)-S(2)'	2.105(3)
Ce-S(1)'	2.838(1)	Na-S(2)	2.884(2)
Ce-S(2)	3.010(1)		
S(1)-Ce-S(1)^a	81.80(2)	S(1)^a-Ce-S(2)	83.44(4)
S(1)-Ce-S(1)^c	155.25(7)	S(1)^a-Ce-S(2)^b	159.53(3)
S(1)^a-Ce-S(1)^b	96.58(6)	S(2)-Ce-S(2)^a	40.93(5)
S(1)-Ce-S(2)	77.93(4)	S(2)-Ce-S(2)^b	89.50(5)
S(1)-Ce-S(2)^a	118.29(3)	S(2)^a-Ce-S(2)^b	103.64(5)

$NaLnS_3$ has some of the same structural motifs of the known Ln/Q_x binary systems which were discussed in the introduction. The structure of CeS_2[40] will serve as a good example of this relationship. In that phase, the Ce^{3+} are in an unusual nine-coordinate environment shown schematically in Figure 2.17. On one side of the lanthanide are the five monosulfides of the Ln^{3+}/Q^{2-} bilayer. On the opposite side of its coordination sphere, the Ce cation makes four bonds to three disulfides; two bonds are to both atoms of a disulfide while two more are to sulfur atoms from two separate disulfide units. Figure 2.18 shows a comparison of the projections of the monosulfide environments of CeS_2 and $NaLnS_3$. Essentially the same lanthanide/monosulfide bilayer is repeated in both structures; the lanthanide cations in $NaLaS_3$ have merely shifted from having four nearly coplanar monosulfides to two, with the accompanying change in the number of coordinating monosulfides from the neighboring layer (1 to 2). This results in four $Ln\text{-}S^{2-}$ bonds as opposed to 5 in CeS_2. The Ln^{3+}/Q^{2-} bilayer is sandwiched between layers of disulfide units in both cases, albeit with different coordination patterns to the lanthanides. While the binary compounds possess the alternating bilayer/disulfide motif, the new ternary materials have both an extra layer of disulfides (reminiscent of the pattern in the $LnTe_3$ phases) and an extra bilayer of Na cations (Figure 2.19).

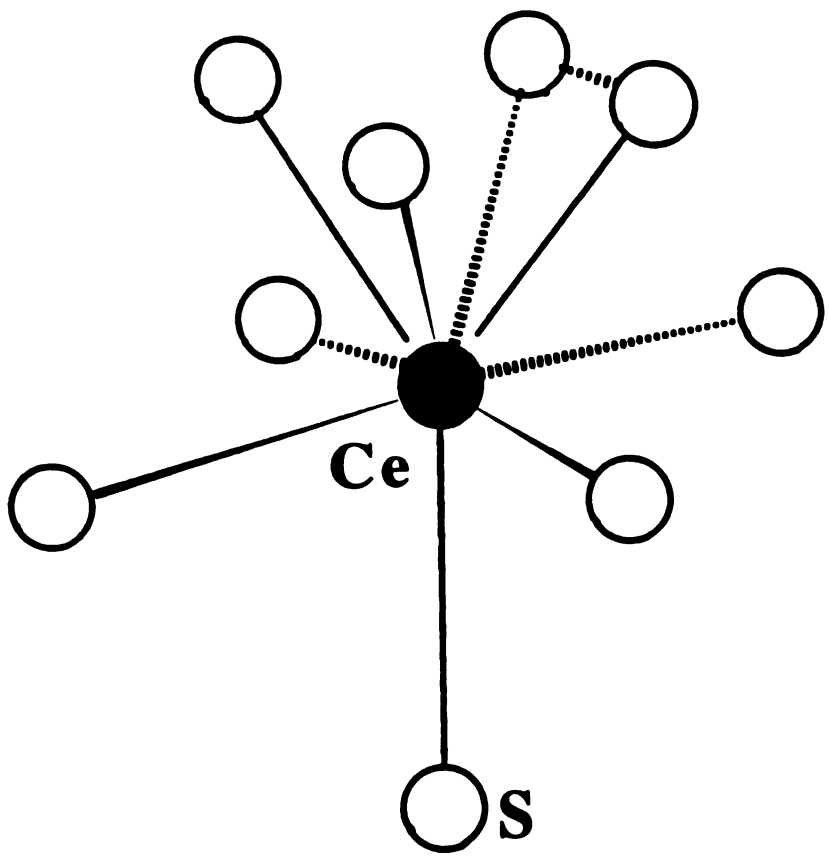

Figure 2.17: Schematic drawing of the immediate coordination environment of a Ce atom in the structure of CeS_2.

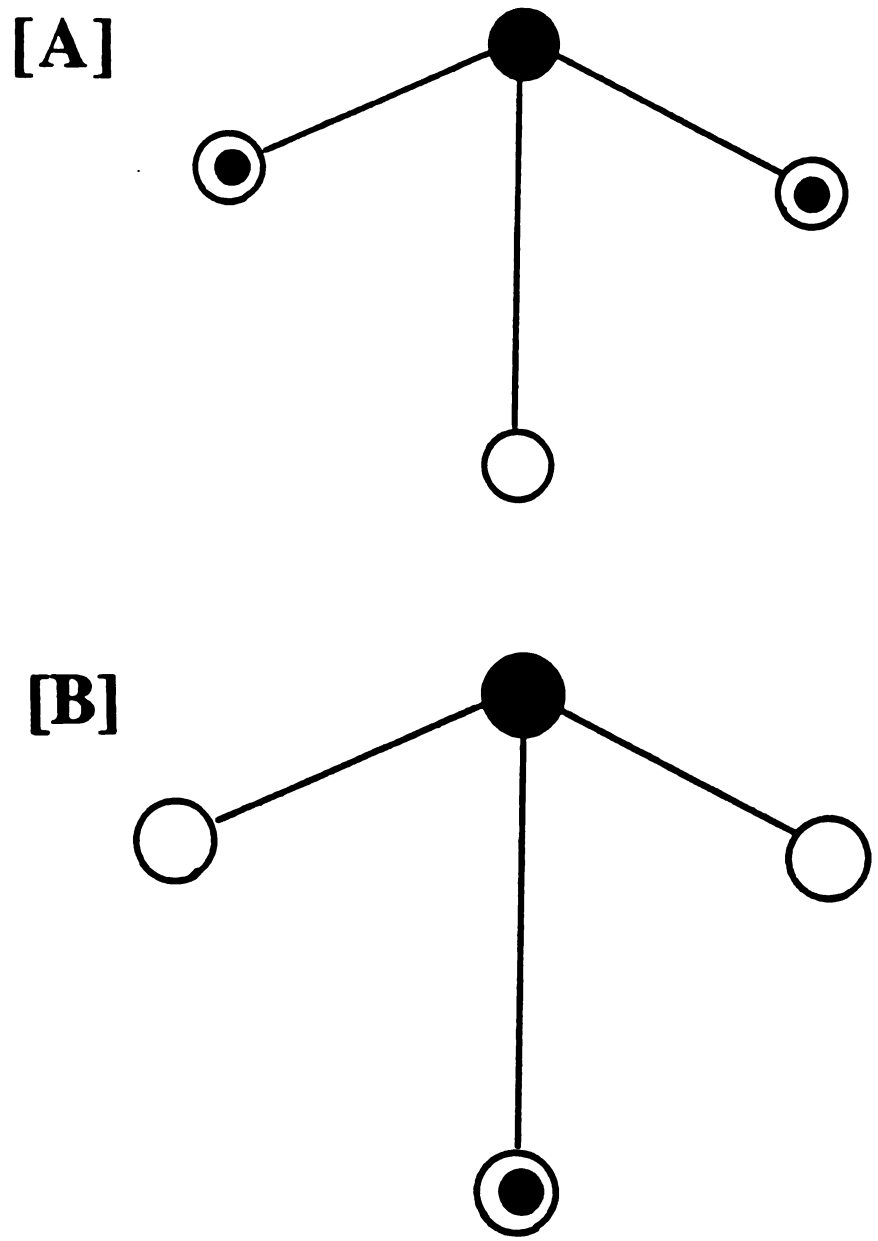

Figure 2.18: A schematic showing the monosulfide environments about the lanthanide cations in the structures of (A) CeS_2 and (B) $NaLnS_3$.(solid circles: metal; open circle: sulfide; semisolid circle: two eclipsed sulfides)

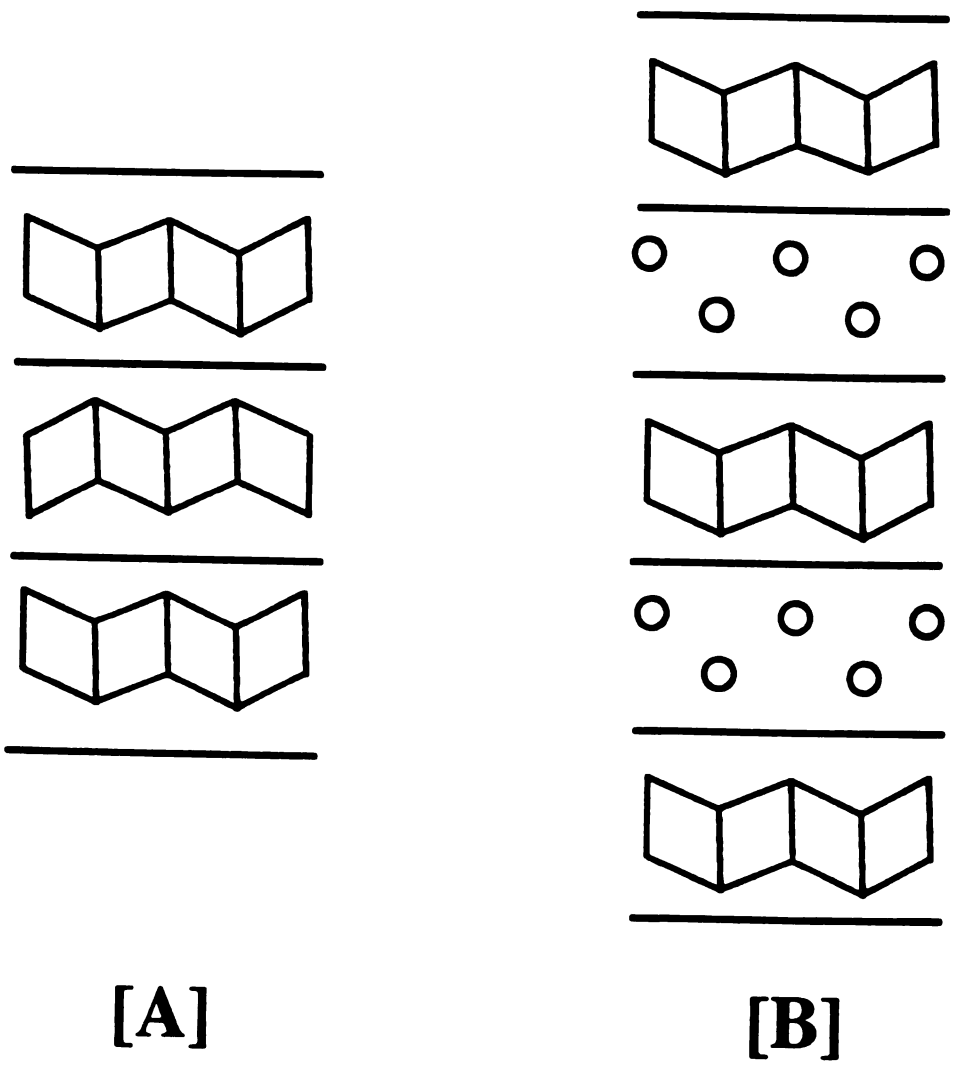

Figure 2.19: Schematic drawings of the (A) CeS_2 and (B) $NaLnS_3$ structures where the edge sharing rhombi represent bilayers of Ln^{3+} and S^{2-}; the solid lines, sheets of $(S_2)^{2-}$; and the open circles, Na^+ cations.

Magnetic Susceptibility -- The temperature dependent magnetic susceptibility response of $NaCeS_3$ at 2000 G is shown in Figure 2.20. Despite the change in chalcogenide environment, the magnetic behavior of the Ce^{3+} remains similar to that seen in $KCeSe_4$: a Curie-Weiss paramagnet at high temperatures with deviations caused by crystal field splitting ensuing as the temperature drops. Above the onset of deviation, an μ_{eff} of 2.3±0.2 BM and a Θ of -71±1 K were estimated by fitting a straight line to the data. Again the μ_{eff} is close to that calculated for the free ion, consistent with the known insensitivity of f-orbitals to chemical environments. The magnetic response of $NaLaS_3$ was not investigated as La^{3+} is an f^0 cation and so is expected to be diamagnetic.

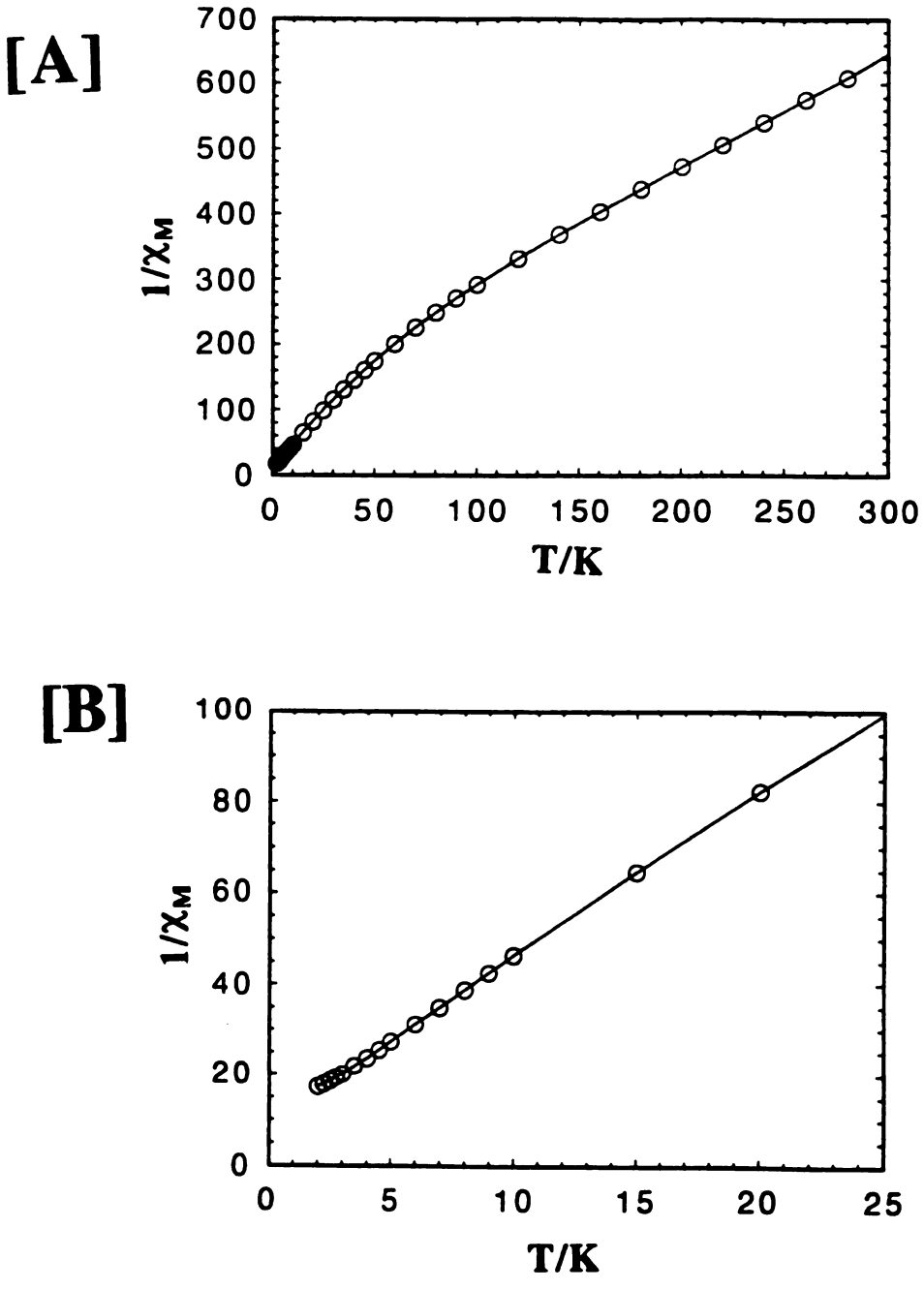

Figure 2.20: Inverse molar magnetic susceptibility ($1/\chi_M$) plotted against temperature (2-300 K) for $NaCeS_3$ (2000 G). (B) shows an expanded view of the region 2-25 K.

Spectroscopy -- As would be expected from their isostructural nature, the solid state far-IR spectra of $NaCeS_3$ and $NaLaS_3$ are very similar, with only the frequencies of the peaks shifting in response to the slight mass difference between the two lanthanides. Both materials show a strong peak in the region corresponding to S-S vibrations (493 cm^{-1} for $NaCeS_3$ and 490 cm^{-1} for $NaLaS_3$). A manifold of strong overlapping peaks is seen at lower energies which have been assigned as the Ln-S vibrations of their respective compounds. In $NaCeS_3$ these peaks are at 277, 243, 218, 193, and 177 cm^{-1} and a final, and much weaker peak exists at 137 cm^{-1}. The peaks of the corresponding manifold in $NaLaS_3$ are at 276, 241, 209, 188, 174, and 137 cm^{-1}.

The solid state diffuse reflectance spectra of $NaCeS_3$ and $NaLaS_3$ are shown in Figure 2.21. The difference in color of the two phases is clearly evident in the change in band gap between the two. The red $NaCeS_3$ exhibits a band gap of 2.15 eV while that of the yellow La analog increases to 2.61 eV. $NaCeS_3$ has a considerable tailing below the initial absorption edge which suggests either sample impurity or indirect character in the material's band gap. The difference in band gap between the two suggests that it may be possible to produce solid solutions of the formula $NaLa_{1-x}Ce_xS_3$ in which the band gap of the material would be tunable based on the lanthanide ratio. Preliminary synthetic investigation of such phases were made by reacting various ratios of La/Ce in the previously described flux reaction for the ternary phase. Although evidence for solid solution behavior was observed, the final products were not of uniform homogeneity.

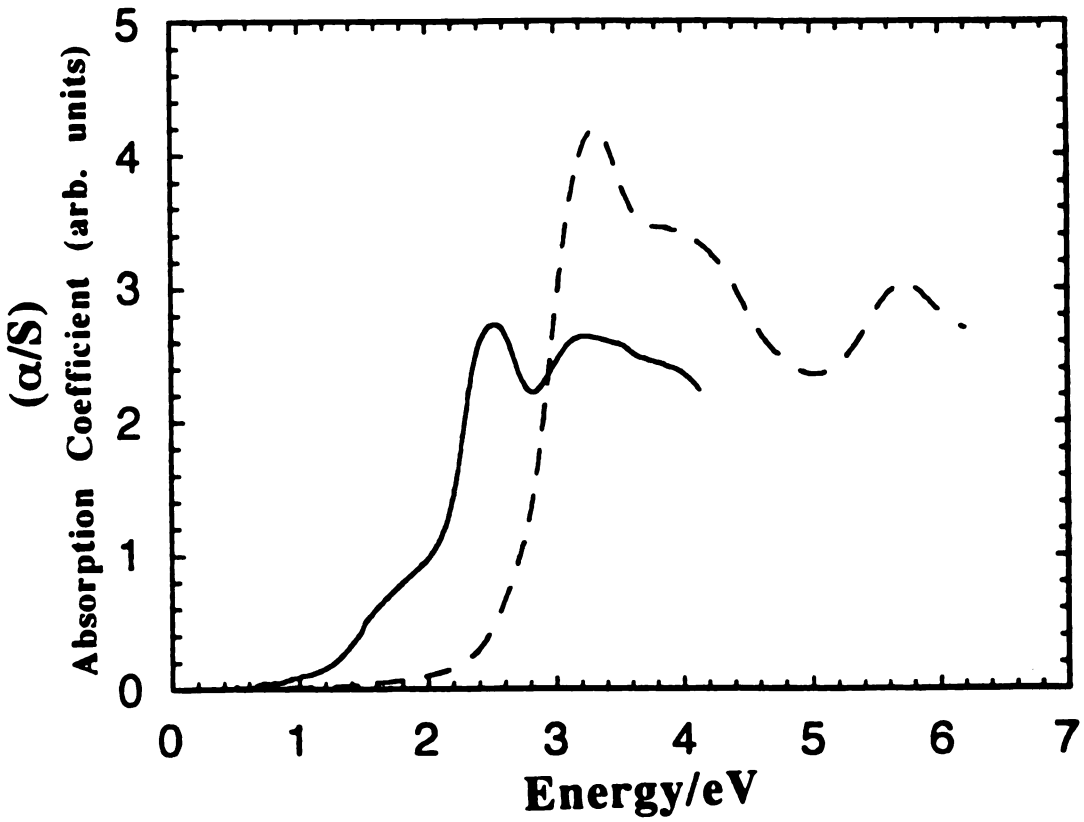

Figure 2.21: The solid state diffuse reflectance spectra of $NaCeS_3$ (solid line) and $NaLaS_3$ (dashed line) plotted as absorption coefficient (α/S) vs. energy (eV).

D. Conclusions

Although the conditions of the molten A_2Q_x flux have given rise to new phases in these systems, much of what has been described in this chapter has some similarity to previously known f-block/chalcogenide chemistry.

The most similarities were found in the $NaLnS_3$ structure type, which possesses several features closely related to those seen in the known polychalcogenide containing binaries. From a compositional stand point, this is not too surprising because $NaLnS_3$ has only one equivalent of S more than LnQ_2, and it has exactly the same Ln/Q stoichiometry as the $LnTe_3$ phases. Because of the unique ability of Te to form infinite covalently bonded nets, the LnQ_3 phase had not been seen in either S or Se systems. No doubt the increased electronegativity of the lighter congeners does not support such extended sharing of electrons, and the preference instead is to localize them into $(Q_2)^{2-}$ units. The formation of a phase with increased amounts of S or Se is only possible if some cationic species is available to balance the charge. With some help from Na, the Ln/S in $NaLnS_3$ framework merely expands along known structural themes.

The $ALnQ_4$ phases move slightly further from the known base of Ln/Q_x binaries while still retaining some similarities. There is no Ln/Q^{2-} bilayer here as there was in $NaLnS_3$; instead the "naked" Ln^{3+} cations are coordinated directly and exclusively to $(Q_2)^{2-}$. The layering motif of previous compounds is, however, retained as the cations and anions in $ALnQ_4$ are all segmented into perfectly coplanar sheets. This also warrants comparison to the known $ALnQ_2$ phases. Conceptually, if two extra equivalents of Q could be stuffed into the anionic layer of $ALnQ_2$, then packing forces could respond by forming Q-Q bonds, to minimize

electrostatic repulsion, and by expanding the coordination environment about the cations. Since both the $ALnQ_4$ and $NaLnS_3$ structure types have such strong relationships to the known binary compounds, it is likely that any further phases isolated from these systems will possess variations on the discussed structural themes.

The most chalcogenide rich phase in this chapter is, of course, $K4USe_8$. Rather than forming an extended structure, the $[USe_8]^{4-}$ dodecahedron is stabilized. Why this should be so is a mystery. Actinides have a slightly greater covalent character to their bonding than do the lanthanides because of the increased orbital size in going from 4f to 5f. Although this may give an increased tendency to form discrete complexes, it certainly does not preclude extended networks. The lack of other examples of A/U/Q compounds at this time makes speculation difficult.

REFERENCES

1) (a) Flomer, W. A., Kolis, J. W., *J. Am. Chem. Soc.*, **1988**, 110, 3682-3683. (b) Flomer, W. A., O'Neal, S. C., Pennington, W. T., Jeter, D., Cordes, A. W., Kolis, J. W., *Angew. Chem. Int.Ed. Engl.*, **1988**, *27*, 1702-1703. (c) Eichhorn, B. W., Haushalter, R. C., Cotton, F. A., Wilson, B., *Inorg. Chem.*, **1988**, 27, 4084-4085. (d) Kanatzidis, M.G., Huang, S.-P., *J. Am. Chem. Soc.*, **1989**, 111, 760-761. (e) Kanatzidis, M.G., Huang, S.-P., *Angew. Chem. Int.Ed. Engl.*, **1989**, *28*, 1513-1514. (f) Kanatzidis, M. G., *Commonts Inorg. Chem.*, **1990**, 10, 161-195. (g) Ansari, M. A., Ibers, J. A., *Coord. Chem. Rev.*, **1990**, 100, 223-266. (h) Kolis, J. W., *Coord. Chem. Rev.*, **1990**, 105, 195-219.

2) Kanatzidis, M. G., and Sutorik, A. C., *Prog. Inorg. Chem.*, in press.

3) Kanatzidis, M. G., and Huang, S.-P., *Coord. Chem. Rev.*, **1994**, 130, 509-621.

4) (a) Draganjac, M., and Rauchfuss, T. B., *Angew. Chem. Int. Ed. Engl.*, **1985**, 24, 742-757. (b) Müller, A., *Polyhedron*, **1986**, 5, 323-340. (c) Müller, A., and Diemann, E., *Adv. Inorg. Chem.*, **1987**, 31, 89-122.

5) Sunshine, S. A., Kang, D., and Ibers, J. A., *J. Am. Chem. Soc.*, **1987**, 109, 6202.

6) Kang, D., and Ibers, J. A., *Inorg. Chem.*, **1988**, 27, 549-.

7) Schreiner, S., Aleandri, L. E., Kang, D., and Ibers, J. A., *Inorg. Chem.*, **1989**, 28, 392-

8) Flahaut, J., in *Handbook on the Physics and Chemistry of Rare Earths: Vol. 4 Non-Metallic Compounds* (Eds.: K. A. Gschneidner,

Jr. and L. Eyring), North-Holland Publishing Company, **1979**, p. 1 and references therein.

9) (a) Lin, W., Steinfink, H., Weiss, E. J., *Inorg. Chem.*, **1965**, 4, 877. (b) Norling, B. K., Steinfink, H., *Inorg. Chem.*, **1966**, 5, 1488.

10) Pardo, M. P., Flahaut, J., *Bull. Soc. Chim. Fr.*, **1967**, 10, 3658.

11) Ben Salem, A., Meerschaut, A., Rouxel, J., *C. R. Acad. Sci.*, **1984**, 299, 617.

12) Kronert, V. W., Plieth, K., *Z. Anorg. Allg. Chem.*, **1965**, 336, 207-

13) Noel, H., Levet, J. C., *J. Solid State Chem.*, **1989**, 79, 28-33.

14) Compounds of the type $ALnQ_2$ (A=Na; Ln=La,Ce,Pr, Nd; Q=S) were first synthesized by Ballestracci and Bertaut[14a] with the range of compounds expanded to include A=Li, K, Rb, Cs; Q=Se; and several other Ln metals by themselves and others.[14b-h] (a) Ballestracci, R., and Bertaut, E. F., *Bull. Soc. Fr. Mineral. Crystallogr.*, **1964**, 87, 512. (b) Ballestracci, R., and Bertaut, E. F., *Bull. Soc. Fr. Mineral. Crystallogr.*, **1965**, 88, 136. c) Ballestracci, R., *Bull. Soc. Fr. Mineral. Crystallogr.*, **1965**, 88, 207. d) Tromme, M., *C. R. Acad. Sci. Ser. C* , **1971**, 273, 849. e) Bronger, W., Elter, R., and Schmidt, E., *Rev. Chim. Miner.*, **1974**, 10, 147. f) Kabre, S., Julien-Pouzol, M., and Guittard, M., *Bull. Soc. Chim. Fr.*, **1974**, 10, 1881. g) Plug, C. M., and Verschoor, G. C., *Acta Crystallogr.*, **1976**, B32, 1856. h) Ohtani, T., Honjo, H., and Wada, H., *Mat. Res. Bull.*, **1987**, 22, 829-840. i) Bronger, W., *Crystallography and Crystal Chemistry of Materials with Layered Structures,* (Ed.: F. Levy), D. Reidel Publishing Company; Dordrecht, Holland; **1976**, p.93. j) Brunel, M., DeBergevin, F., and Gondrand, M., *J. Phys. Chem. Solids,* **1972**, 33, 1927.

15) Foran, B., Lee, S., Aronson, M., *Chem. Mater.*, **1993**, 5, 974-978.

16) (a) Julien-Pouzol, M., Guittard, M., *Ann. Chim., Paris* ; **1972**, *7*, 253-262. (b) Julien-Pouzel, M., Guittard, M., *Bull. Soc. Chim. France* ; **1968**, *6*, 2293-2295. (c) Collin, G., Rouyer, F., Loriers, J., *Compt. Rendus Hebdom. Seances Acad. Sciences, Series C: Scienes Chim.* ; **1968**, *266C* , 689-691. (d) Pardo, M.-P., Dung, N. H., *Comtes Rendus Seances de l'Acadamie des Sciences, Series 2* ; **1987**, *304(12)*, 637-639.

17) Julien-Pouzol, M., Laruelle, P., *Acta Crystallogr.*, **1977**, 33B, 1510-1512.

18) (a) Julien-Pouzol, M., Guittard, M., *C. R. Acad. Sci., Ser. C,* **1969**, 269, 316. (b) Julien-Pouzol, M., Guittard, M., *Ann. Chim. Paris*, **1973**, 8, 139.

19) (a) Padiou, J., Guillevic, J., *C. R. Hebdo. Seances Acad. Sc. Ser. C.*, **1969**, 268, 822-824. (b) Noel, H., Potel, M.; *J. Less Com. Met.* ; **1985**, 113, 11-15. (c) Noel, H., *J. Less Com. Met.* ; **1980**, 72, 45-49.

20) (a) Sutorik, A. C., Kanatzidis, M. G., *J. Am. Chem. Soc.*, **1991**, 113, 7754-7755. (b) Sutorik, A. C., Kanatzidis, M. G., *Angew. Chem. Int. Ed. Engl.*, **1992**, 31, 1594-1596.

21) Feher, F., *Handbuch der Praparativen Anorganischen Chemie* : Brauer, G., Ed. ; Fedinand Enke: Stuttgart, Germany, **1954**; p. 280-281.

22) (a) Wendlandt, W. W., Hecht, H. G., *Reflectance Spectroscopy;* Interscience Publishers, **1966**. (b) Kotum, G., *Reflectance Spectroscopy*; Springer Verlag, New York, **1969**. (c) Tandon, S. R., Gupta, J. P., *Phys. Stat. Solidi*; **1970**, *38*, 363-367.

23) Walker, N., Stuart, D., *Acta Cryst.* ; **1983**, *A39* , 158-166.

24) Gilmore, G. J., *J. Appl. Cryst.*, **1984**, 17, 42-46.

25) (a) G. M. Sheldrick, in *Crystallographic Computing 3* ; Sheldrick, G. M., Kruger, C., Doddard, R., Eds.; Oxford University Press: Oxford, England, **1985**, p. 175-189. (b) Gilmore G. J., *Appl. Cryst.* ; **1984**, *17* , 42-46.

26) Wells, A. F.; *Structural Inorganic Chemistry, 4th ed.* ; **1975**, p. 69.

27) (a) Stomberg, R.; *Acta Chem. Scanda.* ; **1969**, 23, 2755-2763. (b) Stomberg, R.; *Acta Chem. Scanda.* ; **1963**, 17, 1563-1566. (c) Mathern, G., and Weiss, R.; *Acta Crystallogr.* ; **1971**, B27, 1598-1609. (d) Stomberg, R.; *J. Less-Common Met.* ; **1988**, 143, 363-371.

28) Tatsumi, K., Matsubara, I., Inoui, Y., Nakamura, A., Cramer, R., Tagosi, G., Golen, J., Gilje, J.; *Inorg. Chem.*; **1990**, 29, 4928-4938.

29) (a) Perry, D. L.; *Inorg. Chim. Acta* ; **1978**, 48, 117-124. (b) Perry, D. L., Templeton, D. H., Zalkin, A.; *Inorg. Chem.*; **1978**, 17, 3699-3701. (c) Bowman, K., Dori, Z.; *J. Chem. Soc., Chem. Commun.*; **1968**, 636. (d) Graziani, R., Zarli, B., Cassol, A., Bombieri, G., Forsellini, E., Tondello, E.; *Inorg. Chem.*; **1970**, 9, 2116-2124. (e) Bagnall, K. W., Holah, D. G.; *Nature (London)* ; **1967**, 215, 623. (f) Bagnall, K. W., Brown, D., Holah, D. G.; *J. Chem. Soc. A* ; **1968**, 1149-1153. (g) Bibler, J. P., Karraker, D. G.; *Inorg. Chem.*; **1968**, 7, 982-985. (h) Bombieri, G., Croatto, U., Forsellini, E., Zarli, B., Graziani, R.; *J. Chem. Soc. Dalton Trans.*; **1972**, 560-564. (i) Ryan, R. R., Smith, B. F., Ritchey, J. M.; *Inorg. Chim. Acta* ; **1987**, 129, 139-148.

30) Perry, D., Zalkin, A., Ruben, H., Templeton, D. H.; *Inorg. Chem.*; **1982**, 21, 237-240.

31) Many solid state ternary uranium chalcogenides have been discovered over the last twenty years, and most commonly occurring are those of the types MUQ_3[9a-c], MU_8Q_{17}[9b-e], and MU_2Q_5[9f] (where M=transition metal, or, in the case of MU_2Q_5, an alkali-earth, and Q=S,Se). All have been made with traditional high temperature (800-1100 °C) synthetic methods, resulting in compounds with extended solid state structures and monochalcogenides. (a) Noel, H., Padiou, J., Prigent, J.; *C.R. Seances Acad. Sc. Ser. C* ; **1975**, 280, 123-126. (b) Noel, H.; *C.R. Seances Acad. Sc. Ser. C* ; **1973**, 277, 463-464. (c) Noel, H.; *C.R. Seances Acad. Sc. Ser. C* ; **1974**, 279, 513-515. (d) Vovan, T., Rodier, N.; *C.R. Seances Acad. Sc. Ser. C* ; **1979**, 289, 17-20. (e) Noel, H., Potel, M., Padiou, J.; *Acta Cryst.*; **1975**, B31, 2634-2637. (f) Brochu, R., Padiou, J., Prigent, J.; *C.R. Seances Acad. Sc. Ser. C* ; **1972**, 274, 959-961. (g) Noel, H., Daoudi, J.; *J. Solid State Chem.* ; **1985**, 60, 131-134. (h) Noel, H.; *J. Less Com. Met.* ; **1980**, 72, 45-49.

32) Figgis, B. N. in "*Introduction to Ligand Fields*", Interscience Publishers John Wiley and Sons, 1966

33) Noel, H., Troc, R.; *J. Solid State Chem.* ; **1979**, 27, 123-135.

34) Poix, P., *C. R. Acad. Sci. Paris Sec. C*, **1970**, 270, 1852-1853.

35) Hulliger,F., *Structure and Bonding* ; **1968**, 4, 83-229.

36) Selte, K., Kjekshus, A., *Acta Chem. Scanda.*; **1964**, 18, 690-696.

37) a) Lueken, H., Bruggemann, W., Bronger, W., Fleischhauer, J., *J. Less-Common Met.*; **1979**, 65, 79-88. b) Duczmal, M., Pawlak, L., *J. Magn. Magn. Mater.*; **1988**, 76-77, 195-196.

38) Greenwood, N. N., Earnshaw, A., *Chemistry of the Elements*; Pergamon Press, **1984**, p.1443.

39) Casey, A. T., Mitra, S., in *Theory and Applications of Molecular Paramagnetism* (Eds.:Boudreaux, E. A., Mulay, L. M.), John Wiley and Sons, New York, **1976**, p.306.

40) (a) Marsh, R. E., Herbstein, F. H., *Acta Crystollagr.* ; **1983**, *39B*, 280-287. (b) Yanagisawa, Y., Kanamaru, F., Kume, S., *Acta Crystallogr.* ; **1979**, *35B*, 137-139.

MICHIGAN STATE UNIVERSITY LIBRARIES
3 1293 01016 4550

pt. 2

LIBRARY
Michigan State
University

PLACE IN RETURN BOX to remove this checkout from your record.
TO AVOID FINES return on or before date due.

DATE DUE	DATE DUE	DATE DUE

MSU Is An Affirmative Action/Equal Opportunity Institution
c:\circ\datedue.pm3-p.1

New
Reac

Chapter 3

New Quaternary Compounds Resulting from the Reaction of Copper and f-block Metals in Molten Polychalcogenide Salts at Intermediate Temperatures

A.

which
chalco
these
structu
and no
elemen
lanthan
compou
chemist
two me
structur
new pha
In
are of p
propertie
transitio
bonding
supercon
mixtures
$La_{2-x}(C$
an induc
changes
temperat
material,

A. Introduction

The reactions of lanthanides in A_2Q_x fluxes have led to new phases which repeat several structural themes seen in known binary and ternary chalcogenides. The next question to be asked is how can the reaction of these metals be modified in order to access phases which are less structurally related to known compounds and so more likely to feature new and novel characteristics. The simplest approach is to react another element, such as a transition metal, in the A_2Q_x flux along with the lanthanide or actinide with an eye towards forming new quaternary compounds. The extra element would be chosen such that its coordination chemistry is very different from that of the f-block metal. Thus, when the two metals come together in a new compound, the interplay of dissimilar structural and coordination requirements should help to insure that any new phases would be clear departures from what has been seen before.

Investigations into quaternary systems with lanthanides and actinides are of particular interest because of the intriguing structural and physical properties which have been known to result from the interplay of covalent transition metal bonding and the more ionic lanthanide and actinide bonding. For example, the current state of the art in high Tc copper oxide superconductors is dominated by compounds containing heterometallic mixtures of highly electropositive cations (i.e. $Tl_2Ba_2Ca_2Cu_3O_{10}$ [1] and $La_{2-x}(Ca, Sr, Ba)_xCuO_4$ [2]). It has been speculated that these cations have an inductive effect on the anionic Cu-O framework resulting in subtle changes in the covalency of those bonds which in turn impacts the critical temperature.[3] In the complicated cooperative environment of a solid state material, there are many effects in which the cations may participate. A

better u
wider i
cations
searchi
chalcog

N
reaction
the poi
then us
approac
element
was syn
readily
ligand i
Cs; M=
selenop
and P_2(
differen
$(P_2S_7)^4$
in KM
compo
(SnS_4)
Examp
Rb_2Cu
was p
temper

better understanding of the interplay of these effects could be achieved if a wider base of compounds containing mixtures of highly electropositive cations were available for study. As such we have been interested in searching for such compounds in quaternary systems containing the chalcogenide elements.

Many examples already exist of quaternary compounds isolated from reactions in molten A_2Q_x fluxes. Some systems have even been refined to the point where certain species can be formed reproducibly *in situ* and then used as ligands to the remaining metal cations in the flux. This approach has worked well in several quaternary systems where the fourth element is a non-metal. The anion $(TeS_3)^{2-}$, isoelectronic with $(SO_3)^{2-}$, was synthesized for the first time from a molten salt reaction.[4] It forms readily from sulfur rich fluxes and has been used as a multifunctional ligand in such compounds as $Cs_2Cu_2(TeS_3)_2(S_6)_2$ [4], $AMTeS_3$ (A=K, Rb, Cs; M=Ag, Cu) [5], and $A_2Mn(TeS_3)_2$ [6]. Several thiophosphonate and selenophosphonate species have been isolated from the reaction of a metal and P_2Q_5 in excess A_2Q_x flux. Depending on reaction conditions, several different species can be stabilized. Observed ligands to date have been $(P_2S_7)^{4-}$ in $ABiP_2S_7$ (A=K, Rb) [7], $(PS_4)^{3-}$ in $K_3Bi(PS_4)_2$ [8], and $(P_2Se_6)^{4-}$ in KMP_2Se_6 (M=Bi, Sb) [9]. Mixed metal reactions with Sn as one of the components have led to the characterization of phases in which either $(SnS_4)^{4-}$ or $(Sn_2S_6)^{4-}$ act as thiometallate ligands to the second metal. Examples of such compounds include $ACuSnQ_3$ (A=K, Rb; Q=S, Se), $Rb_2Cu_2SnS_4$, $K_2Au_2SnS_4$, and $K_2Au_2Sn_2S_6$ [10]. All of the above chemistry was performed via reactions of A_2Q_x fluxes in the intermediate temperature regime as defined in this thesis (250-600 °C). A substantial

b
m
sy
rea
inc
(M
AC

bloc
inves
at pro
Sn. N
produ
here is
materia
other p
solubili
solubiliz
species a
other rea
known to
for easy
with the
phase sep
Ag conta

body of work also exists where quaternary phases have been isolated from molten A_2Q_x reactions run at the high temperatures of classical solid state synthesis (>600 °C). The bulk of this work has involved mixed metal reactions between Cu and early transition metal elements, and examples include $K_2CuNbSe_4$ [11], KCu_2MSe_4 (M=Nb [12], Ta [13]), $K_3Cu_3M_2Q_8$ (M=Nb, Ta; Q=S, Se) [14], $K_3CuNb_2Se_{12}$ [11], and several members of the $ACuMQ_3$ family [15,16].

In attempting to develop similar quaternary chemistry with the f-block elements as components, several heterometallic systems were investigated. Of these systems only the reactions using Cu were successful at providing new quaternary phases. Every other metal tried (Ag, Hg, Au, Sn, Ni, Pt, and Fe) invariably resulted in inhomogeneous mixtures of products in which the metals occurred in separate phases. The limitation here is likely to be diffusion related; in quaternary reactions, the starting materials, once solubilized, must migrate through the flux to find each other prior to nucleating effects. If this migration is limited, then solubilized metals will find their own kind close to their own point of solubilization well before encountering other metals. Whatever soluble Cu species are present in the flux appear to have adequate mobility to reach the other reacting metal. Based on this argument, one would think Ag, also known to have a high ionic mobility, would make another likely candidate for easy incorporation into quaternaries. This is not the case in reactions with the f-block elements in intermediate temperature fluxes, however, and phase separation still dominates. Clearly other factors are at work in the Ag containing systems (i.e.. differing rates of solubilization between the

two
pha

Cu a
chem
unco

B.

metal
Matthey
WI; lan
mesh, A
Phillipst
Paris, KY
cesium
dimethyl
Gibbstow
Mallinckr
Pot
performed
Pot
from that

two metal species), or perhaps Ag^+ is too mobile, making any potential phase extremely kinetically sensitive.

Despite the lack of general success with other metals, the reaction of Cu and f-block metals in molten A_2Q_x fluxes has resulted in ample new chemistry in these systems with indications that even more is waiting to be uncovered.

B. Experimental

1. Synthesis

Reagents -- The following reagents were used as obtained: copper metal _ mesh, Fisher Scientific Co., ; cerium, 40 mesh, Johnson M. Matthey Co., Ward Hill, MA; uranium metal, 60 mesh, Cerac, Milwaukee, WI; lanthanum, 40 mesh, Cerac, Milwaukee, WI; selenium powder, 100 mesh, Aldrich, Milwaukee, WI; sulfur powder, sublimed, JT Baker Co., Phillipsburg, NJ; potassium metal, analytical reagent, Mallinckrodt Inc., Paris, KY; sodium metal, analytical reagent, Mallinckrodt Inc., Paris, KY; cesium metal, Johnson M. Matthey Co., Ward Hill, MA; dimethylformamide (DMF), analytical reagent grade, EM Science, Inc., Gibbstown, NJ; methanol, anhydrous, analytical reagent grade, Mallinckrodt Inc., Paris, KY.

Potassium Selenide, K_2Se -- Synthesis of this material was performed as described in Chapter 2, Sec. B.1.

Potassium Sulfide, K_2S -- The following procedure was modified from that given in the literature [17]. 7.094 g (182 mmol) K is sliced in an

N2 fil
round
bath a
atmosp
stirred
evapora
N2 (ap
evapora
resultin
taken in
stored.

C
mmol) c
of the n
adapter
connecte
flask is c
100 ml c
a dark bl
N2 flow
by 1.217
of the re
product
glove box

Po
mmol) K
g (4.0 mr

N_2 filled glove box and combined with 2.908 (91 mmol) S into a 250 ml round bottom flask. The flask is chilled to -78 °C using a dry ice/acetone bath and approximately 100 ml of NH_3 was condensed, under an N_2 atmosphere, onto the reagents, giving a dark blue solution. The solution is stirred via magnetic stir bar while the liquid NH_3 is allowed to slowly evaporate off as the reaction warmed to room temperature under a flow of N_2 (approx. 8 hr.). A second portion of NH_3 is usually added and the evaporation repeated to insure complete reaction of the reagents. The resulting yellow product is evacuated on a Schlenk line overnight and then taken into an N_2 filled glove box where it is ground to a fine powder and stored.

Cesium Sulfide, Cs_2S -- In an N_2 filled glove box, 10.089 g (75.9 mmol) of Cs is weighed into a 250 ml three-neck round bottom flask. Two of the necks are stoppered, and the remaining one is connected to a glass adapter with a stopcock joint. The apparatus is removed from the box and connected to a cold finger condenser adapted to allow for N_2 flow. The flask is chilled to -78 °C using a dry ice/acetone bath and approximately 100 ml of NH_3 is condensed, under an N_2 atmosphere, onto the Cs, giving a dark blue solution. One of the flask stoppers is gently removed and, with N_2 flow maintained, a magnetic stir bar is added to the solution, followed by 1.217 g (38.0 mmol) of S once the solution is stirring. The remainder of the reaction proceeds as described above, resulting in a pale yellow product which was ground to a fine powder and stored in an N_2 filled glove box.

Potassium copper dicerium hexasulfide, $KCuCe_2S_6$ -- 0.110 g (1.0 mmol) K_2S, 0.016 g (0.25 mmol) Cu, 0.070 g (0.50 mmol) Ce, and 0.128 g (4.0 mmol) S are weighed into a vial in an N_2 filled glove box. The

st
Th
co
hel
foll
awa
N2
Poly
conc
conc
additi
mater
based
compa
calcula
product
extende
Th
temperat
°C, yello
KCuCe
doubling
and runni
this proc
the single

starting materials are mixed thoroughly and loaded into a pyrex tube. The tube is then evacuated to <3 x 10-3 mbar and flame-sealed. In a computer controlled furnace, the reaction is heated to 270 °C over 12 hr, held at that temperature for 6 days and cooled to 120 °C at 3 °C/hr followed by quenching to 50 °C. The product is isolated by dissolving away residual K_2S_x flux with successive washing of degassed DMF under N_2 flow, in order to prevent oxidation of polysulfide to sulfur. Polysulfides dissolved in DMF give a dark blue-green solution when concentrated, and the isolation was continued by carefully decanting the concentrated DMF and replacing it with a fresh portion until such an addition remained clear, signaling complete K_2S_x removal. The remaining material was red microcrystalline needles of $KCuCe_2S_6$; a yield of 68%, based on Ce, is typical. Purity of the material was confirmed by comparing the X-ray powder diffraction pattern of the product with one calculated using data from the single crystal study (Table 3.1). The product is insoluble in water, methanol, and DMF, and is stable in air for extended periods.

The above reaction was found to yield good quality product over a temperature range from 260-350 °C. At temperatures greater than 350 °C, yellow powder of CeS_2 begins to contaminate the product. Typically, $KCuCe_2S_6$ is microcrystalline, but single crystals were obtained by doubling the amounts of K_2S and S, hence doubling the amount of flux, and running the reaction at 350 °C for 5 d., cooling at 2 °C/hr. However, this procedure also results in a small amount of CeS_2 powder mixed with the single crystals of $KCuCe_2S_6$.

Tab

Table 3.1 Calculated and Observed X-ray Powder Diffraction Pattern for $KCuCe_2S_6$ (Cu radiation)

h k l	d_{calc}/(Å)	d_{obs}/(Å)	I/I_{max} obs (%)
0 2 0	10.58	10.84	100.00
1 1 0	6.31	6.40	2.55
0 2 1	5.61	5.69	1.97
0 4 0	5.29	5.36	9.17
1 3 -1	4.316	4.363	22.30
0 4 1	4.130	4.178	1.35
1 3 1	3.581	3.611	5.70
0 6 0	3.526	3.560	11.64
1 5 -1	3.344	3.375	2.18
0 0 2	3.307	3.331	4.49
2 0 0	3.306		
0 2 2	3.156	3.180	9.02
2 2 0	3.156	3.143	4.176
1 5 1	2.965	2.989	22.91
0 4 2	2.804	2.824	3.38
2 4 0	2.803		
2 0 -2	2.728	2.744	6.44
0 8 0	2.644	2.661	12.76
2 2 -2	2.642		

Table 3.1 Calculated and Observed X-ray Powder Diffraction Pattern for $KCuCe_2S_6$ (Cu radiation) (cont.)

h k l	d_{calc}/(Å)	d_{obs}/(Å)	I/I_{max} obs (%)
0 6 2	2.412	2.427	14.57
2 6 0	2.412		
1 1 -3	2.268	2.279	4.51
3 1 -1	2.268		
1 3 -3	2.170	2.184	3.29
3 3 -1	2.170		
2 6 -2	2.159	2.169	12.78
2 6 1	2.136	2.128	3.82
0 10 0	2.115		
2 0 2	2.078	2.090	4.88
0 8 2	2.065	2.077	11.18
2 8 0	2.065		
2 2 2	2.039	2.049	1.84
1 5 -3	2.008	2.018	2.46
3 5 -1	2.008		
1 9 -2	1.9208	1.9207	2.55
2 8 -2	1.8988	1.9079	3.48
1 3 3	1.8725	1.8812	2.21
3 3 1	1.8723		

Table

1
1
3
1
2
0
3
2
4
0
4
2
4
2
0
4
2
4
1 1
0 1
2 1

Table 3.1 Calculated and Observed X-ray Powder Diffraction Pattern for $KCuCe_2S_6$ (Cu radiation) (cont.)

h k l	d_{calc}/(Å)	d_{obs}/(Å)	I/I_{max} obs (%)
0 6 3	1.8692		
1 11 0	1.8466	1.8565	4.57
1 7 -3	1.8206		
3 7 -1	1.8205	1.8227	4.79
1 11 -1	1.8138		
2 6 2	1.7903		
0 12 0	1.7628	1.7711	3.68
3 5 -3	1.6711	1.6732	2.05
2 0 -4	1.6665	1.6664	0.94
4 0 -2	1.6663		
0 0 4	1.6533	1.6584	1.58
4 0 0	1.6531		
2 2 -4	1.6462	1.6414	2.97
4 2 -2	1.6460		
2 8 2	1.6339		
0 2 4	1.6335	1.6356	2.03
4 2 0	1.6333		
2 4 -4	1.5894	1.5921	1.95
4 4 -2	1.5893		
1 13 -1	1.5594	1.5666	2.81
0 12 2	1.5556		
2 12 0	1.5555		

(1.0 r

0.128

The re

isolati

to KC

produc

89%. b

in wate

Potassium copper dilanthanum hexasulfide, $KCuLa_2S_6$ -- 0.110 g (1.0 mmol) K_2S, 0.016 g (0.25 mmol) Cu, 0.069 g (0.50 mmol) Ce, and 0.128 g (4.0 mmol) S are weighed into a vial in an N_2 filled glove box. The rest of the synthesis proceeds as described above for $KCuCe_2S_6$. After isolation, a yellow powder remained which was confirmed as isostructural to $KCuCe_2S_6$ by comparison of the powder X-ray diffraction pattern of the product to that of the structurally known analog (Table 3.2). A yield of 89%, based on La, is typical. Like the Ce analog, the product is insoluble in water, methanol, and DMF, and is stable in air for extended periods.

Table 3.2 Calculated X-ray Powder Diffraction Pattern for $KCuCe_2S_6$ and Observed X-ray Powder Diffraction Pattern for $KCuLa_2S_6$ (Cu radiation)

h k l	d_{calc}/(Å)	d_{obs}/(Å)	I/I_{max} obs (%)
0 2 0	10.58	10.69	100.00
0 4 0	5.29	5.34	18.30
1 3 -1	4.316	4.348	22.76
1 3 1	3.581	3.618	5.36
0 6 0	3.528	3.553	19.16
0 0 2	3.307	3.337	16.94
2 0 0	3.306		
0 2 2	3.1561	3.185	9.28
2 2 0	3.1556		
1 5 1	2.9649	2.994	23.35
0 4 2	2.8037	2.828	5.40
2 4 0	2.8034		
2 0 -2	2.7285	2.746	8.67
0 8 0	2.6442	2.664	18.78
2 2 -2	2.6420		
0 6 2	2.4119	2.433	16.47
2 6 0	2.4117		
1 1 -3	2.6779	2.286	6.87
3 1 -1	2.2676		

Table

1
3
2
0
3
2
1
3
0 1
2
4
0
4
2
4

Table 3.2 Calculated X-ray Powder Diffraction Pattern for $KCuCe_2S_6$ and Observed X-ray Powder Diffraction Pattern for $KCuLa_2S_6$ (Cu radiation) (cont.)

h k l	d_{calc}/(Å)	d_{obs}/(Å)	I/I_{max} obs (%)
1 3 -3	2.1703	2.1885	5.56
3 3 -1	2.1700		
2 6 -2	2.1578	2.1740	15.60
0 10 0	2.1154	2.1339	8.21
3 3 0	2.1038	2.1021	9.79
2 0 2	2.0782	2.0822	13.88
1 7 -3	1.8206	1.8284	5.43
3 7 -1	1.8205		
0 12 0	1.7628	1.7765	3.14
2 0 -4	1.6665	1.6786	4.53
4 0 -2	1.6663		
0 2 4	1.6335	1.6499	3.95
4 2 0	1.6333		
2 4 -4	1.5894	1.5736	3.71
4 4 -2	1.5893		

mmol
g (2.5
reager
x 10-3
hr. he
follow
manne
The id
ray po
data fr
attainab
stable i
S
studies
(0.125 r
reagents
followe
isolation
were ma
which w

Cesium copper dicerium hexasulfide, $CsCuCe_2S_6$ -- 0.149 g (0.50 mmol) Cs_2S, 0.016 g (0.25 mmol) Cu, 0.070 g (0.50 mmol) Ce, and 0.080 g (2.5 mmol) S are weighed into a vial in an N_2 filled glove box. The reagents are loaded into a pyrex tube, and the tube is then evacuated to $<3 \times 10^{-3}$ mbar and flame-sealed. The reaction is heated to 400 ^{o}C over 12 hr, held at that temperature for 3 days and cooled to 200 ^{o}C at 4 ^{o}C/hr followed by quenching to 50 ^{o}C. After removal of the excess flux (in the manner described above), a red/brown microcrystalline powder remained. The identity and purity of the material was confirmed by comparing the X-ray powder diffraction pattern of the product with one calculated using data from the single crystal study (Table 3.4). An average yield of 80% is attainable. The product is insoluble in water, methanol, and DMF, and is stable in air for extended periods.

Single crystals of a size and quality sufficient for X-ray diffraction studies were grown from a reaction of 0.335 g (1.12 mmol) Cs_2S, 0.008 g (0.125 mmol) Cu, 0.035 g (0.25 mmol Ce) and 0.128 g (4.0 mmol) S. The reagents were loaded into tubes as above and heated at 450 °C for 2 d. followed by cooling to 200 °C at 4 °C/ hr. and quenching to 50 °C. After isolation with degassed DMF, a handful of large red needles of $CsCuCe_2S_6$ were manually removed from the bulk of the yellow powdery product, which was CeS_2 by powder X-ray diffraction.

Table

h
0
0
1
1
0
1
0
1
0
1
2
2
1
2
2
1
0
2
1

Table 3.3 Calculated and Observed X-ray Powder diffraction Pattern for $CsCuCe_2S_6$ (Cu radiation)

h k l	d_{calc}/(Å)	d_{obs}/(Å)	I/I_{max} obs (%)
0 2 0	11.22	11.08	100.00
0 4 0	5.61	5.56	3.64
1 1 0	5.34	5.32	3.06
1 3 0	4.432	4.405	31.53
0 6 0	3.742	3.722	73.05
1 2 1	3.202	3.188	13.54
0 5 1	3.069	3.054	27.83
1 4 1	2.870	2.857	4.44
0 8 0	2.806	2.793	4.75
1 7 0	2.770	2.758	7.95
2 0 0	2.750	2.737	7.27
2 2 0	2.671	2.659	3.83
1 6 1	2.492	2.481	5.53
2 4 0	2.470	2.459	3.52
2 1 1	2.290	2.280	4.83
1 9 0	2.272	2.263	10.47
0 10 0	2.245	2.236	44.83
2 6 0	2.216	2.207	11.47
1 8 1	2.149	2.141	23.51

Table 3.3 Calculated and Observed X-ray Powder diffraction Pattern for $CsCuCe_2S_6$ (Cu radiation) (cont.)

h k l	d_{calc}/(Å)	d_{obs}/(Å)	I/I_{max} obs (%)
0 0 2	2.102	2.097	4.32
2 5 1	2.048	2.040	5.44
2 8 0	1.9641	1.9573	3.09
1 11 0	1.9133	1.9061	4.30
1 3 2	1.8996	1.8936	3.46
0 12 0	1.8707	1.8655	6.39
0 6 2	1.8329		
2 9 1	1.6915		
2 0 2	1.6703		
3 2 1	1.6620		
1 13 0	1.6475	1.6434	13.02
3 4 1	1.6099	1.5987	3.95

(1.0 r

0.316

The re

<3 x

12 hr.

follow

manne

identi

powde

from th

Ce. Th

air for

T

so unsu

crystals

describe

°C/hr t

modifica

enough

contami

diffracti

Potassium copper dicerium hexaselenide, $KCuCe_2Se_6$ -- 0.157 g (1.0 mmol) K_2Se, 0.032 g (0.50 mmol) Cu, 0.070 g (0.50 mmol) Ce, and 0.316 g (4.0 mmol) Se are weighed into a vial in an N_2 filled glove box. The reagents are loaded into a pyrex tube, and the tube is then evacuated to <3 x 10-3 mbar and flame-sealed. The reaction is heated to 400 ^oC over 12 hr, held at that temperature for 2 days and cooled to 200 ^oC at 4 ^oC/hr followed by quenching to 50 ^oC. After removal of the excess flux (in the manner described above), a black microcrystalline powder remains. The identity and purity of the material were confirmed by comparing the X-ray powder diffraction pattern of the product with one calculated using data from the single crystal study (Table 3.4). A typical yield is 39%, based on Ce. The product is insoluble in water, methanol, and DMF, and is stable in air for extended periods.

The product of the above reaction is a microcrystalline powder and so unsuitable of single crystal X-ray diffraction studies. In order to grow crystals of the needed size, a reaction was run using half the amounts of the described reagents and with two days of heating at 450 °C (cooling at 4 °C/hr to 250 °C followed by quenching to 50 °C). Although these modifications produced black, plank-shaped crystals of $KCuCe_2Se_6$ large enough for single crystal study, the bulk product was not pure, being contaminated by some unknown species as evidenced by powder X-ray diffraction.

Table 3.4 Calculated and Observed X-ray Powder diffraction Pattern for $KCuCe_2Se_6$ (Cu radiation)

h k l	d_{calc}/(Å)	d_{obs}/(Å)	I/I_{max} obs (%)
0 2 0	11.12	11.01	100.00
0 4 0	5.56	5.54	20.33
1 3 0	4.516	4.506	3.23
0 6 0	3.706	3.693	1.37
1 2 1	3.278	3.237	1.20
0 5 1	3.090	3.086	1.41
1 4 1	2.919	2.936	7.58
2 0 0	2.848	2.828	2.63
0 8 0	2.780	2.774	7.82
2 2 0	2.758	2.750	1.90
2 4 0	2.534	2.531	1.54
1 6 1	2.517	2.513	2.41
2 1 1	2.360	2.368	2.32
2 3 1	2.260	2.267	1.27
2 6 0	2.258	2.256	3.01
0 10 0	2.224	2.221	14.19
1 8 1	2.160	2.157	2.27
0 0 2	2.148		
0 4 2	2.004	2.000	2.65

Table 3.4 Calculated and Observed X-ray Powder diffraction Pattern for $KCuCe_2Se_6$ (Cu radiation) (cont.)

h k l	d_{calc}/(Å)	d_{obs}/(Å)	I/I_{max} obs (%)
2 8 0	1.9890	1.9865	0.66
1 11 0	1.9050	1.9025	2.29
2 7 1	1.9014		
0 12 0	1.8530	1.8518	5.15
3 0 1	1.7364		
2 0 2	1.7151	1.7199	1.29
2 9 1	1.7117	1.7120	0.59
3 4 1	1.6575	1.6551	2.00
2 4 2	1.6388	1.6388	1.59
1 12 1	1.6303	1.6292	0.70
0 14 0	1.5883	1.5879	1.34
2 6 2	1 5565	1.5557	0.57

Dipotassium dicopper cerium tetrasulfide, $K_2Cu_2CeS_4$ -- Pure phase of $K_2Cu_2CeS_4$ is obtained by the reaction of 0.231 g (2.09 mmol) K_2S, 0.016 g (0.25 mmol) Cu, 0.018 g (0.125 mmol) Ce, and 0.128 g (4.0 mmol) S. The reagents are loaded into pyrex tubes and evacuated in the manner described above. The reaction is heated to 260 ^oC over 12 hr, held at that temperature for 5 days, and cooled to 210 ^oC at 2 ^oC/hr followed by quenching to room temperature. The excess flux is removed by washing with one portion of degassed distilled water (left in contact with the sample for <15 min.) and several portions of degassed DMF in the manner described previously. The remaining material is black microneedles. Purity is confirmed by comparing the X-ray powder diffraction pattern of the product to one calculated from single crystal X-ray data (Table 3.5), and typically, a small amount of CeO_2 (1-5%) was seen as an impurity. Taking this into account, an approximate yield of 70%, based on Cu was estimated. The product is insoluble in methanol and DMF, and appears stable in dry air for extended periods. Although stable in distilled water for a short time (<12 hr), prolonged exposure causes decomposition to CeO_2 and presumably soluble Cu containing species.

As with several other compounds already described, the purity of $K_2Cu_2CeS_4$ is very dependent on reaction temperature. Here, any temperature above 260 ^oC will result in impurities of KCu_4S_3 and some as yet unknown phase. Black, brick-shaped single crystals of $K_2Cu_2CeS_4$, suitable for X-ray diffraction studies, were obtained by increasing the amount of K_2S to 0.248 g (2.25 mmol) and increasing the reaction temperature to 420 ^oC for 5 d. (cooling at 2 ^oC/hr) but were accompanied by the above mentioned impurities.

Table

h
0
2
1
2
4
0
1
4
3
1
4
3
3
6
0
4
5
6
6
3
3

Table 3.5 Calculated and Observed X-ray Powder Diffraction Pattern for $K_2Cu_2CeS_4$ (Cu radiation)

h k l	d_{calc}/(Å)	d_{obs}/(Å)	I/I_{max} obs (%)
0 0 1	7.05	7.02	100.00
2 0 1	4.212	4.201	2.46
1 1 0	3.800	3.797	1.73
2 0 -2	3.677	3.671	2.58
4 0 -1	3.541		
0 0 2	3.527	3.520	21.59
1 1 -1	3.487		
4 0 0	3.369	3.366	2.30
3 1 -1	2.988	2.989	6.76
1 1 -2	2.718	2.719	8.24
4 0 1	2.705	2.704	8.76
3 1 -2	2.574	2.575	6.01
3 1 1	2.542	2.541	7.05
6 0 -1	2.386	2.386	3.01
0 0 3	2.351	2.352	2.20
4 0 -3	2.334	2.335	3.06
5 1 -1	2.319	2.322	1.98
6 0 -2	2.275	2.275	2.06
6 0 0	2.246	2.246	4.59
3 1 -3	2.085	2.085	3.66
3 1 2	2.057	2.056	3.43

Table

Table 3.5 Calculated and Observed X-ray Powder Diffraction Pattern for $K_2Cu_2CeS_4$ (Cu radiation)

h k l	d_{calc}/(Å)	d_{obs}/(Å)	I/I_{max} obs (%)
2 0 3	2.018	2.018	2.09
6 0 -3	1.9960	1.9964	2.20
0 2 0	1.9805	1.9825	3.28
6 0 1	1.9573	1.9592	1.78
		1.9535	1.64
0 2 1	1.9068	1.9079	2.74
2 2 0	1.9001	1.9007	1.51
2 0 -4	1.8678	1.8681	1.80
4 0 -4	1.8387	1.8401	2.26
7 1 -2	1.7837	1.7851	2.09
8 0 -1	1.7801		
0 0 4	1.7635	1.7635	2.85
7 1 0	1.7315		
4 2 -1	1.7286	1.7285	1.66
0 2 2	1.7269		
3 1 -4	1.6917	1.6937	1.76
3 1 3	1.6708	1.6725	3.85
6 0 2	1.6574	1.6584	1.96
7 1 -3	1.6553	1.6579	1.33
4 2 1	1.5980	1.5994	1.43

CsCuC

g (0.25

The re

and fla

temper

hr. Th

distille

portion

remain

compar

calculat

amount

an appr

insolubl

periods

prolong

oxophili

A

ray diffr

CsCuCe

be repe

mmol) (

prepared

their pyr

amounts

areas of

Cesium copper cerium trisulfide, $CsCuCeS_3$ -- Single phase of $CsCuCeS_3$ is obtained by the reaction of 0.148 g (0.50 mmol) Cs_2S, 0.016 g (0.25 mmol) Cu, 0.035 g (0.25 mmol) Ce, and 0.040 g (1.25 mmol) S. The reagents are loaded into pyrex tubes and evacuated to $<3x10^{-3}$ mbar and flame-sealed. The reaction is heated to 400 °C over 12 hr, held at that temperature for 4 days, and cooled to 200 °C in 50 hr. and to 50 °C in 1 hr. The excess flux is removed by washing with one portion of degassed distilled water (left in contact with the sample for <15 min.) and several portions of degassed DMF in the manner described previously. The remaining material is black microneedles. Purity is confirmed by comparing the X-ray powder diffraction pattern of the product to one calculated from single crystal X-ray data (Table 3.6), and typically, a small amount of CeO_2 (1-5%) is seen as an impurity. Taking this into account, an approximate yield of 70%, based on Cu is estimated. The product is insoluble in methanol and DMF, and appears stable in dry air for extended periods. Although stable in distilled water for a short time (<12 hr), prolonged exposure is likely to decompose the phase due to the high oxophilicity of Ce^{3+}.

As is common in this chemistry, large single crystals suitable for X-ray diffraction studies were prepared via a separate method. In the case of $CsCuCeS_3$, a large amount of luck came into play, as the reaction has yet to be repeated. A mixture of 0.298 g (1.0 mmol) Cs_2S, 0.008 g (0.126 mmol) Cu, 0.018 g (0.128 mmol) Ce and 0.064 g (2.0 mmol) S was prepared as previously described except that while sealing the reactants in their pyrex tube, an exothermic reaction occurred which splattered various amounts of the contents throughout the length of the tube. When cooled, areas of semi-glassy globules of reagent had formed. The origin of the

exoth
unrea
mish
over
the f
inhor
were
used
diffic
exact
to the

exothermic reaction probably lies in there being a very small amount of unreacted Cs metal somewhere in the Cs_2S starting material. Despite the mishap, the reaction was heated at 390 °C for 5 days and cooled to 110 °C over 20 hr., followed by further cooling to 50 °C over 1 hr. Removal of the flux with 3 portions of degassed distilled water resulted in a very inhomogenous product of which some large, black, plank-shaped crystals were one of the major components. These were the crystals subsequently used in the single crystal X-ray determination of $CsCuCeS_3$. Clearly the difficulty in repeating this reaction is in approximating (i.e., guessing) the exact composition of whichever portion of the splattered reactants gave rise to these crystals.

Table

Table 3.6 Calculated and Observed X-ray Powder diffraction Pattern for $CsCuCeS_3$ (Cu radiation)

h k l	d_{calc}/(Å)	d_{obs}/(Å)	I/I_{max} obs (%)
0 2 0	7.58	7.58	72.91
0 2 2	4.274	4.267	43.54
0 4 2	3.788	3.786	100.00
1 1 1	3.641	3.632	18.95
0 4 1	3.558	3.547	7.80
1 3 0	3.147	3.143	24.16
1 1 2	3.109	3.104	34.89
0 4 2	3.057	3.059	12.57
1 3 1	3.011	3.008	53.76
1 3 2	2.689	2.685	26.83
0 0 4	2.588	2.582	32.87
0 2 4	2.449	2.446	9.84
1 5 0	2.421	2.418	10.39
1 3 3	2.326	2.322	12.58
0 6 2	2.270	2.271	25.21
1 5 2	2.193	2.192	29.74
1 1 4	2.155	2.151	8.46
0 4 4	2.137	2.134	19.81
2 0 0	2.012	2.008	21.17

Table

Table 3.6 Calculated and Observed X-ray Powder diffraction Pattern for $CsCuCeS_3$ (Cu radiation) (cont.)

h k l	d_{calc}/(Å)	d_{obs}/(Å)	I/I_{max} obs (%)
1 3 4	1.9991	1.9954	7.28
1 7 0	1.9065	1.9097	7.45
0 8 0	1.8943	1.8953	17.67
1 7 1	1.8749	1.8768	13.00
0 8 1	1.8633	1.8655	8.25
2 2 2	1.8204	1.8186	13.98
2 4 0	1.7770	1.7742	7.26
1 3 5	1.7298	1.7271	12.18
0 2 6	1.6824	1.6779	6.71
2 4 2	1.6807		
1 7 3	1.6688	1.6678	9.49
2 0 4	1.5885	1.5879	11.00
1 1 6	1.5772	1.5754	8.05

Potassium copper uranium triselenide, $KCuUSe_3$ -- Single phase of $KCuUSe_3$ is obtained by the reaction of 0.078 g (0.50 mmol) K_2Se, 0.032 g (0.50 mmol) Cu, 0.120 g (0.50 mmol) U, and 0.237 g (3.0 mmol) Se. The reagents are loaded into pyrex tubes and evacuated to $<3x10^{-3}$ mbar and flame-sealed. The reaction is heated to 400 °C over 12 hr, held at that temperature for 2 days, and cooled to 200 °C in 50 hr. and to 50 °C in 1 hr. The excess flux is removed by washing with several portions of degassed DMF in the manner described previously. The remaining material is black needles. Purity is confirmed by comparing the X-ray powder diffraction pattern of the product to one calculated from single crystal X-ray data (Table 3.7), and typically, a small amount of USeO (<3%) is seen as an impurity. Even with this impurity, the yield of KCuUSe3 is still nearly quantitative (90-95 %). The product is insoluble in water, methanol and DMF, and appears stable in air for extended periods. Presumably, however, the compound is likely to decompose upon prolonged exposure to both air and water due to the highly oxophilic nature of the U^{4+}.

$KCuUSe_3$ is a particularly hearty phase. Whereas the other compounds described in this chapter have limited windows of temperature and flux composition for their formation, $KCuUSe_3$ is isolated from reactions run from 300 to 450 °C and with a metal to selenium ratio as high as 1/24. All of these other conditions produce varying amounts of elemental Se as a major contaminant, but no evidence of phase separation of the metal reactants into binary or ternary compounds was observed. This points to a particularly high thermodynamic stability for $KCuUSe_3$.

Tabl

Table 3.7 Calculated and Observed X-ray Powder diffraction Pattern for $KCuUSe_3$ (Cu radiation)

h k l	d_{calc}/(Å)	d_{obs}/(Å)	I/I_{max} obs (%)
0 2 0	7.22	7.16	100.00
0 2 1	5.98	5.92	1.83
0 0 2	5.34	5.30	33.76
0 2 2	4.292	4.269	23.07
1 1 0	3.955	3.933	2.14
0 4 0	3.609	3.591	8.89
0 4 1	3.419	3.394	2.81
0 2 3	3.192		
1 1 3	3.178	3.174	20.11
1 3 0	3.126	3.112	9.63
1 3 1	3.000	2.985	5.99
1 3 2	2.698	2.685	11.44
0 0 4	2.669	2.655	61.49
1 1 3	2.645	2.630	1.97
0 2 4	2.503	2.492	44.85
0 6 0	2.406	2.395	3.94
1 5 0	2.363	2.355	3.52
1 3 3	2.349	2.332	1.01
1 1 4	2.212	2.203	5.05

Table 3.7 Calculated and Observed X-ray Powder diffraction Pattern for $KCuUSe_3$ (Cu radiation) (cont.)

h k l	d_{calc}/(Å)	d_{obs}/(Å)	I/I_{max} obs (%)
0 6 2	2.194	2.185	17.40
1 5 2	2.161	2.154	11.01
0 4 4	2.146	2.137	13.79
2 0 0	2.056	2.050	2.74
0 2 5	2.044	2.040	3.49
1 3 4	2.030	2.022	3.01
0 6 3	1.9932	1.9855	3.42
2 2 0	1.9774	1.9708	1.99
1 5 3	1.9685	1.9621	3.14
		1.9612	1.97
2 2 1	1.9443	1.9449	1.47
1 1 5	1.8787	1.8724	1.04
2 2 2	1.8542	1.8476	0.97
0 8 0	1.8046	1.7977	4.57
0 6 4	1.7871	1.7820	2.41
2 4 0	1.7865		
0 8 1	1.7794	1.7742	2.01
0 0 6	1.7792		
1 5 4	1.7692	1.7650	1.71
1 3 5	1.7631	1.7582	3.36

Table 3.7 Calculated and Observed X-ray Powder diffraction Pattern for $KCuUSe_3$ (Cu radiation) (cont.)

h k l	d_{calc}/(Å)	d_{obs}/(Å)	I/I_{max} obs (%)
2 4 1	1.7620		
1 7 2	1.7425	1.7381	2.11
2 2 3	1.7284		
0 2 6	1.7275	1.7213	3.37
0 8 2	1.7096	1.7049	10.21
2 4 2	1.6941	1.6882	1.38
1 7 3	1.6369	1.6324	1.52
2 0 4	1.6287	1.6254	1.70
1 1 6	1.6225	1.6185	2.95
0 6 5	1.5970	1.5921	5.07
0 4 6	1.5958	1.5867	3.90
2 2 4	1.5888	1.5801	1.42
2 6 0	1.5631	1.5580	1.61
1 3 6	1.5463	1.5421	1.70

Hexapotassium docecacopper diuranium pentadecasulfide $K_6Cu_{12}U_2S_{15}$ -- During investigations into forming uranyl ($[UO_2]^{2+}$) containing species (See Chapter 4), $K_6Cu_{12}U_2S_{15}$ was discovered as a minor product in a reaction of 0.083 g (0.75 mmol) K_2S, 0.008 g (0.126 mmol) Cu, 0.030 g (0.126 mmol) U, 0.014 g (0.126 mmol) SeO_2, and 0.048 g (1.50 mmol) S. The reactants are loaded into a pyrex tube in the usual manner. The reaction is heated to 400 °C over 12 hr., held at that temperature for 4 days, and cooled to 200 °C over 50 hr. and 50 °C in 1 hr. The excess flux is removed by washing with several portions of degassed methanol in the manner described previously. The remaining material was a mixture of water-soluble, hexagonal-shaped chunks and needles and water-insoluble, black needles and cubic chunks. The water-soluble portion was assumed to be the K^+ salt of the $[(UO_2)(S_2)_3]^{4-}$ anion (see Chapt. 4). Elemental analysis of the insoluble components revealed the black needles to have K/Cu/S in an approximate ratio of 1/4/3 and so was assumed to be KCu_4S_3, which is often observed in these quaternary reactions when phase separation occurs. Analysis of the black cubic chunks showed them to have K/Cu/U/S in an approximate ratio of 4/2/1/12. Subsequent X-ray single crystal studies revealed this phase to be $K_6Cu_{12}U_2S_{15}$.

Although not yet synthesized in pure phase, $K_6Cu_{12}U_2S_{15}$ has been reproduced from a mixture of 0.083 g (0.75 mmol) K_2S, 0.008 g (0.126 mmol) Cu, 0.030 g (0.126 mmol) U, and 0.048 g (1.50 mmol) S heated at 400 °C for 4 d. (cooling rate:4°C/hr.). The quaternary phase is clearly seen in the powder X-ray diffraction pattern of the grey microcrystalline product (Table 3.8) but is contaminated by small amounts of CuS chunks and large amounts of an unknown K/U/S microcrystalline phase.

Table

2	
2	
4	
4	
4	
5	
6	
6	
5	
4	
6	
6	
6	
8	
8	
8	
7	
8	

Table 3.8 Calculated and Observed X-ray Powder diffraction Pattern for $K_6Cu_{12}U_2S_{15}$ (Cu radiation)

h k l	d_{calc}/(Å)	d_{obs}/(Å)	I/I_{max} obs (%)
2 1 1	7.61	7.59	21.56
2 2 0	6.59	6.57	100.00
4 0 0	4.660	4.646	25.45
4 2 2	3.805	3.793	28.37
4 3 1	3.656	3.643	9.05
5 2 1	3.404	3.394	9.75
6 1 1	3.024	3.016	13.57
6 2 0	2.948	2.939	34.48
5 4 1	2.876	2.868	23.41
4 4 4	2.691	2.714	36.09
6 4 0	2.585	2.579	15.49
6 3 3	2.537	2.520	18.70
6 4 2	2.491	2.484	69.13
8 0 0	2.330	2.325	9.76
8 2 0	2.261	2.255	6.37
8 2 2	2.197	2.191	14.68
7 5 2	2.111	2.106	20.79
8 4 0	2.084	2.078	15.45

Tabl

Table 3.8 Calculated and Observed X-ray Powder diffraction Pattern for $K_6Cu_{12}U_2S_{15}$ (Cu radiation)

h k l	d_{calc}/(Å)	d_{obs}/(Å)	I/I_{max} obs (%)
7 6 1	2.010		
6 5 5	2.010		
9 2 1	2.010		
6 6 4	1.9872	1.9815	8.38
7 6 3	1.9228	1.9281	10.71
8 4 4	1.9026	1.9189	18.52
8 5 3	1.8831	1.8980	18.88
9 4 1	1.8831		
10 1 1	1.8458		
7 7 2	1.8458		
8 6 2	1.8280	1.8251	10.87
9 4 3	1.8107		
10 3 3	1.7161	1.7220	6.66
10 4 2	1.7018	1.6993	8.37
9 5 4	1.6878		
9 6 3	1.6608	1.6604	14.79
10 5 1	1.6608		
11 2 1	1.6608		

meas
ray
(diff

studi
and
pelle
probe
curre
cross
calibr
comp
power
requir
across
were
therma
were u
the vo
gradie
1.0 K
with
electro
Mount
K for

2. Physical Measurements

The instrumentation and experimental setup for the following measurements are the same as described in Chapt. 2, Sec. B.2: powder X-ray diffraction, infrared spectroscopy, UV/Vis/near IR spectroscopy (diffuse reflectance mode), and magnetic susceptibility measurements.

Charge-Transport Measurements -- DC electrical conductivity studies were performed on single crystals approximately 1-2 mm in length, and thermopower measurements were made on pressed polycrystalline pellets. Conductivity measurements were performed in the usual four-probe geometry with 60- and 25-mm diameter gold wires used for the current and voltage electrodes, respectively. Measurements of the sample cross-sectional area and voltage probe separation were made with a calibrated binocular microscope. Conductivity data were obtained with the computer-automated system described elsewhere [18]. Thermoelectric power measurements were made by using a slow ac technique [19] which requires the production of a slowly varying periodic temperature gradient across the samples and measuring the resulting sample voltage. Samples were suspended between quartz block heaters by 60-mm gold wires thermally grounded to the block with GE 7031 varnish. The gold wires were used to support and conduct heat to the sample, as well as to measure the voltage across the sample resulting from the applied temperature gradient. The magnitude of the applied temperature gradient was generally 1.0 K. Smaller temperature gradients gave essentially the same results but with somewhat lower sensitivity. In both measurements, the gold electrodes were held in place on the sample with conductive gold paste. Mounted samples were placed under vacuum (10^{-3} Torr) and heated to 320 K for 2-4 hr to cure the gold contacts. For a variable-temperature run,

data (conductivity or thermopower) were acquired during sample warming. The average temperature drift rate during an experiment was kept below 0.3 K/min. Multiple variable-temperature runs were carried out for each sample to ensure reproducibility and stability. At a given temperature, reproducibility was within $\pm$ 5%.

Single Crystal X-ray Diffraction -- Intensity data was collected using a Rigaku AFC6S four-circle automated diffractometer equipped with a graphite crystal monochromator. An ω-2θ scan mode was used. The crystals' stability was monitored with three standard reflections whose intensities were checked every 150 reflections, and unless noted, no crystal decay was detected. An empirical absorption correction based on ψ scans was applied to all data during initial stages of refinement. An empirical DIFABS correction [20] was applied after full isotropic refinement, after which full anisotropic refinement was performed. The structures were solved by direct methods using SHELXS-86 software [21a] (for all compounds), and full matrix least squares refinement was performed using the TEXSAN software package [21b]. Crystallographic data for the compounds in this section are given in Table 3.9.

Tab

a. Å

b. Å

c. Å

β. °

V. Å

space

Z

F.W.,

$d_{calc.}$

μ. cm

crysta

dimen

radiati

2θ ma

data co

temp.,

data

uniq

F_o^2>

of va

R/Rw.

final D

max. p

[a] $R = \Sigma$

Table 3.9: Crystallographic Data for $KCuCe_2S_6$, $CsCuCe_2S_6$, $KCuCe_2Se_6$, $K_2Cu_2CeS_4$, $CsCuCeS_3$, $KCuUSe_3$, and $K_6Cu_{12}U_2S_{15}$

	$KCuCe_2S_6$	$CsCuCe_2S_6$	$KCuCe_2Se_6$
a, Å	6.859(2)	5.500(1)	5.695(1)
b, Å	21.154(2)	22.45(1)	22.236(6)
c, Å	6.8599(8)	4.205(4)	4.297(2)
β, °	105.41(2)	90	90
V, $Å^3$	959.6(6)	519.3(6)	544.1(3)
space group	C2/c (#15)	Immm (#71)	Immm (#71)
Z	4	2	2
F.W., g/mol	575.24	669.05	856.64
d_{calc}, g/cm^3	3.982	4.279	5.228
μ, cm^{-1}	133.09	153.28	305.05
crystal dimensions, mm^3	0.02 x 0.04 x 0.50	0.01 x 0.04 x 0.24	0.02 x 0.06 x 0.44
radiation	Mo, Kα	Mo, Kα	Mo, Kα
2θ max.	60.0°	60.0°	60.0°
data collection temp., °C	23	23	-100
# data collected	1552	451	494
# unique data	1409	451	494
# $F_o^2>3\sigma$	1036	384	396
# of variables	35	22	22
R/Rw, % [a]	3.2/5.7	3.4/4.3	3.5/4.2
final Dif. map max. peak, $e^-/Å^3$	1.31	1.54	1.42

[a] $R= \Sigma(|Fo|-|Fc|)/\Sigma|Fo|$ $Rw=\{\Sigma w(|Fo|-|Fc|)^2/\Sigma w|Fo|^2\}^{1/2}$

Tab

a. Å

b. Å

c. Å

β. °

V. Å

spac

Z

F.W.

$d_{calc.}$

μ. cm

cryst

dimer

radiat

2θ ma

data c

temp.

data

uni

F_o^2

of

R/Rw

final

max.

[a] R=

Table 3.9: Crystallographic Data for $KCuCe_2S_6$, $CsCuCe_2S_6$, $KCuCe_2Se_6$, $K_2Cu_2CeS_4$, $CsCuCeS_3$, $KCuUSe_3$, and $K_6Cu_{12}U_2S_{15}$ (cont.).

	$K_2Cu_2CeS_4$	$CsCuCeS_3$	$KCuUSe_3$
a, Å	14.320(3)	4.024(2)	4.112(2)
b, Å	3.961(1)	15.154(2)	14.437(3)
c, Å	7.496(2)	10.353(3)	10.675(2)
β, °	109.77(2)	90	90
V, $Å^3$	400.1(2)	631.3(4)	633.7(3)
space group	C2/m (#12)	Cmcm (#63)	Cmcm (#63)
Z	2	4	4
F.W., g/mol	473.65	423.75	577.55
d_{calc}, g/cm^3	3.931	4.552	6.719
μ, cm^{-1}	129.27	170.84	243.2
crystal dimensions, mm^3	0.04 x 0.08 x 0.20	0.02 x 0.10 x 0.22	0.02 x 0.04 x 0.20
radiation	Mo, Kα	Mo, Kα	Mo, Kα
2θ max.	60.0°	59.9°	60.0°
data collection temp., °C	-80	-100	23
# data collected	505	532	536
# unique data	486	532	517
# $F_o^2>3\sigma$	436	450	401
# of variables	29	23	23
R/Rw, % [a]	2.0/2.6	3.2/4.2	3.3/4.2
final Dif. map max. peak, $e^-/Å^3$	0.68	1.70	2.61

[a] $R= \Sigma(|Fo|-|Fc|)/\Sigma|Fo|$ $Rw=\{\Sigma w(|Fo|-|Fc|)^2/\Sigma w|Fo|^2\}^{1/2}$

Table

a. Å

b. Å

c. Å

β. °

V. Å3

space

Z

F.W.,

$d_{calc.}$

μ. cm-

crystal

dimens

radiati

2θ ma

data co

temp.,

data

uniq

F_o^2>

of va

R/Rw,

final D

max. p

[a] $R = \Sigma$

Table 3.9: Crystallographic Data for $KCuCe_2S_6$, $CsCuCe_2S_6$, $KCuCe_2Se_6$, $K_2Cu_2CeS_4$, $CsCuCeS_3$, $KCuUSe_3$, and $K_6Cu_{12}U_2S_{15}$ (cont.).

	$K_6Cu_{12}U_2S_{15}$
a, Å	18.642(7)
b, Å	
c, Å	
β, °	90
V, Å^3	6478(2)
space group	Ia-3d
Z	8
F.W., g/mol	1954.1
d_{calc}, g/cm^3	4.007
μ, cm^{-1}	94.4
crystal dimensions, mm^3	0.20 x 0.20 x 0.24
radiation	Mo, Kα
2θ max.	50.0°
data collection temp., °C	23
# data collected	604
# unique data	483
# $F_o^2>3\sigma$	192
# of variables	28
R/Rw, % [a]	2.9/3.1
final Dif. map max. peak, e$^-$/Å^3	0.94

[a] $R= \Sigma(|Fo|-|Fc|)/\Sigma|Fo|$ $Rw=\{\Sigma w(|Fo|-|Fc|)^2/\Sigma w|Fo|^2\}^{1/2}$

C. Results and Discussion

1. $ACuLn_2Q_6$

Structure -- As shown in Table 3.9, phases with this stoiciometry have been found to crystallize in either the monoclinic space group C2/c (#15) for $KCuLn_2S_6$ (Ln= La, Ce) or the orthorhombic space group Immm (#71) for $CsCuCe_2S_6$ and $KCuCe_2Se_6$. The shift to higher symmetry for the later two compounds essentially only reduces the number of symmetry independent atoms relative to the monoclinic forms. The basic structural framework remains common to all of these phases.

Despite the plan to form new structure types by the incorporation of Cu and Ln cations into the same lattice, the $ACuLn_2Q_6$ family turns out to have the same Ln/Q framework as that found in the ternary phases $NaLnS_3$ (Chapter 2, Sec C.3). As discussed earlier, that framework is analogous to the $ZrSe_3$ structure type [22]. The Ln are coordinated by a bicapped trigonal prism of Q atoms made of two $(Q_2)^{2-}$ units forming the short sides of the prism and four Q^{2-} ions at the apex and capping positions. Anionic layers are formed when the trigonal prisms stack in one dimension by sharing triangular faces and neighboring chains cap each other by sharing monosulfides in the second dimension. In the quaternary compounds the space between the chains of prisms, which was void in the ternary phases, now contains Cu atoms residing in tetrahedral sites formed by two bonds to two monochalcogenides and two bonds to one atom on two separate dichalcogenides.

Figure 3.1 shows the extended structure of $KCuCe_2S_6$ (as seen down the [101] direction) both with and without Cu atoms in the intralayer grooves between prismatic chains. Atomic coordinates are given in Table

3.10. In the monoclinic $KCuCe_2S_6$ there are two crystallographically distinct sites for both Cu and Ce atoms. A fragment of the structure, showing the immediate coordination environment of these sites, is shown in Figure 3.2, and selected bond distances are listed in Table 3.11. The Ce-S distances range from 2.838(1) Å to 3.010(1) Å and are comparable with those found in compounds such as $KCeS_2$ (2.878 Å [23]), CeS_2 (2.88-3.26 Å [24]), and $NaCeS_3$ (2.838-3.010 Å). The disulfide bond of 2.105(3) Å is also reasonable. Two Cu sites are present which occupy alternating tetrahedral positions within the intralayer grooves, and refinement of the multiplicity of those sites showed that a lone Cu atom is disordered over both sites. Each site resides on a mirror plane, giving them, crystallographically, 1/2 occupancies, but when allowed to refine, the Cu(1) site occupancy becomes 0.427, where that for Cu(2) becomes 0.073. No disorder was found on the K^+ site. Bond distances are consistent on the more fully occupied Cu(1) site at 2.363 and 2.335 Å but exhibit a larger range on the Cu(2) site (2.18 and 2.45 Å), probably owing to the Cu(2)'s higher temperature factor, reflecting greater uncertainty in its position. For comparison, the Cu-S bonds in α- and β-$KCuS_4$ range from 2.298 to 2.432 Å [25].

There is also a correlation in $KCuCe_2S_6$ between Cu occupancy and the bonds between Ce and the disulfide. The more fully occupied Cu(1) is bonded to the S(2) atom of the disulfide which then has a Ce-S distance of 3.017(3) Å. Meanwhile, the S(1) atom coordinated to the lesser occupied Cu(2) site experiences shortened Ce-S bonds (2.880(2) Å). The lack of coordination to Cu(2) must allow for a stronger interaction between S(1) and Ce.

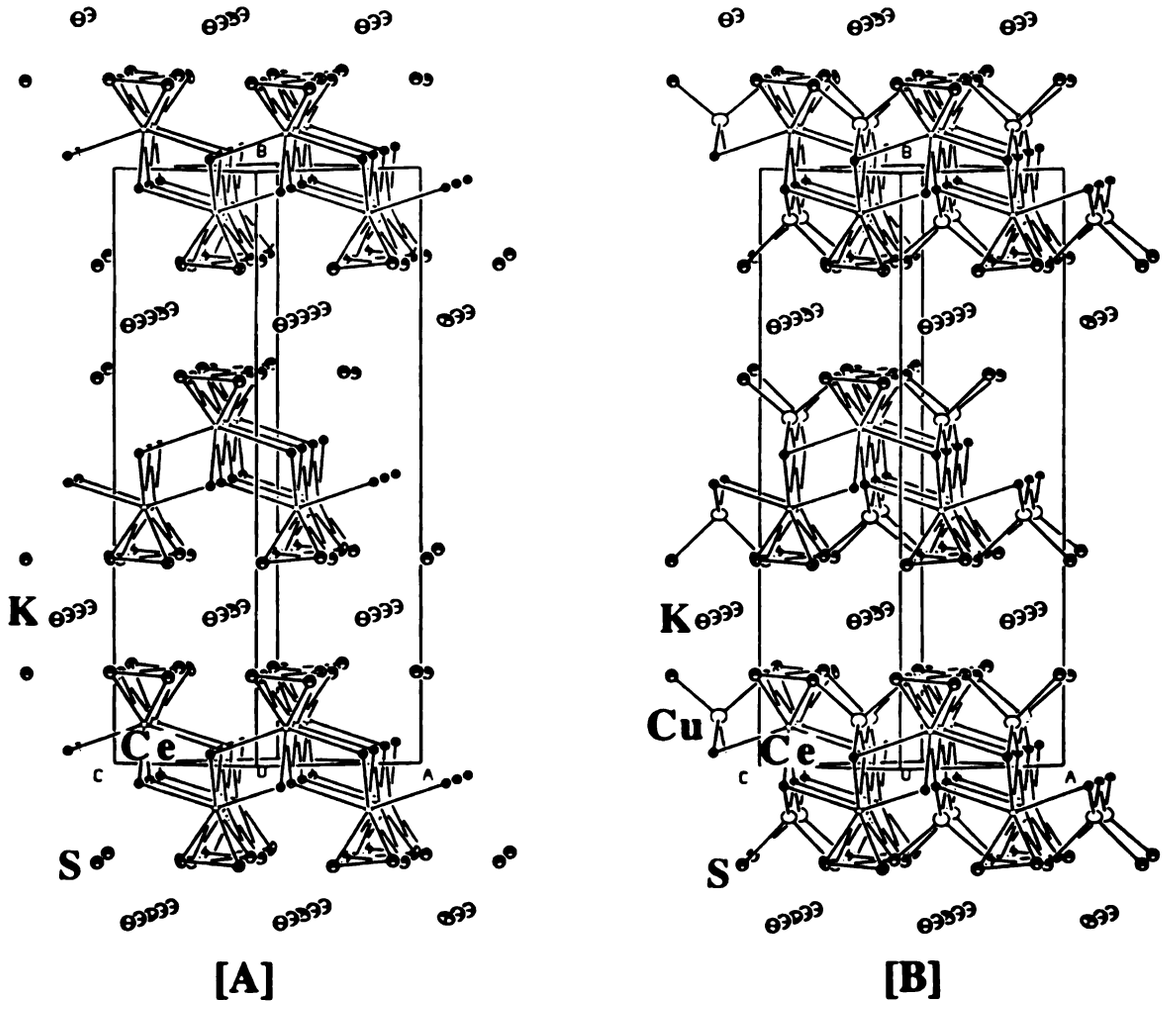

Figure 3.1 The extended structure of $KCuCe_2S_6$ as seen down the [101] direction both without (A) and with (B) the compound's Cu+ cations (Circles with nonshaded octants: K; large open circles: Cu; small open circles: Ce; circles with shaded octants: S)

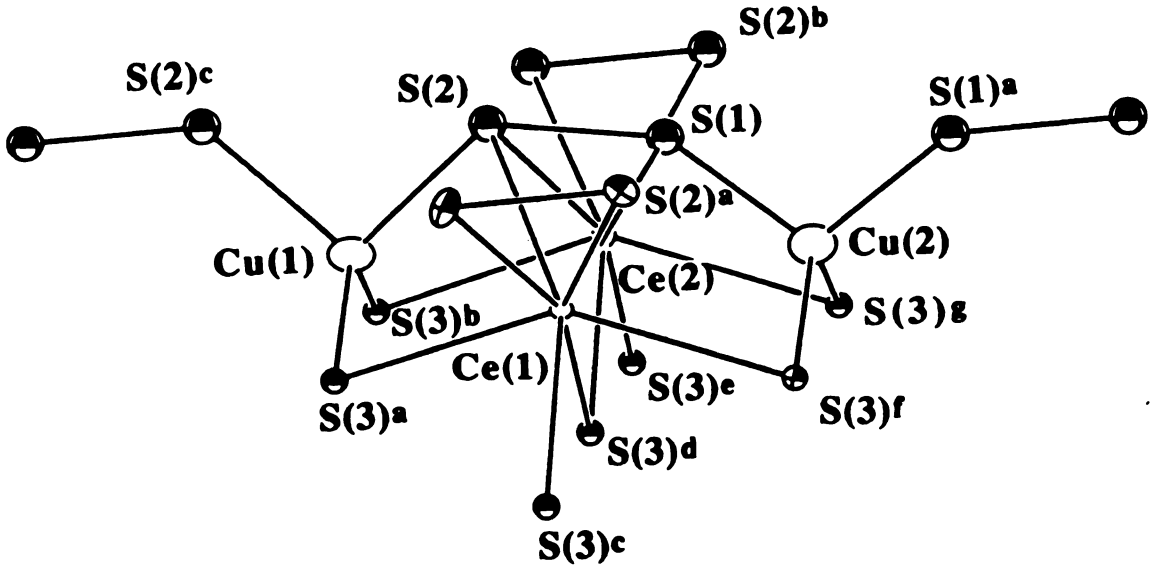

Figure 3.2 A fragment of the anionic structure of $KCuCe_2S_6$ highlighting the coordination environment of the compounds Cu and Ce atoms.

Table 3.10: Fractional Atomic Coordinates and B_{eq}[a] values for $KCuCe_2S_6$ with Estimated Standard Deviations in Parentheses

atom	x	y	z	B_{eq}[a]
Ce(1)	0	0.06763(3)	3/4	0.55(3)
Ce(2)	-1/2	0.07059(4)	1/4	0.68(3)
Cu(1)	-1/2	0.0808(1)	3/4	1.87(9)
Cu(2)	0	0.0840(8)	1/4	2.2(6)
S(1)	0.1523(4)	0.1500(1)	1.0947(4)	1.4(1)
S(2)	0.3442(5)	0.1591(1)	0.9032(4)	1.4(1)
S(3)	0.2558(4)	0.0263(1)	0.5057(4)	0.71(7)
K	-3/4	1/4	1/2	1.9(1)

[a] B values for anisotropically refined atoms are given in the form of the isotropic equivalent displacement parameters defined as $B_{eq} = (4/3)[a^2B(1,1) + b^2B(2,2) + c^2B(3,3) + ab(\cos\gamma)B(1,2) + ac(\cos\beta)B(1,3) + bc(\cos\alpha)B(2,3)$.

Table 3.11: Selected Bond Distances (Å) and Angles (°) for $KCuCe_2S_6$ with standard deviations in parentheses

Ce(1)-S(1)	2.899(3) (x2)	Ce(2)-S(1)	2.880(2) (x2)
Ce(1)-S(2)	3.017(3) (x2)	Ce(2)-S(2)	2.992(3) (x2)
Ce(1)-S(3)^{a,f}	2.866(3)	Ce(2)-S(3)^{b,g}	2.885(3)
Ce(1)-S(3)^{c,d}	2.910(3)	Ce(2)-S(3)^{d,e}	2.885(3)
Cu(1)-S(2)	2.363(3) (x2)	Cu(2)-S(1)	2.18(1) (x2)
Cu(1)-S(3)^{a,b}	2.335(3)	Cu(2)-S(3)^{f,g}	2.451(9)
S(1)-S(2)	2.101(4)		

S(1)-Ce(1)-S(2)	41.55(8)	S(1)-Ce(2)-S(2)	41.88(8)
S(1)-Ce(1)-S(3)^{d}	83.68(8)	S(1)-Ce(2)-S(3)^{d}	84.46(8)
S(1)-Ce(1)-S(2)^{a}	88.73(8)	S(1)-Ce(2)-S(2)^{b}	90.86(9)
S(1)-Ce(1)-S(3)^{f}	81.38(8)	S(1)-Ce(2)-S(3)g	81.75(8)
S(3)^{c}-Ce(1)-S(3)^{d}	93.9(1)	S(3)d-Ce(2)-S(3)^{e}	89.5(1)
S(2)-Cu(1)-S(2)^{b}	91.0(2)	S(1)-Cu(2)-S(1)^{a}	100.5(7)
S(2)-Cu(1)-S(3)^{b}	110.5(1)	S(1)-Cu(2)-S(3)g	108.3(1)
S(2)-Cu(1)-S(3)^{a}	110.0(1)	S(1)-Cu(2)-S(3)^{f}	108.9(1)
S(3)^{a}-Cu(1)-S(3)^{b}	120.8(2)	S(3)f-Cu(2)-S(3)g	120.3(7)

The lack of single crystal studies on $KCuLa_2S_6$, of course, makes any detailed discussion of its structural features impossible; however, it is expected that similar changes in bond distances as were seen in the $NaLnS_3$ (Ln=La, Ce) phases would also be observed here.

Although of a higher symmetry than $KCuCe_2S_6$, the orthorhombic $CsCuCe_2S_6$ and $KCuCe_2Se_6$ have essentially the same structure. The orthorhombic cells are oriented such that the direction of the intralayer grooves is now parallel to the a-axis (Figure 3.3). The fractional atomic coordinates of the two phases are given in Tables 3.12 and 3.13. A fragment showing the immediate coordination environments of the metals is shown in Figure 3.4, and selected bond distances are given in Table 3.14. The Ce-S bond distance range narrows slightly in $CsCuCe_2S_6$ (2.892(1)-2.967(3) Å) while the disulfide bond shortens to 2.088(6) Å. The distances for selenide analog are in line with what would be expected both for the Ce-Se values (3.0136(9)-3.092(1) Å) and the diselenide distance (2.374(3) Å). For example in $KCeSe_4$ the Ce-Se distance is 3.075 Å and the Se-Se distance, 2.385 Å [26]. Of particular note is that once again the Cu sites of these structures experience occupancy disorder. The higher symmetry of the orthorhombic space group requires there be only one Cu site, but the occupancy of that site refines at only 50%, meaning that on the average a Cu atom is only present half of the time. The alkali cations remain fully occupied in both structure. This implies that a full layer of alkali cation is needed for lattice stabilization regardless of the space group, and the structures seem to have the ability to pull in only enough Cu+ ions to achieve neutrality.

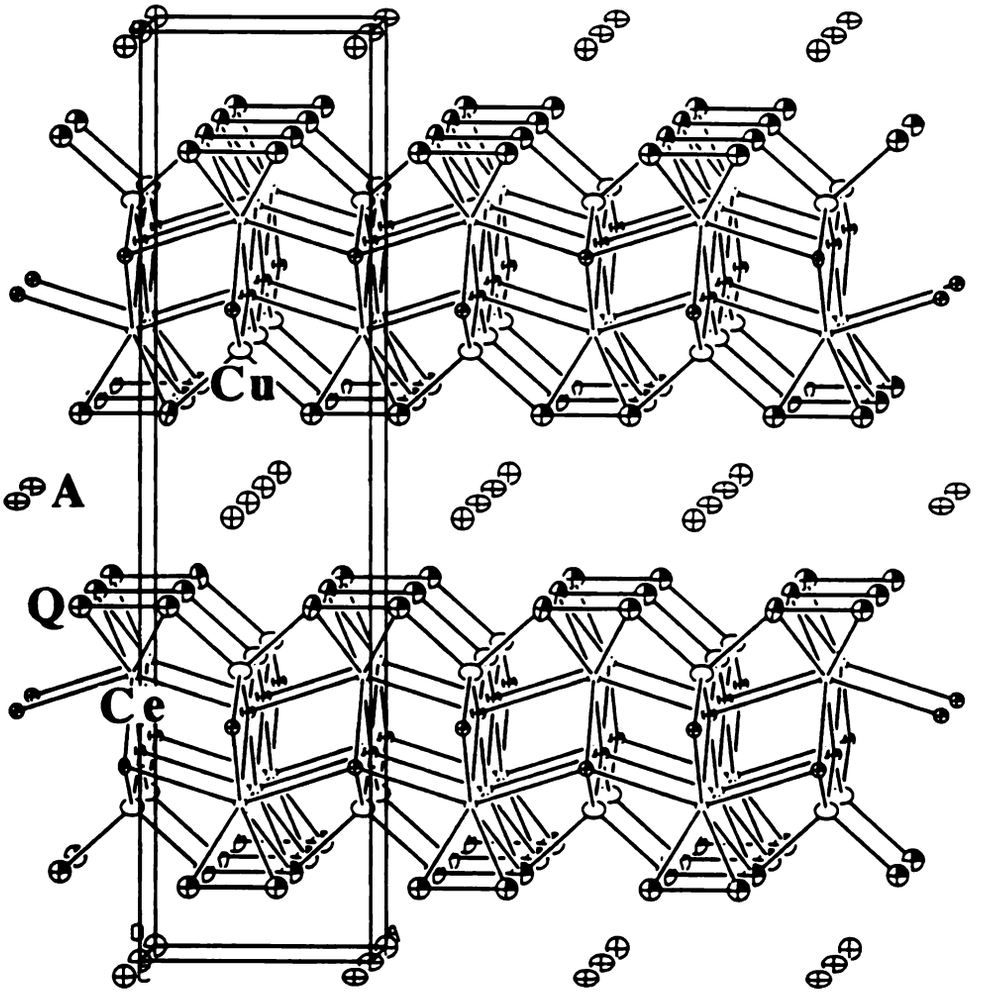

Figure 3.3 The extended structure of the orthorhombic form of $ACuCe_2Q_6$ as seen down the a-axis (Circles with nonshaded octants: A; large open circles: Cu; small open circles: Ce; circles with shaded octants: Q)

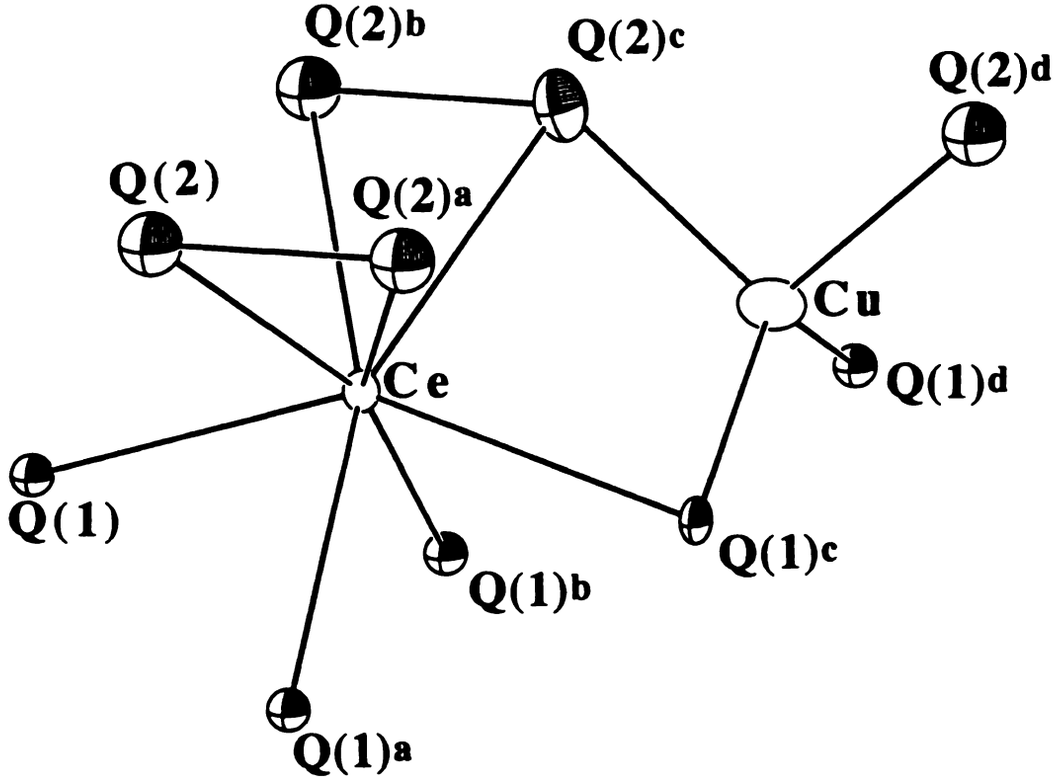

Figure 3.4 A fragment of the anionic structure of $ACuCe_2Q_6$ (A=Cs, Q=S; A=K, Q=Se) highlighting the coordination environment of the compounds Cu and Ce atoms.

Table 3.12: Fractional Atomic Coordinates and B_{eq}[a] values for $CsCuCe_2S_6$ with Estimated Standard Deviations in Parentheses

atom	x	y	z	B(eq)[a]
Ce	-1/2	0.18509(4)	0	0.77(3)
Cs	0	0	0	2.21(6)
Cu	-1	0.1731(2)	-1/2	1.7(2)
S(1)	-1	0.2249(2)	0	0.9(2)
S(2)	-0.6898(5)	0.1043(2)	-1/2	2.1(2)

[a] B values for anisotropically refined atoms are given in the form of the isotropic equivalent displacement parameters defined as $B_{eq} = (4/3)[a^2B(1,1) + b^2B(2,2) + c^2B(3,3) + ab(\cos\gamma)B(1,2) + ac(\cos\beta)B(1,3) + bc(\cos\alpha)B(2,3)$.

Table 3.13: Fractional Atomic Coordinates and B_{eq}[a] values for $KCuCe_2Se_6$ with Estimated Standard Deviations in Parentheses

atom	x	y	z	B(eq)[a]
Ce	1/2	0.17980(4)	0	0.49(3)
Cu	0	0.1735(2)	-1/2	1.5(2)
K	0	0	-1	1/7(2)
Se(1)	0	0.22420(4)	0	0.57(6)
Se(2)	0.2916(2)	0.09526(7)	-1/2	1.40(5)

[a] B values for anisotropically refined atoms are given in the form of the isotropic equivalent displacement parameters defined as $B_{eq} = (4/3)[a^2B(1,1) + b^2B(2,2) + c^2B(3,3) + ab(\cos\gamma)B(1,2) + ac(\cos\beta)B(1,3) + bc(\cos\alpha)B(2,3)$.

Table 3.14: Selected Bond Distances and Angles for $CsCuCe_2S_6$ and $KCuCe_2Se_6$ with standard deviations in parentheses.

	$CsCuCe_2S_6$	$KCuCe_2Se_6$
Ce-Q(1)	2.892(1)	3.0136(9)
Ce-Q(1)[a,b]	2.917(3)	3.029(2)
Ce-Q(2)	2.967(3)	3.092(1)
Cu-Q(1)[c,d]	2.403(3)	2.426(3)
Cu-Q(2)[c,d]	2.302(4)	2.405(4)
Q(2)-Q(2)[a]	2.088(6)	2.374(3)
A-Q(2)	3.580(3)	3.444(1)
Q(1)-Ce-Q(1)[a]	77.64(4)	76.65(2)
Q(1)-Ce-Q(1)[b]	144.0(1)	141.76(7)
Q(1)[a]-Ce-Q(1)[c]	92.3(1)	90.36(6)
Q(1)-Ce-Q(2)	81.62(8)	80.59(4)
Q(1)-Ce-Q(2)[a]	121.57(7)	124.19(3)
Q(1)[a]-Ce-Q(2)	85.00(9)	86.31(4)
Q(1)[a]-Ce-Q(2)[b]	159.18(6)	157.15(3)
Ce-Q(2)[c]-Cu	81.4(1)	79.93(7)
Ce-Q(1)[c]-Cu	81.41(6)	81.25(4)
Q(1)[c]-Cu-Q(1)[d]	122.1(2)	124.6(2)
Q(1)[c]-Cu-Q(1)[a]	108.95(7)	109.64(5)
Q(1)[a]-Cu-Q(1)[d]	95.7(2)	87.3(2)

The interlayer grooves undergo some slight modifications between the ternary and quaternary structures, responding to the absence or presence of Cu^+ cations. Two parameters give a good idea about the general size of the groove: the Ce-S-Ce angle along the bottom of the groove and the S-S distance across the top. In $NaCeS_3$ these values are 155.2° and 3.58 Å, respectively, while in $KCuCe_2S_6$ they are 143.2° and 3.36 Å and in $CsCuCe_2S_6$, 144.0° and 3.41 Å. Apparently, without the covalent interactions of Cu atoms, the grooves are free to open up somewhat, implying that they may be able to accommodate cations over a limited range of sizes.

The disorder observed in the Cu atom positions of both $ACuM_2Q_6$ structure types, coupled with fact that those sites are totally empty in $NaLnS_3$ phases, gives strong indication that these phases would have appreciable Cu^+ mobility through the intralayer grooves. Not only an intriguing property in itself, such mobility would also allow for ion exchange capabilities. Even reductive intercalation chemistry could be possible in these phases; the compound TiS_3, isostructural to $ZrSe_3$, is known to undergo Li^+ intercalation after the reduction of the $(Se\text{-}Se)^{2-}$ units to 2 Se^{2-} with n-BuLi [27].

From the discussion so far, one can reasonably postulate the existence of two structurally related compounds: $CuLnQ_3$ and $ALnQ_3$ (A=K, Cs). The former, with all Cu^+ sites at full occupancy, would have the interlayer galleries cleared of counterions. The latter, with the extra K^+ in a bilayer such as in $NaLnS_3$, would have totally empty intralayer grooves. There is no obvious reason why $CuLnQ_3$ should not exist, and it might be formed from fluxes of reduced alkali cation content. Making $ALnQ_3$ congeners with anything larger than Na may be problematic.

It seems from the $NaLnS_3$ structure that the Na^+ cations are actually helping to stabilize the empty intralayer grooves. Figure 3.5 shows a side-by side comparison of the structures of $NaLnS_3$ and $ACuLnQ_3$. In the ternary, the Na^+ are positioned directly above the intralayer grooves and have contacts to the S atoms (2.910(1) Å in $NaLaS_3$ and 2.884(2) Å in $NaCeS_3$) which are even shorter than some of the compound's Ln-S distances. This suggests that Na^+ may be helping to prop open the empty grooves. The larger sizes of the heavier alkali cations preclude such close interactions. Although still positioned above the intralayer grooves, the A^+ in $ACuLn_2Q_6$ are much further from the layers of dichalcogenides (3.416(3) and 3.289(3)Å in $KCuCe_2S_6$, 3.580(3) Å in $CsCuCe_2S_6$, 3.444(1) Å in $KCuCe_2Se_6$), and so the task of "propping" the grooves falls to the Cu^+. Whether this is a task crucial to the stabilization of the grooves in the presence of heavier alkali cations remains to be fully confirmed. Ternary molten A_2Q_x reactions in the Cs/Ce/S system invariably led to CeS_2 under acidic, S rich conditions and to $CsCeS_2$ under basic, S poor conditions. Similar results were observed in the potassium system, although one phase was obtained whose X-ray powder diffraction pattern bore similarities to the orthorhombic $ACuLn_2Q_6$ phases. Elemental analysis revealed an average composition of $K_{1.5}Ce_{2.5}S_{6.5}$, but single crystals of this phase could not be grown. Perhaps the difficulty in forming samples of high crystallinity is a result of the inability of the larger K^+ to stabilize the empty intralayer grooves in the same fashion as the smaller Na^+ do in $NaLnS_3$.

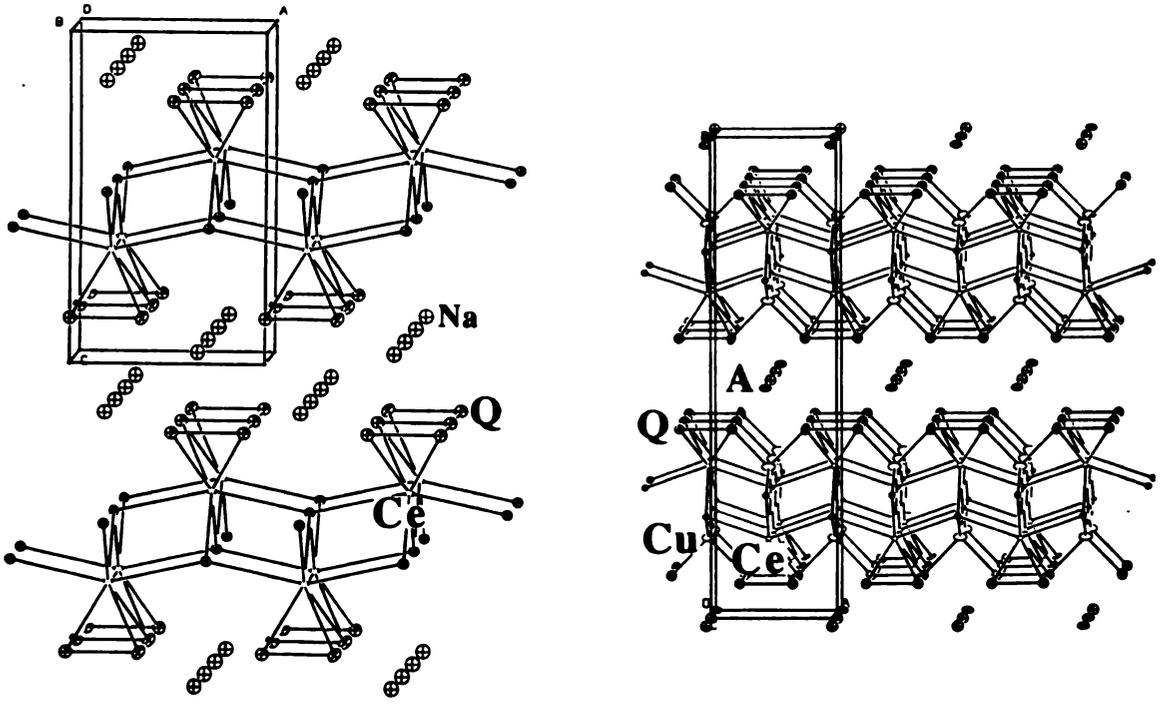

[A] [B]

Figure 3.5 (A) The extended structure of the $NaLnS_3$ structure type. (B) The extended structure of the $ACuLn_2Q_6$ structure type (Circles with nonshaded octants: A; large open circles: Cu; small open circles: Ce; circles with shaded octants: Q).

Magnetic Susceptibility Studies -- The temperature dependent magnetic susceptibility of $KCuCe_2S_6$, taken at 2000 G over the range 2-300 K, is shown in Figure 3.6. Curie-Weiss behavior is evident with some local ferromagnetic ordering at low temperatures indicated. Below 160 K, the data deviate negatively from a straight line extrapolated from higher temperatures. This phenomenon has been observed in other Ce^{3+} chalcogenides and has been attributed to crystal field splitting of the cation's $^2F_{5/2}$ ground state [28]. The data conform to a straight line at temperatures above 160 K and in that region a μ_{eff} of 3.1 BM for $KCuCe_2S_6$ was calculated. Since there are two Ce^{3+} ions (hence two $4f^1$ electrons) per formula, the μ_{eff} is based on the summation of the susceptibilities of these two ions. By dividing the calculated μ_{eff} by $\sqrt{2}$ (since μ_{eff} varies as the square root of χ_M), we estimate a μ_{eff} of 2.2 BM per Ce^{3+}. This is close to both the values seen experimentally (2.3-2.5 BM) and to the calculated theoretical value (2.54 BM) for a Ce^{3+} ion [29]. Lanthanides in general have μ_{eff} values which seldom vary with the chemical environment due to the shielding effect the valence orbitals have on the more deeply buried 4f electrons.

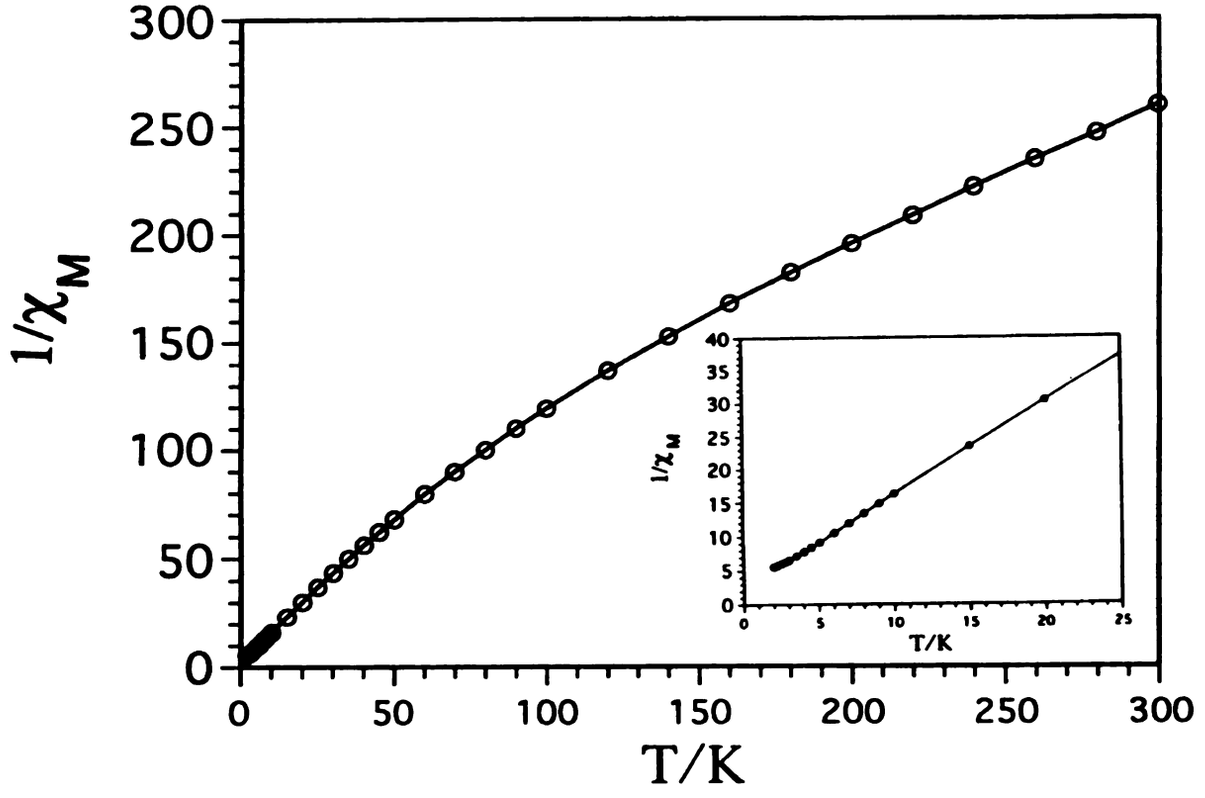

Figure 3.6: Inverse molar magnetic susceptibility ($1/\chi_M$) plotted against temperature (2-300 K) for $KCuCe_2S_6$ (2000 G). The inset graph shows an expanded view of the region 2-25 K.

This shielding of the $4f^1$ electrons causes the magnetic response of the Ce^{3+} cations in $CsCuCe_2S_6$ and $KCuCe_2Se_6$ bares strong resemblance to that observed in $KCuCe_2S_6$. This would be expected in the case of the Cs containing analog as the chemical environments about the Ce^{3+} are identical save for small changes in symmetry, and the plot of $1/\chi$ vs. T is nearly identical (Figure 3.7). A μ_{eff} of 2.1 BM/Ce^{3+} was calculated from applying a straight line curve fit to the data above 100 K, and a corresponding θ of -96 K indicates a fairly substantial amount of local antiferromagnetic ordering. For the selenium analog (Figure 3.8) the high temperature μ_{eff} was estimated at 2.4 BM, but the θ changes to about -47 K, indicating that in this coordination geometry the Se 4p orbitals are somehow less conducive to superexchange mediated ordering between Ce^{3+} ions than the S 3p orbitals.

Magnetic studies were not performed on $KCuLa_2S_6$ because La^{3+} is a $4f^0$ cation and is expected to be diamagnetic.

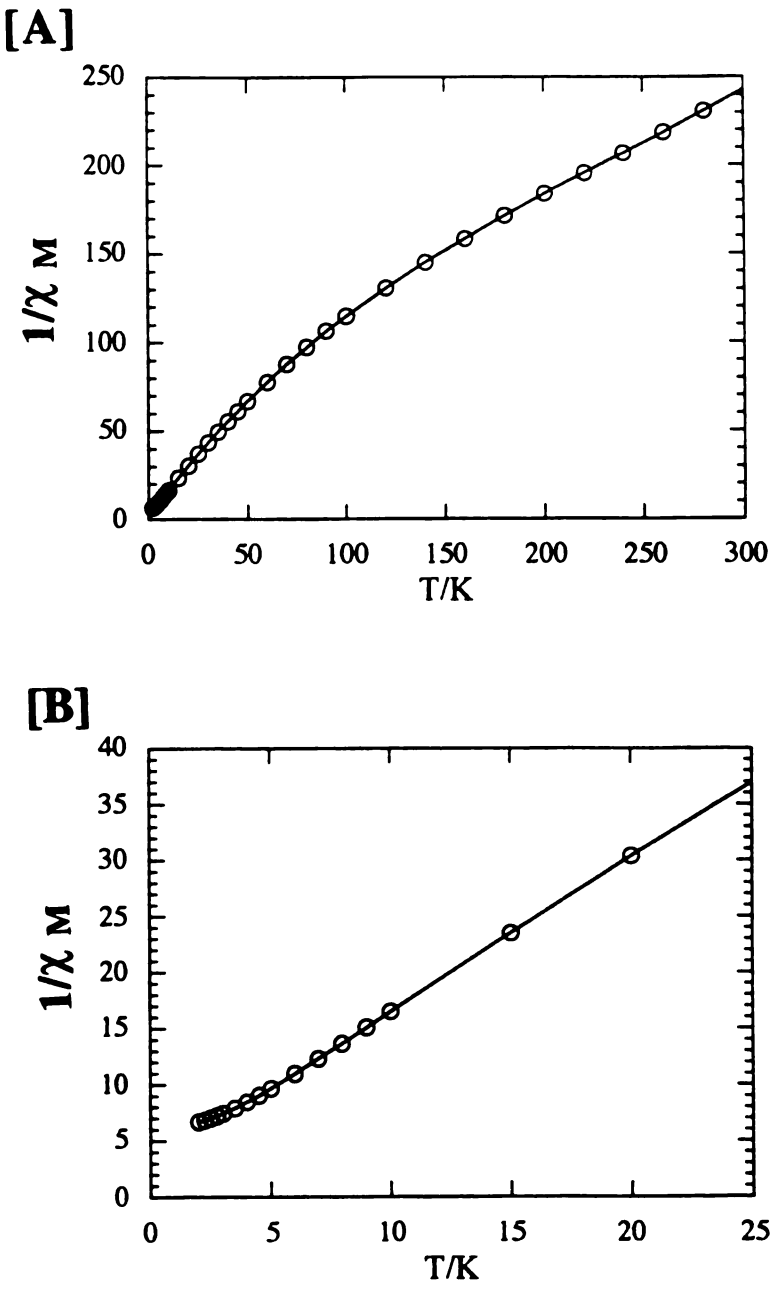

Figure 3.7: Inverse molar magnetic susceptibility ($1/\chi_M$) plotted against temperature (2-300 K) for $CsCuCe_2S_6$ (2000 G). (B) shows an expanded view of the region 2-25 K.

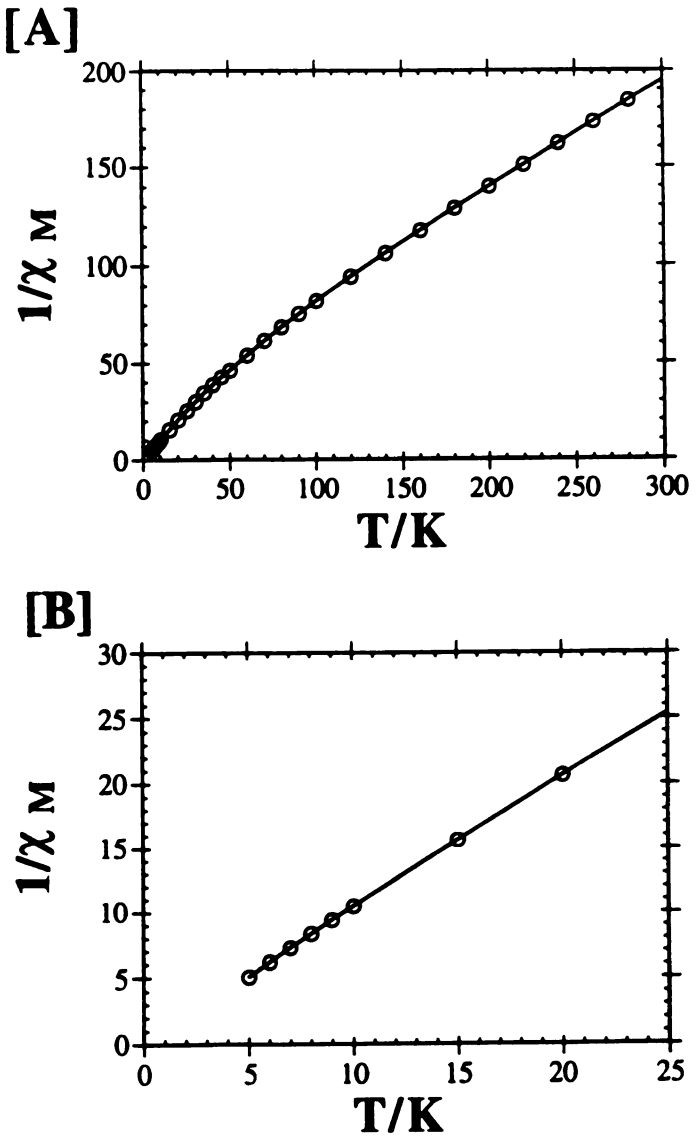

Figure 3.8: Inverse molar magnetic susceptibility ($1/\chi_M$) plotted against temperature (2-300 K) for $KCuCe_2Se_6$ (2000 G). (B) shows an expanded view of the region 2-25 K.

Spectroscopic Data -- The optical absorption spectra of the three sulfide analogs of $ACuLn_2Q_6$ are shown in Figure 3.9. The onset of a sharp change in (α/S) corresponds to an estimate of the sample's band gap, which for $KCuCe_2S_6$ is 1.81 eV, for $CsCuCe_2S_6$, 2.0 eV, and for $KCuLa_2S_6$, 2.4 eV. Hence, these phases are expected to be semiconductors. This, in conjunction with the magnetic studies, confirms the valence precise nature of these materials, and so oxidation states can be formalized as $A(Cu^{1+})(Ln^{3+})_2(Q^{2-})_2(Q_2^{2-})_2$. The tail of absorbance occurring below the band edge for both $KCuCe_2S_6$ and $CsCuCe_2S_6$ may indicate either amorphous impurities or the presence of an indirect band gap character to the electronic structure.

Figure 3.10 shows the optical absorption spectrum of $KCuCe_2Se_6$. This black material shows only weak absorbance, but by extrapolating the absorption edge to zero, a band gap of 0.55 eV can be estimated.

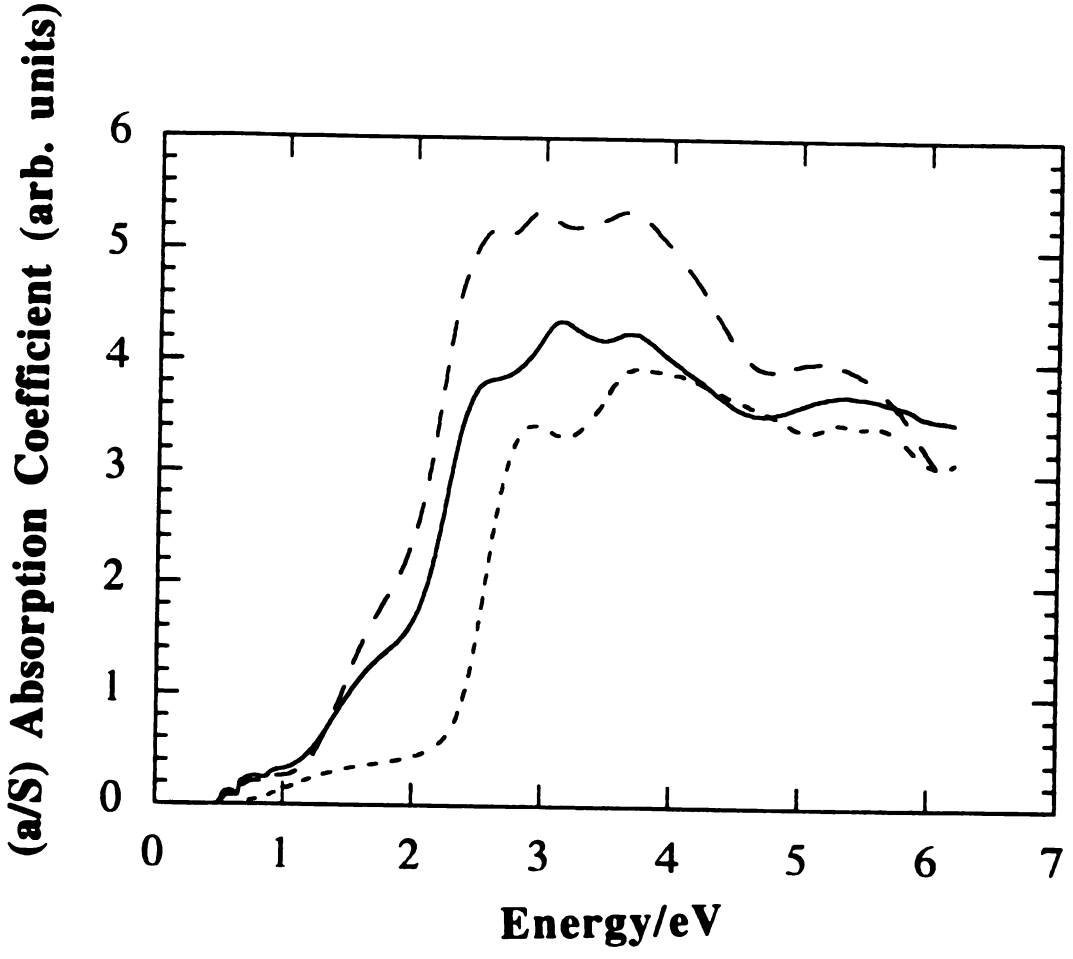

Figure 3.9: The solid state diffuse reflectance spectra of $KCuCe_2S_6$ (—), $CsCuCe_2S_6$ (- - -), and $KCuLa_2S_6$ (---) plotted as absorption coefficient (α/S) vs. energy (eV).

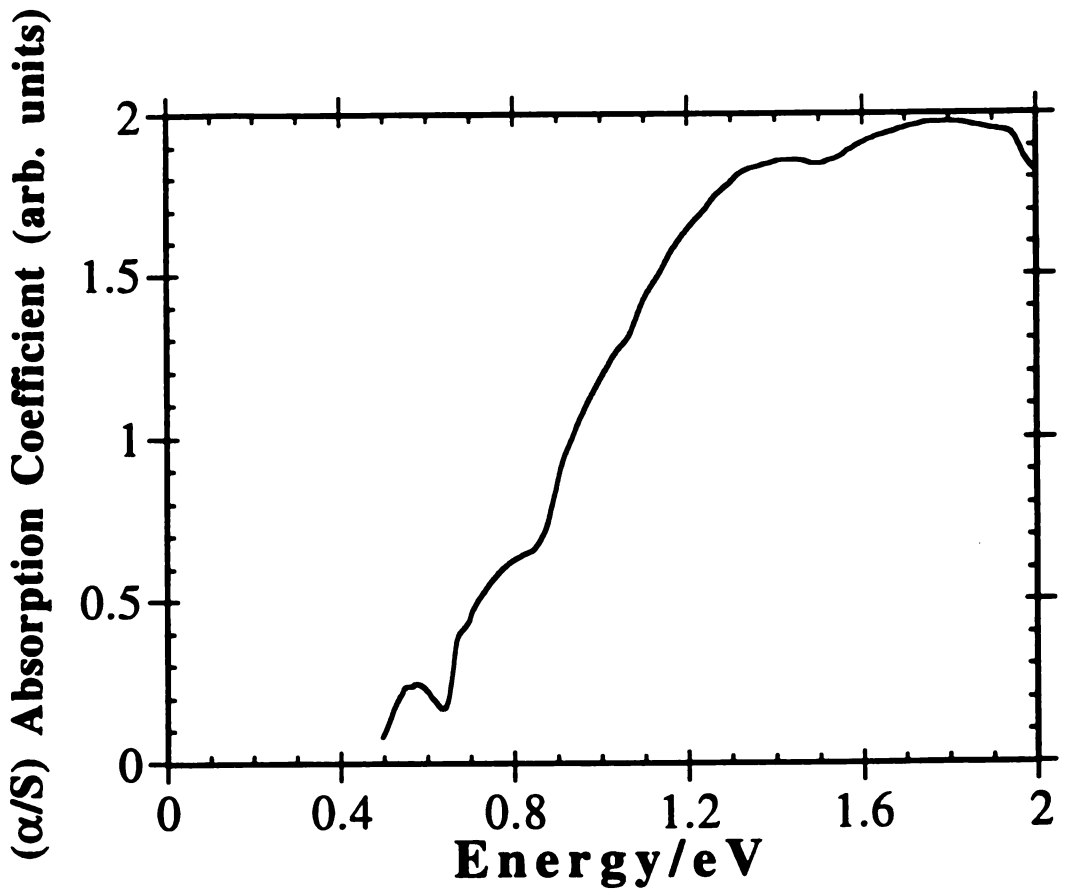

Figure 3.10: The solid state diffuse reflectance spectra of $KCuCe_2Se_6$ plotted as absorption coefficient (α/S) vs. energy (eV).

Peaks from the solid-state far-IR spectra of all $ACuLn_2Q_6$ analogs are summarized in Table 3.12. For the sulfides peaks in three general regions are observed. A medium to weak intensity peak occurs from 468-475 cm^{-1} which corresponds to a S-S stretching vibration. From 302-358 cm^{-1} are very weak and broad peaks which are presumably due to Cu-S bonds, the disordered nature of which probably contributes to their small intensities. Finally, a series of very strong peaks occurs in the region from 270-148 cm^{-1} and have been assigned as Ce-S vibrations.

In the solid-state far-IR spectrum of $KCuCe_2Se_6$ a medium intensity peak of 264 cm^{-1} is observed which corresponds to the sample's Se-Se vibration. As with the sulfides, a manifold of low energy peaks (132-199 cm^{-1}) is assigned to the samples Ce-Se vibrations. Presumably vibrations for the Cu-Se bond would appear at slightly higher energies than that of the Se-Se bond, but in fact none are observed. These vibrations must be either too weak to be seen or are simply IR inactive.

Table 3.15 Peaks from the Far-IR spectra of $KCuCe_2S_6$, $KCuLa_2S_6$, $CsCuCe_2S_6$, and $KCuCe_2Se_6$

$KCuCe_2S_6$ (cm^{-1})	$KCuLa_2S_6$ (cm^{-1})	$CsCuCe_2S_6$ (cm^{-1})	$KCuCe_2Se_6$ (cm^{-1})
473 (m)	468 (m)	475 (m)	
358 (w)			
307 (w)			
264 (s)			
258 (s)	250 (s)	258 (s)	263 (m)
214 (s)	212 (s)	217 (s)	
204 (s)	198 (s)	202 (s)	200 (s)
156 (s)	150 (s)	175 (s)	172 (s)
		148 (s)	141 (s)
			131(s)

2. $K_2Cu_2CeS_4$

Structure -- The structure of $K_2Cu_2CeS_4$ is also layered, with Ce, Cu, and S again forming the anionic layers and K in the interlayer gallery. Fractional atomic coordinates are given in Table 3.16. The Ce are octahedrally coordinated in $K_2Cu_2CeS_4$, forming edge sharing chains in one dimension. These chains are connected into layers via [CuS_4] tetrahedra. The [CuS4] share two edges with octahedra in one chain while forming a corner-sharing connection to an axial S on the neighboring chain. The Cu-centered tetrahedra also edge share with each other, forming a fragment of anti-PbO structure type between the chains of [CeS_6] octahedra. A view of the extended anionic layers is shown in Figure 3.11 (a view parallel to the anionic layers and including K^+ ions is provided in Figure 3.12), and selected bond distances and angles are given in Table 3.17. Short Cu-Cu contacts are also present (2.785(1) and 2.793(1) Å) and are characteristic of well known d^{10}-d^{10} interactions [30].

Although relatively rare for the early lanthanides in general, octahedral coordination are seen in the $ALnQ_2$ series of compounds which possess either NaCl or α-$NaFeO_2$ structure types [23,31]. The Ce-S distances for $K_2Cu_2CeS_4$ are 2.737(1) Å and 2.744(1) Å in the equatorial positions and 2.718(2) Å in the axial positions. These are unusually short Ce-S bonds for six coordinate Ce. Poix has tabulated the average Ce-S bond for six coordinate Ce^{3+} as 2.93 Å [32], and in $KCeS_2$, which adopts the α-$NaFeO_2$ structure type (a derivative of NaCl), the Ce-S distance is 2.878 Å [23]. The Cu-S distances in $K_2Cu_2CeS_4$ exhibit nothing unusual (range: 2.334(2)-2.418(2) Å, average: 2.382(3) Å).

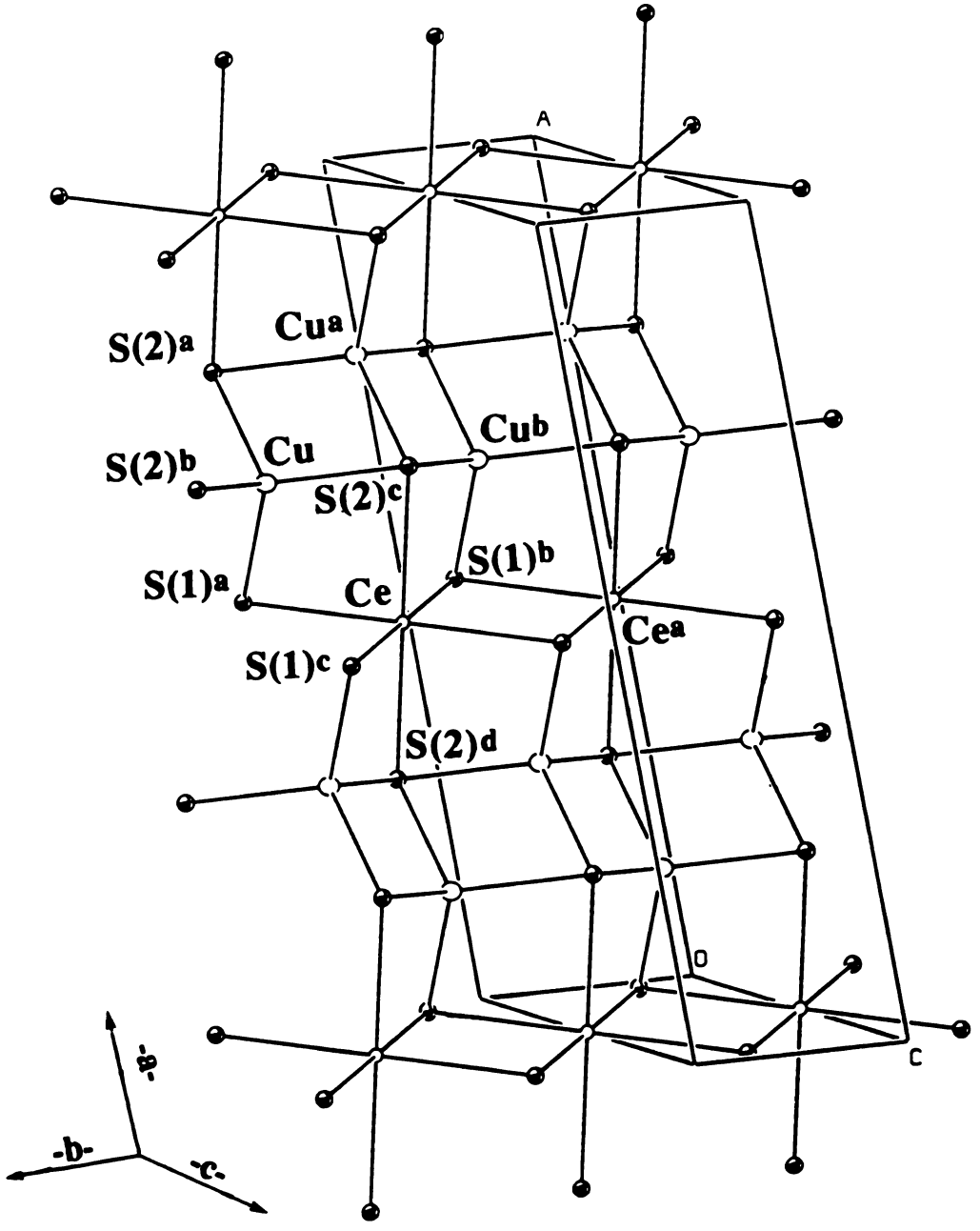

Figure 3.11: The view of a single anionic layer of $K_2Cu_2CeS_4$ (Large open circles: Cu; small open circles: Ce; circles with shaded octants: S)

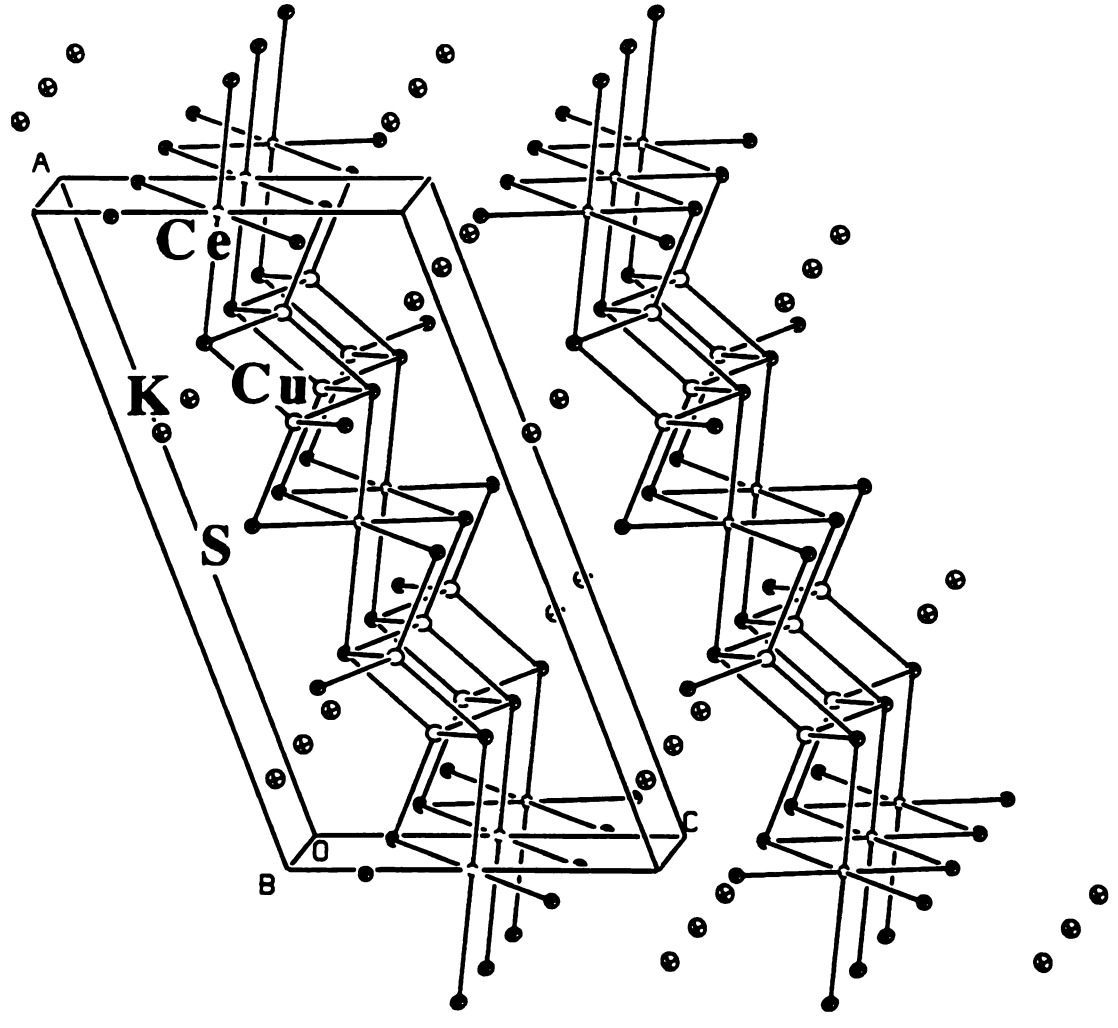

Figure 3.12: The extended structure of $K_2Cu_2CeS_4$ as seen down the b-axis, parallel to the anionic layers (Circles with nonshaded octants: K; large open circles: Cu; small open circles: Ce; circles with shaded octants: S)

Table 3.16: Fractional Atomic Coordinates and B_{eq} values for $K_2Cu_2CeS_4$ with Estimated Standard Deviations in Parentheses

atom	x	y	z	B_{eq}
Ce	0	0	0.5	0.40(2)
Cu	-0.17940(6)	-1/2	0.5132(1)	0.88(3)
K	0.1367(1)	0	0.0623(2)	0.99(5)
S(1)	-0.0198(1)	-1/2	0.7374(2)	0.59(5)
S(2)	0.2001(1)	0	0.6744(2)	0.64(6)

[a] B values for anisotropically refined atoms are given in the form of the isotropic equivalent displacement parameters defined as $B_{eq} = (4/3)[a^2B(1,1) + b^2B(2,2) + c^2B(3,3) + ab(\cos\gamma)B(1,2) + ac(\cos\beta)B(1,3) + bc(\cos\alpha)B(2,3)$.

Table 3.17: Selected Bond Distances (Å) and Angles (°) for $K_2Cu_2CeS_4$ with standard deviations in parentheses.

Ce-S(1)^a	2.744(1) (x2)	Cu-S(2)^a	2.418(2)
Ce-S(1)^{b,c}	2.737(1)	Cu-S(2)^b	2.387(1)
Ce-S(2)^{c,d}	2.718(2)	Cu-S(2)^c	2.391(1)
		Cu-S(1)^a	2.334(2)
S(1)^a-Ce-S(1)^b	92.54(6)	S(1)^a-Cu-S(2)^a	109.30(7)
S(1)^a-Ce-S(1)^c	87.46(2)	S(1)^a-Cu-S(2)^b	108.77(5)
S(1)^a-Ce-S(2)^c	89.26(4)	S(1)^a-Cu-S(2)^c	108.61(5)
S(1)^a-Ce-S(2)^d	90.74(4)	S(2)^a-Cu-S(2)^b	108.92(5)
S(1)^b-Ce-S(2)^c	89.42(4)	S(2)^a-Cu-S(2)^c	109.22(5)
S(1)^b-Ce-S(2)^d	90.58(4)	S(2)^b-Cu-S(2)^c	112.00(8)
Ce-S(1)^b-Ce^a	92.54(6)	Cu-S(2)^c-Cu^b	112.00(8)
		Cu-S(2)^c-Cu^a	71.08(5)
		Cu^a-S(2)^a-Cu^b	70.78(5)

$K_2Cu_2CeS_4$ represents a new structure type but is closely related to that of Mg_2SiO_4 (olivine) [33]. Olivine features a hexagonal closest packed net of oxygen atoms with Mg^{2+} occupying 1/2 the octahedral sites in each layer and Si^{4+} occupying 1/4 of the tetrahedral sites in every other layer. Few ternary chalcogenides adopt this structure [34], but it has recently been found to form for the quaternary chalcogenides $CaYbInQ_4$ (Q=S, Se) [35], where the Ca^{2+} and Yb^{3+} occupy the Mg^{2+} sites and In^{3+}, the Si^{4+} sites. This leads to $(YbInS_4)^{2-}$ layers similar to the anionic layers in $K_2Cu_2CeS_4$. The differences between $K_2Cu_2CeS_4$ and olivine occur in two ways. First, and most obviously, there are twice as many Td sites occupied in $K_2Cu_2CeS_4$ as there are in olivine. Second, while the Td sites in $K_2Cu_2CeS_4$ are coordinated to one axial S of a neighboring chain of octahedra, in olivine, the analogous bond is made to an equatorial atom. The chains are, thus, shifted away from the olivine type of orientation. This also leads to a different coordination environment around the interlayer K^+, that of a seven-coordinate, irregular polyhedron.

Another closely related structure is $FeTaTe_3$ [36]. It possesses layers similar to those in $K_2Cu_2CeS_4$ except that $[TaTe_6]$ octahedra form edge-sharing double chains, rather than single chains, which then are linked by edge-sharing $[FeTe_4]$ tetrahedra in the manner of $K_2Cu_2CeS_4$. Such layers were also recently reported in the anionic framework of $NaCuTiS_3$ and $NaCuZrQ_3$ (Q=Se, Te) [16].

Although the formal valence charges in $ACuM_2Q_6$ balance nicely, uncertainties exist for $K_2Cu_2CeS_4$. Formally, two extremes on the valence of the Cu and Ce could exist: either $K_2(Cu^{1+})_2(Ce^{4+})S_4$ or $K_2(Cu^{1+})(Cu^{2+})(Ce^{3+})S_4$. Chemically, neither extreme is favorable since both Cu^{2+} and Ce^{4+} are too oxidizing to exist in conjunction with S^{2-}, and

no examples of either have ever been confirmed. Rather than form these high oxidation states, phases tend to either form oxidized disulfide bonds to the extent necessary to achieve charge balance, as in CuS [37] and CeS2 [38], or possess a mixture of S^{2-} and S^{1-} oxidation states, as in KCu_4S_3 [39]. The closest S-S distance in $K_2Cu_2CeS_4$ is only 3.783(4) Å, ruling out the possibility of disulfide formation, and so a reasonable formalism may be $K_2(Cu^{1+})_2(Ce^{3+})(S^{2-})_3(S^{1-})$. Such a compound would be paramagnetic, due to the $4f^1$ electron of Ce^{3+}, and if the S^{1-} hole were to be delocalized throughout the sulfur 3p band as in KCu_4S_3, p-type metallic behavior should be observed [40]. The formalism using all Ce^{4+} would be a diamagnetic semi-conductor. Hence, magnetic and conductivity measurements would be useful in elucidating the various oxidation state ambiguities present in this compound.

Magnetic Susceptibility Studies -- The temperature dependent magnetic susceptibility of $K_2Cu_2CeS_4$, taken at 1000 Gauss over 2-300 K, is shown in Figure 3.13. No clear Curie-Weiss portion of the data exist although the data drop off much more rapidly below 150 K than above. To estimate the level of magnetization of $K_2Cu_2CeS_4$ in the region above 150 K, Curie-Weiss behavior was approximated by applying a linear curve fit to the data, resulting in a μ_{eff} of 2.38 BM/formula and a very large θ of -440 K. This corresponds to the value previously discussed for a Ce^{3+} ion and is consistent with the formalism in which a localized Ce^{3+} is charge balanced by a delocalized S^{1-} state.

As noted in the magnetics of $ACuM_2Q_6$, Ce^{3+} compounds typically have a certain degree of non-Curie-Weiss behavior to their paramagnetic response. The main source of this effect is the weak crystal field splitting of the ion's $^2F_{5/2}$ ground state although it has been shown that different amounts of superexchange are possible through the excited and ground states and that this exchange anisotropy contributes to the shape of the $1/\chi_M$ vs. T curve. Such behavior was modeled for the Ce^{3+} in $NaCeS_2$ by Lueken et al. [28]. Attempts to fit our data to that model have yet to produce a consistent set of parameters, probably due to CeO_2 and possibly other impurities present in the microcrystalline samples of $K_2Cu_2CeS_4$. However, such treatments do indicate a large amount of antiferromagnetic superexchange taking place through the excited state. If accurate, a hole in the sulfur 3p band may be playing a role in facilitating this exchange as is thought to occur in the spinel compounds $CuCr_2Q_4$ (Q=S, Se,Te) [41].

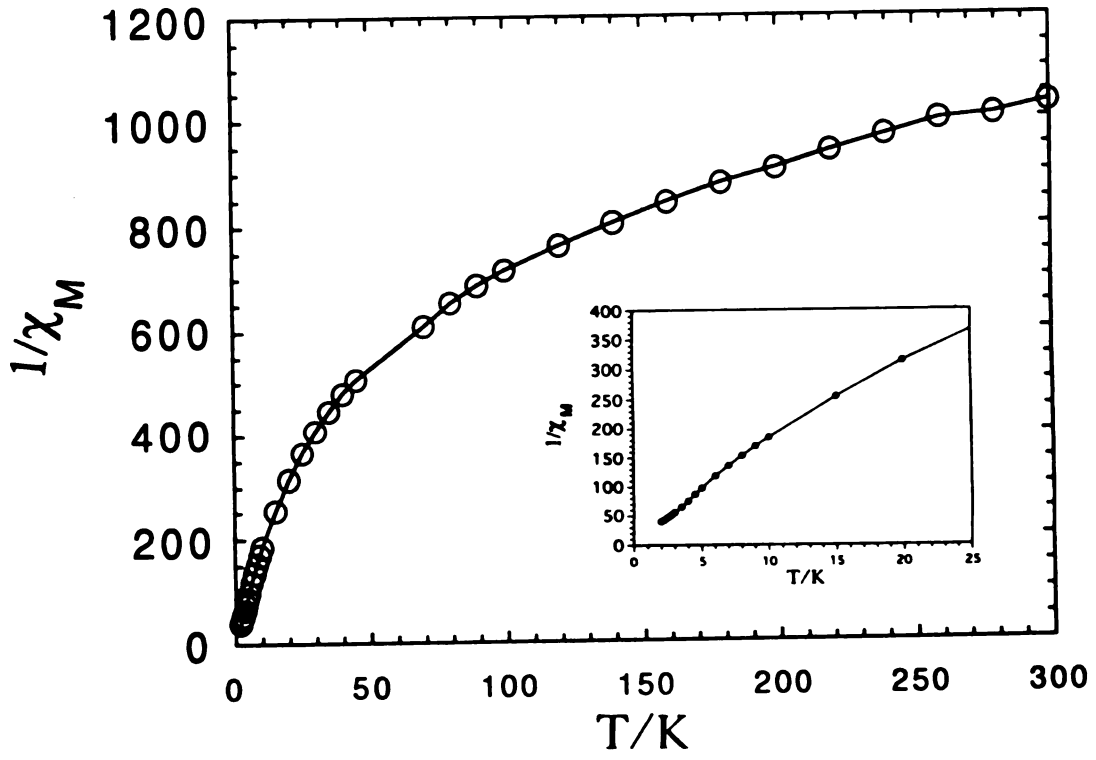

Figure 3.13: Inverse molar magnetic susceptibility ($1/\chi_M$) plotted against temperature (2-300 K) for $K_2Cu_2CeS_4$ (1000 Gauss). The inset graph shows an expanded view of the region 2-25 K.

Charge-Transport Measurements -- The mixed S^{2-}/S^{1-} oxidation state model for $K_2Cu_2CeS_4$ suggests that the compound would exhibit significant charge transport properties. This, however, is not supported in experiments on the material's single crystal conductivity. Variable temperature measurements shown in Figure 3.14 reveal decreasing conductivity with falling temperatures, the characteristic behavior of semiconductors rather than metals. The low magnitude of the room temperature conductivity (ca. 10^{-3} S/cm) also indicates semiconducting behavior. These results were consistently reproduced using crystals from different synthetic batches.

Although the effects of grain boundaries in polycrystalline pellets generally complicate the interpretation of electrical conductivity data, this is not the case with thermopower (TP) measurements [42]. Because the technique is essentially zero-current and as such independent of sample defects or grain boundaries, TP measurements are very reliable in determining a sample's charge transport type. The TP response as a function of temperature of a polycrystalline pressed pellet of $K_2Cu_2CeS_4$ is shown in Figure 3.15. The positive values confirm that holes are the dominant charge carriers, and this is in keeping with the mixed valent model which places holes on the sulfur p-band. Although the trend of a decreasing TP tending towards zero with falling temperature is consistent with metallic behavior, the magnitude of the TP values is much larger than would be expected for a metallic compound. Below 150 K, the sample became too resistive to give reliable data.

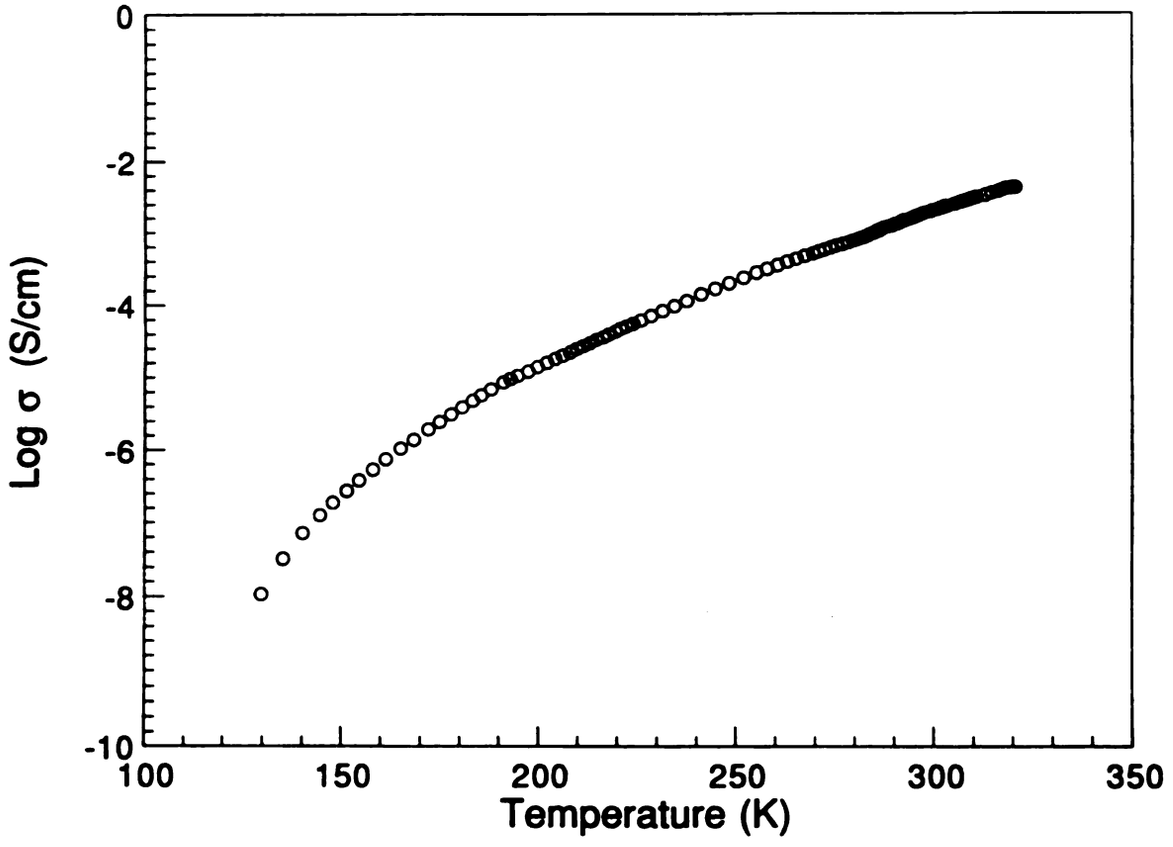

Figure 3.14: Conductivity (log S/cm) plotted against temperature (K) for a pressed pellet sample of $K_2Cu_2CeS_4$

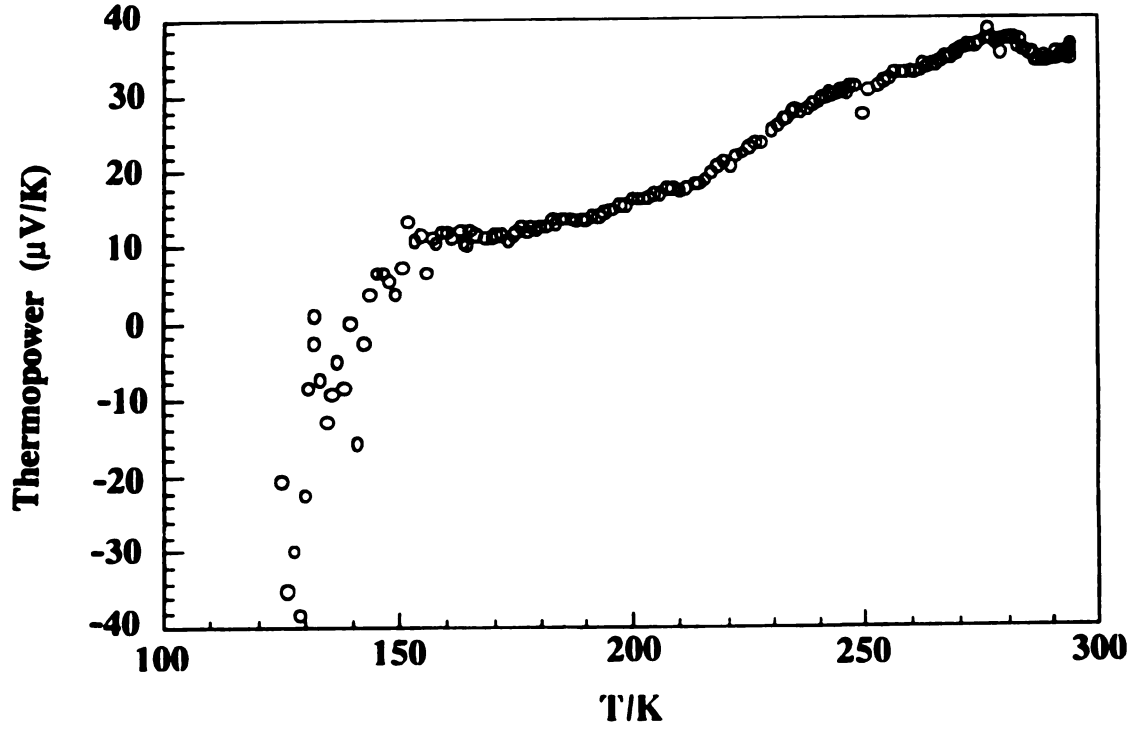

Figure 3.15: Thermopower (μV/K) plotted against temperature (K) for a pressed pellet sample of $K_2Cu_2CeS_4$

Explanations for these results lie in considering the pathways of conduction through the structure of $K_2Cu_2CeS_4$. Although discussed as a layered material, conduction would in fact primarily take place via the chains of edge-sharing [CuS4] tetrahedra. This is because the Ce^{3+} are largely ionic in their bonding, with the 4f orbitals buried among the core electrons and the valence 5d, 6s, and 6p orbitals too high in energy to contribute significantly to the valence band comprised mainly of sulfur 3p orbitals. As such the valence band along the direction from chain to chain would be extremely narrow, leaving the $[CuS_2]_n$ chain as the preferred route of conduction. Band width in the direction parallel to these chains would also be very narrow due to the orbital overlap being restricted to one dimension. Besides requiring that the single crystal orientation be precisely known, a one dimensional conduction pathway for $K_2Cu_2CeS_4$ would make it very susceptible to crystal defects which would break the $[CuS_2]_n$ chains, thus rupturing the conduction pathways. Conduction would then rely on thermal excitation of electrons across defect boundaries, leading to a semiconductor style response.

Although undoubtedly a factor, defects and misoriented crystals do not account for the high values of the TP measurements because the technique is independent of such variables. A further explanation is that the narrow valence bands of $K_2Cu_2CeS_4$ may be enough to result in the formation of small polarons in the material. A polaron is simply a charge carrier, be it electron or hole, which is trapped in the potential which it induces in the field around it. The mobility of the carrier is then limited by having to drag the induced field around with it. Key to the formation and subsequent low mobility of small polarons is a very narrow band for the polaron to travel in. This increases the effective mass of the carrier

and decreases the mean free path of the polaron. Hence, small polaron formation leads to the effective localization of the carrier and conduction can only proceed via thermal excitation from site to site. Such behavior has been described theoretically by Austin and Mott [43] and studied in semiconducting $V_2O_5 \cdot nH_2O$ xerogels [44]. Usually the phenomenon is used to explain semiconducting properties in transition metal oxides which, through crystal defects, possess a small amount of metal ions in mixed oxidation states. Such a conducting mechanism would explain the observed behavior in $K_2Cu_2CeS_4$. If localized as small polarons, then some unusual coupling scheme must be rendering the S^{1-} magnetically silent as well. This could also contribute to the sharply deviating $1/\chi_M$ vs. T response already discussed.

Spectroscopy -- Diffuse reflectance measurements on $K_2Cu_2CeS_4$ show no absorption edge, and hence no band gap, in the region of 250-2500 nm. The level of reflectance remained low ($\leq$10%) throughout the region with both $BaSO_4$ and CdS used as 100% reflectance standards.

The solid state far-IR spectrum of $K_2Cu_2CeS_4$ shows three strong peaks all of which occur in the region of Ce-S stretching: 272, 213, and 159 cm^{-1}. Apparently any IR activity from Cu-S is either too weak to be seen or is simply IR inactive.

3. $ACuMQ_3$ (A=Cs, M=Ce, Q=S; or A=K, M=U, Q=Se)

Structure -- The structure of the $ACuMQ_3$ phases have several features in common with the previous quaternary phase, $K_2Cu_2CeS_4$. The f-block metal is coordinated to an octahedron of monochalcogenides. These $[MQ_6]$ units edge-share with each other, again forming one-dimensional chains, this time parallel to the a-axis. In the $ACuMQ_3$ structure, these chains of octahedra are not separate from each other as they were in $K_2Cu_2CeS_4$, but rather fuse through corner-sharing into a corrugated two-dimensional sheet (Figure 3.16). The overall anionic network remains layered as the Cu^+ cations occupy tetrahedral sites in the folds of the layers of octahedra (Figure 3.17) and so provide no extra dimensionality to the framework. As usual, alkali cations occupy sites within the interlayer galleries. If the Cu^+ were to be ignored, the remaining atoms would possess the anti-Pd_3Te_2 structure type in which Te atoms occupy both the octahedral sites and the interlayer gallery positions [45]. An example of a ternary compound with this structure is $BaIrO_3$ [46]. Interestingly, $BaUS_3$ is a known phase as well [47] but possesses a distorted perovskite structure in which $[US_6]$ octahedra corner-share in three-dimensions, rather forming the two-dimensional layers of $ACuMQ_3$. Although this structure type has not been seen before in f-block/chalcogenide chemistry, it has recently been reported to form for several phases with tetravalent early transition metal cations [15,16].

Bond distances for $CsCuCeS_3$ are summarized in Table 3.18 and follow the patterns seen in $K_2Cu_2CeS_4$. While the Cu-S distances remain consistent with those that have been observed in other phases, the Ce-S distances are slightly shorter than is normal (2.712 Å and 2.730 Å vs. 2.93 Å for an average 6-coordinate Ce^{3+} [32]). For $KCuUSe_3$ (Table 3.18) bond

distances about both the U and Cu are as expected. The atomic coordinates for $CsCuCeS_3$ are given in Table 3.19 and for $KCuUSe_3$, in Table 3.20.

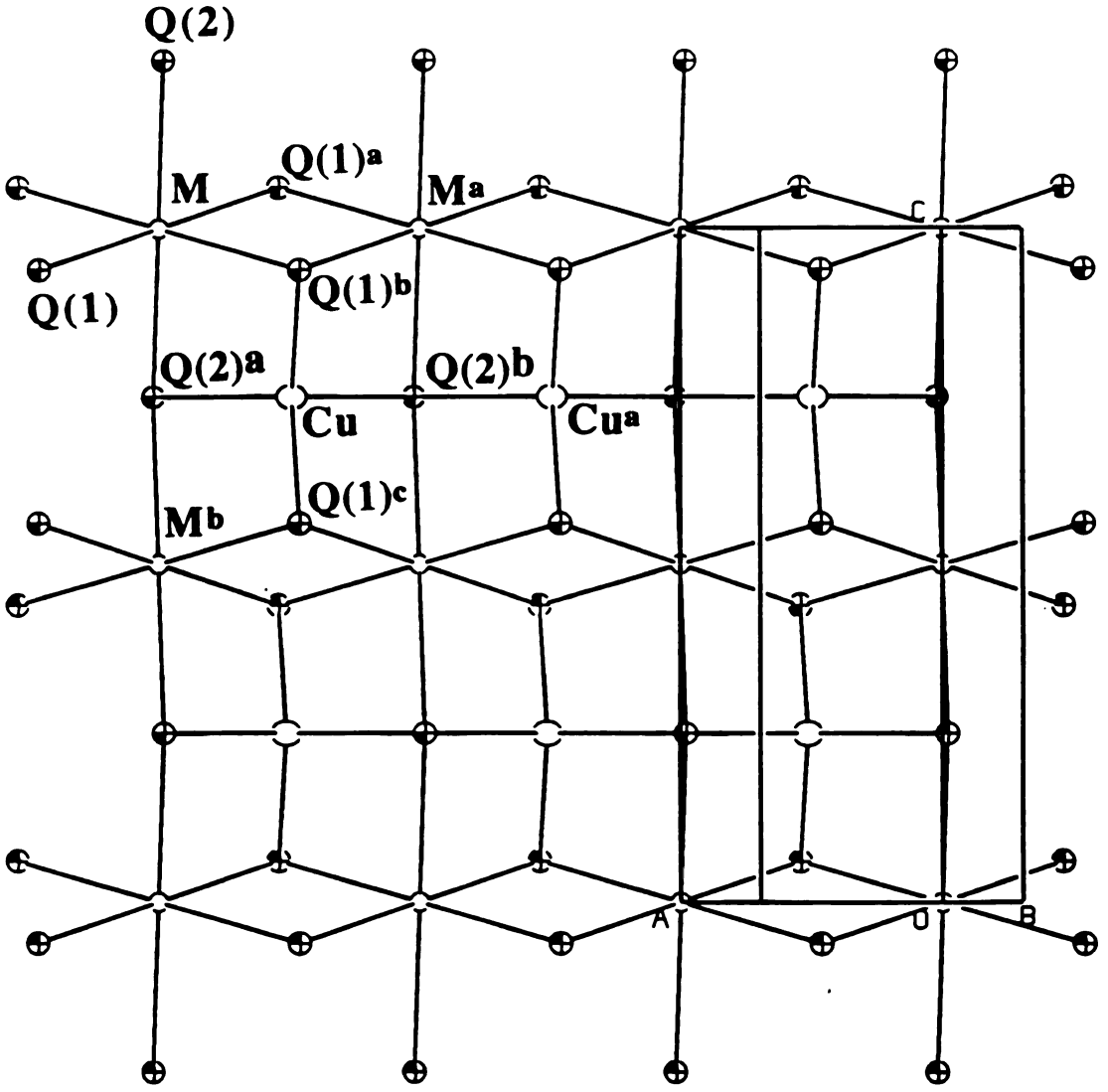

Figure 3.16: The view perpendicular to a single anionic layer of the $ACuMQ_3$ structure type, where A=Cs, M=Ce, Q=S; or A=K, M=U, Q=Se (Large open circles: Cu; small open circles: M, circles with shaded octants: Q)

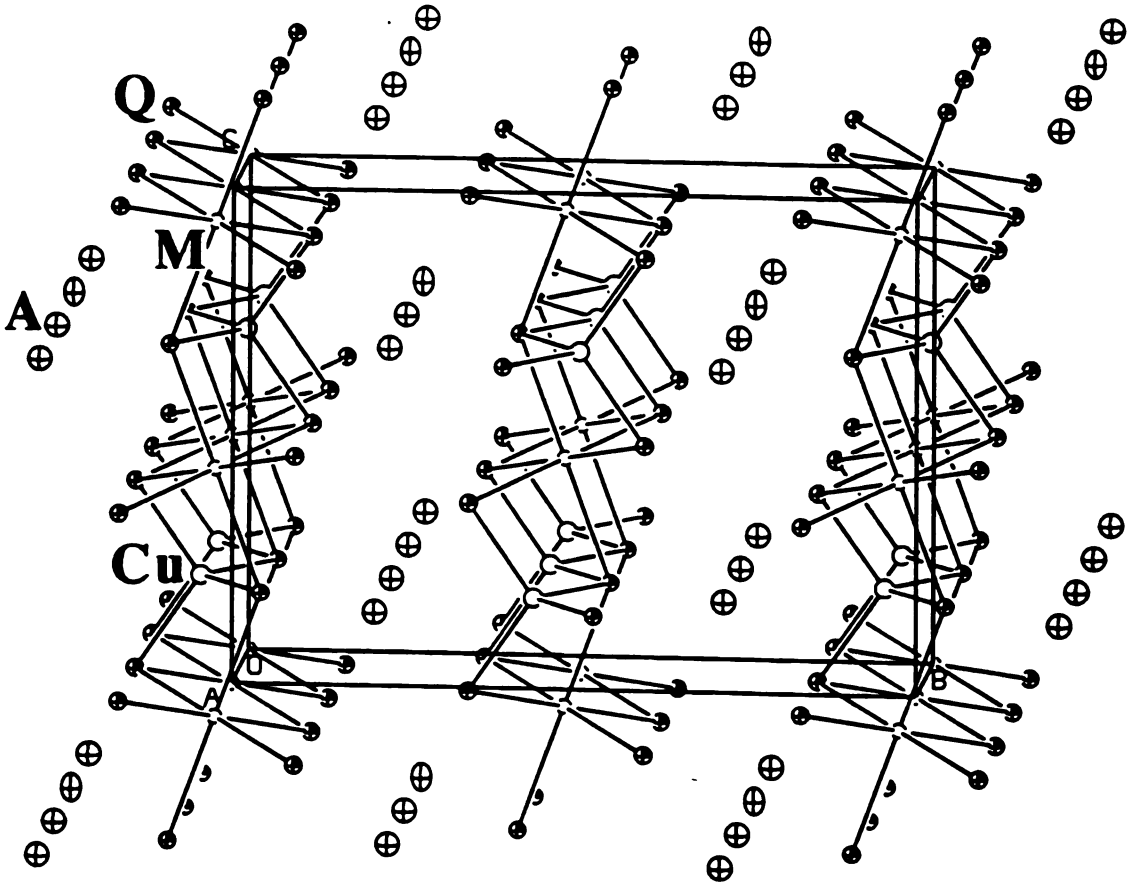

Figure 3.17: The $ACuMQ_3$ structure type (A=Cs, M=Ce, Q=S; or A=K, M=U, Q=Se) as seen down the a-axis, parallel to the anionic layers (circles with nonshaded octants: A; large open circles: Cu; small open circles: M, circles with shaded octants: Q)

Table 3.18: Selected Bond Distances and Angles for $CsCuCeS_3$ and $KCuUSe_3$ with standard deviations in parentheses.

	$CsCuCeS_3$	$KCuUSe_3$
M-Q(1)	2.730(2)	2.848(1)
M-Q(2)	2.712(1)	2.839(1)
Cu-Q(1)	2.319(3)	2.447(3)
Cu-Q(2)	2.413(2)	2.514(3)
A-Q(2)	3.474(3)	3.299(5)
$Q(1)$-M-$Q(1)^a$	180.00	180.00
$Q(1)$-M-$Q(1)^b$	94.93(9)	92.41(5)
$Q(1)^a$-M-$Q(1)^b$	85.07(9)	87.59(5)
$Q(1)^a$-M-Q(2)	91.41(7)	90.47(5)
$Q(1)^b$-M-Q(2)	88.59(7)	89.53(5)
Q(2)-M-$Q(2)^a$	180.00	180.00
$Q(1)^b$-Cu-$Q(1)^c$	116.7(1)	111.1(2)
$Q(1)^b$-Cu-$Q(2)^a$	106.84(5)	108.99(3)
$Q(2)^a$-Cu-$Q(2)^b$	113.0(2)	109.7(2)
M-Q(1)-M^a	94.93(9)	92.41(5)
M-$Q(1)^b$-Cu	81.77(7)	79.58(6)
M-Q(2)-M^b	145.3(1)	140.1(1)
M-$Q(2)^a$-Cu	80.53(6)	78.67(4)
Cu-$Q(2)^b$-Cu^a	113.0(2)	109.7(2)

Table 3.19: Fractional Atomic Coordinates and B_{eq}[a] values for $CsCuCeS_3$ with Estimated Standard Deviations in Parentheses

atom	x	y	z	B(eq)[a]
Ce	0	0	1/2	0.42(3)
Cu	0	0.5345(1)	1/4	0.74(6)
Cs	0	0.25980(6)	1/4	0.92(3)
S(1)	0	-0.0533(2)	1/4	0.5(1)
S(2)	0	0.3851(2)	0.5593(2)	0.66(8)

[a] B values for anisotropically refined atoms are given in the form of the isotropic equivalent displacement parameters defined as $B_{eq} = (4/3)[a^2B(1,1) + b^2B(2,2) + c^2B(3,3) + ab(\cos\gamma)B(1,2) + ac(\cos\beta)B(1,3) + bc(\cos\alpha)B(2,3)$.

Table 3.20: Fractional Atomic Coordinates and B_{eq}[a] values for $KCuUSe_3$ with Estimated Standard Deviations in Parentheses

atom	x	y	z	B(eq)[a]
U	0	0	1/2	0.74(3)
Cu	-1/2	-0.0331(2)	1/4	1.4(1)
K	-1/2	-0.2458(4)	3/4	2.0(2)
Se(1)	-1/2	-0.1289(1)	0.4390(1)	1.02(6)
Se(2)	0	0.0671(2)	1/4	0.95(8)

[a] B values for anisotropically refined atoms are given in the form of the isotropic equivalent displacement parameters defined as $B_{eq} = (4/3)[a^2B(1,1) + b^2B(2,2) + c^2B(3,3) + ab(\cos\gamma)B(1,2) + ac(\cos\beta)B(1,3) + bc(\cos\alpha)B(2,3)$.

In another similarity to $K_2Cu_2CeS_4$, the formal oxidation states of the elements in $CsCuCeS_3$ do not balance with the known chemical limitations of Cu and Ce in their sulfide chemistries. A formalism with all S^{2-} would require either a Cu^{2+} or Ce^{4+} to achieve charge neutrality, and since both are very oxidizing relative to S^{2-}, there is again the likelihood of an S^{1-} state being present but delocalized through the sulfur 3p band. That this phenomenon reoccurs in conjunction with shortened Ce-S bonds appears to indicate that the lanthanide is particularly sensitive to changes in the "charge" on the S atoms. This is consistent with the highly ionic nature of Ln bonding; a reduction in charge on the S atoms would mean a reduction in their average ionic radii and so would shrink the Ce-S bonds. Bonds between Cu and S, being highly covalent, would be much less affected.

Mixed oxidation states on the chalcogenides of $KCuUSe_3$ are not expected. U^{4+} is very common in all its chalcogenide chemistry, and so with the formalism $K(Cu^{+})(U^{4+})(Se^{2-})_3$, the compound is expected to be a semiconductor.

Magnetic Susceptibility -- The magnetic response of $CsCuCeS_3$ takes on extra significance because in addition to the search for unusual magnetic phenomenon, it can also be used to support the $Cs(Cu^{+})(Ce^{3+})(S^{2-})2(S^{1-})$ formalism. The temperature dependent magnetic susceptibility of $CsCuCeS_3$ is shown in Figure 3.18. Empirically, it is very similar to that of $K_2Cu_2CeS_4$; the plot of $1/\chi_M$ vs. T has a continually changing slope but one which increases more rapidly below 150 K than above. Quantitatively, however, the data are quite different. Over several trials, the average μ_{eff} (from 160-300 K) was found to be 1.8 BM, much less than both the theoretically and experimentally expected values. A large q value is also present (-150 K) Although the presence of paramagnetism rules out the formalism invoking a Ce^{4+}, which would be diamagnetic $(Cs(Cu^{+})(Ce^{4+})(S^{2-})_3)$, the exact nature of the oxidation states remains unclear.

Several possible explanations exist. First, and most likely, is the presence of amorphous impurities. The powder X-ray diffraction patterns of samples taken before and after measurement were identical and, at most, indicated a few percent of CeO_2 contamination. Powder diffraction will only detect crystalline impurities, however. Any amorphous species would remain invisible to this technique, and the microcrystalline nature of the sample makes amorphous components difficult to detect visually, even with the aid of light microscopes. Perhaps an amorphous oxide even forms on the surface of powders, oxidizing the accessible Ce^{3+} to Ce^{4+}. The μ_{eff} values of $K_2Cu_2CeS_4$ were observed to decrease over time, and perhaps whatever phenomenon drove that change is at work in $CsCuCeS_3$ as well.

Another possible source of the small μ_{eff} is that some unknown crystal field affect may be increasing the energy separation between the

ground and excited states more than is normally observed. Such a model would make the ground state more likely to be populated and so would result in a lower μ_{eff}.

The large negative value for θ indicates a large amount of local antiferromagnetic ordering, and if such an effect is carrying over to the room temperature regime then this may also serve to drive down the μ_{eff}. The magnetic response of $K_2Cu_2CeS_4$ also exhibited a large θ (-440 K) but possessed a more conventional μ_{eff} (2.38 BM). Although both structures feature Ce^{3+} cations in octahedra of S atoms, recall that in $K_2Cu_2CeS_4$ these octahedra edge-share in one dimension whereas those in $CsCuCeS_3$ form a two-dimensional network of edge- and corner-sharing octahedra. Perhaps the extended Ce-S bonding in $CsCuCeS_3$ is enhancing sulfur mediated antiferromagnetic superexchange between the Ce^{3+} cations, leading to the low μ_{eff} values. As in $K_2Cu_2CeS_4$, a hole in the sulfur 3p band may also be playing a role in facilitating this exchange as is thought to occur in the spinel compounds CuCr2Q4 (Q=S, Se, Te) [41].

Barring any impurity or coupling effects, the low μ_{eff} of $CsCuCeS_3$ make speculation on the presence of Ce^{4+} cations in the lattice tempting; however, the lack of precedents for such a valence in a sulfide environment causes such speculations to be viewed skeptically. More detailed studies on samples of exceptional purity (preferably ground from large single crystals) would be needed before any claim to an unprecedented Ce valance is made.

Fig

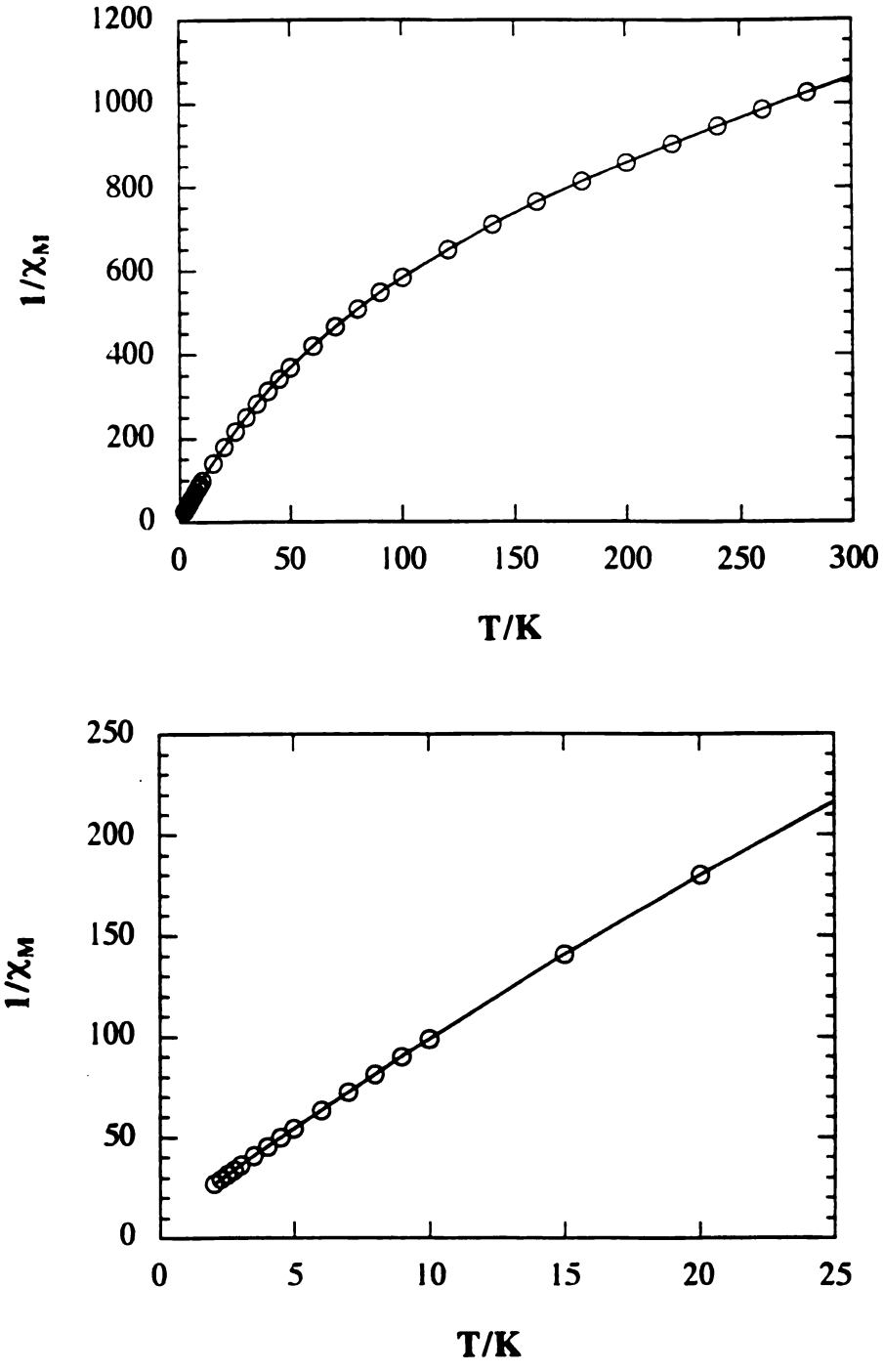

Figure 3.18: Inverse molar magnetic susceptibility ($1/\chi_M$) plotted against temperature (2-300 K) for $CsCuCeS_3$ (1000 Gauss). Plot (B) shows an expanded view of the region 2-25 K.

The magnetic behavior of $KCuUSe_3$ is somewhat more straight forward. The $1/\chi_M$ vs. T plot of data taken at 5000 Gauss (Figure 3.19) is actually similar to that of $CsCuCeS_3$ in that the data have no straight line region but change slope much more dramatically as the temperature is lowered. For T>150 K, a μ_{eff} of 3.65 BM and a θ of -378 K were estimated by fitting a straight line to the data. The μ_{eff} is consistent with that expected for a U^{4+} (3.58 BM) [28], and the value for θ indicates a large amount of local antiferromagnetic ordering. The rapidly changing slope of the data at low temperature suggests that the U^{4+} is experiencing some of the same crystal field effects in this lattice that are observed for Ce^{3+} in $K_2Cu_2CeS_4$ and $CsCuCeS_3$. Because the 5f orbitals are less shielded by the valence electrons than the more contracted 4f orbitals of the lanthanides, U^{4+} has exhibited pronounced crystal field effects in several dilute salt paramagnetic compounds such as UCl_4•4MeCN, UBr_4•4MeCN, UCl_4•2Et_2NH, UCl_4•2 bipyridine, and others [48]. The influence of a crystal field can also have a dramatic affect on the μ_{eff} of the compound. Many of the salts mentioned above have quite low μ_{eff} values (2.61-2.92 BM [48]), but in various transition metal/U/chalcogenide solid state compounds, μ_{eff} values for the U^{4+} were estimated from 3.0-3.6 BM [49].

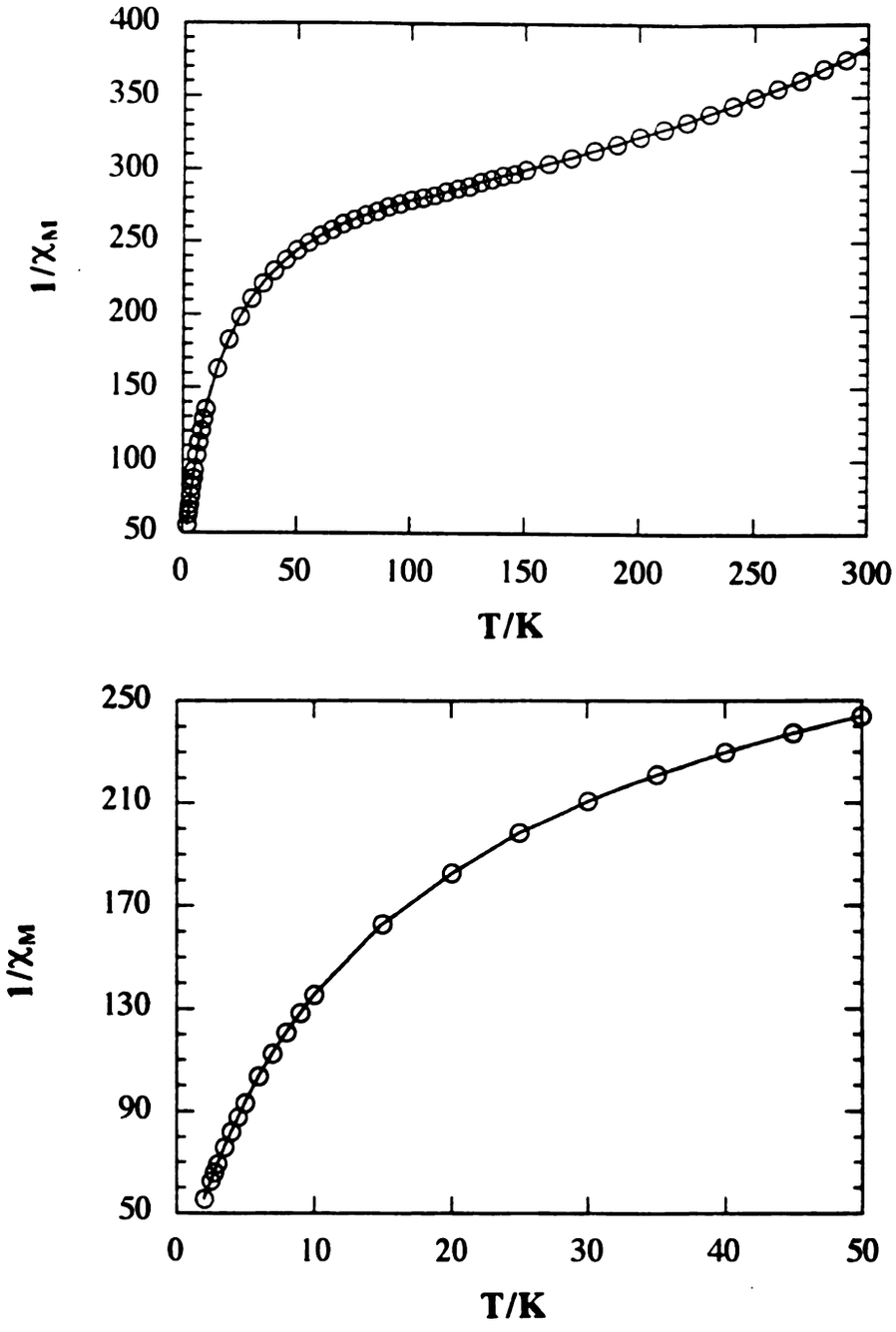

Figure 3.19: Inverse molar magnetic susceptibility ($1/\chi_M$) plotted against temperature (2-300 K) for $KCuUSe_3$ (5000 Gauss). Plot (B) shows an expanded view of the region 2-50 K.

Spectroscopy -- Being black, both $KCuUSe_3$ and $CsCuCeS_3$ showed total absorbance in their diffuse reflectance spectra (500-2500 nm). This indicates either metallic compounds or band gaps lower than 0.5 eV.

The far-IR spectrum of $CsCuCeS_3$ shows four strong peaks at 288, 262, 227, and 205 cm^{-1}. All of them can be reasonably assigned as Ce-S vibrations since peaks in this region have been observed in the spectra of other Ce/S compounds. The region in which the stretching vibrations of Cu-S are commonly seen (ca. 430 cm^{-1}) remains blank.

For $KCuUSe_3$, three strong peaks at 195, 190, and 145, and one very weak one at 130 cm^{-1} are all in the realm of previously seen U-Se vibrations. For example, in K_4USe_8 peaks were observed at 168 and 153 cm^{-1}. No other spectral features are present and so the Cu-Se bands remain unobserved as did the Cu-S bands of $CsCuCeS_3$.

Charge transport measurements -- Figure 3.20 shows a plot of conductivity vs. temperature for a pressed pellet sample of $CsCuCeS_3$. The data show an increasing conductivity with increasing temperature, the characteristic property of semiconductors. This may arise because of the polycrystalline nature of the pressed pellet samples in which current must traverse the grain boundaries between crystallites, a thermally activated process. Despite this a fairly high conductivity is achieved at room temperature: 1 S/cm. In general, polycrystalline pressed pellets are 1000 times less conductive than single crystals, and so a conductivity of 1000 S/cm could, in fact , be possible.

The thermopower response of $CsCuCeS_3$ with changing temperature is shown in Figure 3.21. As stated in the discussion for $K_2Cu_2CeS_4$, thermopower is a zero current technique and thus gives information on the charge transport properties of the sample despite grain boundaries. The positive values for the thermopower indicate holes as the primary charge carriers, consistent with a delocalized S^{1-} oxidation state. Both the magnitude of the thermopower values and the shape of the plot point to something other than a common metallic mechanism at work in the material's conductivity. Whatever that mechanism it appears to undergo a transition a 150 K from a temperature independent thermopower to one which tends towards zero, as metals are known to do. Some manner of carrier localization, possibly in the form of small polarons formation, may be at work in $CsCuCeS_3$ as it was in $K_2Cu_2CeS_4$.

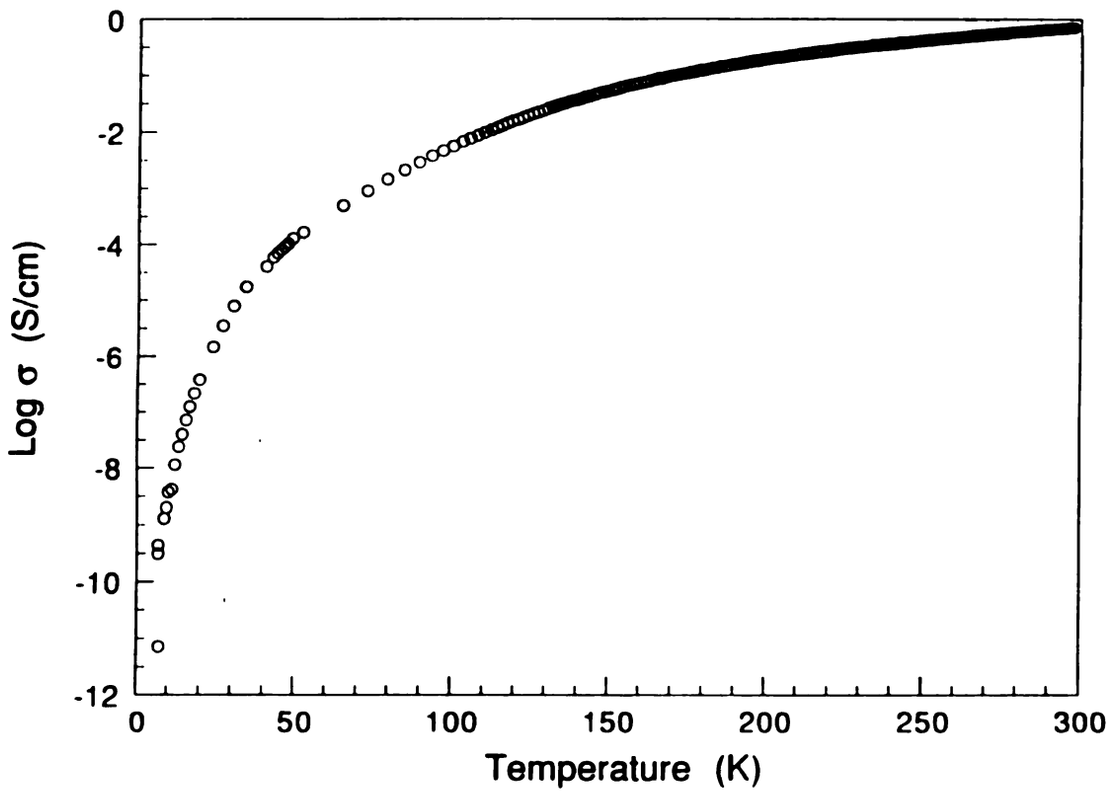

Figure 3.20: Conductivity (log S/cm) plotted against temperature (K) for a pressed pellet sample of $CsCuCeS_3$

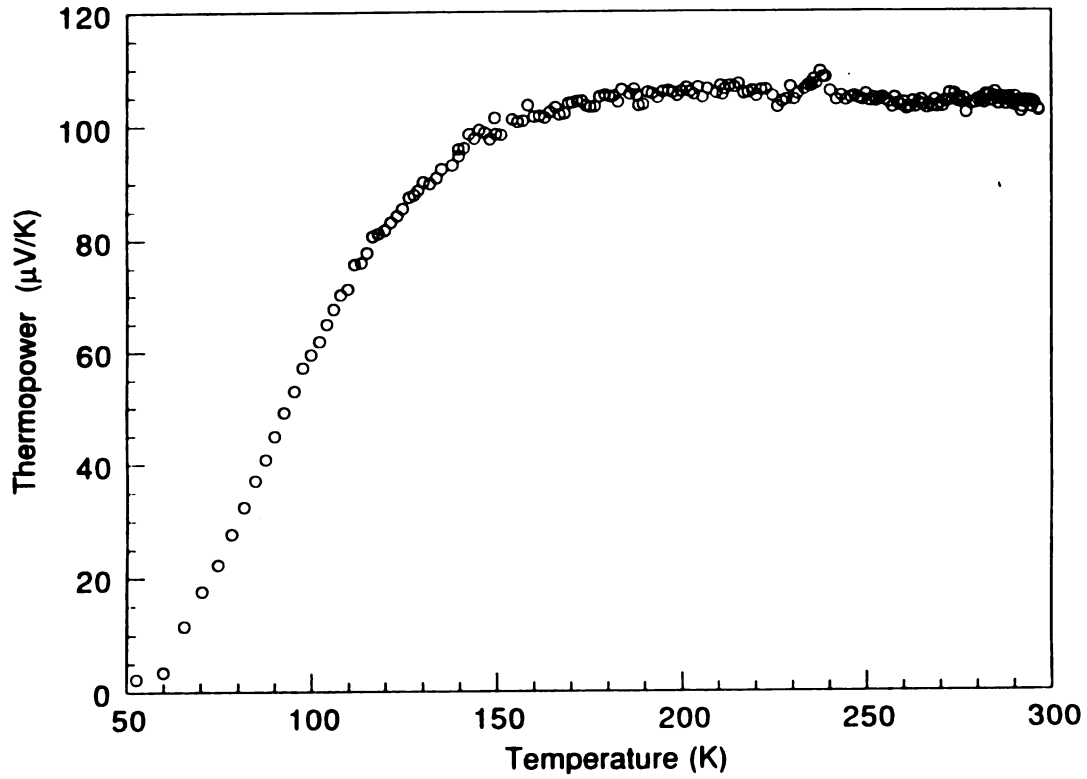

Figure 3.21: Thermopower (μV/K) plotted against temperature (K) for a pressed pellet sample of $CsCuCeS_3$

Unlike most of the compounds discussed so far, large single crystals of $KCuUSe_3$ could be easily grown from fluxes very rich in Se and at increased reaction temperatures (for example, $K_2Se/Cu/U/Se$ = 1/1/1/24 heated at 450 °C for 2 d.). Such crystals were easily manipulated for charge transport studies. Figure 3.22 shows conductivity (S/cm) plotted as a function of 1000/T for two different crystals of $KCuUSe_3$. The increasing conductivity with increasing temperatures shows unambiguously that the compound is semiconducting with a rather poor value at 300 K of $2x10^{-2}$ S/cm. From these data the activation energy to charge transport was estimated to be in the range of 0.164-0.167 eV, a very low value.

Figure 3.23 shows the thermopower measurements taken on single crystals of $KCuUSe_3$. The positive values indicate p-type carriers while the negative slope to the data is characteristic of a semiconductor.

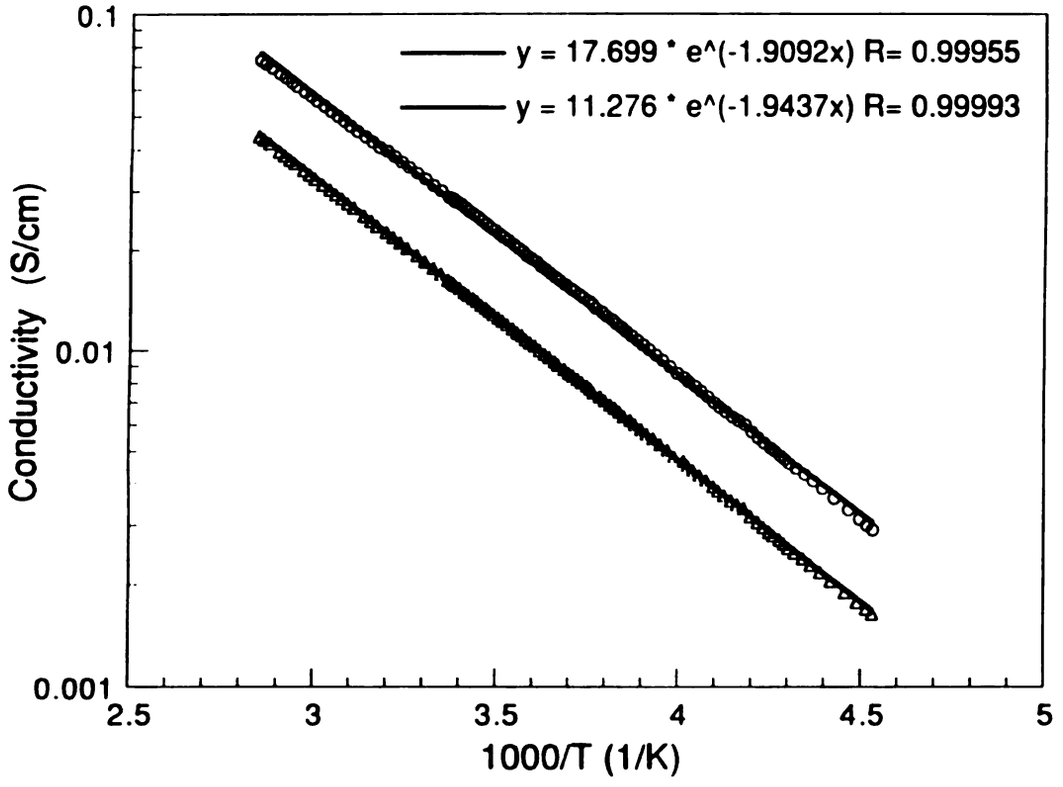

Figure 3.22: Conductivity (log S/cm) plotted against temperature (1000/K) for a pressed pellet sample of $KCuUSe_3$

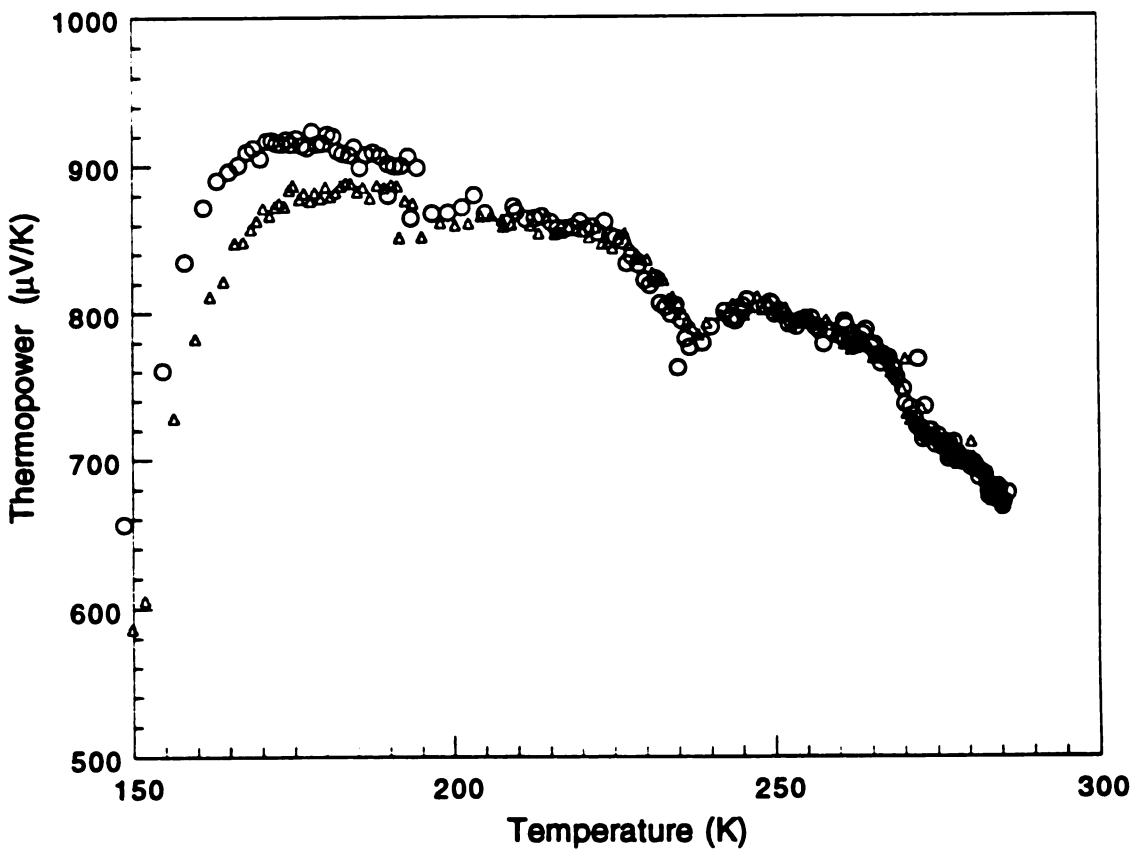

Figure 3.15: Thermopower (μV/K) plotted against temperature (K) for two different single crystals of $KCuUSe_3$

4. $K_6Cu_{12}U_2S_{15}$

Structure -- Compounds of the $ACuMQ_3$ formula had $[MQ_6]$ octahedra which, through edge- and corner-sharing, formed a two-dimensional layer. In $K_2Cu_2CeS_4$, $[MQ_6]$ units were again present, this time in a one-dimensional chain of edge-sharing octahedra. This progression of reducing $[MQ_6]$ connectivity continues with $K_6Cu_{12}U_2S_{15}$. This phase features $[US_6]$ octahedra which are totally isolated from each other but are joined into a three-dimensional lattice via bridging $[CuS_3]$ trigonal planar units.

The complex, yet elegant, structure of $K_6Cu_{12}U_2S_{15}$ is based on the exotic cubic space group Ia-3d (#230). Atomic coordinates are given in Table 3.22. The basic structural units are $[US_6]$ octahedra connected to six $[CuS_3]$ trigonal planes. Each one shares an edge with the $[US_6]$, which are located on two opposite faces of the octahedra (Figure 2.24). The remaining S atom, S(2), in the $[CuS_3]$ unit is connected to a second Cu atom, making a corner-sharing bridge to the trigonal planes of the neighboring repeating unit. This pattern continues in one dimension, resulting in columns of the type shown in Figure 2.25. The S(2) atoms simultaneously bridge trigonal planes in two neighboring chain and so act as the points of extended connectivity in the structure. The geometry about the S(2) atoms is a distorted tetrahedron with an angle between opposite edges, and hence between neighboring columns, of 110.51°. Figure 3.26 (and the accompanying stereo view in Figure 3.27) show two neighboring columns connected by an S(2) atom. With each set of three S(2) atoms on a central column, three bridges to three other columns are made. The overall affect looks similar to a barber pole except that instead of stripes wrapping around the central pole there are three other poles lying tangent

to it. The intercolumn connectivity is further complicated in that the direction of tilt between the columns is reversed from each set of S(2) connections (Figure 3.28).

This complex interweaving of columns continues through three dimensions, and one view of the result is given in Fig. 3.29, with a companion stereo view in Figure 3.30. From the direction parallel to the x-axis we see the presence of small channels running through the structure which house the compound's K^+ ions. Since the cell is cubic, such channels run in all three dimensions. Figure 3.31 shows the unit cell as seen in the [1-10] direction (stereo view Figure 3.32). This view highlights a single column running along the [111] direction with a veritable nest of neighboring columns wrapping around its midsection. Finally, Figure 3.33 and Figure 3.34, with the stereo view, show the view down one of the corners of the cell, in this case the [1-11] direction. This provides an end-on view of two columns, one approximately parallel to the [2-11] and the other at [2-10]. From all of these views it can be seen that the K^+ ions are always outside of the anionic columns; the pocket formed inside the column between the corner-sharing [CuS_3] units remains void.

Although no precedents in A/Cu/U/Q systems exist, there is one example of a structurally characterized ternary compound, $Cu_2U_6S_{13}$ [50]. The structure is dominated by uranium in either of two 8-coordinate environments: bicapped trigonal prismatic or triangulated dodecahedral. These polyhedra form a complex three-dimensional lattice into which Cu^+ occupy trigonal planar sites.

Selected bond distances for $K_6Cu_{12}U_2S_{15}$ are given in Table 3.22. All U-S(1) distances are equivalent at 2.619(5) Å. This is considerably shorter than that seen for the eight coordinate U atoms of $Cu_2U_6S_{13}$ which

range from 2.702-2.939 Å [50]. It also represents a slight decrease from that of 6-coordinate U. For example, in $BaUS_3$, which has a distorted perovskite structure, the U-S bonds range from 2.680(5)-2.709(5) Å [47]. Bond angles about the [US_6] octahedron in $K_6Cu_{12}U_2S_{15}$ are nearly ideal, with S-U-S angles defined by S atoms in the same face being slightly larger (93.0(1)°) than the "trans-facial" angles (87.0(1)Å).

Meanwhile, Cu-S bonds in $K_6Cu_{12}U_2S_{15}$ are 2.205(2) and 2.256(5) Å. For a trigonal planar Cu, these bonds are not unusual. In CuS such distances are slightly shorter at 2.192 Å [52], and trigonal planar Cu atoms in $CsCuTeS_3$ have bonds to S at 2.245 Å [53]. The compound $Cu_2U_6S_{13}$ has distances about its [CuS_3] units at both ends of the range: 2.167, 2.225, and 2.255 Å [50].

One further unusual distance in $K_6Cu_{12}U_2S_{15}$ is that between U atoms and nearest neighbor Cu atoms at 3.016(2) Å. A similarly short distance was observed in $Cu_2U_6S_{13}$ at 3.186 Å [50]. Such a short distance implies some amount of direct U-Cu bonding. In fact, the intermetallic compound UCu_5, in which the U atoms are 16-coordinate, has twelve U-Cu bonds at 2.92 Å and four at 3.05 Å [54]. If the coordination to Cu is also considered, the U atoms of $K_6Cu_{12}U_2S_{15}$ become twelve coordinate, and the six extra Cu atoms form a second, somewhat larger octahedron enclosing the one defined by S(1) atoms.

As with $K_2Cu_2CeS_4$ and $CsCuCes_3$, an all S^{2-} formalism cannot balance the charges in $K_6Cu_{12}U_2S_{15}$ without invoking oxidation states on the metals higher than Cu^+ or U^{4+}. By using these traditional ions as a starting place, a mixed valent formalism of $K_6(Cu^+)_{12}(U^{4+})_2(S^{2-})_{11}(S^{1-})_4$ is estimated. If true, the compound should exhibit p-type conductivity and paramagnetism based on two U^{4+} cations per formula.

Table 3.21: Fractional Atomic Coordinates and B_{eq}[a] values for $K_6Cu_{12}U_2S_{15}$ with Estimated Standard Deviations in Parentheses

atom	x	y	z	B(eq)[a]
U	0	0	0	0.8220(2)
Cu	0.1426(1)	0.0761(1)	0.0077(1)	1.69(9)
K	-0.0330(6)	1/8	0.2830(6)	2.381(4)
S(1)	-0.1280(2)	0.0384(3)	-0.0434(2)	1.5(2)
S(2)	1/4	1/8	0	1.2(2)

[a] B values for anisotropically refined atoms are given in the form of the isotropic equivalent displacement parameters defined as $B_{eq} = (4/3)[a^2B(1,1) + b^2B(2,2) + c^2B(3,3) + ab(\cos\gamma)B(1,2) + ac(\cos\beta)B(1,3) + bc(\cos\alpha)B(2,3)$.

Table 3.22: Selected Bond Distances (Å) and Angles (°) for $K_6Cu_{12}U_2S_{15}$ with standard deviations in parentheses.

U-Cu	3.016(2)	Cu-S(1)	2.256(5)
U-S(1)	2.619(5)	Cu-S(2)	2.205(2)
S(1)-U-S(1)^a	93.0(1)	U-S(1)^c-Cu	76.1(1)
S(1)-U-S(1)^b	180.00	Cu-S(1)-Cu^a	86.2(2)
S(1)-U-S(1)^c	87.0(1)	Cu-S(2)-Cu^b	106.8(1)
S(1)^b-Cu-S(1)^c	114.8(2)	Cu-S(2)-Cu^c	131.1(1)
S(1)^b-Cu-S(2)	122.8(1)	Cu-S(2)-Cu^d	93.0(1)
S(1)^c-Cu-S(2)	121.4(1)	Cu^c-S(2)-Cu^d	106.8(1)

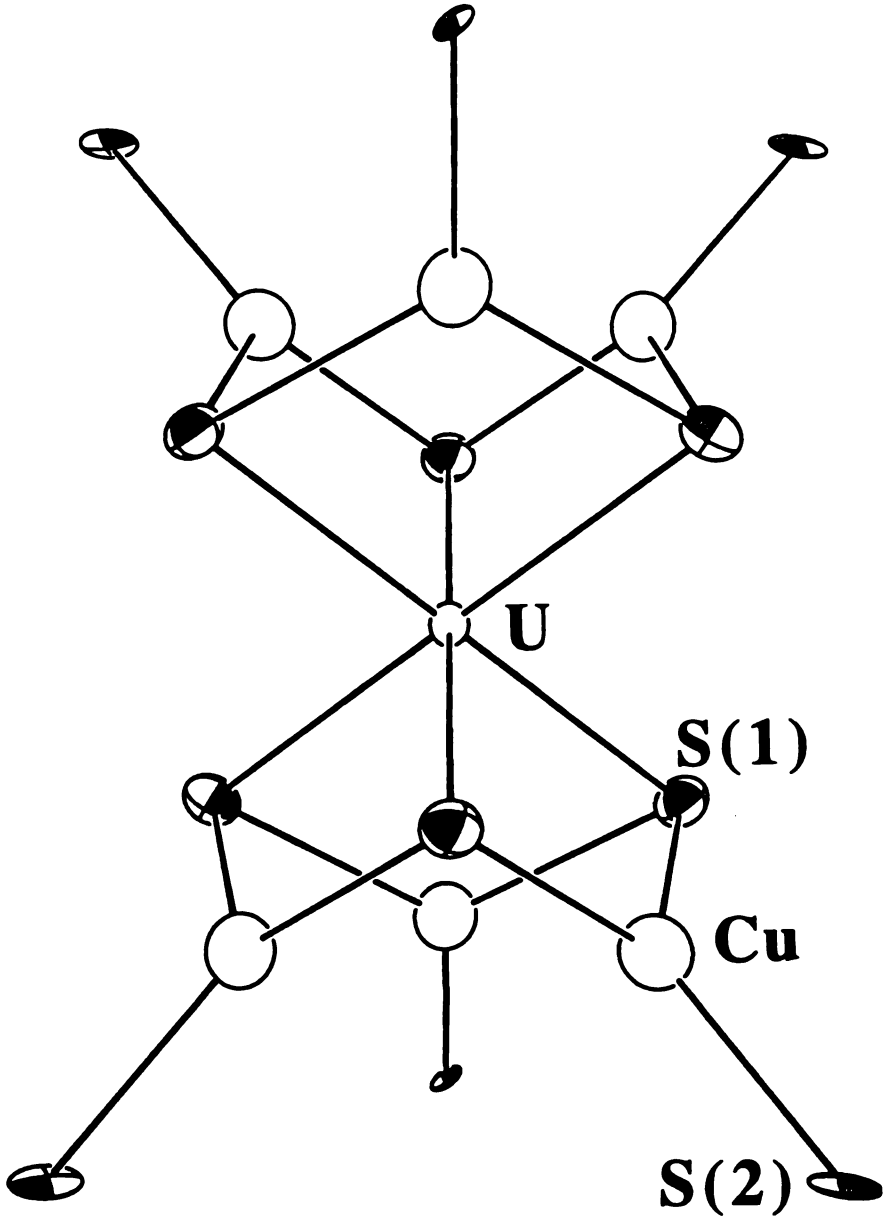

Figure 3.24: The basic structural building block of $K_6Cu_{12}U_2S_{15}$: a $[US_6]$ octahedra edge-sharing with six $[CuS_3]$ trigonal planes

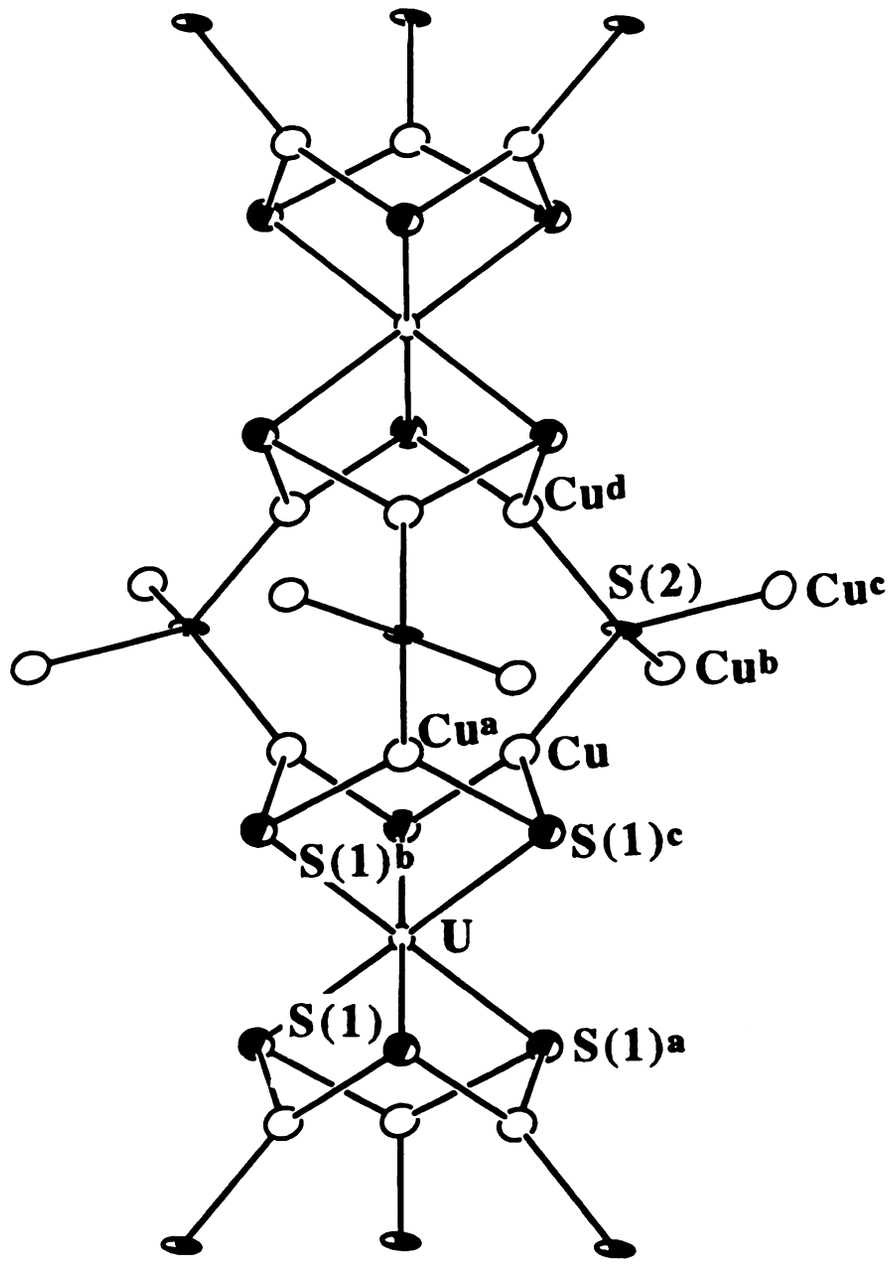

Figure 3.25: A fragment of the one-dimensional columns of $K_6Cu_{12}U_2S_{15}$ which are formed by corner-sharing connections between [CuS_3] trigonal planes on neighboring building blocks

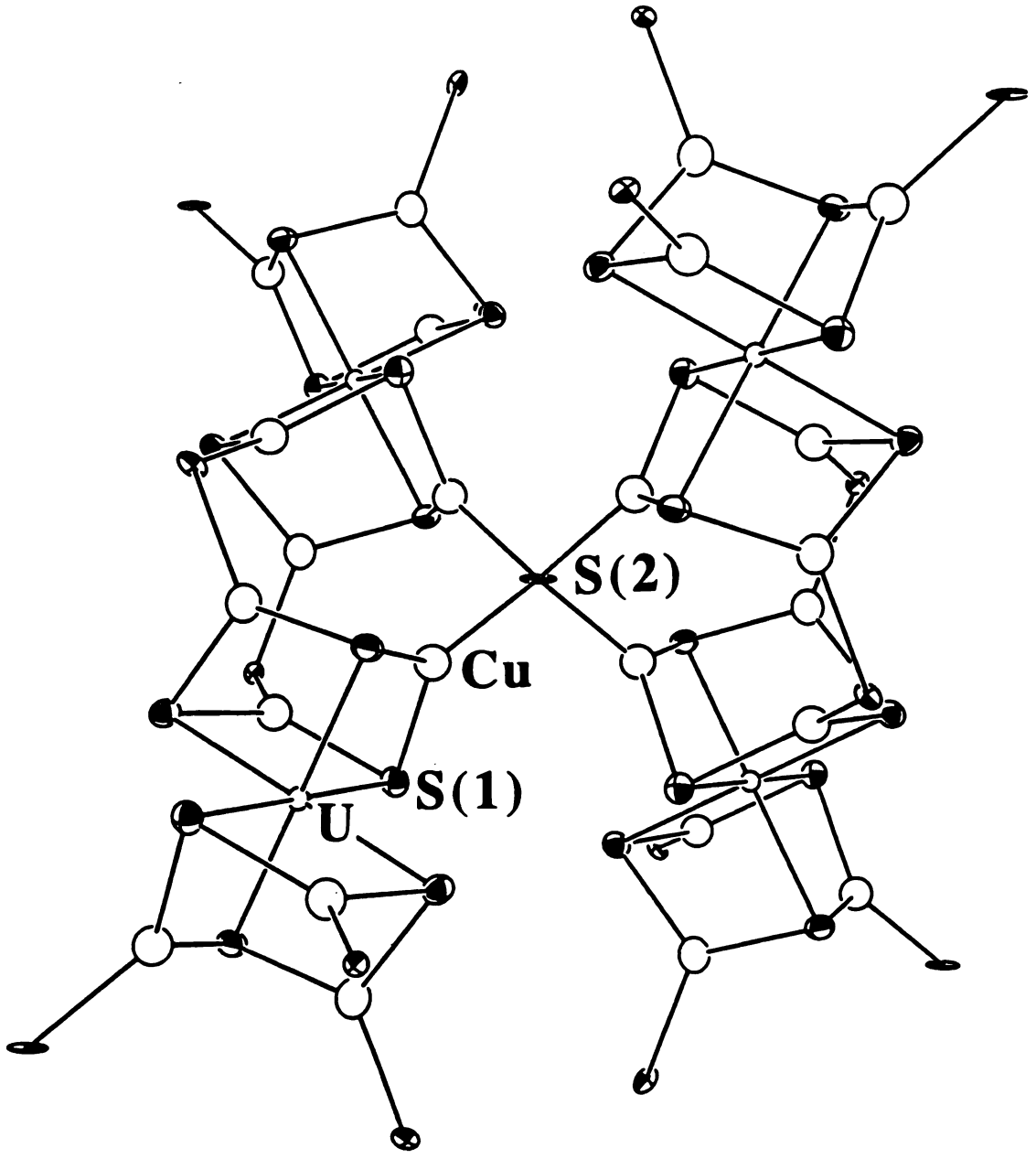

Figure 3.26: A fragment of $K_6Cu_{12}U_2S_{15}$ highlighting an S(2) atom in its function as a bridge between two neighboring columns

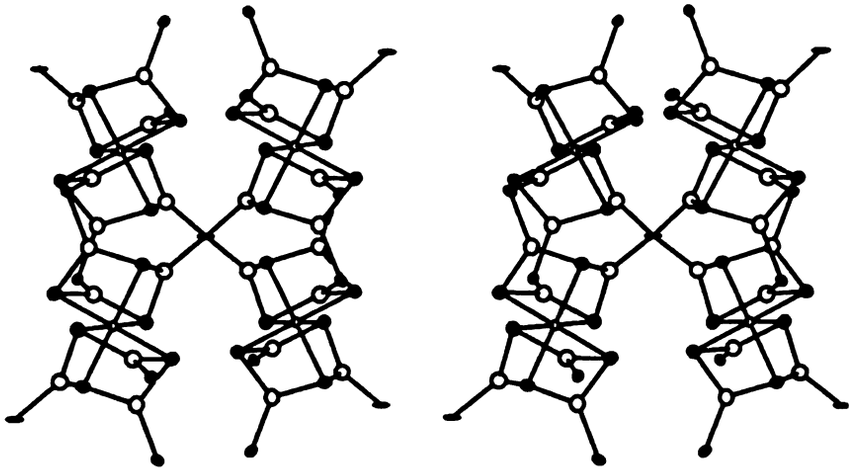

Figure 3.27: A stereo view of a fragment of $K_6Cu_{12}U_2S_{15}$, highlighting an S(2) atom in its function as a bridge between two neighboring columns

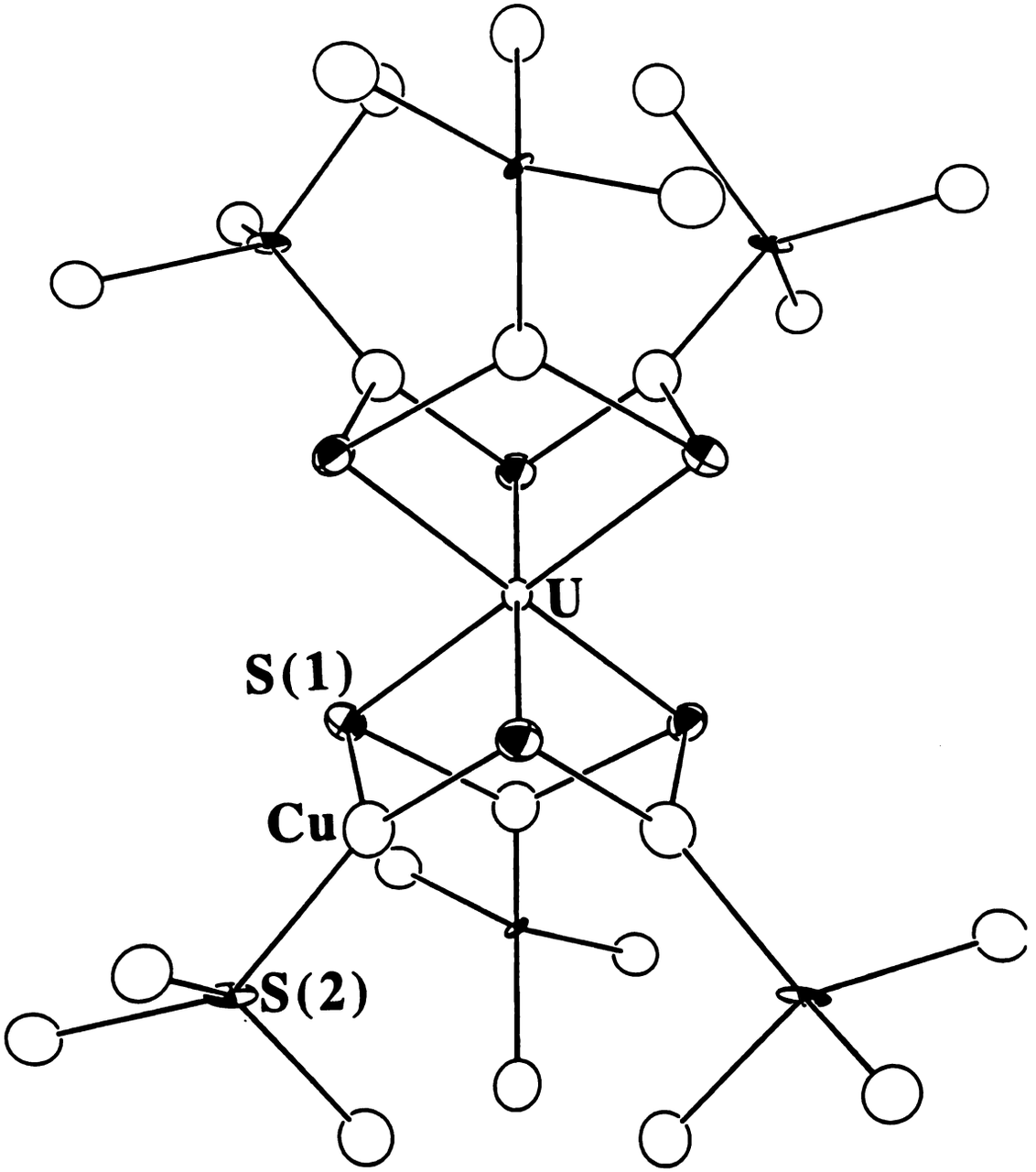

Figure 3.28: A fragment of the one-dimensional columns of $K_6Cu_{12}U_2S_{15}$ highlighting how the tetrahedra about the S(2) atoms alternate their directions along the column

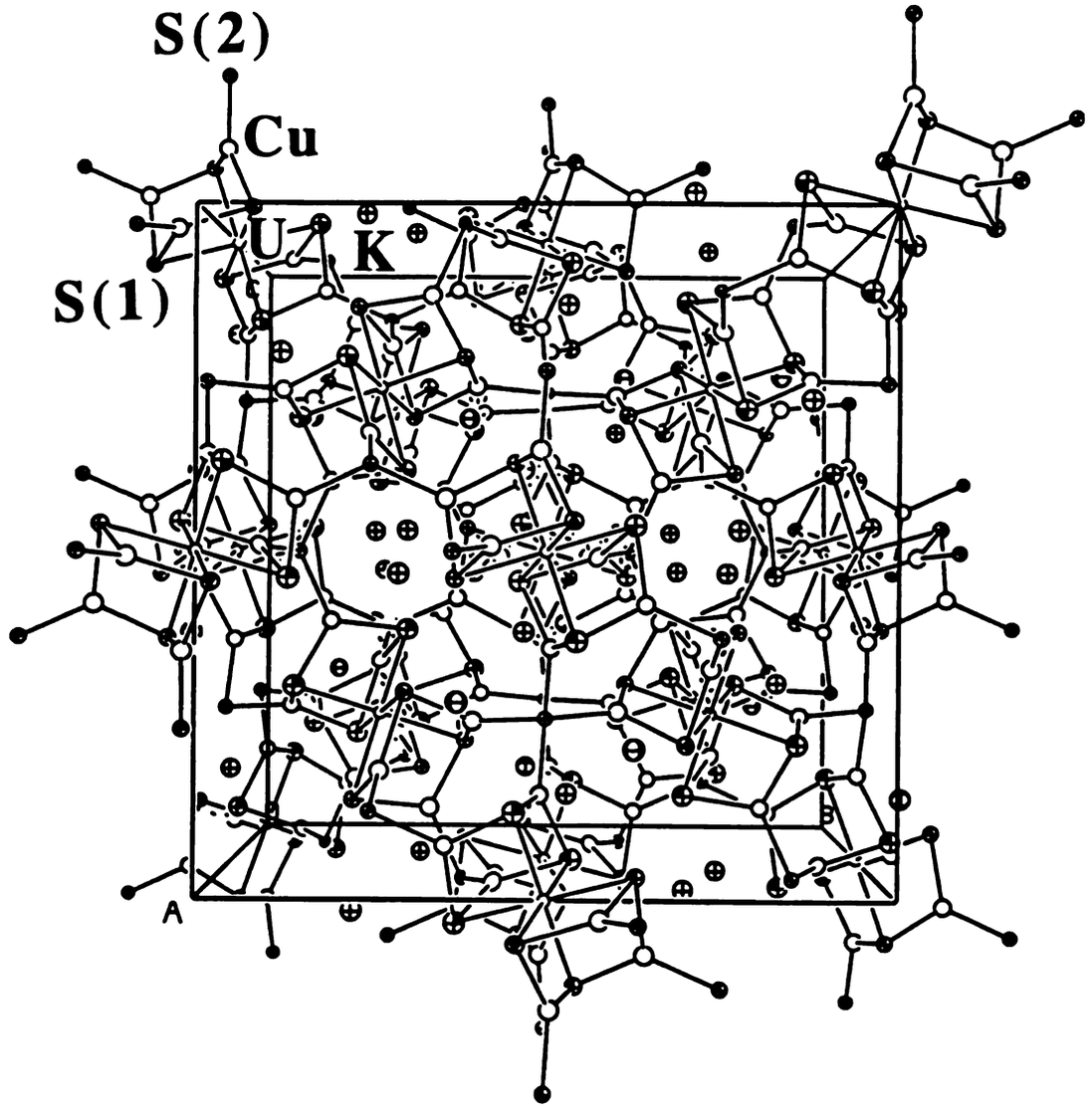

Figure 3.29: The unit cell of $K_6Cu_{12}U_2S_{15}$, as seen parallel to the a-axis

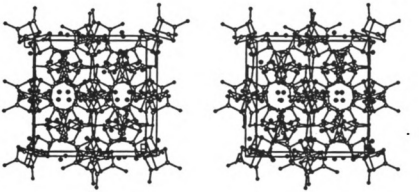

Figure 3.30: A stereo view of the unit cell of $K_6Cu_{12}U_2S_{15}$, as seen parallel to the a-axis

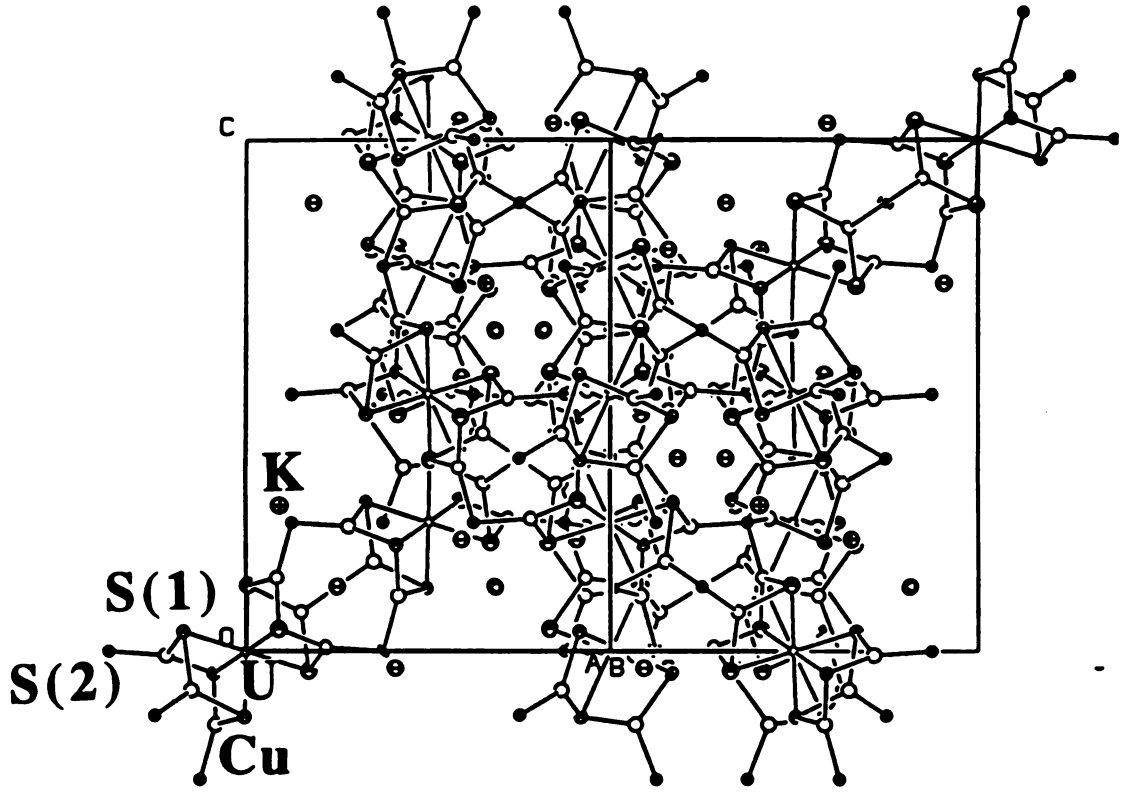

Figure 3.31: The unit cell of $K_6Cu_{12}U_2S_{15}$, as seen parallel to the [1-10] direction

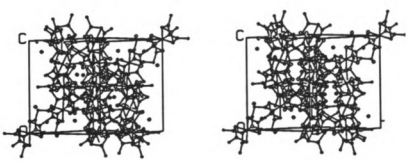

Figure 3.32: A stereo view of the unit cell of $K_6Cu_{12}U_2S_{15}$, as seen parallel to the [1-10] direction

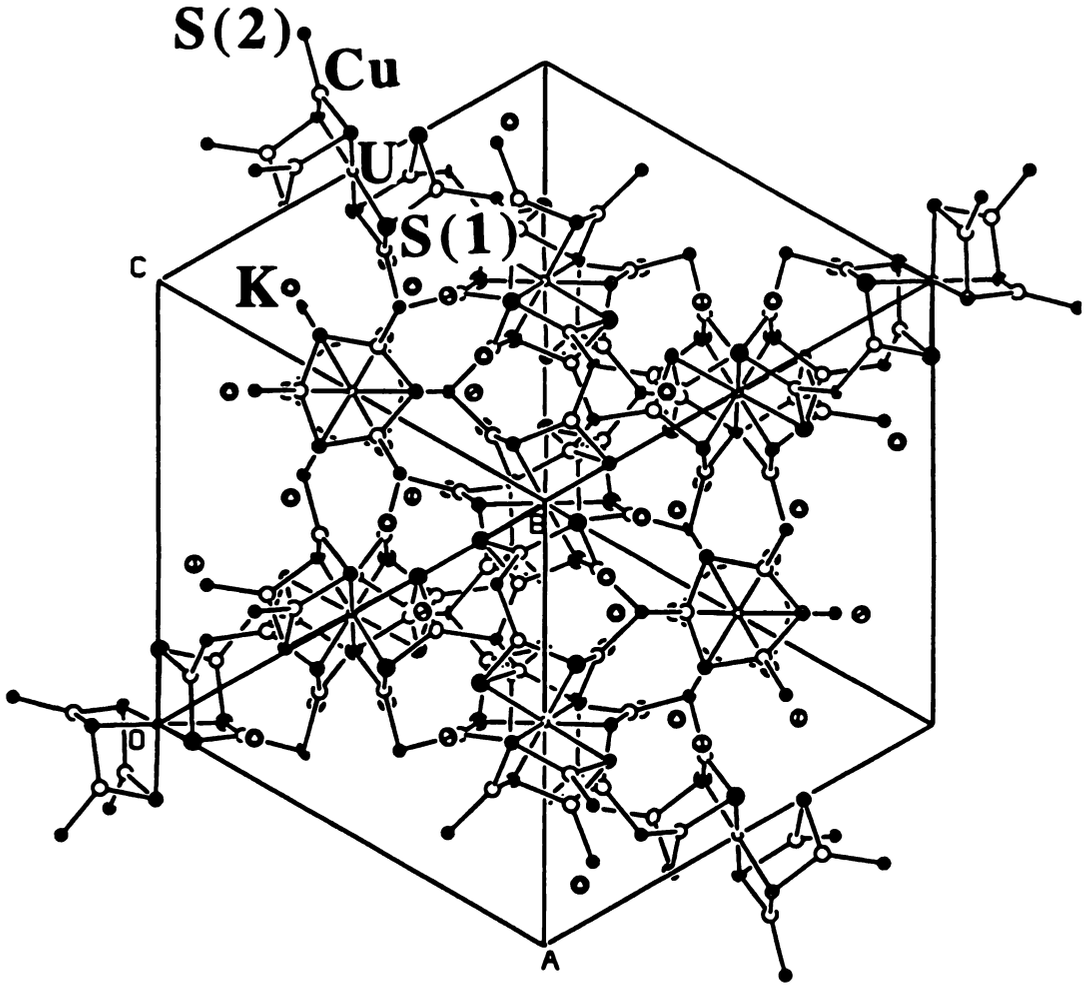

Figure 3.33: The unit cell of $K_6Cu_{12}U_2S_{15}$, as seen parallel to the [1-11] direction

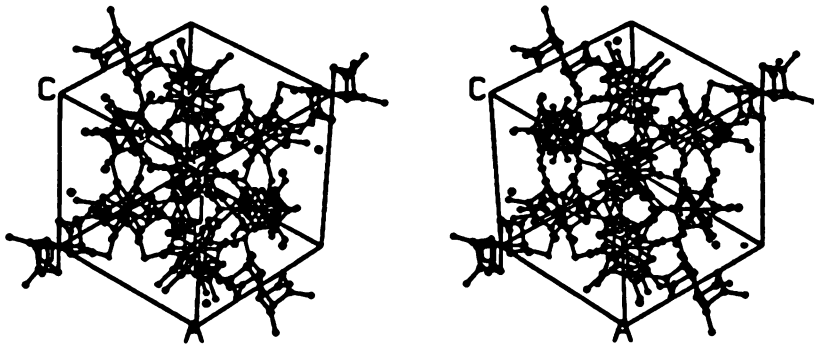

Figure 3.34: A stereo view of the unit cell of $K_6Cu_{12}U_2S_{15}$, as seen parallel to the [1-11] direction

D. Summary and Conclusions

As the Cu/f-block metal ratio in the phases described in this chapter has increased, there has been a steady and progressive adaptation of the forming structures to the increased Cu content. In the $ACuM_2Q_6$ phases, which have the smallest Cu/M ratio, the structure is simply an M/Q network, previously observed in $NaLnS_3$ (chapt. 3, sec. C.3), with Cu^+ diffused into tetrahedral sites within the lattice. Aside from pointing to the stability of this particular lanthanide/chalcogenide framework, this result shows how the phase formation was dominated by the lanthanide being in excess of Cu. In compounds where the Cu/M ratio is 1, $ACuMQ_3$, a breakdown of the M dominated framework is observed. Although similar to $ACuM_2Q_6$ in that Cu finds tetrahedral sites to occupy in a previously known structure type (anti-Pd_3Te_2), this particular M/Q framework had not been seen previously for the f-block metals under study. The increased amount of Cu drove the system to a phase which was less influenced by the f-block metal. Also at this Cu/M ratio, octahedral coordinations about the lanthanides and actinides begin to be observed. In moving to $K_2Cu_2CeS_4$ with its Cu/Ce ratio of two, Cu makes its presence felt by fragmenting the M/Q network from two- to one-dimensional, and the chains of $[CeS_6]$ octahedra are fully separated from one another by intervening $[CuS_4]$ tetrahedra. Finally, $K_6Cu_{12}U_2S_{15}$ (Cu/U=6) exhibits no interconnectivity whatsoever between $[US_6]$ octahedra, which are bridged into a 3-D network solely by $[CuS_3]$ units. Clearly, the amount of Cu is not the only structurally determining parameter in these reactions. The chemistry of the f-block element is still very much a factor as $ACuMQ_3$ is the only structure type which has been seen for both a lanthanide and an actinide. However, where the chemistry of the second metal will allow it, the

amount of Cu in the reaction produces a pronounced affect on the structural outcome.

This suggests that additional new phases may be possible via systematically varying the amount to Cu in the reactions. The present compounds are very selective in that the f-block/Q framework is either fully two-, one-, or zero-dimensional; no examples were characterized which contained "intermediate" dimensionality (i.e., two one-dimensional chains fusing into a single ribbon). Perhaps such phases could be achieved by running mixed A or mixed M reactions in conjunction with changing amounts of Cu.

Mixed chalcogenide valency was also observed repeatedly in several phases. Not only did this occur when the Cu content was in amounts greater or equal to the f-block metal but also to the alkali metal as well. All phases were also synthesized in very basic fluxes, giving rise to their exclusively monochalcogenide environments. As previously noted in the discussion of these compounds, there exist many examples of A/Cu/Q phases which have been shown to possess mixed Q^{2-}/Q^{1-} oxidation states, and this property of Cu is clearly transferring to this new Cu/f-block chemistry. An apparent requirement is that the f-block element involved have some high oxidation state available which is not stable in chalcogenide environments. For example, although Ce^{3+} forms mixed S^{2-}/S^{1-} phases in both $K_2Cu_2CeS_4$ and $CsCuCeS_3$, simple elemental substitution with La^{3+} did not yield the expected analogs. Perhaps at the elevated reaction temperatures the A_2Q_x flux becomes oxidizing enough that high valent species such as Cu^{2+}, Ce^{4+}, and U^{6+} are stable, for at least a finite time, as solubilized intermediates. Upon cooling and crystallization, the roles are

reversed, and these metal cations oxidize the surrounding chalcogenide environment, leading to the observed mixed valences.

The holes in the conduction band which result from mixed S^{2-}/S^{1-} states should impart some metallic behavior to the phases. Full investigation is somewhat hampered by the lack of large single crystals suitable for charge transport studies, there is evidence that these phases possess a nontraditional conductivity. Although not of a classical metallic mechanism, the conductivity does appear to be closely tied to structure. $K_2Cu_2CeS_4$ exhibited a fairly low conductivity, even for a pressed pellet sample. Its anisotropic structure would be especially susceptible to crystal defects which would disrupt conduction pathways. In $CsCuCeS_3$ the conductivity was nearly one thousand times greater than that of $K_2Cu_2CeS_4$. Although the chains of corner-sharing $[CuS_4]$ tetrahedra are distinctly separated from each other, the slightly greater orbital overlap from the layers of $[CeS_6]$ octahedra must be just enough to cause a significant change in the compound's band structure, producing high carrier mobility. It will be intriguing to see if the conductivity of $K_6Cu_{12}U_2S_{15}$ is still higher (because of the three-dimensional connectivity of the entire lattice) or lower (because the $[US_6]$ octahedra are isolated from each other rather than connected into a sub-framework).

REFERENCES

1) Sleight, A.W., *Chemistry of High-Temperature Superconductors; ACS Symposium Series 351*; American Chemical Society: Washington D. C., **1987**; Chapter 1, p. 2.

2) (a) Sheng, Z. Z. , Herman A. M., *Nature* ; **1988**, 332, 138. (b) Parkin, S. S., et. al., *Phys. Rev. Lett.* ; **1988**, 61, 750.

3) (a) Bednorz, J. G. and Muller, K. A., *Z. Phys.* ; **1986**, B64, 189,. (b) Cava R. J., vanDover, R. B., Batlogg, B., and Reitman, E. A., *Phys. Rev. Letts.* ; **1987**, 58 , 408.

4) McCarthy, T., Zhang, X., Kanatzidis, M. G., *Inorg. Chem.* ; **1993**, 32, 2944-2948.

5) Zhang, X., Kanatzidis, M. G., *J. Am. Chem. Soc.*, **1994**, 116, 1890.

6) Zhang, X., Kanatzidis, M. G., *Inorg. Chem.*, **1994**, 33, 1238.

7) McCarthy, T. M. , Kanatzidis, M. G.,*Chem. Mater.*, **1993**, 5, 1061.

8) T. M. McCarthy, Ph. D. Dissertation, Michigan State University, E. Lansing, MI, **1994**.

9) McCarthy, T. M. , Kanatzidis, M. G., *J. Chem. Soc., Chem. Commun.*, **1994**, 1089.

10) Liao, J.-H., Kanatzidis, M. G., *Chem. Mater.*, **1993**, 5, 1561.

11) Lu, Y.-J., Ibers, J. A., *Inorg Chem.*, **1991**, 30, 3317.

12) Lu, Y.-J., Ibers, J. A., *J. Solid State Chem.*, **1991**, 94, 381.

13) Lu, Y.-J., Ibers, J. A., *J. Solid State Chem.*, **1993**, 107, 58.

14) Lu, Y.-J., Ibers, J. A., *J. Solid State Chem.*, **1992**, 98, 312.

15) Mansuetto, M. F., Keane, P. M., Ibers, J. A., *J. Solid State Chem.*, **1992**, 101, 257.

16) Mansuetto, M. F., Keane, P. M., Ibers, J. A., *J. Solid State Chem.* ; **1993**, 105, 580-587.

17) Feher, F., *Handbuch der Praparativen Anorganischen Chemie* : Brauer, G., Ed. ; Fedinand Enke: Stuttgart, Germany, **1954**; p. 280-281.

18) Lyding, J. W., Marcy, H. O., Marks, T. J., Kannewurf, C. R., *IEEE Trans. Instrum. Meas.* ; **1988**, 37, 76-80.

19) Marcy, H. O., Marks, T. J., Kannewurf, C. R., *IEEE Trans. Instrum. Meas.*; **1990**, 39, 756-760.

20) Walker, N., Stuart, D., *Acta Crystallogr.* ; **1983**, A39 , 158-166.

21) (a) Sheldrick, G. M., in *Crystallographic Computing 3* ; Sheldrick, G. M., Kruger, C., Doddard, R., Eds.; Oxford University Press: Oxford, England, **1985**, p. 175-189. (b) Gilmore G. J., *Appl. Cryst.* ; **1984**, 17, 42-46.

22) Kroniert, W., Plieth, K., *Z. Anorg. Allg. Chem.* ; **1965**, 336, 207

23) Plug, C. M., Verschoor, G. C., *Acta Crystallogr.* ; **1976**, B32, 1856. h) Ohtani, T., Honjo, H., Wada, H., *Mat. Res. Bull.* ; **1987**, 22, 829-840.

24) (a) Marsh, R. E., Herbstein, F. H., *Acta Crystallogr.* ; **1983**, 39B, 280-287. (b) Yanagisawa, Y., Kanamaru, F., Kume, S., *Acta Crystallogr.* ; **1979**, 35B, 137-139.

25) Kanatzidis, M.G., Park, Y.; *J. Am. Chem. Soc.*; **1989**, 111, 3767-3769.

26) Sutorik, A.C., Kanatzidis, M. G., *Angew. Chem. Int. Ed Engl.* ; **1992**, 31, 1594-1596.

27) Murphy, D. W., Trumbore, F. A., *J. Electrochem. Soc.*, **1976**, 123, 960.

28) a) Lueken, H., Bruggemann, W., Bronger, W., Fleischhauer,V, *J. Less-Common Met.* ; **1979**, 65 , 79-88. b) Duczmal, M., Pawlak, L., *J. Magn. Magn. Mater.* ; **1988**, 76-77, 195-196.

29) Greenwood, N. N., Earnshaw, A., *Chemistry of the Elements* ; Pergamon Press, **1984**, p.1443.

30) (a) Mertz, K. M., Jr., Hoffmann, R., *Inorg. Chem.* ; **1988**, 27, 2120-2127. (b) Jansen, M., *Angew. Chem.* ; **1987**, 99, 1136; *Angew. Chem. Int. Ed. Engl.* ; **1987**, 26, 1098-1111.

31) Compounds of the type $ALnQ_2$ (A=Na; Ln=La,Ce,Pr, Nd; Q=S) were first synthesized by Ballestracci and Bertaut[31a] with the range of compounds expanded to include A=Li, K, Rb, Cs; Q=Se; and several other Ln metals by themselves and others.[31b-h] In general the compounds with large values for the radius ratio, R_{Ln3+}/R_{A+} favor the disordered NaCl structure whereas smaller values (0.6-1.2) tend toward the α-$NaFeO_2$ structure type.[31i,j] a) Ballestracci, R., Bertaut, E. F., *Bull. Soc. Fr. Mineral. Crystallogr.* **1964**, 87, 512. b) Ballestracci, R., Bertaut, E. F., *Bull. Soc. Fr. Mineral. Crystallogr.* ; **1965**, 88, 136. c) Ballestracci, R., *Bull. Soc. Fr. Mineral. Cristallogr.* ; **1965**, 88, 207. d) Tromme, M., *C. R. Acad. Sci. Ser. C* ; **1971**, 273, 849. e) Bronger, W., Elter, R., Mans, E., Schmidt, T., *Rev. Chim. Miner.* ; **1974**, 10, 147. f) Kabre, S.,

Julien-Pouzol, M., Guittard, M., *Bull. Soc. Chim.Fr.* ; **1974**, 10, 1881. g) Plug, C. M., Verschoor, G. C., *Acta Cryst.* ; **1976**, B32, 1856. h) Ohtani, T., Honjo, H., Wada, H., *Mat. Res. Bull.* ; **1987**, 22, 829-840. i) Bronger, W., *Crystallography and Crystal Chemistry of Materials with Layered Structures* ;(Ed.: F. Levy), D. Reidel Publishing Company; Dordrecht, Holland; **1976**, p.93. j) Brunel, M., DeBergevin, F., Gondrand, M., *J. Phys. Chem. Solids* ; **1972**, 33, 1927.

32) Poix, P., *C. R. Acad. Sci. Paris, Ser. C* ; **1970**, 270, 1852-1853.

33) *Rock-Forming Minerals, Orthosilicates* ; Deer, W. A., Howie, R. A., Zussman, J., Eds., vol. 1A; Longman: London and New York, **1982**.

34) *Person's Handbook of Crystallographic Data for Intermetallic Phases* ; 2nd Ed., Villars, P., Calvert, L. P., Eds. ; ASM International, USA, **1991**, p.232.

35) Carpenter, J. D., Hwu, S. J., *Chem. Mater.* ; **1992**, 4 , 1368-1372.

36) Liu, S.-X., Cai, G.-L., Huang, J.-L., *Acta Crystallogr.* ; **1993**, C49 , 4-7.

37) Berry, L. G., *Am. Mineral.* ; **1954**, 39 , 504.

38) (a) Ring, S. A., Tecotzky, M., *Inorg. Chem.* ; **1964**, 3, 182-185. (b) Marcon, J. P., Pascard, R., *C. R. Acad. Sci. Ser. C* ; **1968**, 266 , 270 -272.

39) Folmer, J. C. W., Jellinek, F., *J. Less-Common Metals* ; **1980**, 76, 153-162

40) Brown, D. B., Zubieta, J. A., Vella, P. A., Wrobleski, J. T., Watt, T., Hatfield, W. E., Day, P., *Inorg. Chem.* ; **1980**, 19, 1945-1950.

41) (a) Lotgering, F. K., van Stapele, R. P., *J. Appl. Phys.* ; **1968**, 39, 417. (b) Hollander, J. C. Th., Sawatzky, G., Haas, C., *Solid State Commun.* ; **1974**, 15, 747.

42) Marks, T. J., *Angew. Chem. Int. Ed. Engl.* ; **1990**, 29, 857-879.

43) (a) Austin, I. G., Mott, N. F., *Adv. Phys.* ; **1969**, 18, 41. (b) Mott, N. F., *J. Non-Cryst. Solids* ; **1968**, 1, 1.

44) Livage J., *Chem. Mater.* ; **1991**, 3, 578-593.

45) Matkovic, P., Schubert, K., *J. Less-Common Met.*, **1977**, 52, 217-220.

46) Rodi, V. F., Babel, D., *Z. Anorg. Allg. Chem.*, **1965**, 336, 17-23.

47) Lelieveld, R., Ijdo, D. J. W., *Acta Crystallogr.*, **1980**, 36B, 2223-2226.

48) Siddall, III, T. H., in *Theory and Applications of Molecular Paramagnetism* (Eds.:Boudreaux, E. A., Mulay, L. M.), John Wiley and Sons, New York, **1976**, p.306.

49) Noel, H., Troc, R., *J. Solid State Chem.*, **1979**, 27, 123-135.

50) Noel, H., Potel, M., *J. Less-Common Met.*, **1985**, 113, 11-15.

51) (a) Takeuchi, K., Kodoh, Y., Sato, G., *Z. Kristallogr.*, **1985**, 173, 119-128. (b) Fjelliag, H., Gronvold, F., Stolen, S., *Z. Kristallogr.*, **1988**, 184, 111-121.

52) Baenziger, N. C., Rundle, R. E., Snow, A. I., Wilson, A. S., *Acta Crystallogr.*, **1950**, 3, 34-40.

Chapter 4

New Metal/Oxychalcogenide Compounds Resulting from Reactions in Molten Polychalcogenide Salts: A Measure of Kinetic Control in the Fight Against Thermodynamically Stable Binary Oxides

Part I: Introduction

Using molten A_2Q_x salts as reactive media at intermediate temperatures (250-600 °C) has provided a unique access point to the study of f-block metal/polychalcogenide chemistry, resulting in many new phases. Not only has the lower reaction temperatures (relative to traditional solid state synthetic methods) helped in the isolation of these new phases, but the ability to react polychalcogenides and lanthanides or actinides directly eliminates a substantial source of oxygen contamination by removing the need for the polar solvent media which conventional solution techniques require. Even so, the oxygen-free integrity of these reactions must be rigorously maintained because the highly oxophilic nature of the metals means their reactions are susceptible to even small amounts of oxygen contamination. Usually such contamination leads to the formation of exceedingly stable metal oxides, but because the A_2Q_x flux reactions are run in the intermediate temperature regime, conditions exist where the thermodynamically stable oxides can be avoided and more kinetically stable phases may be synthesized which contain both oxygen and chalcogenide (or polychalcogenide) in the lattice. Such reactions would not be limited to f-block metals but could be applied to the transition metals as well, especially in the early, more oxophilic, part of the periodic table.

Solid state oxychalcogenide compounds (that is, compounds in which O^{2-} and Q^{2-} are discrete rather than combined in an anionic unit) are generally rare. Known examples are dominated by lanthanide containing species, in both ternary [1] and quaternary systems [2]. For transition metals ZrOS and HfOS are the only known ternary compounds with extended structures [3], but a compound composed of discrete anionic clusters is found

in $Ba_6(NbS_4)(NbS_3O)$ [4]. Among main group elements, Sb_2S_2O, the mineral known as kermesite, is a naturally occurring oxysulfide [5], and the synthesis and structure of Bi_2O_2Q (Q=S, Se) has been reported [6]. Several quaternary phases containing transition metals exist, but they also possess a lanthanide as one of the components. These consist of the layered phases $Fe_2La_2O_3Q_2$ (Q=S, Se) [7] and MLaOS (M=Cu, Ag) [1] and the three dimensional structures of $CrLnOS_2$ [8], $CrLaOSe_2$ [8], $V_3La_5O_7S_6$ [9], $La_2Ta_3O_8S_2$ [10a], and $Ln_2Ta_3O_8Se2$ [10b] (Ln=lanthanide). The general investigation into oxychalcogenides has no doubt been inhibited by the high stability of the polyatomic anions and binary metal oxides, both of which would be the most likely thermodynamic roadblocks to new compound formation. The less thermodynamically demanding conditions of molten A_2Q_x fluxes could provide an environment in which oxychalcogenide may be encountered.

The possibility of using A_2Q_x fluxes to study metal/oxychalcogenide chemistry admittedly arose largely by accident. The high oxophilicity of the f-block elements, and some early transition metals, which were under study lead to the serendipitous characterization of several new phases which turned out to be oxychalcogenides. Sometimes these compounds occurred as minor products in mixtures of other chalcogenides and oxides; sometimes, they were the major product. Some were only isolated when an aged batch of starting material was used and disappeared entirely when fresh reagents were employed, but still others appeared reproducibly regardless of the age of the reagents. The disparate and often "temperamental" nature of these reactions presented a great deal of synthetic challenge, especially when it came to avoiding binary oxide

formation. Although most were overcome, the initial discoveries were still just stumbles in a stroll across a phase diagram.

As investigations proceeded, a more rational approach began to evolve, one involving the *in situ* formation of oxymetal cations which could subsequently be reacted in the A_2Q_x flux to form extended structures. This approach not only provides the metal with a highly stable alternative to binary oxide formation, but also yields an accessible building block about which rational syntheses may be designed. Initial investigations centered on the uranyl cation, $(UO_2)^{2+}$, a natural extension of the f-block metal studies, but the lessons learned using this cation could have potential applications in the synthesis involving other oxymetal cations as well. As long as such species are stable in the molten A_2Q_x environment, they can be used as reproducible starting points to new metal/oxychalcogenide compounds.

This chapter begins with compounds in which the oxygen, although playing a central and specific role in the resulting structures, does not form special oxymetal cationic units. These will be followed by compounds involving rational *in situ* $(UO_2)^{2+}$ incorporation into new phases exhibiting either extended dimensionality or discrete anionic fragments.

REFERENCES

1) The three phases most commonly encountered are Ln_2O_2Q, $Ln_2O_2(S_2)$ and $Ln_4O_4S(Se_2)$, Ln=lanthanide and Q=chalcogenide. Flauhaut, J., in *Handbook on the Physics and Chemistry of Rare Earths, Vol. 4* (Eds.: Gschneidner, Jr., K. A., and Eyring, L.), North-Holland, Amsterdam, **1979**, p. 1-88.

2) Guittard, M., Benazeth, S., Dugué, J., Jaulmes, S., Palazzi, M., Laruelle, P., Flauhaut, J., *J. Solid State Chem.* **1984**, 51, 227-238.

3) (a) Wells, F. A., *Structural Inorganic Chemistry, 5th Ed.* Carendon, Oxford, **1984**, p.786-787. (b) Eisman, G. A., Steinfink, H., *J. Solid State Chem.* **1982**, 43, 225-226. (c) Eisman, G. A., Swinnea, J. S., Steinfink, H., *J. Solid State Chem.* **1985**, 56, 397-398.

4) Rendon-Diazmiron, L. E., Campana, C. F., Steinfink, H., *J. Solid State Chem.* **1983**, 47, 322-327.

5) Baumgardt, E. M., Kupick, V., *J. Cryst. Growth* **1977**, 37, 346.

6) (a) Koyama, E., Nakai, I., Nagashima, K., *Acta Cryst.* **1984**, *B40*, 105-109. (b) Boller, H., *Monatsh Chem.* **1973**, 104, 916-919.

7) Mayer, J. M., Schneemeyer, L. F., Siegrist, T., Waszczak, J. V., Van Dover, B., *Angew. Chem., Int. Ed. Engl.* **1992**, 31, 1645-1647.

8) (a) Vovan, T., Dugué, J., Guittard, M., *Mater. Res. Bull.* **1978**, 13, 1163-1166. (b) Dugué, J., Vovan, T., Viller, J., *Acta Crystallogr. Sect. B* **1980**, 36, 1291-1294. (c) Winterberger, M., Vovan, T., Guittard, M., *Solid State Commun.* **1985**, 53, 227-230. (d) Winterberger, M., Dugué, J., Guittard, M., Dung, N. H., Vovan, T., *J. Solid State Chem.* **1987**, 70, 295-302.

9) Dugué, J., Vovan, Laruelle, P., *Acta Crystallogr., Sect. C* **1985**, 41, 1146-1148.

10) (a) Brennan, T. D., Aleandri, L. E., Ibers, J. A., *J. Solid State Chem.* **1991**, 91, 312-322. (b) Brennan, T. D., Ibers, J. A., *J. Solid State Chem.* **1992**, 98, 82-89.

PART II: $Ba_6Ti_5S_{15}O$: A New Metal/Oxysulfide Resulting from the Inclusion of BaO into the $BaTiS_3$ Structure Type

A. Introduction

In solid state chemistry, a classic synthetic approach to new materials is to modify a known structure type by forcing it, usually through reactions at very high temperatures, to adapt to the inclusion of elements (compositional or structural) from other compounds. This approach can result in new materials possessing recognizable structural fragments of one or both of the starting compounds. In some cases this has led to whole families of related phases in which the size or quantity of the known structural fragments are varied depending on the amount of the second compound "forced in". One such well-known system is $(ZnS)_n(In_2S_3)_m$ [1], and several other examples of new alkali metal/transition metal/chalcogenides have been synthesized in our lab from reactions in molten alkali metal polychalcogenides (A_2Q_x) at intermediate temperatures (250-450 °C) [2]. We had been curious as to whether the methodologies of the A_2Q_x fluxes could be extended to alkaline-earth polychalcogenides as well. It was during investigation of Ti reactivity in molten BaS_x fluxes that we first observed the new oxysulfide $Ba_6Ti_5S_{15}O$. Subsequently prepared from a stoichiometric combination of BaS/BaO/Ti/S, this compound represents the first member of a potential new family of materials with the general formula n(BaO)+m($BaTiS_3$). As implied by this formalism, $Ba_6Ti_5S_{15}O$ is structurally related to $BaTiS_3$ in that the infinite chains of [TiS_6] face-sharing octahedra of the ternary compound

have been fragmented and reconnected into a two-dimensional layered structure by inclusion of BaO.

B. Experimental

1. Synthesis

Reagents -- The following materials were used as obtained: BaS, 100 mesh, 99.999% purity, Cerac, Milwaukee, WI; BaO, 100 mesh, 99.5% purity, Cerac, Milwaukee, WI; Ti metal, 325 mesh, Alfa, Danvers, MA; and sulfur powder, sublimed, JT Baker Co., Phillipsburg, NJ.

Hexabarium pentatitanium, oxydocapentasulfide $Ba_6Ti_5S_{15}O$ -- As mentioned in the introduction, $Ba_6Ti_5S_{15}O$ was first isolated from the reaction of Ti metal in excess BaS_x. 0.271 g BaS (1.6 mmol), 0.019 g Ti (0.4 mmol), and 0.102g S (3.2 mmol) were mixed in a nitrogen filled glove box and loaded into quartz tubes, which were subsequently evacuated on a Schlenk line to $<3x10^{-3}$ mbar and flame-sealed. The reagents were heated in a computer-controlled furnace to 600 °C over 6 hours and left at that temperature for 6 days, followed by cooling at 4 °C/hr to 440 °C and quenching to 50 °C. The excess BaS_x flux was removed by dissolving it with degassed distilled water under N_2 flow. Washings were continued until the solvent no longer turned yellow, signaling that all the polysulfide had been removed. The sample was then dried under vacuum. The major phase from this preparation was very small blue needles of $BaTiS_3$. $Ba_6Ti_5S_{15}O$ was present as a very minor phase but grew as large gray plates which could be manually extracted from the bulk of the product. Single crystal diffraction studies were performed on samples synthesized from the above reaction. The large plates are insoluble in methanol and

dimethylformamide, as well as water, and appear stable in air for extended periods.

The original source of oxygen was determined to be contamination from an aged supply of BaS as switching to a freshly obtained batch yielded only the ternary compound. Initial attempts at rational reproduction of the oxysulfide were made using fresh BaS and BaO, which was added in a 1/5 ratio to the Ti metal in the above reaction. This approach saw no increase in the yield of $Ba_6Ti_5S_{15}O$, which still occurred as large plates in very small yield. The major phase was still $BaTiS_3$ but was now accompanied by a significant amount of TiO_2, as determined by powder X-ray diffraction. The added diffusion which the excess BaS_x provides, although excellent for crystal growth, apparently allowed for too much oxide mobility and hence led to a portion of the very oxophilic Ti^{4+} being converted to TiO_2.

Pure $Ba_6Ti_5S_{15}O$ was successfully synthesized at high temperature from a reaction of BaS/BaO/Ti/S in the exact stoichiometric ratio of the compound: 0.212 g BaS (1.25 mmol), 0.038 g BaO (0.25 mmol), 0.060 g Ti (1.25 mmol), and 0.080 g S (2.5 mmol). The reagents were mixed and loaded into quartz tubes as described above. The tubes were evacuated to $<2x10^{-4}$ mbar and flame-sealed. Samples were heated to 700 °C in 12 hours and isothermed at that temperature for 8 days followed by cooling to 500 °C at 4 °C/hr and quenching to 50 °C. A small amount of residual BaS_x still remained, and so the product was washed with degassed distilled water as described earlier. The remaining material was a gray microcrystalline powder. EDS analysis of the gray powder reveals Ba, Ti, and S in an approximate 1/1/3 ratio. Oxygen cannot be detected by this technique because its emission lines lie below the lower detection limit of

the system. The powder X-ray diffraction (XRD) pattern of the product corresponded to that calculated for $Ba_6Ti_5S_{15}O$ from single crystal diffraction data (Table 4.2.1); no other peaks from $BaTiS_3$, TiO_2, or any other impurity were detected.

As control experiments, this procedure was also performed with two modifications. First, omission of BaO from the above reaction resulted in only $BaTiS_3$ as the final product. Second, the effect of reaction time was investigated. By shortening the isotherm to 2 days, $BaTiS_3$ was again found to be the major phase, implying that the oxysulfide is a thermodynamic product, forming after BaO has a chance to act upon the ternary. After an isotherm of 6 days, $Ba_6Ti_5S_{15}O$ became the major product from the reaction; although no crystalline impurities were observed in the powder XRD pattern, a small amount of white powder was present in this sample. EDS analysis of this impurity revealed a Ba/Ti/S ratio of approximately 1/3.5/1, and so the lack of S implies a substantial amount of oxygen. This phase appears transitory as well because upon 8 days of isotherm the product of the reaction becomes $Ba_6Ti_5S_{15}O$ which is pure by visual inspection and analysis. This progression from ternary to quaternary implies that the high oxophilicity of Ti^{4+} provides driving force for the further reaction of the ternary phase. Meanwhile, the formation of the highly stable TiO_2 is avoided by the lack of oxide diffusion through the sample once most of the flux has been consumed in the initial formation of the ternary. Unless $Ba_6Ti_5S_{15}O$ is highly stable, however, it is likely that at high temperatures oxygen would continue to diffuse through the reaction and, after some even longer isotherm time, result in increasing amounts of TiO_2 in the product.

Table 4.2.1:Calculated and Observed X-ray Powder Diffraction Patterns for $Ba_6Ti_5S_{15}O$ (Cu Radiation)

h k l	d_{calc}	d_{obs}	% I/I_o obs
0 2 1	7.35	7.51	5.52
0 2 2	6.45	6.60	2.38
1 1 2	5.46	5.51	2.16
1 1 3	4.837	4.894	3.42
1 1 4	4.238	4.298	24.41
1 3 0	4.101	4.143	2.29
1 3 1	4.039	4.085	7.22
0 0 6	3.880	3.978	80.20
0 4 0	3.875	3.938	92.22
0 4 1	3.822	3.781	11.17
1 3 3	3.626	3.676	8.85
2 0 0	3.372	3.401	46.31
1 3 4	3.353	3.368	38.16
2 0 1	3.338	3.339	9.04
2 0 3	3.093	3.126	15.88
2 2 0	3.092	3.095	3.45
2 2 2	2.989	2.995	6.81
2 0 4	2.918	2.932	2.42
2 2 3	2.873	2.883	2.98
0 4 6	2.742	2.794	100.00
1 5 2	2.737	2.748	15.19
0 2 8	2.724	2.687	9.16
1 1 8	2.633	2.622	26.23
2 0 6	2.545	2.561	71.58
1 5 4	2.535	2.543	9.98
0 6 2	2.522	2.509	11.01
2 4 2	2.485	2.491	2.79

Table 4.2.1:Calculated and Observed X-ray Powder Diffraction Patterns for $Ba_6Ti_5S_{15}O$ (Cu Radiation) (cont.)

h k l	d_{calc}	d_{obs}	% I/I_o obs
0 2 9	2.454	2.445	3.26
1 5 5	2.410	2.417	6.96
1 3 8	2.373	2.389	7.37
2 0 7	2.368	2.380	7.72
0 0 10	2.328	2.349	1.54
2 2 7	2.265	2.288	1.98
2 0 8	2.203	2.225	7.94
1 1 10	2.179	2.186	2.01
0 4 9	2.151	2.146	5.11
2 4 6	2.127	2.097	5.14
1 7 2	2.070	2.060	7.66
1 7 3	2.030	2.036	7.97
3 1 5	2.008	2.006	13.99
2 2 9	1.9841	1.985	3.73
1 7 4	1.9784	1.967	24.32
0 6 8	1.9318	1.922	2.38
3 3 5	1.8851	1.890	4.02
1 1 12	1.8511	1.861	3.07
0 6 9	1.8278	1.824	2.54
3 3 7	1.7522	1.768	6.12
2 6 7	1.7455	1.731	2.86
1 7 8	1.7049	1.697	7.03
2 8 0	1.6799	1.678	4.42
1 9 2	1.6517	1.658	1.38
4 0 3	1.6478	1.649	2.29
2 4 11	1.6269	1.627	2.54
3 1 10	1.6085	1.596	1.98
4 0 5	1.5855	1.585	2.38
3 7 2	1.5633	1.564	4.17

2. Physical Measurements

Powder X-ray diffraction -- Analyses were performed using a calibrated Rigaku Rotaflex rotating anode powder diffractometer controlled by an IBM computer and operating at 45 kV/ 100 mA, employing Ni-filtered Cu radiation.

Electron Microscopy -- Semi-quantitative microprobe analysis of the samples was performed with a JEOL JSM-35C scanning electron microscope (SEM) equipped with a Tracor Northern energy-dispersive spectroscopy (EDS) detector. Data were acquired using an accelerating voltage of 20 kV and a 30 second accumulation time.

Infrared Spectroscopy -- Infrared spectra, in the far-IR region (600-50 cm^{-1}), were recorded on a computer controlled Nicolet-740 Fourier Transform infrared spectrophotometer in 4 cm-1 resolution. Analyses were performed on solid samples using CsI as the pressed pellet matrix.

UV/Vis/Near IR spectroscopy -- Optical diffuse reflectance measurements were performed at room temperature using a Shimadzu UV-3101PC double beam, double monochromator spectrophotometer. The instrument is equipped with integrating sphere and controlled by personal computer. The reflectance versus wavelength data generated can be used to estimate the band gap by converting reflectance to absorption data using the Kubelka-Munk function as described elsewhere.

Single Crystal X-ray Diffraction -- Intensity data for $Ba_6Ti_5S_{15}O$ were collected at 23 °C using a Rigaku AFC6S four-circle automated diffractometer equipped with a graphite crystal monochromator and Mo Ka radiation. A single plate-like crystal of dimensions 0.1 x 0.4 x 0.5 mm^3 was mounted on a glass fiber for analysis. An ω-2θ scan mode was used. The crystal stability was monitored with three standard reflections

whose intensities were checked every 150 reflections. No decay was detected. An empirical absorption correction based on ψ scans was applied to all data during initial stages of refinement, with a range of transmission factors of 0.1358-1.000 (ave.: 0.6519). No extiction correction was employed. An empirical DIFABS correction [3] was applied after full isotropic refinement, followed by full anisotropic refinement. The structure was solved by direct methods using SHELXS-86 software [4a], and full matrix least squares refinement was performed using the TEXSAN software package [4b]. The neutral atomic scattering factors were taken from Cromer and Waber [5], and data was refined using a sigma weighting function. Anomalous dispersion effects were included in F_{calc} [6]; the values of Df' and Df" were those of Cromer [7].

Crystals of $Ba_6Ti_5S_{15}O$ were determined to be of the orthorhombic space group $C222_1$ (No. 20) with a=6.708(5) Å, b=15.683(4) Å, c=23.740(7) Å, V=2497(2) $Å^3$, Z=4, D_{calc}=4.150 g/cm^3, μ=123 cm^{-1}, $2\theta_{max}$=60.00. The total number of data collected was 2069, with 2052 being unique and 1740 with $F_o^2 > 3\sigma(F_o^2)$ (hkl range: 0 0 0 to 9 22 33). Atomic coordinates and isotropic thermal parameters are shown in Table 4.2.2. Complete anisotropic refinement on 124 variables resulted in a final R/Rw= 3.8%/5.4%. As this is an acentric space group, both enantiomers of the structure were refined. There was only a slight difference in the R/R_w values between the two (R/Rw= 3.8%/5.4% vs. R/Rw= 3.8%/5.5%), but the data reported is from the enantiomer with the slightly better refinement.

Table 4.2.2:Fractional Atomic Coordinates and B_{eq}[a] values for $B_6Ti_5S_{15}O$ with Estimated Standard Deviations in Parentheses

atom	x	y	z	B_{eq}
Ba(1)	0.2074(2)	0.89125(5)	0.33673(4)	1.31(3)
Ba(2)	0.7029(2)	0.85576(6)	0.48386(4)	1.39(3)
Ba(3)	0.2810(1)	0.90019(5)	0.82219(3)	0.99(3)
Ti(1)	-0.1944(5)	1.2580(2)	0.1946(1)	1.1(1)
Ti(2)	0.2315(4)	1.1286(2)	0.4053(1)	1.12(9)
Ti(3)	0.1855(6)	1	1/2	1.3(1)
S(1)	0	0.7451(4)	1/4	1.4(2)
S(2)	-0.2095(8)	1.4014(2)	0.1950(2)	1.6(1)
S(3)	0.2146(7)	1.0880(2)	0.3087(1)	1.0(1)
S(4)	0.4538(6)	1.2368(3)	0.3907(2)	1.1(1)
S(5)	-0.0272(6)	1.2386(3)	0.3855(2)	1.0(1)
S(6)	-0.0469(6)	0.9828(3)	0.5738(2)	1.1(1)
S(7)	-0.5460(6)	1.0148(3)	0.4273(2)	1.0(1)
S(8)	0.7956(7)	0.8467(2)	0.4924(1)	1.0(1)
O	1/2	0.743(1)	1/4	1.7(7)

[a] B values for anisotropically refined atoms are given in the form of the isotropic equivalent displacement parameters defined as $B_{eq} = (4/3)[a^2B(1,1) + b^2B(2,2) + c^2B(3,3) + ab(\cos\gamma)B(1,2) + ac(\cos\beta)B(1,3) + bc(\cos\alpha)B(2,3)$.

C. Results and discussion

Structure -- The repeating unit of $Ba_6Ti_5S_{15}O$ is shown in Figure 4.2.1 and selected bond distances and angles are given in Table 4.2.3. The fragment features 5 Ti-centered, face-sharing octahedra, the actual asymmetric unit being half of this chain due to Ti(3) being positioned on a two-fold axis. The Ti atoms are bonded exclusively to S atoms internally, but the chain's terminal faces are composed of bonds to two S atoms and one O atom. As mentioned, the parent compound, $BaTiS_3$, is composed of infinite chains of face-sharing $[TiS_6]$ octahedra [8], and so the formalism of the oxysulfide as $(BaO)+5(BaTiS_3)$ presents an accurate structural picture of the ternary compound being broken at every fifth octahedron by BaO.

The reconnection of the fragments in Figure 4.2.1 leads to a structure composed of two dimensional anionic layers. A view perpendicular to these layers is given in Figure 4.2.2, and their corrugated nature is shown in the view parallel to the b axis in Figure 4.2.3. The fragments are connected via corner sharing between the terminal octahedra. Only S(1) and O, both of which reside on two-fold axes, are engaged in these linkages; the third atom, S(2), is terminal and directed into the interlayer gallery. The bridges formed by S(1) and O are nearly linear, and although linear bridges are commonly formed with oxygen, they are somewhat rare in the case of sulfur. Linear sulfide bridges have been seen in several Ba/Zr or Hf/S phases including Ba_2ZrS_4 [9a], $Ba_3Zr_2S_7$ [9a], Ba_2HfS_4 [9b], $Ba_6Hf_5S_{16}$ [9c], and $Ba_5Hf_4S_{13}$ [9c], all of which form perovskite-related structures. Interestingly, $BaMS_3$ (M=Zr, Hf) adopts the $GaFeO_3$ structure type, which is a perovskite derivative distorted by bent M-S-M bonds [10]. This leads us to speculate on the necessity of O for the formation of $Ba_6Ti_5S_{15}O$. Does the O force S(1) into a linear bridge or

rather is an all S analog, in fact, possible? We also note that while $BaTiS_3$ has face-sharing octahedra in which all Ti-S-Ti angles are bent, the compound $BaTiO_3$ has the perovskite structure-type, with all the $[TiO_6]$ units corner sharing through linear Ti-O-Ti angles. Hence, many different structure types may be accessible simply on the basis of varying the ratio of linear to bent M-X-M bridges. An interesting feature of the anionic layers in $Ba_6Ti_5S_{15}O$ is the formation of intralayer cavities as seen in Figure 4.2.2. These cavities do not lead to channels through the layers as their position is staggered by half the length of the a-axis from layer to layer. However, they do form the primary location of the Ba^{2+} atoms in the compound. From these cavities the Ba^{2+} protrude only slightly into the interlayer gallery, leaving the spacing between the layers void. As such, $Ba_6Ti_5S_{15}O$ may exhibit intercalation chemistry, perhaps via a reduction of the Ti^{4+} to Ti^{3+} which could then be charge-balanced by small cations such as Li^+ diffusing through the interlayer gallery. If favorable, such behavior could even make $Ba_6Ti_5S_{15}O$ a candidate for a rechargeable battery host material.

A small family of layered alkali/titanate compounds exists, which has some interesting structural similarities to $Ba_6Ti_5S_{15}O$. These compounds have the general formula $(A_2O)(TiO_2)_n$ where A=Na for n=3 ($Na_2Ti_3O_7$) [11], A=K for n=4 ($K_2Ti_4O_9$) [12], and A=Cs for n=5 ($Cs_2Ti_5O_{11}$) [13]. Their structures are based on blocks of edge sharing TiO_6, n octahedra long, which are fused together through further edge sharing into 1-D ribbons. The ribbons are then connected to each other through corners to form corrugated anionic layers, with the alkali ions filling the interlayer gallery. It has been shown that these compounds can be ion-exchanged to produce protonated forms which were subsequently studied for their interesting

intercalation chemistry [14]. Apparently the size of the TiO_2 fragments stabilized in this family is a function of the cation size as well as the A_2O/TiO_2 ratio. Larger cations stabilize larger fragments. As such perhaps $Ba_6Ti_5S_{15}O$ may already represent the optimum balance between cation size and chain fragment length. If this is so, future synthetic exploration of related phases could focus on the effect of changing cation sizes, both homoleptically and as a mixture of different alkaline-earth cations.

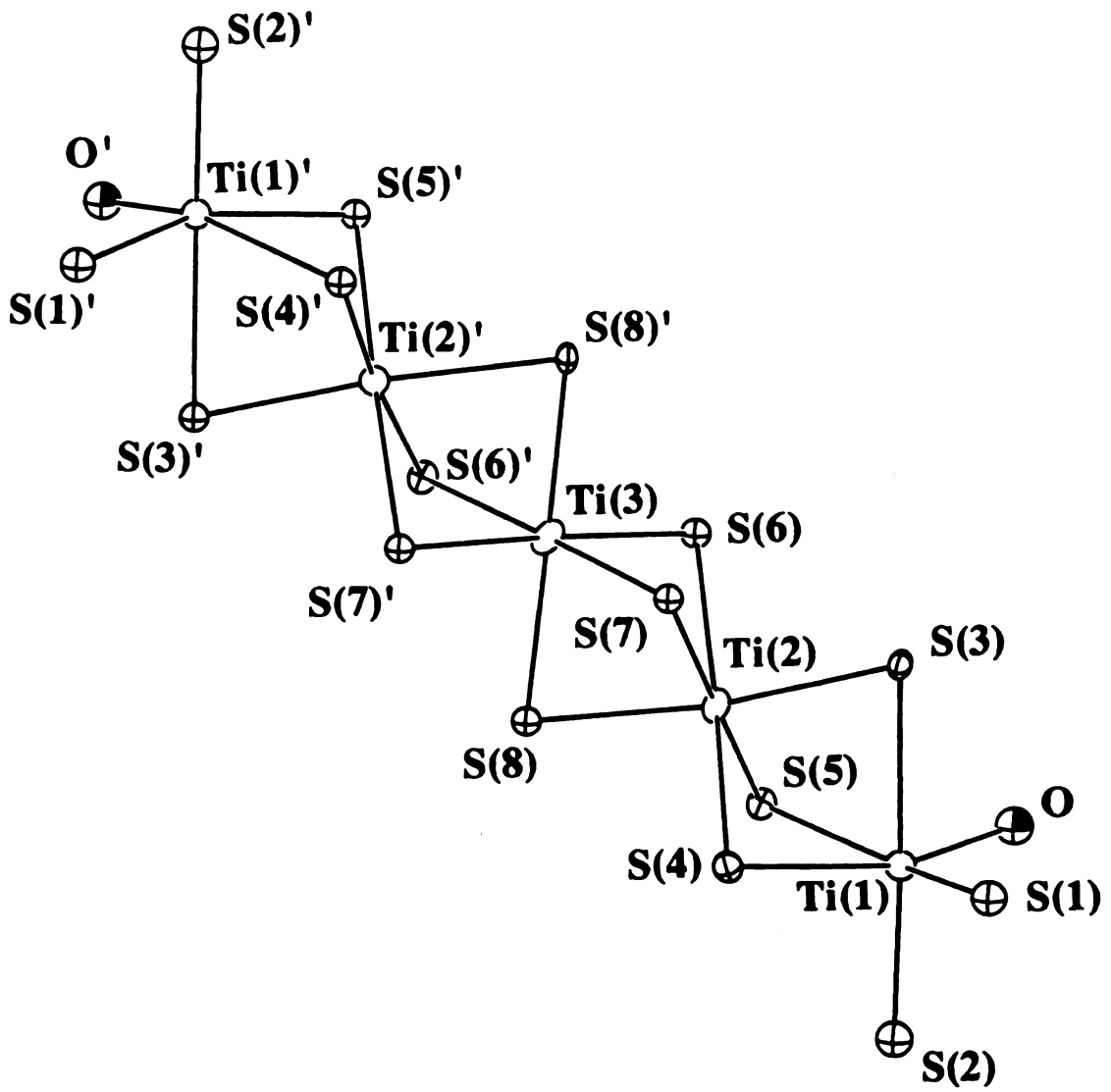

Figure 4.2.1: The basic repeating unit in the structure of $Ba_6Ti_5S_{15}O$: five face-sharing Ti-centered octahedra.

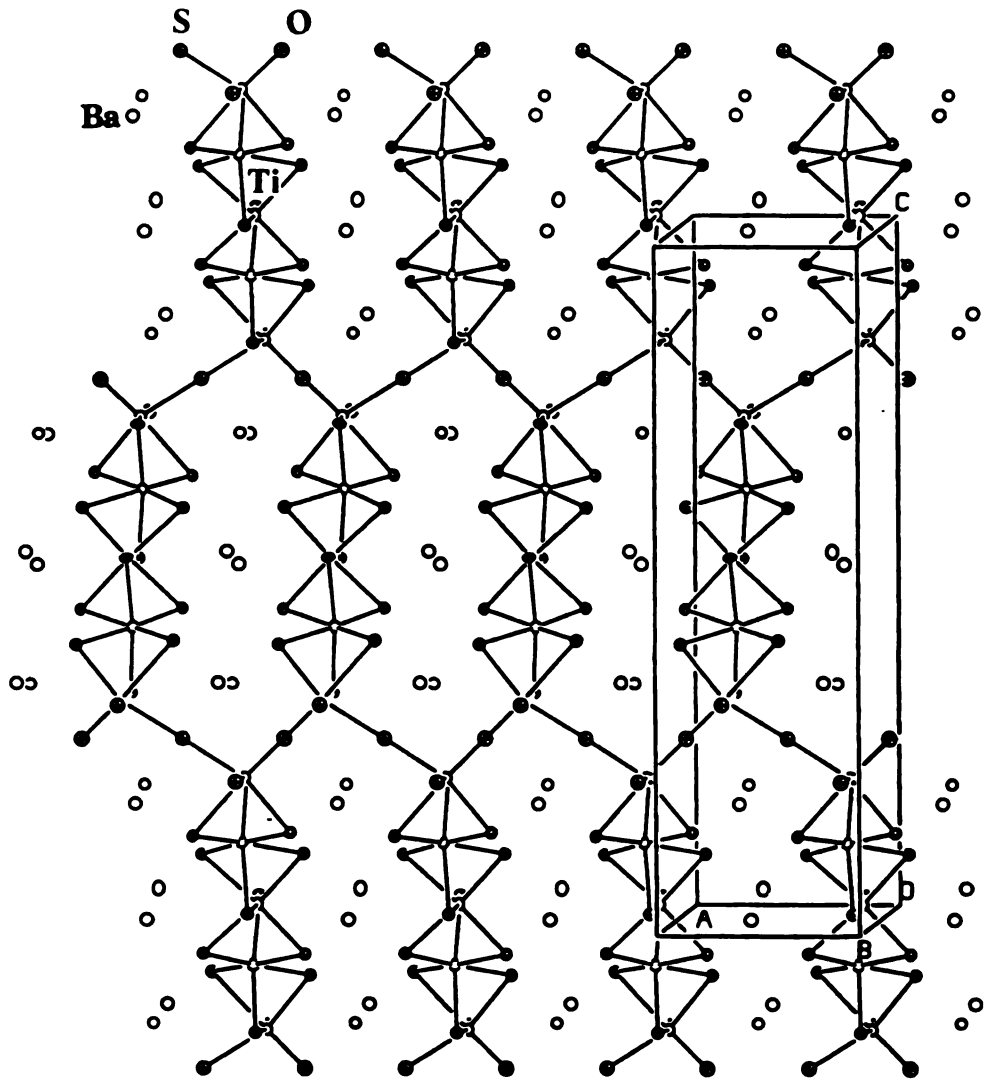

Figure 4.2.2: The view perpendicular to a single anionic layer from $Ba_6Ti_5S_{15}O$

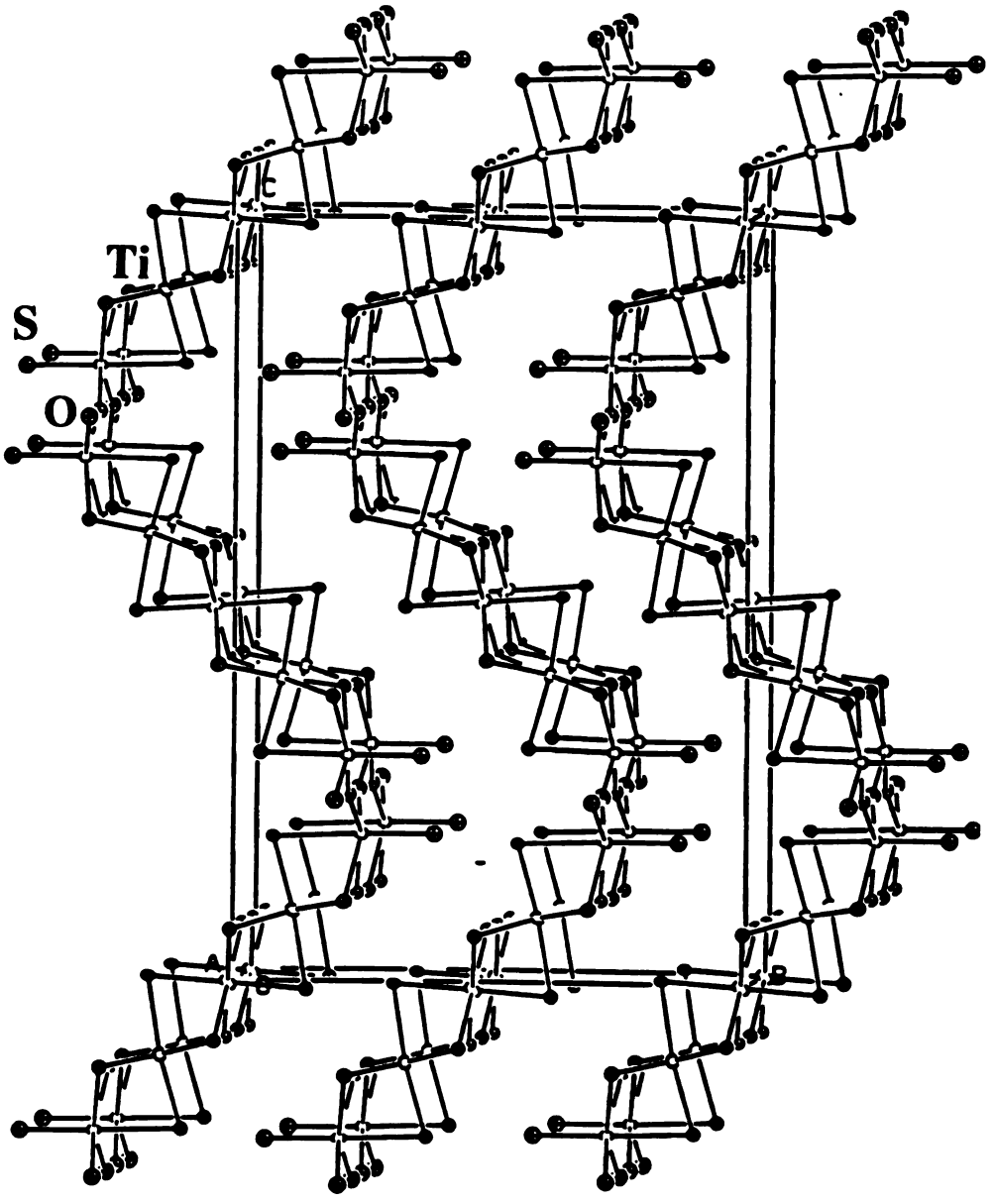

Figure 4.2.3: The structure of $Ba_6Ti_5S_{15}O$ as seen parallel to the a-axis

Table 4.2.3:Selected Bond Distances (Å) and Angles (°) for $Ba_6Ti_5S_{15}O$

Ti(1) -O	1.85(1)	Ti(2) -S(3)	2.34(1)
S(1)	2.44(2)	S(4)	2.28(2)
S(2)	2.23(1)	S(5)	2.48(2)
S(3)	2.64(1)	S(6)	2.60(2)
S(4)	2.67(2)	S(7)	2.37(2)
S(5)	2.41(2)	S(8)	2.42(1)
Ti(3) -S(6)	2.34(2)	Ti(3) -S(8)	2.39(1)
S(7)	2.49(2)		

S(1)-Ti(1)-O	102.7(8)	S(3)-Ti(2)-S(4)	95.0(2)
S(2)	92.3(2)	S(5)	88.4(2)
S(3)	83.8(2)	S(6)	88.0(2)
S(4)	80.2(8)	S(7)	92.2(2)
S(5)	157.4(2)	S(8)	170.2(2)
S(2)-Ti(1)-O	98.9(6)	S(4)-Ti(2)-S(5)	85.9(9)
S(3)	174.3(2)	S(6)	174.0(2)
S(4)	95.5(2)	S(7)	99.4(9)
S(5)	99.0(2)	S(8)	94.7(2)
S(3)-Ti(1)-O	86.0(6)	S(5)-Ti(2)-S(6)	89.0(9)
S(4)	79.7(1)	S(7)	174.6(2)
S(5)	83.4(2)	S(8)	91.0(2)

Table 4.2.3:Selected Bond Distances (Å) and Angles (°) for $Ba_6Ti_5S_{15}O$ (cont.)

S(6)-Ti(3)-S(6)'	95.9(9)	Ti(1)-O-Ti(1)*	166(1)
-S(7)	175.3(2)	Ti(1)-S(1)-Ti(1)*	170.6(3)
-S(7)'	88.7(8)	Ti(1)-S(3)-Ti(2)	76.2(2)
-S(8)	88.5(2)	-S(4)-	76.6(7)
-S(8)'	95.3(2)	-S(5)-	78.1(6)
S(7)-Ti(3)-S(6)'	88.7(8)	Ti(2)-S(6)-Ti(3)	74.3(6)
-S(7)'	86.7(9)	-S(7)-	75.8(6)
-S(8)	90.3(2)	-S(8)-	76.9(1)
-S(8)'	85.5(2)		
S(8)-Ti(3)-S(6)'	95.3(2)		
-S(7)'	90.3(2)		
-S(8)'	174.3(3)		

*represents atom on the neighboring fragment.

Spectroscopic Data -- The optical absorption spectrum of $Ba_6Ti_5S_{15}O$ is shown in Figure 4.2.4. The onset of a sharp change in (α/S) at approximately 1.04 eV corresponds to an estimate of the band gap of this compound. Hence, $Ba_6Ti_5S_{15}O$ is expected to be a semiconductor. As in the semiconducting TiS_2 this absorption arises from the photon excitation of valence band electrons localized mainly on sulfur orbitals to the d-band orbital levels (t_{2g} type) of Ti. Also observed are several higher energy peaks at 1.38, 172, 2.92 and 4.73 eV.

The solid-state far-IR spectrum of $Ba_6Ti_5S_{15}O$ shows the following strong peaks: 418, 389, 359, 329, 292, 234, 209, 199, and 141 cm^{-1}. With the exception of the high energy 418 cm^{-1} band, which is likely caused by Ti-O asymmetric vibrations, the variety of Ti-S bonds in the material make specific assignments of the peaks difficult.

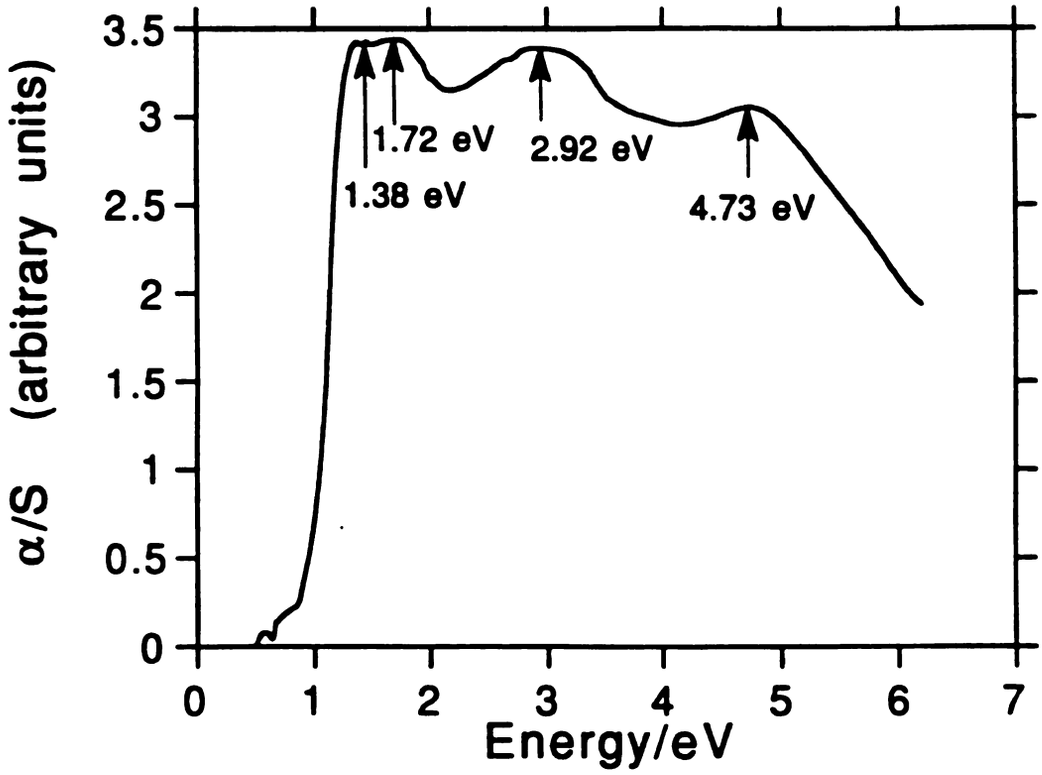

Figure 4.2.4: The solid state diffuse reflectance spectra of $Ba_6Ti_5S_{15}O$ plotted as absorption coefficient (α/S) vs. energy (eV).

D. Conclusions

The new metal/oxysulfide $Ba_6Ti_5S_{15}O$ represents the first member in a potential new family of compounds with the general formula $(BaO)_n(BaTiS_3)_m$. Aside from being of potential interest as a layered intercalation host, the material represents a possible new direction in the underexplored area of solid state oxychalcogenide chemistry. Specifically, it may be possible to use the high oxophilicity of early transition metal elements to drive structural modifications of known non-oxide starting materials by using only small amount of oxide to diffuse through and fragment the parent phase. Such chemistry would no doubt be facilitated by the use of starting phases of reduced dimensionality, as oxide ions could diffuse more readily through such materials. Although potentially accessible by stoichiometric combinations of starting materials, some manner of flux growth may be necessary to form single crystals suitable for structure determination.

REFERENCES

1) (a) Donika, F. G., Klosse, G. A., Radautsan, S. I., Semiletov, S. A., Zhitar, V. F., *Sov. Phys.-Crystallogr. (Engl. Transl.)* **1968**, *12*, 745-749. b) Boorman, R. S., Sutherland, J. K., *J. Mater. Sci.* **1969**, *4(8)*, 658-671. c) Barnett, D. E., Boorman, R. S., Sutherland, J. K., *Phys. Status Solidi A* **1971**, *4(1)*, K49-K52.

2) Kanatzidis, M. G.; *Chem. Mater.* **1990**, *2*, 353-363.

3) Walker, N., Stuart, D., *Acta Cryst.* **1983**, *A39* , 158-166.

4) (a) G. M. Sheldrick, in *Crystallographic Computing 3* Sheldrick, G. M., Kruger, C., Doddard, R., Eds.; Oxford University Press: Oxford, England, **1985**, p. 175-189. (b) Gilmore G. J., *Appl. Cryst.* **1984**, *17* , 42-46.

5) Cromer, D. T., Waber, J. T., in *"International Tables for X-ray Crystallography, Vol. IV"* (Eds. Ibers, J. A., Hamilton, W. C.), The Kynoch Press, Birmingham, England, **1974**, Table 2.2A.

6) Ibers, J. A., Hamilton, W. C., *Acta Cryst.* **1964**, *17*, 781-782.

7) Cromer, D. T., in *"International Tables for X-ray Crystallography, Vol. IV"* (Eds. Ibers, J. A., Hamilton, W. C.), The Kynoch Press, Birmingham, England, **1974**, Table 2.3.1.

8) (a) Clearfield, A.; *Acta Cryst.* **1963**, *16*, 134. (b) Huster, J.; *Z. Naturforsch.* **1980**, *B35*, 775.

9) (a) Saeki, M., Yajima, Y., Onoda, M., *J. Solid State Chem.* **1991**, *92*, 286-294. (b) Chen, B.-H., Eichhorn, B. W., *Mater. Res. Bull.* **1991**, *26*, 1035-1037. (c) Chen, B.-H., Eichhorn, B. W., Fanwick, P. E., *Inorg. Chem.* **1992**, *31*, 1788-1791.

10) Lelieveld, R., Ijdo, D. J. W., *Acta Cryst.* **1980**, *B36*, 2223-2226.

11) Andersson, S., Wadsley, A. D., *Acta Cryst.* **1961**, *14*, 1245.

12) (a) Verbaere, A., Tournoux, M., *Bull Soc. Chim. Fr.* **1973**, 1237. b) Dion, M., Piffard, Y., Tournoux, M., *J Inorg. Nucl. Chem.* **1978**, *40*, 917.

13) (a) Grey, I.E., Madsen, I. C., Watts, J. A., Bursill, L. A., Kwiatkowska, J., *J. Solid State Chem.* **1985**, *58*, 350. (b) Kwiatkowska, J., Grey, I.E., Madsen, I. C., Bursill, L. A., *Acta Cryst.* **1987**, *B43*, 258.

14) (a) Marchand, R., Brohan, L., Tournoux, M., *Mater. Res. Bull.* **1980**, *15*, 1129, (b) Izawa, H., Kikkawa, S., Koizumi, M., *J. Phys. Chem.* **1982**, *86*, 5023. (c) Saski, T., Watanabe, M., Komatsu, Y., Fujiki, Y., *Inorg. Chem.* **1985**, *24*, 2265. (d) Saski, T., Watanabe, M., Komatsu, Y., Fujiki, Y., *Chem. Mater.* **1992**, *4*, 894-899.

PART III: $K_2CuCe_2Se_6O(H?)$: A Kinetically Sensitive Derivative of the $ACuM_2Q_6$ (M=Lanthanide, Q=Chalcogenide) Structure Type with the Possible Presence of a Hydroxide for Charge Neutrality

A. Introduction

The compound $Ba_6Ti_5S_{15}O$ provides an illustration of a oxychalcogenide which formed a very different structure type from that of the parent ternary, $BaTiS_3$, while still retaining some structural elements in common [1]. $K_2CuCe_2Se_6OH$ is another such example, but this phase is even more closely related to its parent, $KCuCe_2Se_6$, than $Ba_6Ti_5S_{15}O$ is to $BaTiS_3$. Both $K_2CuCe_2Se_6OH$ and $KCuCe_2Se_6$ feature stacks of face-sharing $[CeSe_6]$ trigonal prisms linked into anionic layers by capping interactions across the stacks with Cu^+ occupying tetrahedral sites between the stacks. Inclusion of oxygen into the former phase results in distortions from the more symmetrical structure of the parent as the packing forces in the oxygenated offspring adjust to the smaller Ce-O bond distances.

B. Experimental

1. Synthesis

Reagents -- The following reagents were used as obtained: cerium, 40 mesh, Johnson M. Matthey Co., Ward Hill, MA; selenium powder, 100 mesh, Aldrich, Milwaukee, WI; potassium metal, analytical reagent, Mallinckrodt Inc., Paris, KY. Dimethylformamide (DMF) used is obtained in analytical reagent grade from EM Science, Inc., Gibbstown, NJ.

Potassium Sulfide, K_2Se -- Synthesis of this compound was performed as described in Chapter 2, Sec. B.1.

Dipotassium copper dicerium hydroxyhexaselenide, $K_2CuCe_2Se_6OH$ -- A mixture of 0.196 g (1.25 mmol) K_2Se, 0.016 g (mmol) Cu, 0.035 g (0.25 mmol) Ce, and 0.316 g (4.0 mmol) Se are thoroughly mixed in an N_2 filled glove box and loaded into a pyrex tube. The tube is removed from the box and evacuated on a Schlenck line to $<3x10^{-3}$ mbar and flame sealed. The reactants are heated at 300 °C for 4 days and cooled to 180 °C at 4 °C/hr. followed by quenching to 50 °C. Afterwards, the tube is opened with a glass cutter, and the entire solid mass is placed in a 250 mL Erlenmeyer flask, which has a side arm attachment to allow for the purging of the flask contents with N_2. Excess polyselenide flux is removed by dissolving it in successive portions of degassed dimethylformamide (DMF). Approximately 50-100 mL of solvent is added to the flask resulting in a green/brown solution as the excess K_2Se_x is dissolved. Nitrogen flow through the flask is maintained during the isolation to prevent the oxidation of the solubilized polychalcogenide by ambient O_2 which would cause elemental Se to precipitate, contaminating the product. When a portion of solvent becomes saturated (as evidenced by a very dark color to the solution), it is carefully decanted from the remaining solid, and a fresh portion is added. Washings are continued until the solvent remains clear, signaling complete polyselenide removal. The sample is decanted one final time and then dried under vacuum. The remaining material is a mass of red microneedles with small amounts of black, apparently amorphous, powder. The identity of the red microneedles is confirmed by comparing the powder X-ray diffraction pattern of the product against one calculated using X-ray single crystal data (See Table 4.3.1).

Table 4.3.1: Calculated and Observed X-ray Powder diffraction Pattern for $K_2CuCe_2S_6OH$ (Cu radiation)

h k l	d_{calc}/(Å)	d_{obs}/(Å)	I/I_{max} obs (%)
0 0 2	9.20	9.08	100.00
2 0 1	6.41	6.34	5.31
2 0 -3	5.70	5.63	9.06
0 0 4	4.601	4.566	2.90
1 1 -1	4.059		
4 0 -2	3.982	3.958	2.13
2 0 -5	3.793	3.771	2.49
4 0 -4	3.506	3.484	7.24
2 0 4	3.504		
3 1 -1	3.322	3.325	3.12
4 0 2	3.206		
2 0 -6	3.199		
1 1 -4	3.185	3.177	7.87
3 1 1	3.109	3.112	2.74
0 0 6	3.067	3.054	2.59
3 1 -4	2.941	2.964	1.72
1 1 4	2.940	2.927	5.71
3 1 2	2.902	2.890	2.31
1 1 -5	2.851	2.834	2.31
4 0 -6	2.848		
6 0 -2	2.673	2.655	4.92
6 0 -4	2.584	2.570	8.39
4 0 4	2.583		
6 0 0	2.550		
5 1 -1	2.542	2.536	3.17
5 1 -3	2.524	2.522	1.75
5 1 0	2.481		
5 1 -4	2.448	2.459	2.50
6 0 1	2.428	2.406	4.72
1 1 6	2.364	2.355	1.94
4 0 5	2.325	2.317	3.10

Table 4.3.1: Calculated and Observed X-ray Powder diffraction Pattern for $K_2CuCe_2S_6OH$ (Cu radiation) (cont.)

h k l	d_{calc}/(Å)	d_{obs}/(Å)	I/I_{max} obs (%)
0 0 8	2.301	2.292	26.55
5 1 2	2.261	2.249	1.37
5 1 -6	2.211	2.201	2.76
0 2 0	2.120	2.111	1.76
4 0 6	2.104	2.096	5.51
0 2 2	2.066	2.072	1.54
2 0 8	2.040	2.034	6.48
8 0-5	1.9548	1.9487	1.57
5 1 -8	1.9396	1.9327	1.28
		1.9170	1.56
		1.9116	1.35
4 0 -10	1.8966	1.9052	1.96
7 1 -6	1.8851	1.8891	5.95
0 0 10	1.8405	1.8351	4.98
8 0 -8	1.7528	1.7597	2.17
1 1 -10	1.7310	1.7300	1.28
6 0 6	1.7223	1.7227	2.06
4 2 -6	1.7006	1.7163	2.50
6 2 -2	1.6610		
7 1 4	1.6392	1.6299	1.92
4 2 4	1.6388	1.6229	1.85
6 2 -5	1.6097	1.6092	2.27
6 2 1	1.5970	1.5951	2.25
0 2 8	1.5590	1.5551	1.47

The synthesis of $K_2CuCe_2Se_6OH$ has proven to be very sensitive to the reaction conditions. Isotherm temperatures higher than 300 °C will cause $KCuCe_2Se_6$ to become the major phase, with $K_2CuCe_2Se_6OH$ present in only small amounts or totally absent. Also, if the amount of metal is increased in the reaction while maintaining the same low temperature, the product becomes a mixture of $KCuCe_2Se_6$ and KCu_4S_3. It is at first glance unusual that an element with the high oxophilicity of Ce would form a kinetically stable oxide containing phase before proceeding to a phase composed of all soft bases such as $KCuCe_2Se_6$. What likely happens as the reaction progresses is that a portion of $K_2CuCe_2Se_6OH$ is actually converted to CeO_2, and once all the available oxide has been scrubbed from the system by the formation of the stable binary, the remaining Ce^{3+} is left free to react in the more pure polyselenide.

Before the presence of hydrogen was suspected, rational synthesis of $K_2CuCe_2Se_6OH$ was attempted by using mixtures of fresh K_2Se, CuO, Ce, and Se in various ratios at the reaction temperature of 300 °C. The best result from these trials was from a 5/1/2/16 ratio of the above starting materials, but the product was impure with approximately 80% being $K_2CuCe_2Se_6OH$ and the remainder, an unknown black powder. A reaction with the starting materials in their exact stoichiometric ratios (1/1/2/5) saw the red needles of $K_2CuCe_2Se_6OH$ decrease to approximately 25% of a mixture with black powder, and molar ratios with only a slight excess of flux (1.5/1/2/7.5 and 2/1/2/10) resulted in a total absence of $K_2CuCe_2Se_6OH$. Apparently, the phase is best formed under conditions of dilute metal and oxygen content in the flux.

2. Physical Measurements

The instrumentation and experimental setup for the following measurements are the same as described in Chapt. 2, Sec. B.2: powder X-ray diffraction, infrared spectroscopy, and UV/Vis/near IR spectroscopy (diffuse reflectance mode).

Single Crystal X-ray Diffraction -- Intensity data were collected using a Rigaku AFC6S four-circle automated diffractometer equipped with a graphite crystal monochromator. An ω-2θ scan mode was used. The crystal's stability was monitored with three standard reflections whose intensities were checked every 150 reflections, and unless noted, no crystal decay was detected. An empirical absorption correction based on ψ scans was applied to all data during initial stages of refinement. The positions of the compound's Cu and O atoms had to be fixed in order for them to refine successfully An empirical DIFABS correction [2] was applied after full isotropic refinement, after which full anisotropic refinement was performed. The structure was solved by direct methods using SHELXS-86 software [3a] , and full matrix least squares refinement was performed using the TEXSAN software package [3b]. Crystallographic data for the compound is summarized in Table 4.3.2, and fractional atomic coordinates and thermal parameters are given in Table 4.3.3.

All heavy atoms refined well, and both the low residuals (R/Rw=5.9/7.4%) and the consistency between calculated and observed X-ray powder diffraction patterns (Table 4.3.1) indicate a valid structural model. The crystal did experience severe twinning effects however which hampered efforts to obtain a unit cell with improved standard deviations. As a result of the limited quality of the data, the lightest atom of the phase,

oxygen, could not be refined unless all of its atomic coordinates were fixed, and even then the atom only could be refined isotropically.

As refined, the formula of the compound was $K_2CuCe_2Se_6O$, and, with Ce in their common trivalent oxidation state, this would have required another positive charge to balance the extra O^{2-} anion. No significant electron density could be found which would account for a full atom, and the electron density in the O site refined well only at full occupancy. As will be discussed further in the coming sections, the presence of an H^+, forming an $(OH)^-$ group rather than a monoxide, began to be suspected. The position of an H^+ was calculated such that the O atom would be in an approximate tetrahedral environment, but the inclusion of the hydride did not significantly improve the refinement. This is not surprising as finding one H^+ ion in an otherwise heavy atom structure is like trying to see a speck of dust amid bowling balls. The presence of a hydride does seem to be indicated by other techniques, however.

Table 4.3.2: Crystallographic Data for $K_2CuCe_2Se_6OH$.

	$K_2CuCe_2Se_6OH$
a, Å	16.04(2)
b, Å	4.24(1)
c, Å	19.30(1)
β, °	107.5(1)
V, $Å^3$	1252(2)
space group	C2/m (#12)
Z	4
F.W., g/mol	975.29
d_{calc}, g/cm^3	5.174
μ, cm^{-1}	285.27
crystal dimensions, mm^3	0.01 x 0.02 x 0.60
radiation	Mo Kα
2θ max.	59.9°
data collection temp., °C	23
# data collected	1599
# unique data	1244
# $F_o^2>3\sigma$	683
# of variables	66
R/Rw, %	5.9/7.4
final Dif. map max. peak, $e^-/Å^3$	3.63

[a] $R=\Sigma(|Fo|-|Fc|)/\Sigma|Fo|$ $Rw=\{\Sigma w(|Fo|-|Fc|)^2/\Sigma w|Fo|^2\}^{1/2}$

Table 4.3.3 Fractional Atomic Coordinates and B_{eq}[a] values for $K_2CuCe_2Se_6OH$ with Estimated Standard Deviations in Parentheses

atom	x	y	z	B_{eq}
Ce(1)	0.2839(2)	0	0.3101(2)	0.9(1)
Ce(2)	0.4104(2)	-1/2	0.1849(2)	0.9(1)
Cu	0.1034	-1/2	0.2498	2.1(3)
Se(1)	0.4229(3)	-1/2	0.3870(3)	1.2(2)
Se(2)	0.2964(3)	-1/2	0.4283(3)	1.4(2)
Se(3)	0.3447(3)	-1	0.0627(4)	1.5(2)
Se(4)	0.5012(3)	-1	0.1122(3)	1.4(2)
Se(5)	0.2255(3)	-1/2	0.1962(4)	1.1(2)
Se(6)	0.0850(3)	0	0.3059(3)	1.1(2)
K(1)	0.1357(8)	-1	0.0647(8)	1.9(6)
K(2)	0.5959(7)	-1	0.4426(8)	2.3(6)
O	0.3978	0	0.2490	0.7(5)

[a] B values for anisotropically refined atoms are given in the form of the isotropic equivalent displacement parameters defined as $B_{eq} = (4/3)[a^2B(1,1) + b^2B(2,2) + c^2B(3,3) + ab(\cos\gamma)B(1,2) + ac(\cos\beta)B(1,3) + bc(\cos\alpha)B(2,3)$.

C. Results and Discussion

Structure -- The anionic layers of $K_2CuCe_2Se_6OH$ have as their general structural motif stacks of Ce-centered trigonal prisms which interconnect, through capping of the rectangular faces of the prisms, to form a two-dimensional layer while Cu^+ cations occupy tetrahedral sites within these layers. There are two distinct Ce atoms, differentiated by how the oxygen atoms are positioned in their coordination geometries. Ce(1) has a trigonal prism made of two $(Se_2)^{2-}$ units forming the short sides of the triangular faces and two monosulfides at the apex positions. The two capping positions of Ce(1) are occupied by one monoselenide and one oxygen atom. For Ce(2), the bicapped trigonal prismatic environment is repeated, but now the two apex positions are both occupied by O atoms while the capping atoms are both monoselenides. Only one crystallographically unique O atom is present in the formula and it is shared by both Ce environments as shown in Fig 4.3.1. The two Ce atoms also share the Se(5) atoms, which is in the apex position for Ce(1) and the capping position for Ce(2). The connectivity in the layers continues as Se(6) serves as a capping atoms to both Ce atoms, and the view parallel to the extended layers is given in Fig. 4.3.2.

The oxygen atoms appear to be the main factor distorting the $K_2CuCe_2Se_6OH$ structure away from that of the parent $KCuCe_2Se_6$. In order to contend with the shorter Ce-O bonds (Table 4.3.4), the stacks of trigonal prisms must twist in on one another rather than maintain the more symmetrical arrangement seen in the non-oxygen containing phase. This twisting sterically prohibits the consistent sharing of the edges defined by axial and capping atoms that connect the prisms in $KCuCe_2Se_6$ (see Fig.

4.3.3), and so $K_2CuCe_2Se_6OH$ must resort to an alternation between edge-sharing and corner-sharing of the Se(6) atoms.

As in the parent compound, the Cu atoms in $K_2CuCe_2Se_6OH$ occupy tetrahedral sites within an intralayer groove formed between two stacks of trigonal prisms. Because of the oxygen enforced twisting in the layers only one groove now exists which is conducive to the presence of Cu^+ cations, that defined by the Se(4), Se(5), and Se(6) atoms. No copper disorder is present in this structure; occupancy on the sole Cu site refines well at 100%, and the Cu-Se distances are both normal for what has been seen in previous compounds (Table 4.3.4).

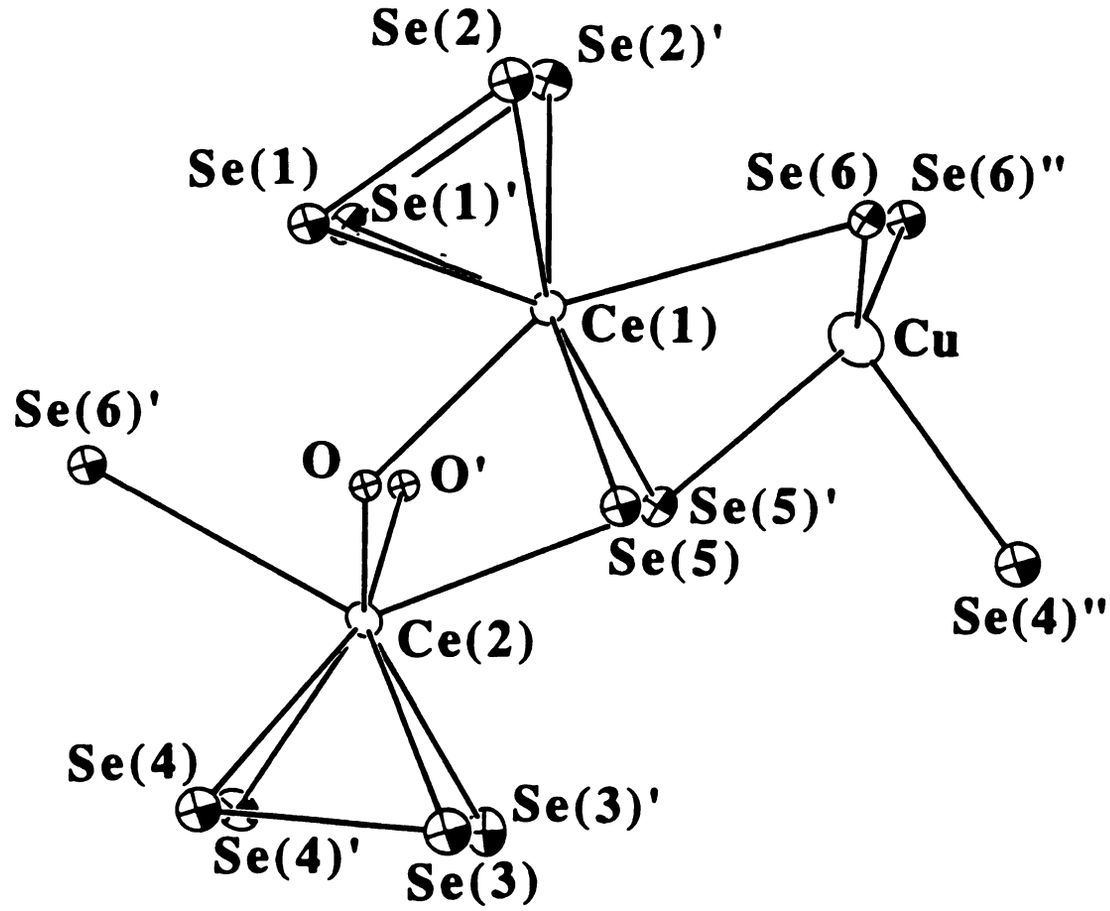

Figure 4.3.1: A fragment on the structure of $K_2CuCe_2Se_6OH$, highlighting the coordination environment of the metal atoms

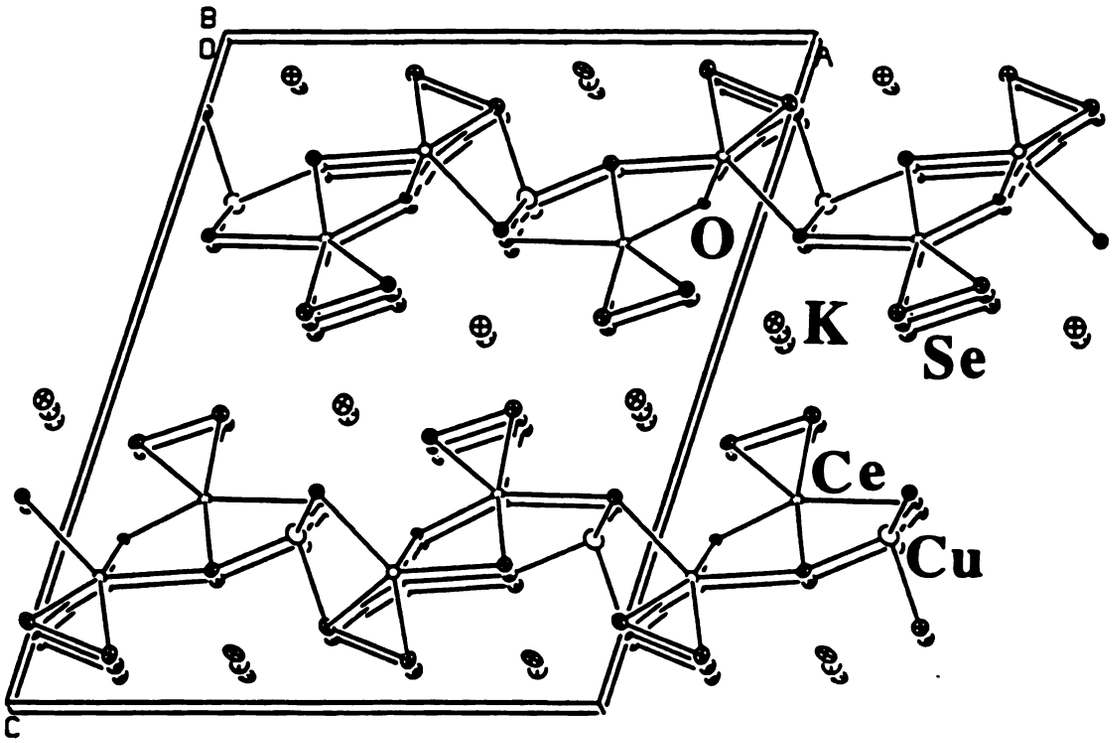

Figure 4.2.3: The extended structure of $K_2CuCe_2Se_6OH$ as seen parallel to the b-axis.

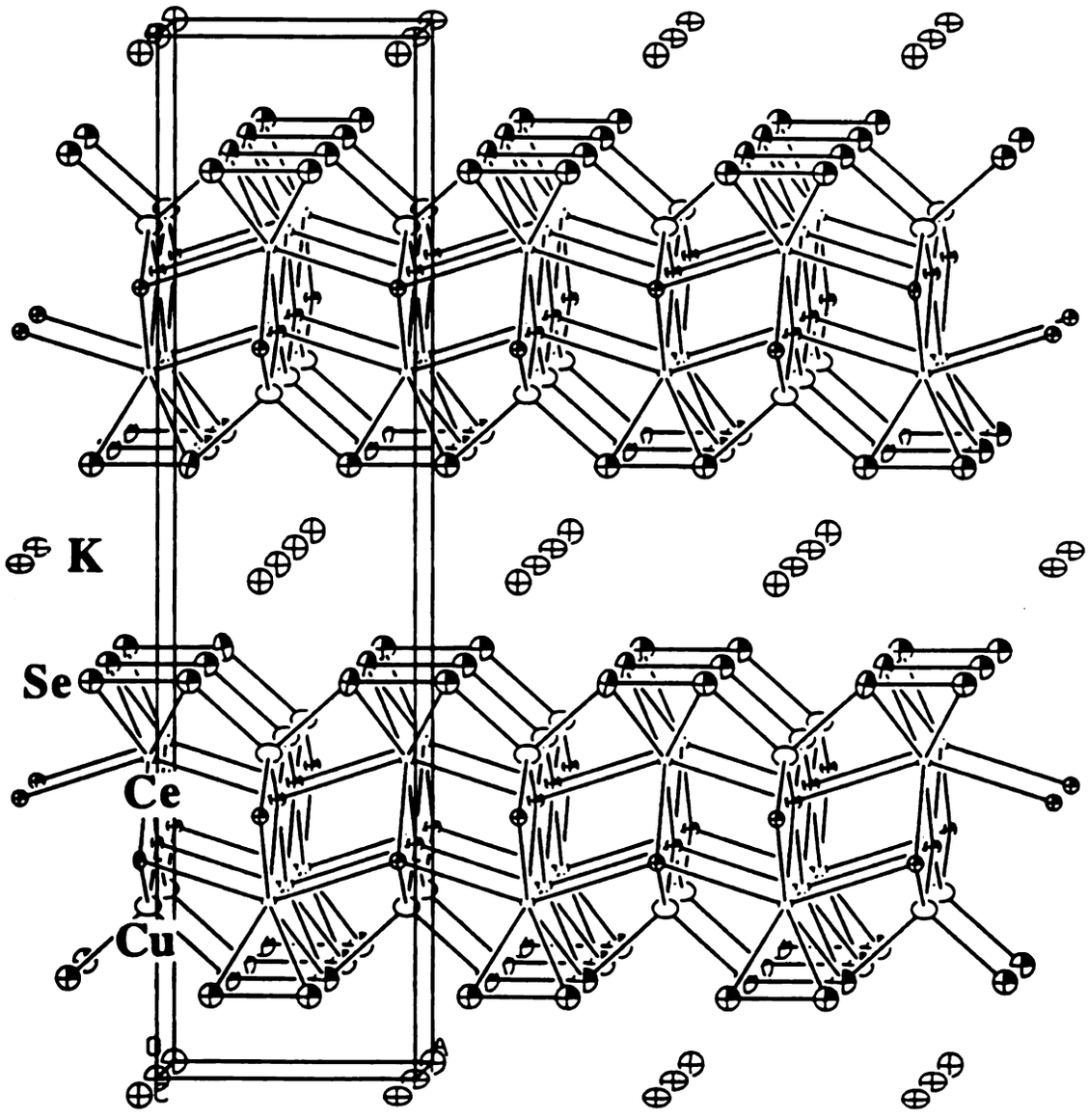

Figure 4.3.3: The extended structure of $KCuCe_2Se_6$ as seen parallel to the c-axis.

Table 4.3.4:Selected Bond Distances (Å) and Angles (°) for $K_2CuCe_2Se_6OH$ (standard deviations in parentheses)

Ce(1)-Se(1)	3.111(7)	Se(1)-Se(2)	2.394(8)
Ce(1)-Se(2)	3.076(7)	Se(3)-Se(4)	2.401(8)
Ce(1)-Se(5)	2.993(7)	Cu-Se(4)"	2.668(7)
Ce(1)-Se(6)	3.167(7)	Cu-Se(5)'	2.474(6)
Ce(1)-O	2.455(4)	Cu-Se(6)	2.438(7)
Ce(1)-Se(3)	3.110(8)	K(1)-Se(3)	3.37(1)
Ce(2)-Se(4)	3.133(7)	K(1)-Se(4)	3.34(1)
Ce(2)-Se(5)'	3.040(7)	K(2)-Se(1)	3.40(1)
Ce(2)-Se(6)'	3.058(8)	K(2)-Se(2)	3.31(1)
Ce(2)-O	2.492(6)		
Se(1)-Ce(1)-Se(1)'	85.9(3)	Se(3)-Ce(2)-Se(3)'	86.0(3)
Se(1)-Ce(1)-Se(2)	45.5(2)	Se(3)-Ce(2)-Se(4)	45.2(2)
Se(1)-Ce(1)-Se(2)'	103.8(2)	Se(3)-Ce(2)-Se(4)'	102.6(2)
Se(1)-Ce(1)-Se(5)	83.6(2)	Se(3)-Ce(2)-Se(5)'	86.5(2)
Se(1)-Ce(1)-Se(5)'	148.6(20	Se(3)-Ce(2)-Se(6)'	127.0(1)
Se(1)-Ce(1)-Se(6)	125.7(1)	Se(3)-Ce(2)-O'	153.7(1)
Se(1)-Ce(1)-O	72.5(1)	Se(3)-Ce(2)-O	74.7(2)
Se(2)-Ce(1)-Se(2)'	87.1(3)	Se(4)-Ce(2)-Se(4)'	85.2(3)
Se(2)-Ce(1)-Se(5)	89.6(2)	Se(4)-Ce(2)-Se(5)'	128.9(1)
Se(2)-Ce(1)-Se(5)'	165.6(2)	Se(4)-Ce(2)-Se(6)'	84.2(2)
Se(2)-Ce(1)-Se(6)	81.9(2)	Se(4)-Ce(2)-O'	156.3(1)
Se(2)-Ce(1)-O	117.7(1)	Se(4)-Ce(2)-O	76.4(2)
Se(5)-Ce(1)-Se(5)'	90.2(3)	Se(5)'-Ce(2)-Se(6)'	129.4(2)
Se(5)-Ce(1)-Se(6)	83.7(2)	Se(5)'-Ce(2)-O	74.8(1)
Se(5)-Ce(1)-O	76.2(1)	Se(6)'-Ce(2)-O	79.3(1)
Se(6)-Ce(1)-O	151.3(2)	O-Ce(2)-O'	116.5(2)
Se(4)"-Cu-Se(5)'	84.9(2)	Ce(1)-Se(5)'-Ce(2)	87.5(2)
Se(4)"-Cu-Se(6)"	108.7(2)	Ce(1)-O-Ce(2)	114.9(1)
Se(5)'-Cu-Se(6)"	113.7(1)	Se(6)-Cu-Se(6)"	120.8(3)

Magnetic Susceptibility -- The magnetic susceptibility as a function of temperature was measure at a constant field strength of 2000 Gauss (2-300 K), and a plot of the resulting data, as $1/\chi_M$ vs. T, is shown in Fig. 4.3.4. At high temperatures (>150 K) the plot has a linear, Curie-Weiss region, and as the temperature drops, values for $1/\chi_M$ begin to deviate negatively from the high temperature extrapolation. This is generally the behavior seen for many Ce^{3+} containing compounds [4,5], with the degree of low temperature deviations varying from compound to compound as a function of crystal field effects on the $^{5/2}F$ state of the lanthanide [5]. The deviations are slight but clearly present, where in $KCuCe_2Se_6$, the parent compound, the $1/\chi_M$ response with temperature was nearly linear [6], indicating that oxygen must be having a slight, but noticeable, effect of the electronic states of the Ce^{3+}. By fitting a straight line to the data above 120 K, a μ_{eff} of 2.55 BM/Ce^{3+} (3.61 BM/formula) was calculated, and this corresponds very well to both the theorectially expected value (2.54 BM) and those seen experimentally (2.3-2.5 BM) [7]. Also from the straight line fit, the Weiss constant (θ) was estimated to be -54 K indicating an appreciable amount of short range antiferromagnetic ordering.

[A]

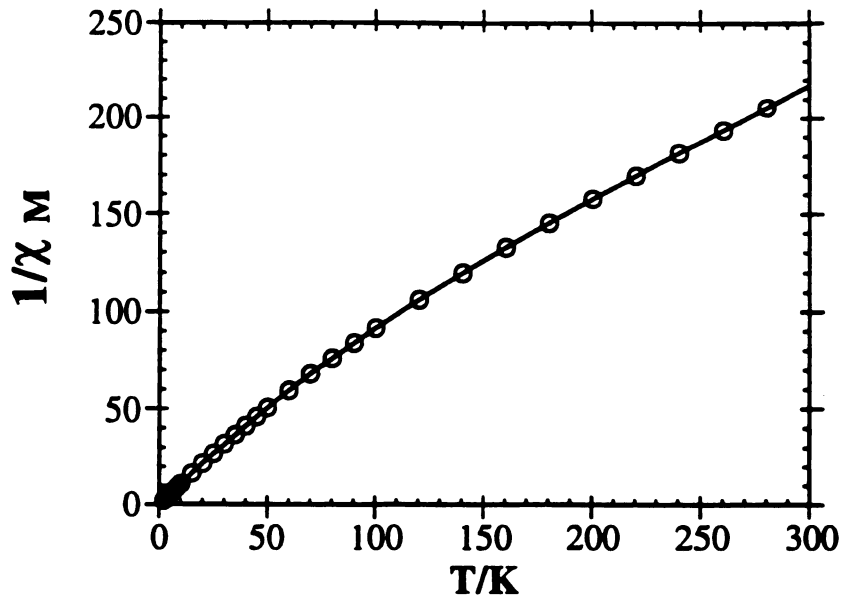

[B]

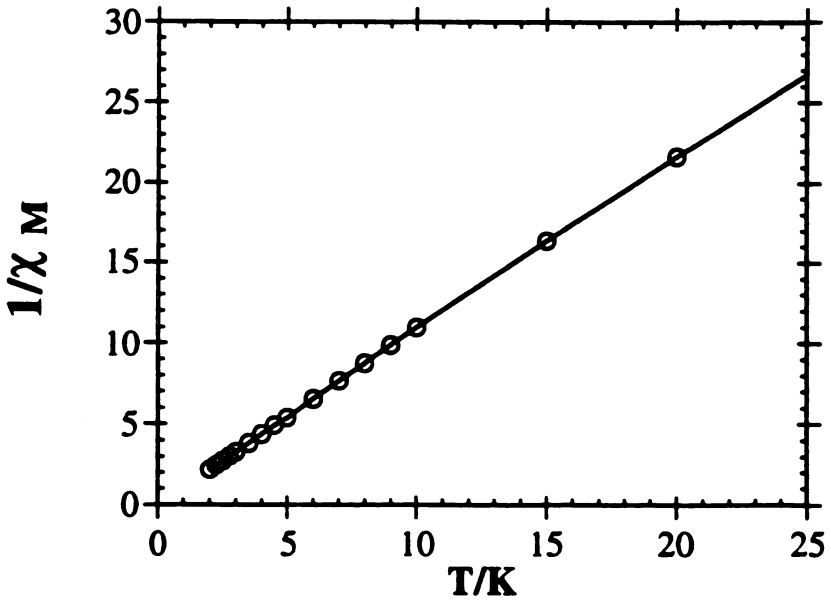

Figure 4.3.4: Inverse molar magnetic susceptibility ($1/\chi_M$) plotted against temperature (2-300 K) for $K_2CuCe_2Se_6OH$ (1000 Gauss). Plot (B) shows an expanded view of the region 2-25 K.

The μ_{eff} values show that Ce^{3+} is the only magnetically observed species in $K_2CuCe_2Se_6OH$. Although this rules out the presence of magnetically localized ions, such as Cu^{2+}, magnetically delocalized species could still be present. Such was the case in $K_2Cu_2CeS_4$; magnetic susceptibility measurements showed only one Ce^{3+} per formula which was charge balanced by S^{1-} states which were delocalized through the sulfur 3p band and consequently were magnetically silent [4b]. If an analogous situation were to exist in this oxyselenide, then a delocalized Se^{1-} should give rise to a dark colored, metallic material. In fact, the compound is red, which indicates a semiconductor. The magnetic studies provide further indications that the formula as derived from the single crystal structure, $K_2CuCe_2Se_6O$, is valence precise, and so charge balance in the compound must be achieved via a source other than modifications to the electronic structure.

Spectroscopy -- The optical diffuse reflectance spectrum of $K_2CuCe_2Se_6O$, plotted as absorption coefficient vs. energy, is given in Fig. 4.3.5. The sharp change in absorbance at 1.94 eV corresponds to an estimate of the material's band gap, and so gives added credence to the valence-precise, semiconduting nature to the compound.

In the solid state Far-IR spectrum of $K_2CuCe_2Se_6OH$ the following peaks are observed: 143, 180, 265, 292, 323, and 344 cm^{-1}. Because of their low energies, the 143 and 180 cm^{-1} bands are likely to be from Ce-Se stretching vibrations. Similar peaks were also seen in $KCuCe_2Se_6$ in the region 132-199 cm^{-1} [6]. The 265 cm^{-1} peak falls in the usual range seen for Se-Se vibrations; for example analogous peaks are present in α-$KCuSe_4$ (249 cm^{-1}) [8], α-$CsCuSe_4$ (252 cm^{-1}) [8], and $(Ph_4P)_2Se_5$ (267 cm^{-1}) [9]. The band at 292 cm^{-1} could likely be due to Cu-Se stretching; in α-$KCuSe_4$ and α-$CsCuSe_4$ tentative assignment of the Cu-Se vibrations was made to peaks at 241 and 246 cm-1, respectively [8]. By process of elimination, the other peaks are assigned as Ce-O bond vibrations.

An extra bit of circumstantial evidence for the presence of a hydroxide group in $K_2CuCe_2Se_6OH$ comes from the mid-IR spectrum which is compared to that of $KCuCe_2Se_6$ in Figure 4.3.6. Several weak peaks are common to both spectra and could be due to some organic contamination, and the origin of the strong low energy bands is unknown. The spectrum of $K_2CuCe_2Se_6OH$ does have an extra blip at 3408 cm^{-1} that is lacking in the all selenide phase. This is, in fact, the region which is characteristic to O-H bond stretches and so is consistent with the charge-balanced formula of the oxygen containing phases as $K_2CuCe_2Se_6OH$. The evidence for a hydrogen atom in the structure is still not fully convincing, however, and more experiments are still required.

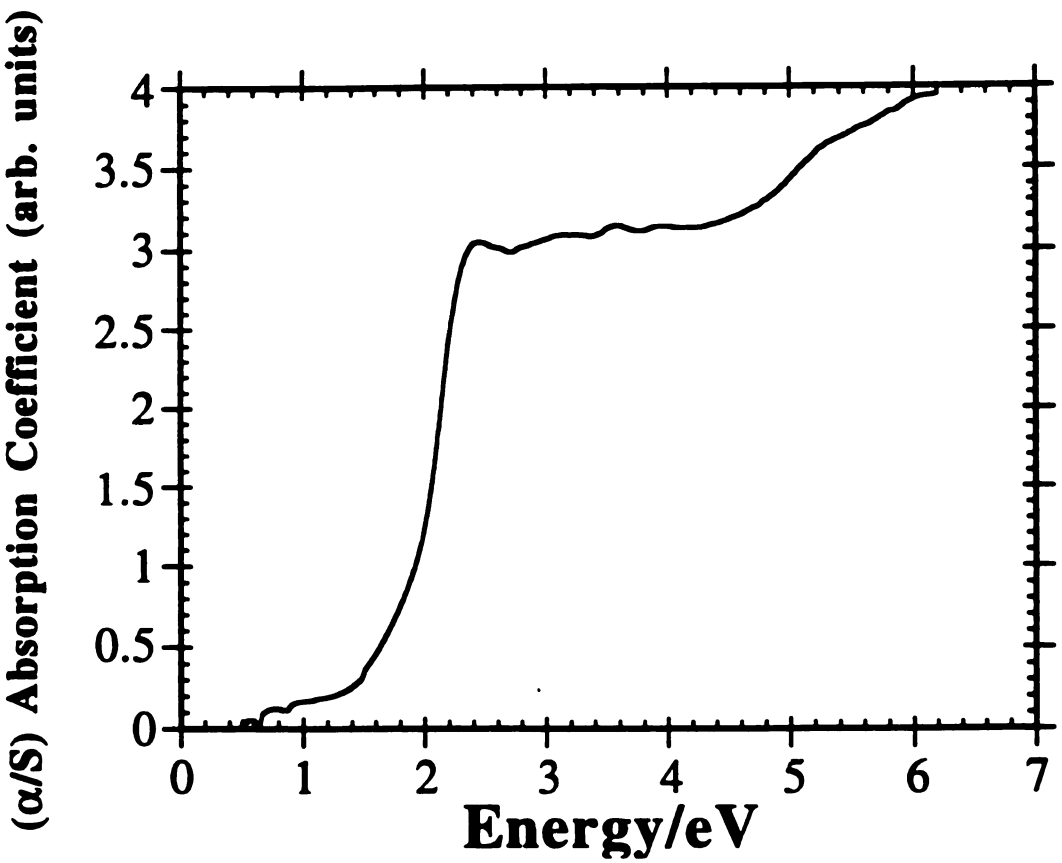

Figure 4.3.5: The solid state diffuse reflectance spectra of $K_2CuCe_2Se_6OH$ plotted as absorption coefficient (α/S) vs. energy (eV).

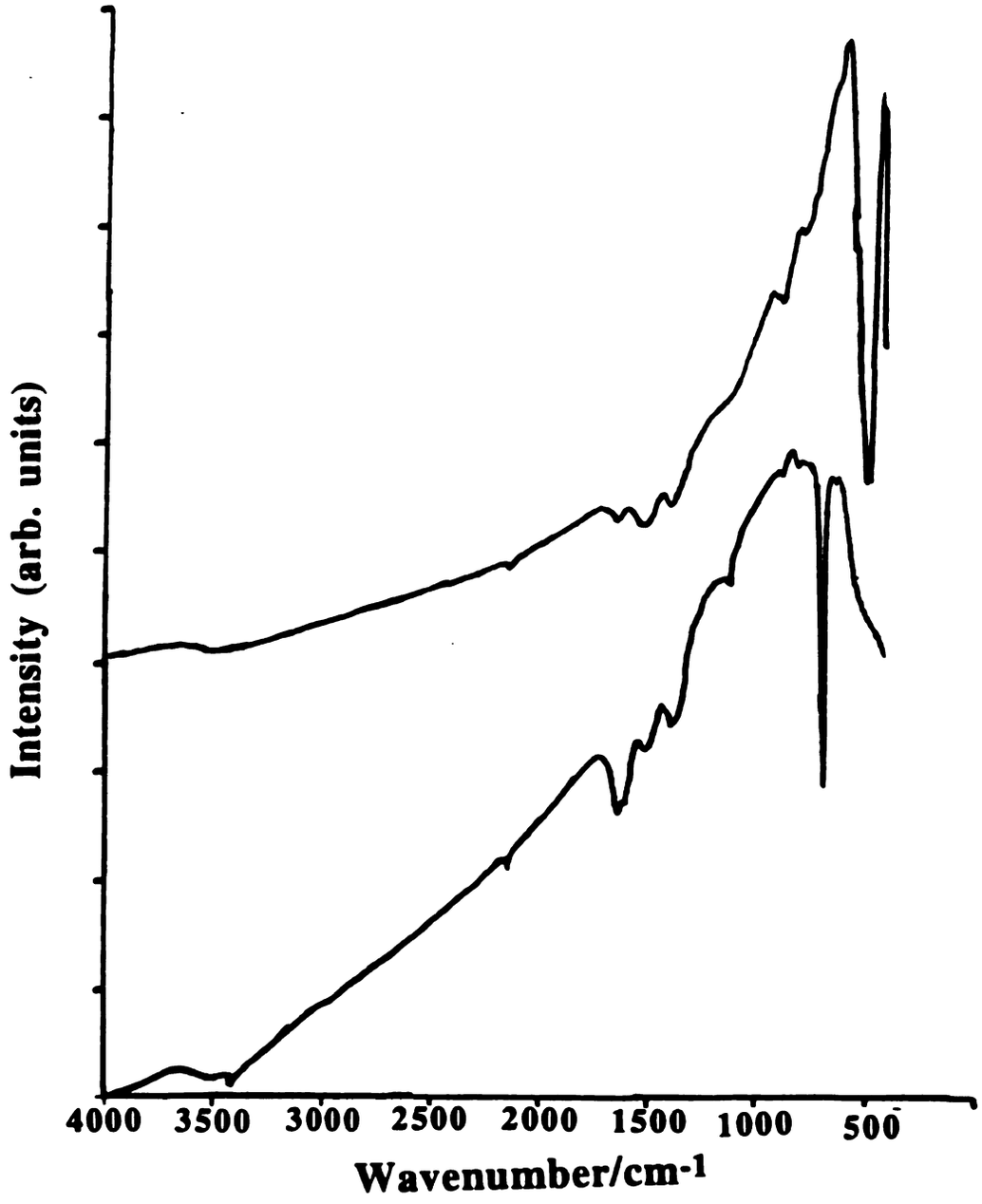

Figure 4.3.6: Spectra in the mid-IR region of (a) $K_2CuCe_2Se_6OH$ and (b) $KCuCe_2Se_6$ (KBr matrix)

D. Conclusions and Summary

With the presence of a hydroxide ligand indicated over that of an oxide, $K_2CuCe_2Se_6OH$ can now be considered as the parent quaternary phase distorted by the addition of an equivalent of KOH. The most likely source of this contamination is simple water adsorbed on the surface of the powdered starting materials. Since the age of the K_2Se does not seem to impact the synthesis of this phases, it would be logical to assume the contaminated reagent to be Se, which is exposed to air and ambient humidity before being brought into the N_2 filled glove box. Also, small amounts of the contaminants could be leached from the walls of the pyrex tubes during synthesis of the compound. The amount of water is apparently just enough to affect the reaction, and points to the difficulty in trying to control such levels of reactants in a rational manner. Although experiments involving anhydrous KOH and highly pure Se are now called for, the observed kinetic sensitivity to formation of CeO_2 and $KCuCe_2Se_6$ will add still another complication to the rational synthetic attempts.

REFERENCES

1) Sutorik, A. C., Kanatzidis, M. G., *Chem. Mater.*, in press.

2) Walker, N., Stuart, D., *Acta Cryst.* **1983**, *A39* , 158-166.

3) (a) G. M. Sheldrick, in *Crystallographic Computing 3* Sheldrick, G. M., Kruger, C., Doddard, R., Eds.; Oxford University Press: Oxford, England, **1985**, p. 175-189. (b) Gilmore G. J., *Appl. Cryst.* **1984**, *17* , 42-46.

4) (a) Sutorik, A. C., Kanatzidis, M. G., *Angew. Chem. Int Ed. Engl.*, **1992**, 31, 1594-1596. (b) Sutorik, A. C., Kanatzidis, M. G., *J. Am. Chem. Soc.*, **1994**, 116,

5) a) Lueken, H., Bruggemann, W., Bronger, W., Fleischhauer, J., *J. Less-Common Met.*; **1979**, 65, 79-88. b) Duczmal, M., Pawlak, L., *J. Magn. Magn. Mater.*; **1988**, 76-77, 195-196.

6) Chapter 3, Sec. 1 or 2

7) Greenwood, N. N., Earnshaw, A., *Chemistry of the Elements*; Pergamon Press, **1984**, p.1443.

8) Park, Y. P., PhD dissertation, Michigan State University, E. Lansing, MI, **1991**.

9) Huang, S.-P., Kanatzidis, M. G., *Inorg. Chem.*, **1991**, 30, 1455-1466.

Part VI: $Cs_4(UO_2)S_6$, $Na_4(UO_2)S_6 \cdot Na_2S_3$, and $Na_4Cu_2(UO_2)S_4$: The *in situ* Formation and Subsequent Reaction of Uranyl Cations in Molten Alkali Metal/ Polychalcogenide Salts

A. Introduction

The major difficulty in attempting to synthesize new metal/oxychalcogenides from molten A_2Q_x fluxes is one that has always hampered exploratory efforts into such compounds: the high stability of the binary metal oxides. The use of relatively mild reaction temperatures (in solid state synthetic terms) of 250-600 °C, which has proven effective in the formation of kinetically stabilized products in so many systems, does not help to overcome the high lattice stability of the oxides. Hence in general, reactions in which oxygen has been included are likely to lead to the formation of separate oxide and chalcogenide phases, rather than their incorporation into a single phase. The examples of metal/oxychalcogenides from molten polychalcogenide fluxes which do exist ($Ba_6Ti_5S_{15}O$ [1], $K_2CuCe_2Se_6OH$ [2], and $Na_{1.9}Cu_2Se_2 \cdot CuO$ [3]) were discovered by accident, usually through contaminated starting materials, rather than by design.

In order to help insure the incorporation of oxide and chalcogenide into the same compound, the system must be given a very thermodynamically stable alternative to phase separation. One way this can be done is through the use of oxymetal cations. Such species are composed of a high valent metal cation multiply bonded to one or two oxygen atoms and include uranyl ($(UO_2)^{2+}$), vanadyl ($(VO)^{2+}$), titanyl ($(TiO)^{2+}$) molybenyl ($(MoO)^{3+}$), tungstenyl ($(WO)^{3+}$), ruthenyl ($(RuO_2)^{2+}$), and

osmyl ($(OsO_2)^{2+}$) [4]. The first two examples have been found to have significant stability with respect to further oxygen coordination and as such have proven to be convenient starting materials for coordination chemistry studies. The metal/oxygen double bonds have the effect of lowering the acidity of the metal cations, making them less likely to form the highly stable solid state oxides. Given their stability these oxymetal cations should prove to be useful building block in molten A_2Q_x reactions as well. Since the f-block reactivity in molten A_2Q_x fluxes was already under investigation in both ternary and quaternary systems, the first oxymetal cation to be investigated was the uranyl, $(UO_2)^{2+}$, and has lead to the discovery of two new oxychalcogenide phases: $Cs_4(UO_2)S_6$ and $Na_4Cu_2(UO_2)S_4$.

B. Experimental

1. Synthesis

Reagents -- The following reagents were used as obtained: uranium metal, 60 mesh, Cerac, Milwaukee, WI; sulfur powder, sublimed, JT Baker Co., Phillipsburg, NJ; sodium metal, analytical reagent, Mallinckrodt Inc., Paris, KY; cesium metal, Johnson M. Matthey Co., Ward Hill, MA; copper metal _ mesh, Fisher Scientific Co., ; methanol, anhydrous, analytical reagent grade, Mallinckrodt Inc., Paris, KY.

Cesium sulfide, Cs_2S -- Synthesis of this compound was performed as described in Chapter 3, Sec. B.1.

Sodium sulfide, Na_2S -- Synthesis of this compound was performed as described in Chapter 2, Sec. B.1.

Tetracesium tris(disulfido)bis-oxo uranate, $Cs(UO_2)S_6$ -- This phase was first observed as a member of an inhomogeneous product from

the reaction of Cs_2S, Cu, U, and S. A mixture of 0.298g (1.0 mmol) Cs_2S, 0.008g (0.126 mmol) Cu, 0.030 g (0.126 mmol) U and 0.064 g (2.0 mmol) S were mixed and sealed into pyrex tubes as described earlier. The reaction was heated in a computer-controlled furnace at 360 °C for 2 d. and cooled to 160 °C at 4 °C/hr. followed by quenching to 50 °C. Excess flux was dissolved in the manner described earlier by using one portion of degassed methanol and several portions of degassed DMF. After drying under vacuum, the remaining material was a mixture of black, water-soluble needles and white powder. Single crystal analysis on the black needles subsequently revealed them to be $Cs_4(UO_2)S_4$.

Although salts of various uranyl cations are commercially available, it was feared that the presence of too many extra species in the A_2Q_x flux would impair reaction homogeneity. Hence to rationally synthesize $Cs_4(UO_2)S_6$, the in situ formation of $(UO_2)^{2+}$ was performed by reacting stoichiometric amounts of U metal and SeO_2 in excess Cs_2S_x flux. Selenium dioxide was chosen as an oxygen source because 1) as a solid it is convenient to manipulate in these closed tube reactions; 2) it should readily decompose to liberate O^{2-} anions as the highly oxidized Se^{4+} cations partially reduce the surrounding polychalcogenide environment and 3) the Se would be in such small amounts, relative to the sulfides of the flux, that its incorporation into a resulting product would be unlikely.

Reproducible, high yield synthesis of $Cs_4(UO_2)S_6$ is achieved by the reaction of 0.223 g (0.78 mmol) Cs_2S, 0.030 g (0.126 mmol) U, 0.014 g (0.126 mmol) SeO_2, and 0.048 g (1.5 mmol) S. The reagents are thoroughly mixed in an N_2 filled glove box and loaded into a pyrex tube. The tubes are removed from the box and evacuated on a Schlenck line to $<3x10^{-3}$ and flame sealed. The reactants are heated at 360 °C for 2 days

and cooled to 160 °C at 4 °C/hr., followed by quenching to 50 °C. Excess polysulfide flux is removed by dissolving it in successive portions of degassed methanol in the manner previously described. Washings are continued until the solvent remains clear, signaling complete polysulfide removal. The sample is decanted one final time and then dried under vacuum. The remaining material is black needles with a very small amount of red/brown, apparently amorphous, powder. The identity of the black needles is confirmed by comparing the product's powder X-ray diffraction pattern against one calculated using the coordinates obtained from the X-ray single crystal analysis (See Table 4.4.1). As the powder patterns are generally weak, Raman-IR is used as an independent comfirmation of the identity and purity of the product. The phase is insoluble in methanol and DMF but is rapidly dissolved, and presumably decomposed, in distilled water. Also the compound will visibly degrade upon overnight exposure to air.

Table 4.4.1: Calculated and Observed X-ray Powder diffraction Pattern for $Cs_4(UO_2)S_6$ (Cu radiation)

h k l	d_{calc}/(Å)	d_{obs}/(Å)	I/I_{max} obs (%)
0 2 0	7.07	7.06	83.25
2 2 0	3.990	3.977	26.86
1 3 -1	3.982		
1 2 -1	3.970		
0 4 0	3.533	3.529	52.22
2 2 1	3.524		
1 3 1	3.513		
3 -2 1	3.504		
3 0 1	3.453		
3 1 0	3.445	3.448	8.52
2 -4 0	3.354		
3 1 -1	3.340	3.346	29.18
3 -3 0	3.328		
2 3 0	3.270	3.276	20.48
0 4 -2	3.150	3.164	33.25
4 -1 0	2.894	2.898	17.31
3 -3 2	2.869		
2 -5 0	2.792	2.790	51.17
2 4 0	2.730	2.733	27.62
1 -3 -3	2.485		
3 -1 3	2.483	2.480	30.77
3 -1 -3	2.474		
0 1 -4	2.469		
3 1 -3	2.469		
0 6 0	2.355	2.352	100.00
4 -4 -2	2.142	2.142	21.82
1 5 2	2.139		
4 4 -2	1.9419	1.9331	20.48
6 -1 -2	1.7996	1.7998	10.31
0 8 0	1.7666	1.7639	78.01
3 7 -1	1.6561	1.6499	31.59

Tetrasodium tris(disulfido)bis-oxo uranate disodium trisulfide. *$Na_4(UO_2)(S_2)_3 \cdot Na_2S_3$* -- Single crystals of this phase were first observed from the reaction of U metal in a Na_2S_x flux. In an N_2 filled glove box, 0.070 g (0.90 mmol) Na_2S, 0.060 g (0.25 mmol) U and 0.064 g (2.0 mmol) S were thoroughly mixed and loaded into a pyrex tube. The tubes were removed from the box and evacuated on a Schlenck line to $<3x10^{-3}$ and flame sealed. The reactants were heated at 400 °C for 2 days and cooled to 200 °C at 4 °C/hr., followed by quenching to 50 °C. Excess polysulfide flux was removed, in the manner described previously, by washing with degassed DMF until the solvent remains clear, signaling complete polysulfide removal. The sample was decanted one final time and then dried under vacuum. The remaining product was a mixture of black powder and black, water-soluble, chunky crystals, which were subsequently found to be $Na_4(UO_2)(S_2)_3 \cdot Na_2S_3$ by single crystal X-ray diffraction. The source of oxygen contamination was determined to be aged Na_2S as reactions using a fresh batch did not yield the phase. Several attempts at rational synthesis were made, none of which ever lead to an ounce of $Na_4(UO_2)(S_2)_3 \cdot Na_2S_3$.

Tetrasodium tetrasulfidobisoxo dicopper uranate *$Na_4Cu_2(UO_2)S_4$* -- Reproducible, high yield synthesis of $Na_4Cu_2(UO_2)S_4$ is achieved by the reaction of 0.078 g (1.0 mmol) Na_2S, 0.016 g (0.25 mmol) Cu, 0.030 g (0.126 mmol) U, 0.014 g (0.126 mmol) SeO_2, and 0.048 g (1.5 mmol) S. The reagents are thoroughly mixed in an N_2 filled glove box and loaded into a pyrex tube. The tubes are removed from the box and evacuated on a Schlenck line to $<3x10^{-3}$ and flame sealed. The reactants are heated at 400 °C for 2 days and cooled to 200 °C at 4 °C/hr., followed by quenching to 50 °C. Excess polysulfide flux is removed, in the manner described

previously, by washing twice with DMF, once with degassed water (which was left in contact with the sample for only 10 min.), and then rinsed several times with degassed DMF until the solvent remains clear, signaling complete polysulfide removal. The sample is decanted one final time and then dried under vacuum. The remaining material is dark blue to black chunky crystals of $Na_4Cu_2(UO_2)S_4$ with a very small amount of white, apparently amorphous, powder. Yield is approximately 65%, based on U. The identity of the phase is confirmed by comparing the product's powder X-ray diffraction pattern against one calculated using X-ray single crystal data (See Table 4.4.2). The phase is insoluble in methanol, DMF, and water, and appears stable in air for extended periods.

Table 4.4.2: Calculated and Observed X-ray Powder diffraction Pattern for $Na_4Cu_2(UO_2)S_4$ (Cu radiation)

h k l	d_{calc}/(Å)	d_{obs}/(Å)	I/I_{max} obs (%)
0 0 2	6.80	6.72	3.87
1 0 0	6.63	6.57	100.00
0 1 2	5.73	5.70	18.43
1 1 0	5.63	5.60	16.20
1 1 -1	5.43	5.39	5.42
0 2 0	5.33	5.29	4.14
1 0 -2	5.11	5.08	2.59
0 2 1	4.961	4.942	5.69
1 1 -2	4.605	4.577	5.88
1 2 0	4.153	4.132	3.44
1 1 2	4.109	4.091	2.77
1 2 -1	4.070	4.052	4.03
1 2 -2	3.686	3.671	5.03
1 2 2	3.417		
0 0 4	3.399	3.387	7.47
2 1 0	3.166		
0 3 2	3.148	3.143	11.35
1 1 -4	3.071	3.054	9.02
1 2 3	2.940	2.905	8.95
1 3 -2	2.916		
2 2 -1	2.822	2.809	46.01
1 1 4	2.772	2.760	3.15
2 2 -2	2.714	2.700	13.73
1 3 -3	2.660	2.646	6.09
1 2 4	2.527	2.515	11.74
2 2 2	2.501		
2 1 -4	2.483	2.487	9.13
1 4 -1	2.454		
2 3 0	2.424	2.411	3.57
1 4 -2	2.362		

Table 4.4.2: Calculated and Observed X-ray Powder diffraction Pattern for $Na_4Cu_2(UO_2)S_4$ (Cu radiation) (cont.)

h k l	d_{calc}/(Å)	d_{obs}/(Å)	I/I_{max} obs (%)
0 4 3	2.297	2.288	5.05
2 2 3	2.276		
0 1 6	2.216	2.200	11.92
1 1 -6	2.191		
1 2 5	2.191		
3 2 -2	2.027	2.026	4.50
1 5 1	1.9947	1.9776	3.71
3 1 2	1.9872		
2 4 -3	1.9518	1.9393	8.45
3 1 -4	1.9467		
0 1 7	1.9106		
0 4 5	1.9029	1.9034	3.92
2 3 4	1.8867		
3 0 -6	1.7020		
3 4 0	1.7010		
1 3 -7	1.7000		
0 0 8	16993	1.6953	3.68
2 2 -7	1.6924		
4 0 0	1.6577	1.6525	23.27
3 4 -3	1.6503	1.6473	13.08
2 1 -8	1.5854	1.5807	4.81

2. Physical Measurements

The instrumentation and experimental setup for the following measurements are the same as described in Chapt. 2, Sec. B.2: powder X-ray diffraction, infrared spectroscopy, and UV/Vis/near IR spectroscopy (diffuse reflectance mode).

Raman spectroscopy -- Raman IR spectra were run, in the diffuse reflectance mode, on a Biorad FT Raman instrument with a 1064 nm Nd:YAG laser source run at 230 μV. Samples used were neat powders loaded into capillary tubes for analysis.

Single Crystal X-ray Diffraction -- Single crystals of compounds in this section were treated as air-sensitive materials. The crystals were coated in mineral oil to protect them from the atmosphere during mounting for single crystal diffraction studies. Each crystal was loaded into a thin walled glass capillary of diameter appropriate to the size of crystal. The capillary was carefully snapped to an appropriate length, and the crystal was held in place by drawing a fast hardening glue into the glass fiber with capillary action. The capillary was then mounted into an aluminum stub, held in place with paraffin wax, and inserted into a goniometer head for analysis.

Intensity data were collected using a Rigaku AFC6S four-circle automated diffractometer equipped with a graphite crystal monochromator. An ω-2θ scan mode was used. The stability of the crystal was monitored with three standard reflections whose intensities were checked every 150 reflections, and unless noted, no crystal decay was detected. An empirical absorption correction based on ψ scans was applied to all data during initial stages of refinement. An empirical DIFABS correction [5] was applied after full isotropic refinement, after which full anisotropic refinement was

performed. The structures were solved by direct methods using SHELXS-86 software [6a] (for all compounds), and full matrix least squares refinement was performed using the TEXSAN software package [6b]. Crystallographic data for the compounds in this section are given in Table 4.4.3.

Table 4.4.3: Crystallographic Data for $Cs_4(UO_2)S_6$, $Na_4(UO_2)S_6 \cdot Na_2S_3$, and $Na_4Cu_2(UO_2)S_4$

	$Cs_4(UO_2)S_6$	$Na_4(UO_2)S_6 \cdot Na_2S_3$	$Na_4Cu_2(UO_2)S_4$
a, Å	11.579(5)	7.180(3)	6.693(4)
b, Å	14.751(9)	7.286(3)	10.656(7)
c, Å	9.879(6)	28.83(1)	13.722(6)
α, °	100.43(6)		
β, °	90.23(4)	93.17(7)	97.81(4)
γ, °	102.79(4)		
V, Å^3	1617(2)	1506(2)	969.7(9)
space group	P-1	$P2_1/c$	$P2_1/c$
Z	2	4	4
F.W., g/mol	994.01	696.51	617.32
d_{calc}, g/cm^3	4.084	3.496	4.228
μ, cm^{-1}	7.8	18.1	53.5
crystal dimensions, mm^3	0.02 x 0.10 x 1.00	0.20 x 0.20 x 0.40	0.012 x 0.20 x 0.20
radiation	Mo Kα	Mo Kα	Mo Kα
2θ max.	50.2°	50	60°
data collection temp., °C	23	-70	23
# data collected	6007	3000	3199
# unique data	5697	2541	2821
# $F_o^2 > 3\sigma$	3707	1695	1980
# of variables	235	163	118
R/Rw, %	5.5/7.1	5.8/7.3	3.5/4.0
final Dif. map max. peak, e$^-$/Å^3	5.76	2.81	1.72

[a] $R = \Sigma(|Fo|-|Fc|)/\Sigma|Fo|$ $Rw = \{\Sigma w(|Fo|-|Fc|)^2/\Sigma w|Fo|^2\}^{1/2}$

C. Results and Discussion

1. $Cs_4(UO_2)S_6$ and $Na_4(UO_2)S_6 \cdot Na_2S_3$

Structure -- $Cs_4(UO_2)S_6$ is composed of discrete anionic clusters separated by intervening Cs^+ cations. Figure 4.4.1 shows a view of one of these species: a $[(UO_2)(S_2)_3]^{4-}$ anion. The uranyl cation is coordinated to three $(S_2)^{2-}$ species such that if the midpoint of each disulfide is treated as a hypothetical atom, then the coordination about the U^{6+} would be trigonal bipyramidal. Each disulfide is in an η^2 chelation mode with the all the sulfur atoms nearly coplanar with the central U atom; there is a slight umbrella shape to the atoms as the central U atom is 0.004 Å above the calculated least squares plane while the S atoms range from 0.030 to 0.054 Å below it. Meanwhile, the oxygen atoms of the uranyl are almost perfectly perpendicular to this equatorial plane of disulfides; the S-U-O angles in this compound only range from 88.6(6)° to 91.7(7)° (Fig. 4.4.2). Because of the strong double bonds between U and O in the uranyl, coordination about the equatorial plane of the cation is a characteristic feature. The uranyl has been known to accommodate anywhere from four to six atoms in these equatorial sites. Several structural analogs to the $[(UO_2)(S_2)_3]^{4-}$ anion exist such as the long known peroxide form, $Na_4[(UO_2)(O_2)_3] \cdot 9H_2O$ [7], and $Na[(UO_2)(O_2CCH_3)_3]$ [8], $Rb[(UO_2)(NO_3)_3]$ [9], and $[Me_4N][(UO_2)(S_2CN(C_2H_5)_2)_3]$ [10] in which the bulk of the three chelating groups forces the coordinating atoms to lie alternatively above and below the uranyl equatorial plane.

There are two distinct $[(UO_2)(S_2)_3]^{4-}$ anions in each asymmetric unit of the structure, and Table 4.4.4 provides a summary of the bond distances and angles of both. They are totally unsurprising. The range of U-S bonds

is 2.772-2.837 Å, and comparable values are seen for eight coordinate U in $Cu_2U_6S_{13}$ (2.702-2.939 Å) [11]. The U-O bonds are from 1.79(2) Å to 1.86(2) Å while in $Na_4[(UO_2)(O_2)_3]\cdot 9H_2O$ the corresponding uranyl distances were 1.814 and 1.909 Å [7]. The bond distances in the disulfides are particularly invariant at either 2.08(1) or 2.09(1) Å, which are comparable to the values for the S-S bonds in α- and β-$KCuS_4$ (2.056-2.089 Å)[12]. Fractional atomic coordinates for this phase are given in Table 4.4.5.

Crystallizing as the Na+ salt does little to alter the environment around the U atom. Fractional atomic coordinates for this phase are given in Table 4.4.6. Bond distances are given in Table 4.4.7, and they are all comparable to what has been seen in the Cs+ analog. One would have expected that the smaller cations would have forced the anions into such a close proximity that bridging S-S bonds would form between anions to relieve electrostatic crowding. The tendency to form the discrete anion is strong, however, as a large interanion distance is maintained by the cocrystallization of a $(S_3)^{2-}$ fragment which in turn requires an extra two Na^+ cations for charge balance. On its own, the uranyl clusters seem to be resisting the drive towards an extended structure with bridging S-S bonds.

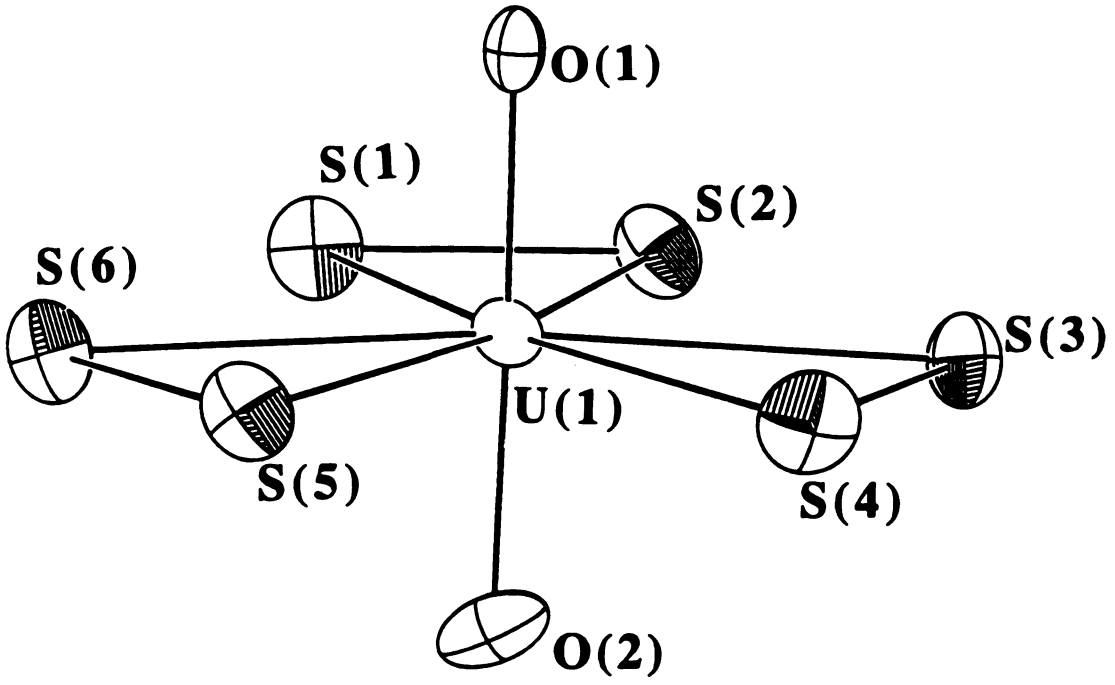

Figure 4.4.1: The $[(UO_2)(S_2)_3]^{4-}$ anion

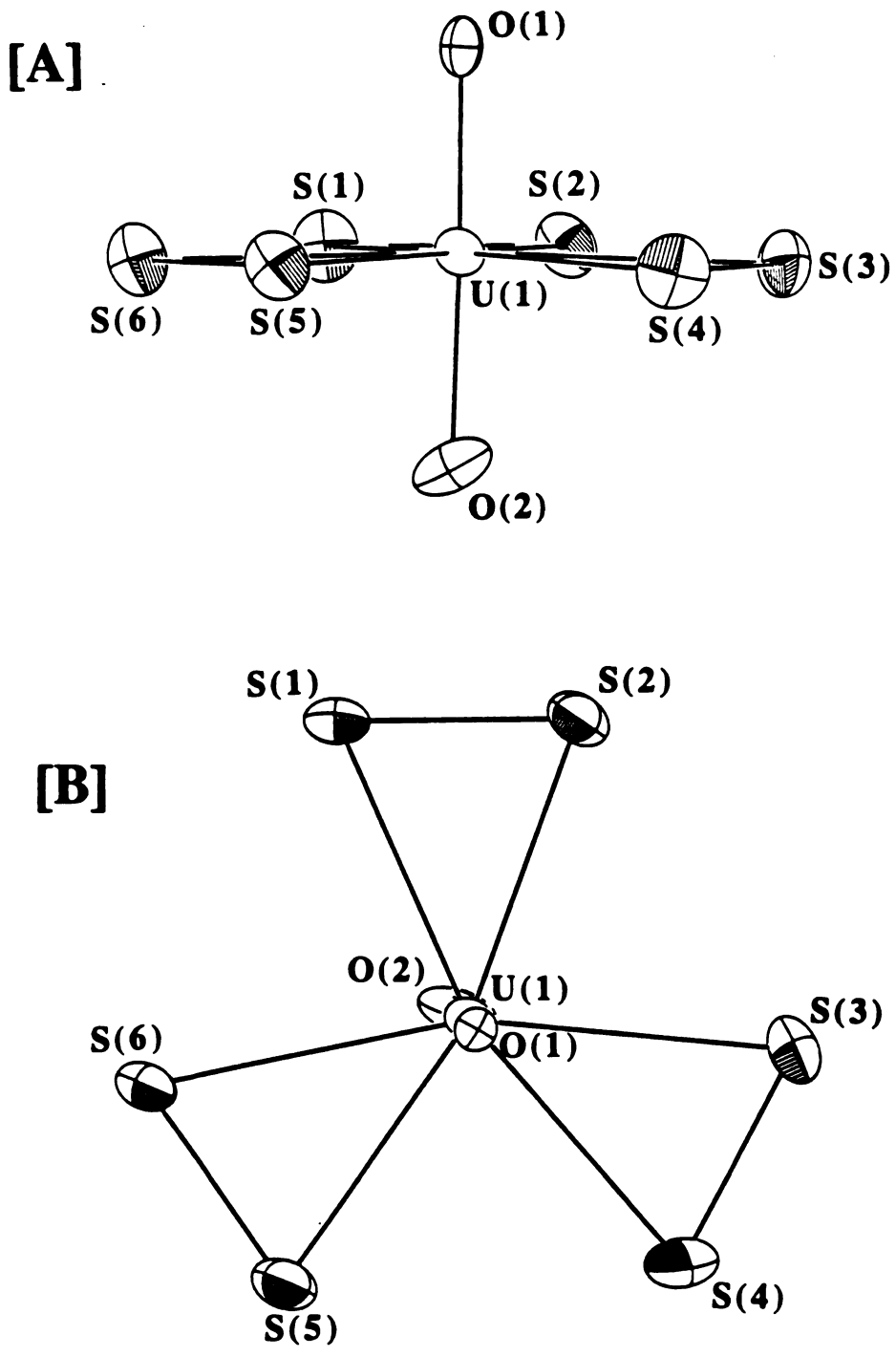

Figure 4.4.2: Two views of the $[(UO_2)(S_2)_3]^{4-}$ anion: (A) parallel and (B) perpendicular to the equitorial plane.

Table 4.4.4: Selected Bond Distances (Å) and Angles (°) for $Cs_4(UO_2)S_6$ (standard deviations in parentheses).

U(1)-S(1)	2.837(9)	U(2)-S(7)	2.793(8)
U(1)-S(2)	2.77(6)	U(2)-S(8)	2.816(8)
U(1)-S(3)	2.788(9)	U(2)-S(9)	2.823(9)
U(1)-S(4)	2.79(1)	U(2)-S(10)	2.804(8)
U(1)-S(5)	2.790(8)	U(2)-S(11)	2.772(9)
U(1)-S(6)	2.831(9)	U(2)-S(12)	2.781(9)
U(1)-O(1)	1.79(2)	U(2)-O(3)	1.82(2)
U(1)-O(2)	1.86(2)	U(2)-O(4)	1.80(2)
S(1)-S(2)	2.08(1)	S(7)-S(8)	2.08(1)
S(3)-S(4)	2.08(1)	S(9)-S(10)	2.09(1)
S(5)-S(6)	2.09(1)	S(11)-S(12)	2.08(1)

Table 4.4.4: Selected Bond Distances (Å) and Angles (°) for $Cs_4(UO_2)S_6$ (standard deviations in parentheses) (cont).

S(1)-U(1)-S(2)	43.4(3)	S(7)-U(2)-S(8)	43.5(3)
S(1)-U(1)-S(3)	119.1(3)	S(7)-U(2)-S(9)	120.5(3)
S(1)-U(1)-S(4)	162.8(3)	S(7)-U(2)-S(10)	164.0(3)
S(1)-U(1)-S(5)	121.6(3)	S(7)-U(2)-S(11)	120.1(3)
S(1)-U(1)-S(6)	78.0(2)	S(7)-U(2)-S(12)	76.0(3)
S(1)-U(1)-O(1)	91.5(6)	S(7)-U(2)-O(3)	88.3(6)
S(1)-U(1)-O(2)	88.3(7)	S(7)-U(2)-O(4)	90.3(6)
S(2)-U(1)-S(3)	75.8(3)	S(8)-U(2)-S(9)	77.0(2)
S(2)-U(1)-O(1)	91.2(6)	S(8)-U(2)-O(3)	88.6(6)
S(2)-U(1)-O(2)	89.6(6)	S(8)-U(2)-O(4)	89.8(6)
S(3)-U(1)-S(4)	43.8(3)	S(9)-U(2)-S(10)	43.6(3)
S(3)-U(1)-O(1)	91.3(7)	S(9)-U(2)-O(3)	89.5(6)
S(3)-U(1)-O(2)	90.0(8)	S(9)-U(2)-O(4)	90.5(7)
S(4)-U(1)-S(5)	75.4(3)	S(10)-U(2)-S(11)	75.8(3)
S(4)-U(1)-O(1)	91.0(7)	S(10)-U(2)-O(3)	89.5(6)
S(4)-U(1)-O(2)	89.6(8)	S(10)-U(2)-O(4)	91.6(6)
S(5)-U(1)-S(6)	43.6(3)	S(11)-U(2)-S(12)	44.0(2)
S(5)-U(1)-O(1)	90.2(6)	S(11)-U(2)-O(3)	89.7(6)
S(5)-U(1)-O(2)	88.7(6)	S(11)-U(2)-O(4)	91.7(7)
S(6)-U(1)-O(1)	90.9(6)	S(12)-U(2)-O(3)	89.1(7)
S(6)-U(1)-O(2)	87.7(7)	S(12)-U(2)-O(4)	91.4(7)
O(1)-U(1)-O(2)	178.6(9)	O(3)-U(2)-O(4)	178.4(8)

Table 4.4.5 Fractional Atomic Coordinates and B_{eq}[a] values for $Cs_4(UO_2)S_6$ with Estimated Standard Deviations in Parentheses

atom	x	y	z	B_{eq}[a]
U(1)	0.5568(1)	0.24386(9)	0.3137(1)	1.36(4)
U(2)	0.92641(9)	0.76739(9)	0.1897(1)	1.23(4)
Cs(1)	1.2035(2)	0.6232(2)	0.1474(2)	2.09(7)
Cs(2)	0.3545(2)	0.3917(2)	0.1018(3)	3.5(1)
Cs(3)	0.9189(2)	0.3814(2)	0.3460(2)	2.21(8)
Cs(4)	0.1785(2)	0.1140(2)	0.2785(2)	2.78(8)
Cs(5)	0.6127(2)	0.8826(2)	0.2254(2)	2.76(8)
Cs(6)	0.7783(2)	0.1154(2)	0.0329(2)	2.16(7)
Cs(7)	0.7760(2)	0.1160(2)	0.5300(2)	2.19(7)
Cs(8)	1.3508(2)	0.3934(2)	0.5989(2)	2.64(8)
S(1)	0.6508(7)	0.3965(7)	0.5320(8)	2.4(3)
S(2)	0.5760(7)	0.2719(7)	0.5991(8)	2.3(3)
S(3)	0.4581(7)	0.0665(7)	0.3748(8)	2.5(3)
S(4)	0.4573(8)	0.0640(7)	0.1636(8)	2.7(3)
S(5)	0.5722(7)	0.2645(7)	0.0387(8)	2.4(3)
S(6)	0.6485(7)	0.3917(7)	0.1699(8)	2.3(3)
S(7)	0.9350(7)	0.7431(7)	0.4631(8)	2.2(3)
S(8)	0.9413(7)	0.6190(7)	0.3277(8)	2.3(3)
S(9)	0.9383(7)	0.6171(6)	-0.0280(8)	2.3(3)
S(10)	0.9307(7)	0.7412(7)	-0.0984(8)	2.5(3)
S(11)	0.9172(7)	0.9424(7)	0.1305(8)	2.4(3)
S(12)	0.9193(7)	0.9441(6)	0.3416(8)	2.3(3)
O(1)	0.415(2)	0.274(1)	0.319(2)	1.5(7)
O(2)	0.705(2)	0.215(2)	0.305(2)	2.4(9)
O(3)	1.087(2)	0.802(2)	0.200(2)	1.6(8)
O(4)	0.767(2)	0.731(2)	0.183(2)	2.1(8)

[a] B values for anisotropically refined atoms are given in the form of the isotropic equivalent displacement parameters defined as $B_{eq} = (4/3)[a^2B(1,1) + b^2B(2,2) + c^2B(3,3) + ab(\cos\gamma)B(1,2) + ac(\cos\beta)B(1,3) + bc(\cos\alpha)B(2,3)$.

Table 4.4.6 Fractional Atomic Coordinates and B_{eq}[a] values for $Na_4(UO_2)S_6 \cdot Na_2S_3$ with Estimated Standard Deviations in Parentheses

atom	x	y	z	B_{eq}
U(1)	0.3590(1)	0.6603(1)	0.08586(3)	0.80(3)
S(1)	0.3201(9)	0.3791(8)	0.1478(2)	1.6(2)
S(2)	0.1164(9)	0.3684(8)	0.0935(2)	1.7(2)
S(3)	0.1112(9)	0.6887(9)	0.0087(2)	1.9(3)
S(4)	0.317(1)	0.8908(8)	0.0086(2)	1.9(3)
S(5)	0.6507(9)	0.9018(8)	0.0964(2)	1.6(2)
S(6)	0.6539(9)	0.7136(8)	0.1513(2)	1.4(2)
S(7)	0.968(1)	0.5544(8)	0.2822(2)	2.0(3)
S(8)	1.169(1)	0.744(1)	0.3043(2)	1.9(2)
S(9)	1.363(1)	0.7207(9)	0.2536(2)	1.9(2)
Na(1)	0.266(1)	0.345(1)	0.2476(3)	2.1(4)
Na(2)	0.692(2)	0.691(1)	-0.0003(3)	2.4(4)
Na(3)	0.017(1)	0.996(1)	0.0721(4)	2.6(4)
Na(4)	1.044(1)	0.659(2)	0.1824(3)	2.6(4)
Na(5)	0.695(1)	0.318(2)	0.1022(3)	3.0(5)
Na(6)	0.388(1)	0.004(1)	0.1787(4)	2.4(4)
O(1)	0.211(2)	0.811(2)	0.1196(5)	1.4(6)
O(2)	0.511(2)	0.509(2)	0.0525(5)	1.5(6)

[a] B values for anisotropically refined atoms are given in the form of the isotropic equivalent displacement parameters defined as $B_{eq} = (4/3)[a^2B(1,1) + b^2B(2,2) + c^2B(3,3) + ab(\cos\gamma)B(1,2) + ac(\cos\beta)B(1,3) + bc(\cos\alpha)B(2,3)$.

Table 4.4.7: Selected Bond Distances (Å) and Angles (°) for $Na_4(UO_2)S_6 \cdot Na_2S_3$ (standard deviations in parentheses) (cont).

U(1)-S(1)	2.741(6)	S(1)-S(2)	2.084(9)
U(1)-S(2)	2.765(6)	S(3)-S(4)	2.085(9)
U(1)-S(3)	2.777(6)	S(5)-S(6)	2.094(8)
U(1)-S(4)	2.793(6)	S(7)-S(8)	2.075(9)
U(1)-S(5)	2.739(6)	S(8)-S(9)	2.08(1)
U(1)-S(6)	2.784(6)		
U(1)-O(1)	1.84(2)	U(1)-O(2)	1.86(2)
S(1)-U(1)-S(2)	44.5(2)	S(3)-U(1)-O(1)	91.0(5)
S(1)-U(1)-S(3)	119.5(2)	S(3)-U(1)-O(2)	89.9(5)
S(1)-U(1)-S(4)	163.4(2)	S(4)-U(1)-S(5)	75.6(2)
S(1)-U(1)-S(5)	120.8(2)	S(4)-U(1)-O(1)	91.3(5)
S(1)-U(1)-S(6)	76.3(2)	S(4)-U(1)-O(2)	89.1(5)
S(1)-U(1)-O(1)	91.2(5)	S(5)-U(1)-S(6)	44.5(2)
S(1)-U(1)-O(2)	88.7(5)	S(5)-U(1)-O(1)	90.9(5)
S(2)-U(1)-S(3)	75.1(2)	S(5)-U(1)-O(2)	88.3(5)
S(2)-U(1)-O(1)	92.0(5)	S(6)-U(1)-O(1)	89.8(5)
S(2)-U(1)-O(2)	88.6(5)	S(6)-U(1)-O(2)	89.3(5)
S(3)-U(1)-S(4)	44.0(2)	O(1)-U(1)-O(2)	179.1(7)
		S(7)-S(8)-S(9)	102.1(4)

Even though the space group of $Cs_4(UO_2)S_6$ is only of P-1 symmetry, the anions pack in a surprisingly ordered fashion. The packing view given in Figure 4.4.3 shows how the cations have naturally aggregated into one-dimensional "pseudo-chains" parallel to the c-axis. The sulfur atoms from anion to anion maintain planarity with each other, but do not interact directly as the shortest interanion S-S distance is only 4.34 Å. This lack of interaction suggests merely a packing effect which is probably driven by the large Cs^+ cations. Their volume is such that the anions can remain well separated and so can arrange themselves more efficiently in order to minimize the void space. Despite the lack of interaction, seeing these well stacked anions suggests that some sort of extended covalent structure many be possible in this system with the appropriate conditions. The cocrystallization of the trisulfide fragment in the Na+ salt demonstrates that, on its own, the discrete uranyl clusters seem to have appreciable stability, and so an alternative approach would be to introduce a species which would covalently bridge the uranyl centers, as was done in the synthesis of $Na_4Cu_2(UO_2)S_4$, to be discussed later.

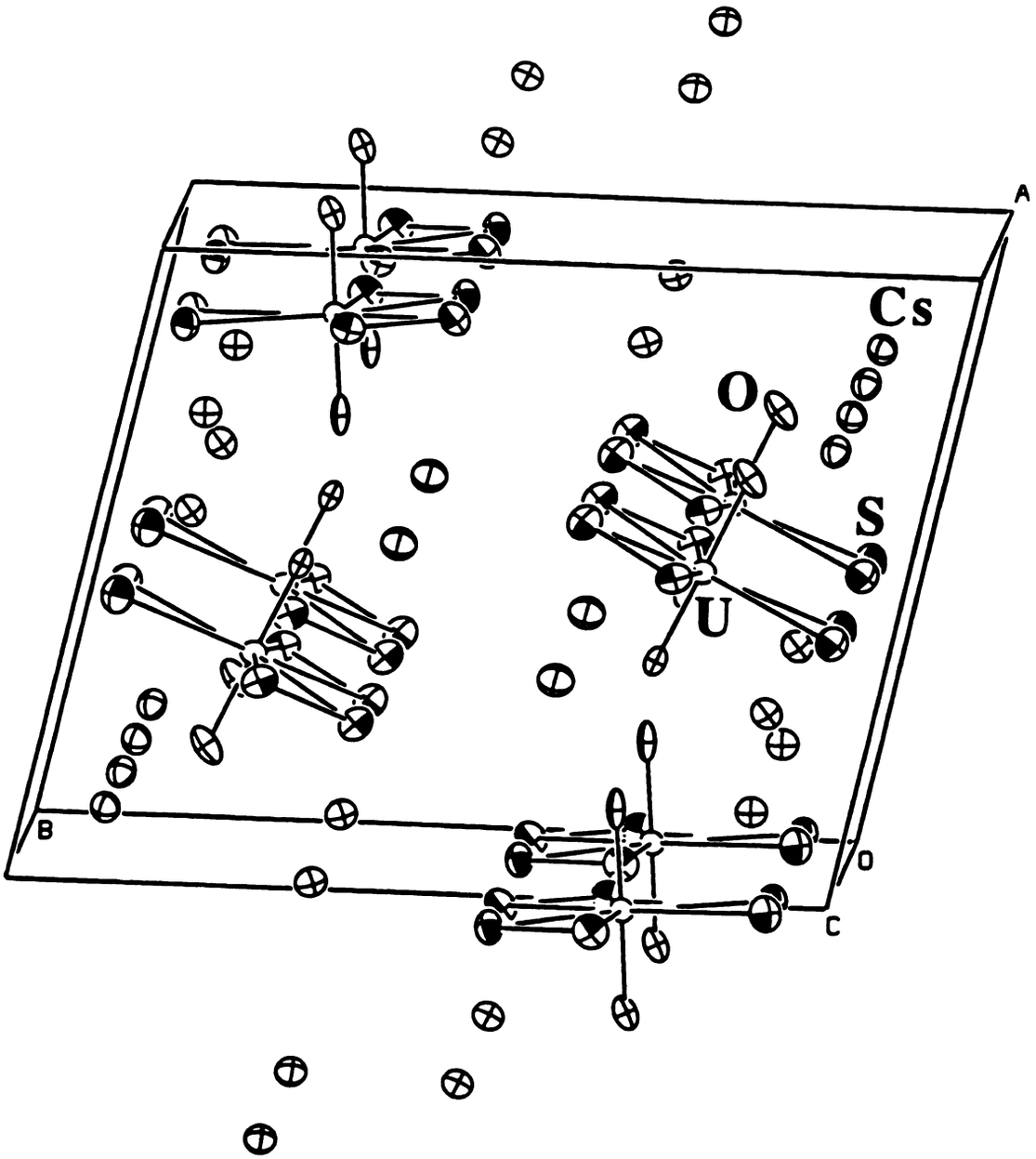

Figure 4.4.3: The unit cell of $Cs_4(UO_2)S_6$ as seen parallel to the b-axis

Spectroscopy -- The Raman-IR spectrum of $Cs_4(UO_2)S_6$ shows peaks at 701, 500, and 220 cm^{-1}. Uranyl cations have a characteristic vibration for the U-O double bond in the range of 880-950 cm^{-1} [13], although bands as low as 730 cm^{-1} were observed in $Na_4[UO_2(O_2)^3]\cdot 9H_2O$ [7]. The proximity of the 701 peak in the Raman IR to this frequency range indicates it is from the uranyl. The peak at 500 cm^{-1} corresponds to S-S stretches observed in known polysulfide compounds [12], and the low energy peak of 220 cm^{-1} is assigned to U-S vibrations.

The solid state diffuse reflectance optical absorbance spectrum of $Cs_4(UO_2)S_6$ is shown in Figure 4.4.4. Two peaks are observed: one at 1.7 eV and a second at 2.3 eV. Their origin probably lies in charge transfer from a mainly sulfur p orbital to a primarily uranium 6d orbital. Because the phase is zero-dimensional, the orbital overlap between anions is very limited. Thus, discrete electronic transitions are seen in $Cs_4(UO_2)S_6$, rather than the sharp absorption edges associated with band gaps [14].

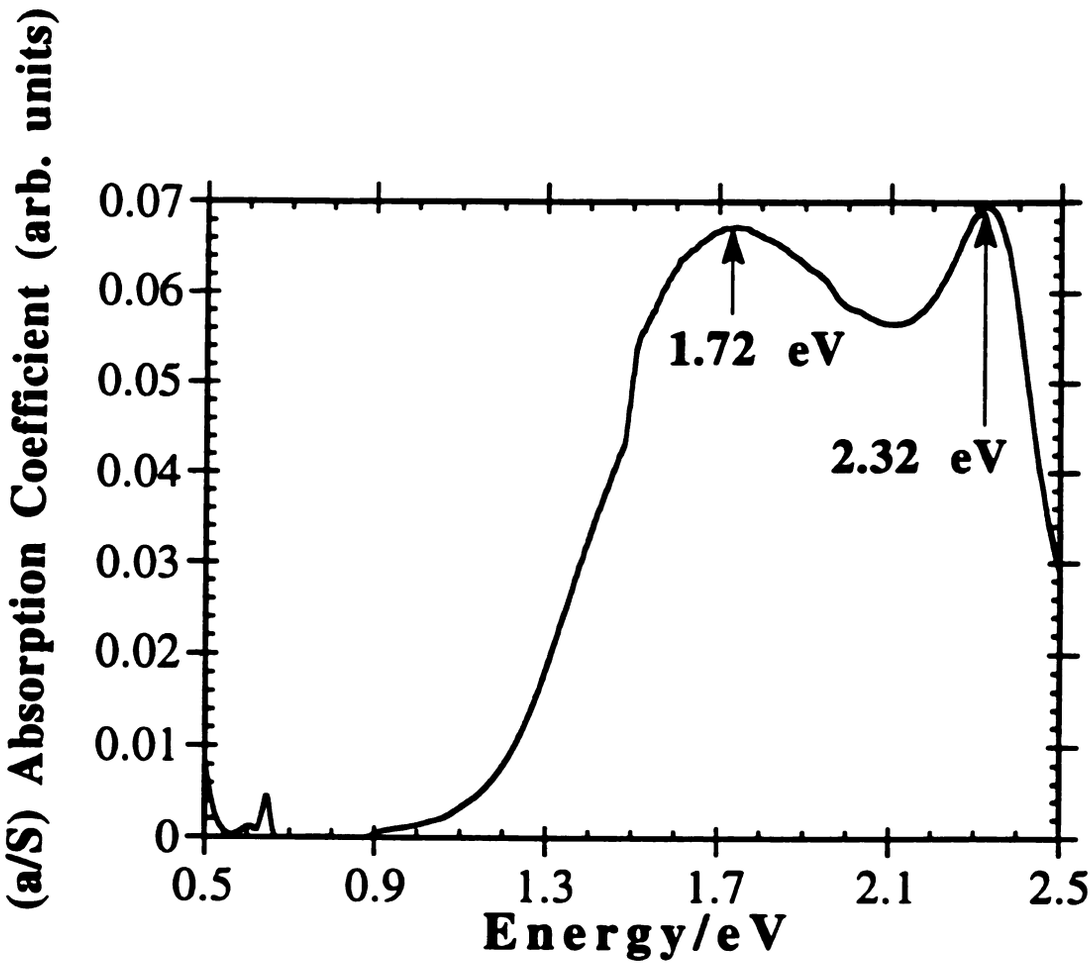

Figure 4.4.4: The solid state diffuse reflectance spectra of $K_2CuCe_2Se_6OH$ plotted as absorption coefficient (α/S) vs. energy (eV).

2. $Na_4Cu_2(UO_2)S_4$

Structure -- Synthesis of this compound represents a successful attempt to link uranyl cations into an extended solid state structure by the inclusion of intervening covalent bridges. These bridges are provided by $[Cu_4S_8]$ clusters which bond to the equatorial planes of four separate $(UO_2)^{2+}$ units, leading to a two-dimensional anionic layer. The view perpendicular to the layers is provided in Figure 4.4.5. The interconnections between $[Cu_4S_8]$ and $(UO_2)^{2-}$ result in large cavities which are aligned from layer to the layer, forming channels through the lattice. The alkali cations of this structure reside within both the cavities and the intralayer grooves.

The $[Cu_4S_8]$ cluster, highlighted in Figure 4.4.6, features an unusual combination of copper atoms in two different coordination environments. The Cu(1) atom is tetrahadral and shares one of its edges with a neighboring Cu(2)-centered trigonal plane. A second edge on the tetrahedron is shared with another Cu(1) centered tetrahedron across a crystallographic inversion symmetry, generating the entire $[Cu_4S_8]$ cluster. The Cu-S bond distances about the trigonal planar Cu(2) (Table 4.4.6) are comparable to those seen in similar environment (2.192 Å in CuS [15] and 2.245 Å in $CsCuTeS_3$ [16]), but the tetrahedral Cu(1) has a bit more variety with two short bonds (2.280(3) and 2.271(3) Å), one average bond (2.446(3) Å), and one quite long bond (2.624(4) Å). In the tetrahedral Cu environment of α- and β- $KCuS_4$ the range of Cu-S bond distances is 2.298-2.378 Å [12]. The $[Cu_4S_8]$ cluster also exhibits short Cu-Cu distances, shown in Figure 4.4.6 as dashed lines. The Cu(1)-Cu(1)' distance is 2.674(4) Å and that of Cu(1)-Cu(2) is even shorter at 2.503(2) Å, less than one of the Cu-S bonds Although short Cu-Cu contacts, resulting from d^{10}-

d^{10} interactions [17], are seen in many compounds, these distances in $Na_4Cu_2UO_2S_4$ are exceptionally short and indicate a slightly stronger interaction than is usually observed.

The $(UO_2)^{2+}$ fragments are bonded around the $[Cu_4S_8]$ clusters at four points, two at edge-sharing connections to $[CuS_4]$ tetrahedra and two more edge-sharing bridges to $[CuS_3]$ trigonal planes. Each uranyl ends up with only four sulfur atoms in the equatorial plane, forming nearly perfect octahedral angles about the central U^{6+} atom with the oxygen atoms in the axial positions (Fig. 4.4.7). There is only one crystallographically unique uranyl cation in the structure, and its connections alternate such that on one side is a bridge to a $[CuS_3]$ fragment and trans from it is a bridge to a $[CuS_4]$ fragment. The U-O and U-S bond distances are in the range to what has been seen before (Table 4.4.6), but there do exist unusually short contacts between the U and nearest Cu atoms. The U-Cu(1) distance is 3.137 Å and is somewhat longer than the bonds seen in UCu_5 (2.92 and 3.05 Å) [18], but the U-Cu(2) bond (3.065 Å) is in the range of the intermetallic values. It is also comparable to the distances in $K_6Cu_{12}U_2S_{15}$ in which each U atom has six long bonds of 3.016 Å to neighboring Cu, which also have trigonal planar S environments [19]. It would seem that there is at least a partial bonding interaction occurring between U and some of the Cu atoms in this compound.

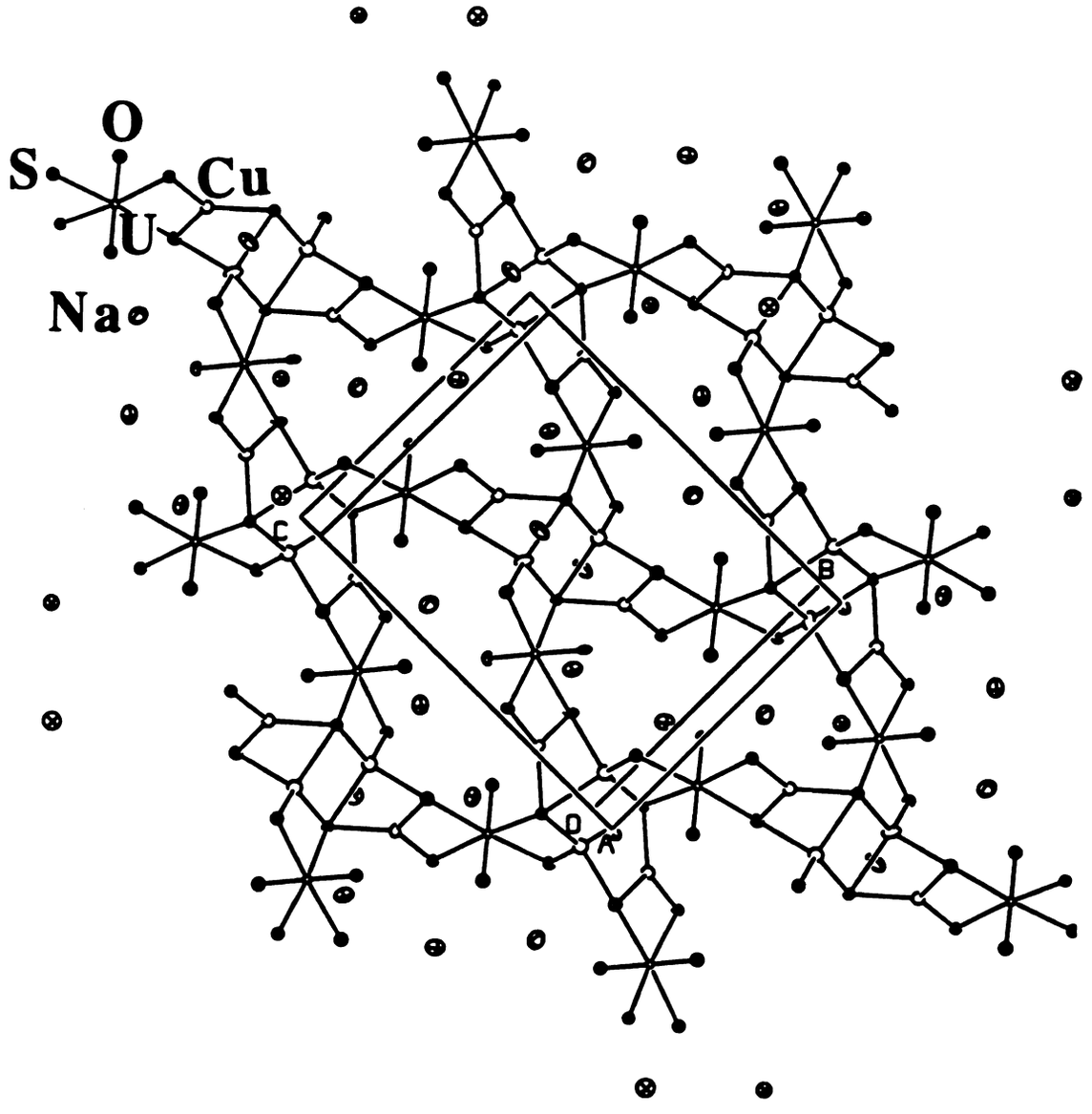

Figure 4.4.5: The view perpendicular to an anionic layer of $Na_4Cu_2(UO_2)S_4$

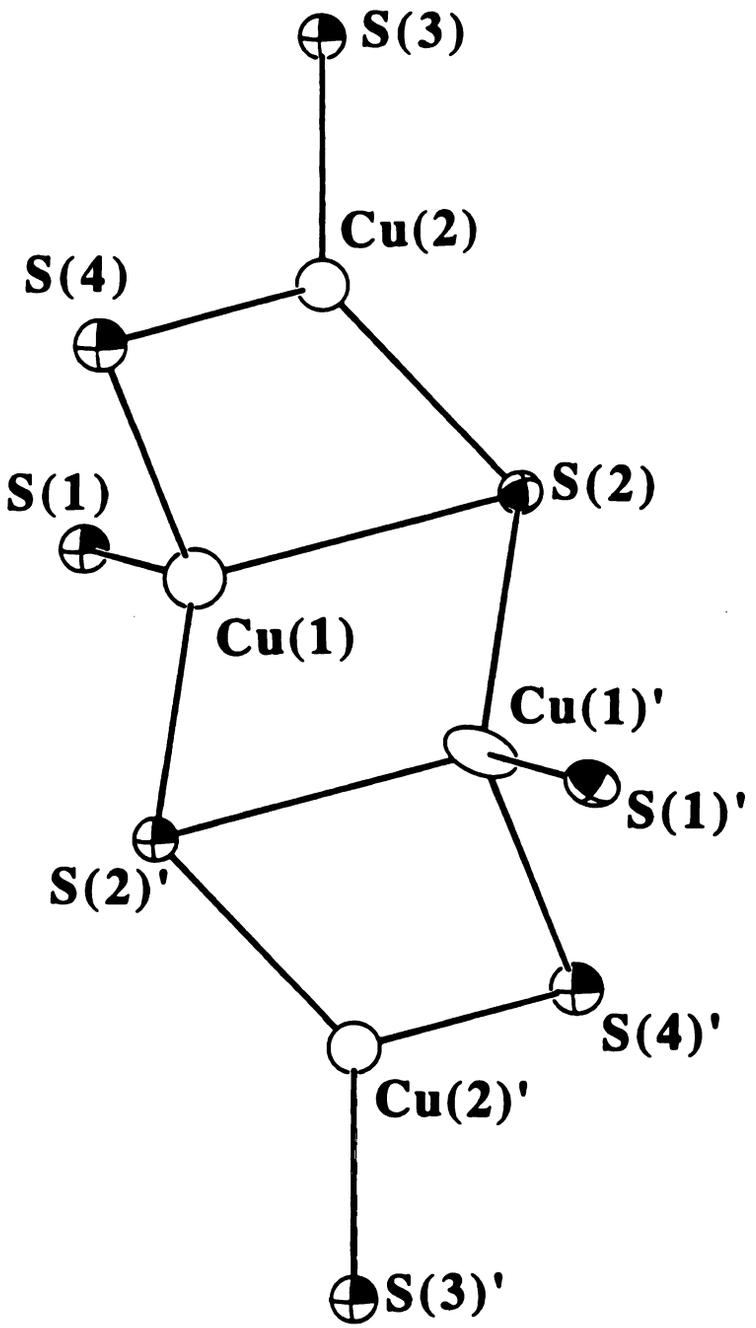

Figure 4.4.6: The $[Cu_4S_8]$ cluster present in the structure of $Na_4Cu_2(UO_2)S_4$.

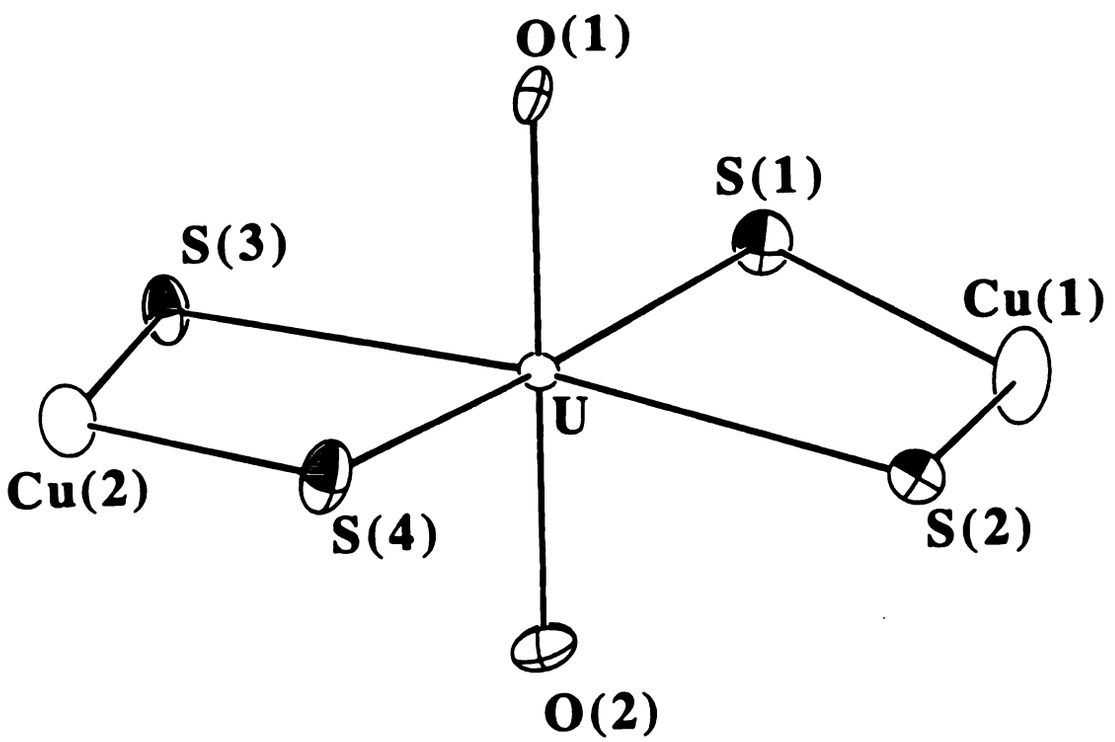

Figure 4.4.7: A fragment of the structure of $Na_4Cu_2(UO_2)S_4$ showing the immediate coordination environment around the U atoms.

Table 4.4.6: Selected Bond Distances (Å) and Angles (°) for $Na_4Cu_2(UO_2)S_6$ with standard deviations in parentheses

U-S(1)	2.702(3)	Cu(1)-S(1)	2.280(3)
U-S(2)	2.769(3)	Cu(1)-S(2)	2.271(3)
U-S(3)	2.745(3)	Cu(1)-S(2)'	2.624(4)
U-S(4)	2.707(3)	Cu(1)-S(4)	2.446(3)
U-O(1)	1.869(8)	Cu(2)-S(2)	2.251(3)
U-O(2)	1.849(8)	Cu(2)-S(3)	2.22693)
U-Cu(1)	3.137(2)	Cu(2)-S(4)	2.293(4)
U-Cu(2)	3.065(2)	Cu(1)-Cu(2)	2.503(2)
		Cu(1)-Cu(1)'	2.674(4)
S(1)-U-S(2)	89.73(9)	S(2)-Cu(1)-S(2)'	114.2(1)
S(1)-U-S(3)	90.60(9)	S(2)-Cu(1)-S(4)	112.5(1)
S(1)-U-S(4)	176.2(1)	S(2)'-Cu(1)-S(4)	99.4(1)
S(1)-U-O(1)	89.3(2)	S(3)-Cu(2)-S(2)'	124.6(1)
S(1)-U-O(2)	92.1(3)	S(3)-Cu(2)-S(4)	118.5(1)
S(2)-U-S(3)	174.01(9)	S(2)'-Cu(2)-S(4)	116.8(1)
S(2)-U-S(4)	89.19(9)	U-S(1)-Cu(1)	77.55(9)
S(2)-U-O(1)	95.6(3)	U-S(2)-Cu(1)	114.2(1)
S(2)-U-O(2)	83.9(3)	U-S(2)-Cu(2)	100.9(1)
S(3)-U-S(4)	90.86(9)	Cu(1)-S(2)-Cu(1)	65.8(1)
S(3)-U-O(1)	90.4(3)	Cu(1)-S(2)-Cu(2)	119.7(1)
S(3)-U-O(2)	90.1(3)	Cu(1)-S(2)-Cu(2)	61.22(9)
S(4)-U-O(1)	87.19(9)	U-S(3)-Cu(2)	75.33(9)
S(4)-U-O(2)	91.5(3)	U-S(4)-Cu(1)'	125.0(1)
S(1)-Cu(1)-S(2)	116.0(1)	U-S(4)-Cu(2)	75.10(9)
S(1)-Cu(1)-S(2)'	102.7(1)	Cu(1)-S(4)-Cu(2)	63.67(9)
S(1)-Cu(1)-S(4)	110.4(1)		

Table 4.4.7 Fractional Atomic Coordinates and B_{eq}[a] values for $Na_4Cu_2(UO_2)S_4$ with Estimated Standard Deviations in Parentheses

atom	x	y	z	B_{eq}
U	0.12525(6)	0.21546(4)	0.37179(2)	0.53(1)
Cu(1)	0.0528(3)	0.3923(2)	0.5464(1)	1.81(6)
Cu(2)	0.1700(2)	0.0188(1)	0.2132(1)	1.31(5)
S(1)	0.3471(4)	0.2860(3)	0.5423(2)	1.13(9)
S(2)	-0.1772(4)	0.3787(3)	0.4090(2)	0.92(9)
S(3)	0.4041(4)	0.0346(3)	0.3443(2)	1.02(9)
S(4)	0.0913(4)	0.1597(3)	0.1959(2)	1.3(1)
Na(1)	0.4429(7)	-0.2371(5)	0.2550(3)	1.9(2)
Na(2)	0.549(1)	0.4951(5)	0.6091(4)	2.8(2)
Na(3)	0.154(1)	0.0890(6)	0.6396(4)	2.7(2)
Na(4)	0.3182(8)	-0.1499(6)	0.4927(4)	2.2(2)
O(1)	0.264(1)	0.3323(8)	0.3049(5)	1.1(3)
O(2)	-0.018(1)	0.0998(8)	0.4353(5)	1.3(3)

[a] B values for anisotropically refined atoms are given in the form of the isotropic equivalent displacement parameters defined as $B_{eq} = (4/3)[a^2B(1,1) + b^2B(2,2) + c^2B(3,3) + ab(\cos\gamma)B(1,2) + ac(\cos\beta)B(1,3) + bc(\cos\alpha)B(2,3)$.

Although chemists have lavished extensive and ongoing attention on the coordination chemistry of $(UO_2)^{2+}$, the cation is present in nearly one hundred naturally occurring minerals in which extended solid state structures are common [20]. In general the bonding of the uranyl cations in these phases occurs through bridging intermediate species connected to the equatorial plane of the $(UO_2)^{2+}$. For example, in the minerals troegerite ($HUO_2AsO_4 \bullet 4H_2O$) and uranospinite ($Ca(UO_2)_2(AsO_4)_2 \bullet nH_2O$), which have been known since the 1870's, the uranyl cations are connected into anionic sheets by four bonds to four separate $(AsO_4)^{3-}$ units (each of which, in turn, connect four uranyls) [21]. The phosphorous containing form of troegerite, $HUO_2PO_4 \bullet 4H_2O$ has been studied extensively for its intercalation and ion exchange chemistry [22]. The coordination number in the uranyl equatorial plane increases to five in both α- and β-$(UO_2)(SO) \bullet 7H_2O$ [23,24]; in this structure the resulting pentagonal bipyramids of $[UO_7]$ are connected into one-dimensional chains via intervening sulfate ions. Extended structures are known even for uranyls which have six bonds in the equatorial plane. The compound $Ca(UO_2)O_2$ has anionic layers of hexagonal symmetry in which each $[UO_8]$ hexagonal bipyramid shares every side of the equatorial hexagon with another $[UO_8]$ unit, all the while maintaining the central uranyl axis perpedicular to the layer [25]. Given what has been observed in its mineralogical chemistry, the uranyl cation clearly has a great deal of potential for use as a solid state building block in further exploratory synthesis in molten A_2Q_x fluxes.

Spectroscopy -- Being black, $Na_4Cu_2(UO_2)S_4$ showed total absorbance in its optical diffuse reflectance spectrum (500-2500 nm), with CdS used as a 100% reflectance standard. This indicates that the valence precise compound is a semiconductor with a band gap lower than 0.5 eV.

D. Conclusions

Not only do the syntheses of $Cs_4(UO_2)S_6$ and $Na_4Cu_2(UO_2)S_4$ call for a further examination of $(UO_2)^{2+}$ chemistry in other A_2Q_x congeners, but also give strong indication that other oxymetal cations could also be used as stable building blocks in molten A_2Q_x fluxes. This is particularly intriguing in the case of asymmetric cations such as $(TiO)^{2+}$, $(VO)^{2+}$, $(MoO)^{3+}$, and $(WO)^{3+}$, whose incorporation into solid state lattices would very likely lead to materials with acentric space groups and which, as a result, may show novel nonlinear optical properties.

Initial experiments towards this goal have already been undertaken in attempts to make vanadyl *in situ* in various A_2S_x fluxes. The vanadyl cation has yet to be observed; instead, characterized phases have shown purely sulfide compounds with vanadium present in the 5+ oxidation state [26]. In vanadyl, the metal is only oxidized to 4+, and so the highly corrosive nature of the A_2S_x flux can easily access the more full oxidized state over that which is needed for vanadyl stabilization. Performing uranyl chemistry does not have this complication as the U atom in that cation is fully oxidized to 6+. Perhaps the vanadyl can still be stabilized if the conditions of the flux are tempered somewhat. This could be done by several methods, taken individually or in combination: 1) lower reaction temperatures at which the fluxes would be less oxidizing; 2) use fluxes which are less polychalcogenide rich so as to reduce the amount of reducing agent in the reaction; and 3) investigate vanadyl formation in less oxidizing polyselenide and polytelluride fluxes.

REFERENCES

1) Sutorik, A. C., Kanatzidis, M. G., *Chem. Mater.*, in press.

2) Sutorik, A. C., Ph. D. dissertation, Michigan State University, E. Lansing, MI, **1994**.

3) Park, Y. P., DeGroot, D. C., Schindler, J., Kannewurf, C., Kanatzidis, M. G., *Chem. Mater.*, **1993**, 5, 8-10.

4) (a) Greenwood, N. N., Earnshaw, A., *Chemistry of the Elements*; Pergamon Press, Oxford, **1984**. (b) Cotton, F. A., Wilkinson, G., *Advanced Inorganic Chemistry*, 5th ed.,John Wiley and Sons, New York, **1988.**

5) Walker, N., Stuart, D., *Acta Cryst.* **1983**, *A39* , 158-166.

6) (a) G. M. Sheldrick, in *Crystallographic Computing 3* Sheldrick, G. M., Kruger, C., Doddard, R., Eds.; Oxford University Press: Oxford, England, **1985**, p. 175-189. (b) Gilmore G. J., *Appl. Cryst.* **1984**, *17* , 42-46.

7) Alcock, N. W., *J. Chem. Soc. (A)*, **1968**, 1588-1594.

8) Zachariasen, W. H., Plettinger, H. A., *Acta Crystallogr.*, **1959**, 12, 526-530.

9) Barclay, G. A., Sabine, T. M., Taylor, J. C., *Acta Crystallogr.*, **1965**, 19, 205-209.

10) Bowman, K., Dori, Z., *J. Chem. Soc., Chem. Commun.*, **1968**, 636.

11) Noel, H., Potel, M., *J. Less-Common Met.*, **1985**, 113, 11-15.

12) Park, Y., Kanatzidis, M.G., *J. Am. Chem. Soc.*, **1989**, 111, 3767-3769.

13) Perry, D. L., Zalkin, A., Ruben, H., Templeton, D. H., *Inorg. Chem.*, **1982**, 21, 237-240.

14) Hoffman, R. *Angew. Chem. Int. Ed. Eng.*, **1987**, 26, 846-878.

15) (a) Takeuchi, K., Kodoh, Y., Sato, G., *Z. Kristallogr.*, **1985**, 173, 119-128. (b) Fjelliag, H., Gronvold, F., Stolen, S., *Z. Kristallogr.*, **1988**, 184, 111-121.

16) X. Zhang and M. G. Kanatzidis, *J. Am. Chem. Soc., 116*, 1890, (1994).

17) (a) Mertz, K. M., Jr., Hoffmann, R., *Inorg. Chem.* ; **1988**, *27*, 2120-2127. (b) Jansen, M., *Angew. Chem.* ; **1987**, *99* , 1136; *Angew. Chem. Int. Ed. Engl.* ; **1987**, *26* , 1098-1111.

18) Baenziger, N. C., Rundle, R. E., Snow, A. I., Wilson, A. S., *Acta Crystallogr.*, **1950**, 3, 34-40.

19) Sutorik, A. C., Ph. D. dissertation, Michigan State University, E. Lansing, MI, **1994**, Chapt.3, Part II, Sec. C.

20) (a) Steacy, H. R., Kaiman, S., *Short Course in Uranium Deposits: Their Mineralogy and Origin*, Kimberley, M. M., Ed., University of Toronto Press, Toronto, Canada, **1978**, p. 126. (b) Fleischer, M.,*Glossary of Mineral Species*, Mineralogical Record Inc., Bowie, Maryland, **1975**. (c) *The Encyclopedia of Mineralogy*, Frye, K., Ed., Hutchinson Ross Publishing Co., Straudsburg, PA, **1981**. (d) Roberts, W. L., Campbell, T. J., Rapp, Jr., G. R., *Encyclopedia of Minerals*, 2nd Ed., Van Nostrand Reinhold Co., New York, NY, **1981**.

21) (a) Shilton, M. G., Howe, A. T., *J. Solid State Chem.*, **1980**, 34, 137. (b) Morosin, B., *Phys. Lett.*, **1978**, 65A, 53. (c) Lloyd, M. H., Bischoff, K., Peng, K., Nissen, H. U., Wessicken, R., *J. Inorg. Nucl. Chem.*, **1976**, 38, 1141.

22) Liu, Y.-J., Kanatzidis, M. G., *Inorg. Chem.*, **1993**, 32, 2989-2991.

23) Zalkin, A., Ruben, H., Templeton, D. H., *Inorg. Chem.*, **1978**, 17, 3701-3702.

24) (a) Brandenburg, N. P., Loopstra, B. O., *Cryst. Struct. Commun.*, **1973**, 2, 243. (b) Cordfunke, E. H. P., *J. Inorg. Nucl. Chem.*, **1972**, 34, 1551.

25) Zachariasen, W. H., *Acta Crystallogr.*, **1948**, 1, 281-285.